

CRANFIELD UNIVERSITY

School of Applied Sciences

PhD THESIS

Inhibition of Weld Corrosion in Flowing Brines
Containing Carbon Dioxide

Khaled Alawadhi

CRANFIELD UNIVERSITY

School of Applied Sciences

PhD THESIS

Academic Years 2005-2009

Khaled Alawadhi

Inhibition of Weld Corrosion in Flowing Brines
Containing Carbon Dioxide

Supervisor: Dr. M. J. Robinson

January 2009

©Cranfield University, 2008. All rights reserved. No part of this publication may be reproduced without a written permission of the copyright holder

Abstract

The aim of this research was to study the effectiveness of a typical oilfield corrosion inhibitor, which is considered to be a green inhibitor (non toxic to the environment) in controlling internal corrosion of welded X65 pipeline steel in brines saturated with carbon dioxide at one bar pressure, under dynamic flowing conditions, over a range of temperatures.

Several experimental configurations were used ranging from a simple flat plate design to a novel rotating cylinder electrode, to allow high shear stress to be achieved.

The rotating cylinder electrode (RCE) apparatus was designed to allow steel from the weld metal, heat affected zone (HAZ) and parent material to be galvanically coupled and tested in high shear stress conditions. In producing the RCE, the three regions of the weld were identified by optical metallography and samples of each were machined to produce cylindrical electrodes, which were mounted on a motor driven shaft. Electrical connections were made to the three electrodes via a high quality slip-ring assembly.

The galvanic currents flowing between the regions of the weld were recorded using zero-resistance ammeters and their self-corrosion rates were found by uncoupling the electrodes and performing polarization resistance measurements.

For static conditions the inhibitor had an effective performance and after a short initial period during which film formation took place, at longer exposure times a dramatic reduction of corrosion rate was obtained.

Under flowing conditions, both the galvanic currents and the self-corrosion rates were found to increase with the shear stress, as the rotational speed of the RCE was increased. The total corrosion rate of each weld region was assessed from the sum of the self-corrosion and galvanic contributions.

In most cases, the weld metal and HAZ were shown to be cathodic to the parent material and this was considered to be a desirable situation as localised corrosion of the weld was minimised. However, in some circumstances, including inhibition of pre-corroded steel surfaces, a current reversal took place, which resulted in accelerated corrosion of the weld. These findings are explained in terms of the protective nature of the films that form on each region of the weld.

Acknowledgements

I would like to express my great gratitude to Dr. Mike Robinson for his generous guidance and moral support of my research. This thesis is attribute to his immense patience and his exceptional guidance and mentorship during my entire stay at Cranfield University.

I would also like to thank the technical staff at Cranfield University, including Mr. Andrew Dyer, Dr Matthew Kershaw, Mrs. Rukhsana Ormesher, Mrs Christine Kimpton, Mr Bryan and Mr Tony Parker for their assistance in technical matters and their precious help during the experimental part of the project, and my fellow students: Jalal Alsarraf, Cardilli, Emanuele, and Allison, Crispin for providing a wonderful research environment. They offered great help and encouragement..

I would also like to acknowledge the contribution of the consortium of PAAET (Public Authority of Training and Applied Education (State of Kuwait) whose continuous financial support and technical guidance made this research possible.

In addition, I would like to acknowledge my indebtedness to my committee members for their supervision.

Lastly, and also most importantly, I would like to thank my Mom, Dad, wife (Sawsan), my lovely daughter (Jana) and all my family members for their love, support, encouragement, and understanding. I know I can always count on them for whatever I need. I would like to dedicate this thesis to them.

Table of contents

CHAPTER 1 INTRODUCTION	1
1.1 Background to this study	1
1.2 Objectives of this study	3
1.3 Scope of this study.....	4
1.4 Overview of this thesis	5
CHAPTER 2 LITERATURE REVIEW	6
2 CORROSION	6
2.1 Basic Concept of Corrosion.....	6
2.2 Types of Corrosion	7
2.2.1 Localized Corrosion	7
2.2.2 Galvanic Corrosion.....	10
2.2.2.1 Preferential Weld Corrosion (PWC).....	11
2.3 CO ₂ Corrosion	16
2.3.1 Formation of reactive species in the bulk.....	17
2.3.2 Electrochemical Reactions (At the surface)	18
2.4 The Corrosion Product Film	20
2.4.1 Iron Carbonate (FeCO ₃)	20
2.4.2 Iron Carbide (Fe ₃ C).....	22
2.5 Factors Affecting CO ₂ Corrosion	22
2.5.1 Effect of Pressure	22
2.5.2 Effect of Temperature.....	24
2.5.3 Effect of Velocity	26
2.6 Laboratory Test Method and Hydrodynamics Relationships	28
2.6.1 The Rotating Cylinder Electrode (RCE)	31
2.6.2 Hydrodynamics Parameters of the RCE (<i>Re</i> , <i>Sc</i> , <i>Sh</i>)	32
2.6.3 RCE Flow Domain and Boundary Conditions	37
2.7 Correlation of the RCE Test Method and Pipe Flow.....	38
2.8 Corrosion Inhibitors.....	41
2.8.1 Types and Mechanisms of Inhibitors	44
2.8.1.1 Environmental Conditions (Scavengers) [98].....	45
Interface Inhibitors	46
2.9 Factors Affecting Inhibitor Performance.....	50
2.9.1 Effect of Carbon Steel Microstructures, Chemical Composition and Pre-corrosion.....	50
2.9.2 Effect of the Temperature.....	54
2.9.3 Effect of Flow.....	55
2.10 Evaluation and Selection of Inhibitors	58
2.10.1 Inhibitor Efficiency.....	59
3 Introduction	60
3.1 Linear polarisation resistance	60
3.2 Zero Resistance Ammeter.....	62
3.3 AC Impedance	63
3.3.1 Concept of A.C. Impedance	64
3.3.2 NYQUIST PLOT	66
3.3.3 Equivalent Circuit Models.....	69
CHAPTER 4 EXPERIMENTAL WORK.....	72
4 SUMMARY.....	72
4.1 Specimen characteristics and preparations	73
4.2 Preliminary electrochemical measurements (Stagnant conditions)	76
4.2.1 Experimental setup and procedures.....	77
4.3 Flow Channel experiment.....	78

4.3.1 Flow Channel Apparatus	79
4.3.2 Experimental setup and procedures	80
4.4 Rotating Cylinder electrode experiments	81
4.4.1 Specimen characteristics and preparations	81
4.4.2 Rotating Cylinder Apparatus	82
4.4.3 Experimental Parameters	89
4.4.4 Experimental setup and procedures	90
4.4.5 Surface Characterisation Techniques	92
4.4.6 Rotating cylinder electrode (EIS investigations)	94
4.4.6.1 Sample Preparation	94
4.4.6.2 AC Impedance System Setup and procedures	94
Preliminary Experiments	97
5 Under Static Conditions.....	97
5.1 Analysis of galvanic couple tests under static & sweet corrosion (CO ₂).....	97
5.2 Analysis of LPR tests under static & sweet corrosion (CO ₂)	99
5.3 Total corrosion rate of weld components in static conditions with CO ₂	101
5.4 Analysis of galvanic couple tests under static & (CO ₂) with inhibitor addition.....	103
5.5 Analysis of LPR tests under static & (CO ₂) with inhibitor addition.....	105
5.6 Analysis of galvanic couple tests under flowing & (CO ₂) conditions	107
5.7 Analysis of LPR test under flowing & CO ₂ conditions	109
5.8 Analysis of galvanic couple tests under flowing & CO ₂ conditions with inhibitor addition....	111
0	
5.9 Analysis of LPR test under sweet corrosion CO ₂ with flow condition and inhibitor addition .	112
5.10 Comparison of the corrosion inhibitor efficiency for the three sections under static and flow conditions	114
6 Rotating Cylinder Electrode Results (Part One).....	117
6.1 Analysis of galvanic couple tests under uninhibited (static -1000 rpm) conditions for 3 Days.....	117
6.2 Analysis of LPR tests under uninhibited conditions for 3 Days	119
6.3 Analysis of galvanic test under inhibited conditions for 3 days	121
6.4 Analysis of LPR tests under inhibited conditions.....	123
6.5 Inhibitor efficiency under (Static – 4000 rpm) and sweet conditions.....	125
7 Overview of the Most Significant Rotating Cylinder Electrode Results	126
7.1 Analysis of galvanic couple tests under uninhibited & CO ₂ conditions for one day	126
7.2 Analysis of LPR under uninhibited & sweet corrosion conditions after one day of exposure	129
7.3 Analysis of galvanic couple tests under inhibited & sweet corrosion conditions.....	131
7.4 Analysis of LPR test under inhibited & (CO ₂) conditions.....	135
7.5 Inhibitor efficiency for uninhibited & inhibited under (static-5000 rpm) conditions.....	137
7.6 Comparison of LPR & galvanic current densities under uninhibited conditions	138
7.7 Comparison of LPR & galvanic current densities under inhibited conditions	139
8 Rotating Cylinder Electrode Results under High Temperatures (50⁰C & 70⁰C)	141
8.1 Analysis of galvanic couple tests under uninhibited and CO ₂ corrosion conditions at 50 ⁰ C & 70 ⁰ C.....	141
8.2 Analysis of LPR tests under uninhibited and CO ₂ corrosion conditions at 50 ⁰ C & 70 ⁰ C ..	145
8.3 Analysis of galvanic couple tests under inhibited and CO ₂ corrosion conditions at 50 ⁰ C & 70 ⁰ C	147
8.4 Analysis of LPR tests under inhibited conditions and CO ₂ corrosion conditions at 50 ⁰ C & 70 ⁰ C	150
9 Electrochemical Impedance Spectroscopy	153
9.1 Preliminary Test	153

9.2 A.C. Impedance under Static & CO ₂ Conditions.....	153
9.3 A.C. Impedance under flowing & CO ₂ conditions with the presence of inhibitor	155
9.3.1 EIS for Parent metal at 50 ⁰ C and 70 ⁰ C	156
9.3.2 EIS for Weld Metal at 50 ⁰ C and 70 ⁰ C	159
9.3.3 EIS for HAZ metal at 50 ⁰ C and 70 ⁰ C	162
10 Discussion.....	165
10.1 Galvanic Current Measurements	166
10.1.1 Uninhibited Conditions.....	166
10.1.2 Inhibited Conditions	167
10.2 Self-corrosion rates.....	168
10.2.1 Uninhibited conditions.....	168
10.2.2 Inhibited conditions	171
10.3 Total corrosion rates.....	172
10.3.1 Uninhibited conditions.....	172
10.3.2 Inhibited conditions	172
10.4 Effects of higher temperatures and the role of surface films.....	173
10.4.1 Uninhibited conditions.....	173
10.4.2 Inhibited conditions	177
10.5 Electrochemical Impedance Spectroscopy (EIS)	178
11 Surface characterisation (XRD, SEM and XPS)	187
11.1 XRD Test.....	187
11.2 SEM/EDX analyses	192
11.2.1 Under Static Conditions.....	192
11.2.2 Under Flowing Conditions.....	195
11.3 XPS analyses	200
12 Conclusions	204
13 Recommendations for future work.....	207
14 References	208
15 Appendixes	219
Appendix (1)	219
Calculation of corrosion rate from LPR measurements	219
Appendix (2)	220
Calculation of shear stress.....	220
Appendix (3)	222
Calculation of RCE hydrodynamic parameters.....	222
Appendix (4)	223
Mass calculation of Fe ²⁺ corroded from known area and test duration of the three weld regions (PM, WM, HAZ).....	223
Appendix (5)	224
Appendix (6)	226

List of Figures

Figure 2-1: A schematic of electrochemical mechanism of iron corrosion [2].....	7
Figure 2-2: The effect of iron carbonate supersaturation on localised attack as quantified by the pitting factor, showing that the most severe pitting is obtained for relatively small supersaturation when partially protective films are formed [11]	9
Figure 2-3: Galvanic corrosion [15].....	10
Figure 2-4: Factors affecting galvanic corrosion [16].....	11
Figure 2-5: Preferential weld attack of 1% nickel weld consumable [6]	12
Figure 2-6: The effect of nickel on the corrosion rate of steel in a sweet environment [25]	14
Figure 2-7: CO ₂ corrosion process for carbon steel under sweet corrosion conditions.....	19
Figure 2-8 : Predicted and experimental measured corrosion rates showing the effect of CO ₂ partial pressure in those experiments no protective films formed [51]	23
Figure 2-9: Predicted and experimentally measured corrosion rates showing the effect of temperature [55]	25
Figure 2-10: Nomogram for predicting CO ₂ corrosion of carbon steel is based on the DeWaard-Milliams equation [60]	26
Figure 2-11: Predicted and experimentally measured corrosion rates showing the effect of velocity in the absence of iron carbonate scales [40]	27
Figure 2-12: Effect of flow on corrosion rate [65]	28
Figure 2-13: Velocity profile for inner cylinder rotating and the outer cylinder at rest [79]	37
Figure 2-14: Effect of inhibitors on polarisation curves [93].....	43
Figure 2-15: Inhibitor classification [97]	45
Figure 3-1: Obtaining R _p from applied – current linear polarisation curve.....	62
Figure 3-2: Schematic diagram of sample connection to Zero Resistance Ammeters.....	63
Figure 3-3: Randles type equivalent circuit components [128].....	65
Figure 3-4: Nyquist plot for a simple electrochemical one time constant system [128]	67
Figure 3-5: R _{ct} & R _s measurements in a pure charge transfer controlled situation [128].....	68
Figure 3-6: Shape of the Nyquist plot when it changes from charge transfer control to diffusion control [128].....	69
Figure 3-7: Equivalent electrical circuit used to represent a parallel resistor, R and capacitor, C , combination (a) and its Nyquist (b) and Bode (c) impedance plots [129]	70
Figure 3-8: Equivalent electrical circuit used to represent the unpainted metal/solution interface (a) and its Nyquist (b) and Bode (c) impedance plots [129]	70
Figure 3-9: Equivalent electrical circuit used to represent the painted metal/solution interface in the absence of diffusion (a) and its Nyquist (b) and Bode (c) impedance plots [129]	71
Figure 3-10: Equivalent electrical circuit used to represent the painted metal/solution interface in the presence of diffusion (a) and its Nyquist (b) and Bode (c) impedance plots [129].....	71
Figure 4-1: Typical microhardness profile over a weldment of PM, WM and HAZ.....	73
Figure 4-2: CCT Diagram with four cooling rates including the phases (A) austenite,.....	74
Figure 4-3: Diagram showing the weldment sectioning	75
Figure 4-4: Parent – Weld – HAZ metallography	75
Figure 4-5: Shows a view of the sample in epoxy mount	76
Figure 4-6: Sample under static conditions.....	78
Figure 4-7: Flow channel assembly	79
Figure 4-8: Flow loop assembly	80
Figure 4-9: Welded cylindrical electrode sections	82

Figure 4-10: Rotating cylinder electrode components (A) Cylindrical working electrodes, (B) Slip ring, (C) Slip ring mounted on top of the cylindrical working electrode shaft, (D) Standard glass cell.....	84
Figure 4-11: Section through electrode (Full size).....	85
Figure 4-12: Rotating cylinder electrode assembly.....	86
Figure 4-13: Rotating cylinder electrode setup.....	87
Figure 4-14: Removable working electrode assemblies.....	88
Figure 4-15: Impedance system components under static conditions.....	95
Figure 4-16: Impedance system components under flowing conditions.....	95
Figure 4-17: EIS parameters.....	96
Figure 5-1: Galvanic current in static & sweet conditions.....	98
Figure 5-2: Galvanic current densities in static & sweet conditions.....	98
Figure 5-3: Galvanic current for repolished surface 10 days.....	99
Figure 5-4: LPR test current density for polished surface under static and CO ₂ conditions in 10 day.....	100
Figure 5-5: LPR Test for polished surface under static & CO ₂ conditions in 10 days.....	100
Figure 5-6: Comparison of LPR & galvanic current density for 10 days.....	102
Figure 5-7: Galvanic current in static condition & inhibitor for 5 Days.....	104
Figure 5-8: Galvanic current densities in static condition & inhibitor for 5 Days.....	104
Figure 5-9: Average galvanic currents for static & inhibitor condition for 5 days.....	105
Figure 5-10: Current density for inhibited samples under static conditions for 5 days.....	106
Figure 5-11: Corrosion rate for inhibited samples under static condition for 5 days.....	106
Figure 5-12: Galvanic current densities under sweet corrosion (CO ₂) & flowing conditions for 10 days.....	108
Figure 5-13: Average galvanic currents for flow & sweet corrosion over 10 days.....	108
Figure 5-14: Current density under flowing & CO ₂ conditions after 10 days.....	109
Figure 5-15: Corrosion rate under flowing & CO ₂ conditions after 10 days.....	110
Figure 5-16: Galvanic current density under inhibited & flowing conditions for 10 Days.....	111
Figure 5-17: Average galvanic current densities under inhibited and flowing conditions over 10 days.....	112
Figure 5-18 Current density for inhibited samples under flow conditions for 10 days.....	113
Figure 5-19 Corrosion rate for inhibited samples under flow conditions for 10 Days.....	113
Figure 5-20: Corrosion rate comparisons for static conditions with inhibitor and no inhibitor after 5 days.....	115
Figure 5-21: Corrosion rate comparisons under flowing conditions with inhibitor and no inhibitor after 10 days.....	115
Figure 5-22: Comparisons of the inhibitor efficiency under static (5 days) and flowing conditions for 10 days.....	116
Figure 7-1: Galvanic current under uninhibited & CO ₂ corrosion conditions.....	127
Figure 7-2: Galvanic current density under uninhibited & CO ₂ corrosion conditions.....	128
Figure 7-3: Average galvanic currents under uninhibited & CO ₂ corrosion conditions.....	128
Figure 7-4: Corrosion current density under uninhibited & CO ₂ conditions (Exp 1).....	130
Figure 7-5: Current density under uninhibited & CO ₂ conditions (Exp 3).....	130
Figure 7-6: Corrosion rate under uninhibited & CO ₂ conditions.....	131
Figure 7-7: Galvanic current under inhibited & CO ₂ conditions (Exp 2).....	132
Figure 7-8: Galvanic current under inhibited & CO ₂ conditions (Exp 4).....	133
Figure 7-9: Galvanic current density under inhibited & CO ₂ conditions (Exp2).....	133
Figure 7-10: Galvanic current density under inhibited & CO ₂ conditions (Exp 4).....	134
Figure 7-11: Average galvanic current density under inhibited & CO ₂ conditions.....	134
Figure 7-12: Current density under inhibited & CO ₂ conditions (Exp2).....	135
Figure 7-13: Current density under inhibited & CO ₂ conditions (Exp 4).....	136
Figure 7-14: Corrosion rate under inhibited and sweet corrosion.....	136
Figure 7-15: Inhibitor efficiency under CO ₂ corrosion conditions (Exp1 – Exp 2).....	137

Figure 7-16: Inhibitor efficiency under CO ₂ corrosion conditions (Exp 3 – Exp 4)	138
Figure 7-17: Comparison of LPR & galvanic current density under uninhibited conditions....	139
Figure 7-18: Comparison of LPR & galvanic current densities under inhibited conditions	140
Figure 8-1: Galvanic current under uninhibited conditions	142
Figure 8-2: Galvanic current under uninhibited conditions at 70°C.....	142
Figure 8-3: Galvanic current density under uninhibited conditions at 50°C	143
Figure 8-4: Galvanic current density under uninhibited conditions at 70°C	143
Figure 8-5: Average galvanic current under uninhibited at 50°C Conditions	144
Figure 8-6: Average galvanic current under uninhibited at 70°C Conditions	144
Figure 8-7: Current density under uninhibited and sweet corrosion at 50°C	145
Figure 8-8: Current density under uninhibited and sweet corrosion at 70°C	145
Figure 8-9: Corrosion rate under uninhibited and sweet corrosion at 50°C	146
Figure 8-10: Corrosion rate under uninhibited and sweet corrosion at 70°C	146
Figure 8-11: Galvanic current under inhibited conditions at 50°C.....	147
Figure 8-12: Galvanic current density under inhibited conditions at 70°C	148
Figure 8-13: Galvanic current density under inhibited conditions at 50°C	148
Figure 8-14: Galvanic current density under inhibited conditions at 70°C	149
Figure 8-15: Average galvanic current under inhibited conditions at 50°C	149
Figure 8-16: Average galvanic current under inhibited at 70°C Conditions	150
Figure 8-17: Current density under inhibited and sweet corrosion at 50°C	151
Figure 8-18: Current density under inhibited and sweet corrosion at 70°C	151
Figure 8-19: Corrosion rate under inhibited and sweet corrosion at 50°C	152
Figure 8-20: Corrosion rate under inhibited and sweet corrosion at 70°C	152
Figure 9-1: Nyquist plot for preliminary test carried out with a dummy cell	153
Figure 9-2: Nyquist plot of carbon steel under static and CO ₂ conditions at initial stage of immersion.....	154
Figure 9-3: Nyquist plot of carbon steel under static and CO ₂ conditions after 10 hour of immersion.....	155
Figure 9-4: A) Nyquist plot for PM at 50°C under Flowing and CO ₂ conditions after 10 hour of immersion, B) higher magnification of the high frequency region	156
Figure 9-5: A) Nyquist plot for PM at 70°C under flowing and CO ₂ conditions after 10 hour of immersion, B) higher magnification of the high frequency region	157
Figure 9-6: shows circuit parameters for PM at 50°C under inhibited and flowing conditions at lower frequency region.....	158
Figure 9-7: shows circuit parameters for PM at 70°C under inhibited and flowing conditions at lower frequency region.....	158
Figure 9-8: A) Nyquist plot for WM at 50°C under flowing and CO ₂ conditions after 10 hour of immersion, B) higher magnification of the high frequency region	160
Figure 9-9: A) Nyquist plot for WM at 70°C under flowing and CO ₂ conditions after 10 hour of immersion, B) higher magnification of the high frequency region	160
Figure 9-10: Shows circuit parameters for WM at 50°C under inhibited and flowing conditions	161
Figure 9-11: Shows circuit parameters for WM at 70°C under inhibited and flowing conditions	161
Figure 9-12: Nyquist plot for HAZ under flowing and CO ₂ conditions after 10 hour of immersion at 50°C	162
Figure 9-13: Nyquist plot for HAZ under flowing and CO ₂ conditions after 10 hour of immersion at 70°C	163
Figure 9-14: Shows circuit parameters for HAZ at 50°C under inhibited and flowing conditions	163
Figure 9-15: Shows circuit parameters for HAZ at 70°C under inhibited and flowing conditions	164
Figure 10-1: Galvanic current values as a function of the calculated shear stress and rpm.....	166

Figure 10-2: Corrosion rates of C steel as a function of shear stress for the RCE [75]	168
Figure 10-3: Nomograph for predicting CO ₂ corrosion of welded X65 carbon steel based on stagnant and room temperature conditions [60].....	169
Figure 10-4: LPR test under different temperature and uninhibited conditions.....	174
Figure 10-5: Corrosion rate densities as a function of the rotation speed of the electrode and solution temperature [135]	175
Figure 10-6: Relative concentration of carbonate species as a function of pH, 25C, 1 bar [135]	176
Figure 10-7: LPR test under different temperature and inhibited conditions.....	177
Figure 11-1: XRD patterns of corrosion products of weldment metal after 5 days of exposure in 3.5% artificial seawater under different scan periods:	189
Figure 11-2: XRD patterns of corrosion products of weldment metal after 5 days of exposure in 3.5% artificial seawater for an overnight scan	190
Figure 11-3: SEM image of weld metal X65 C-steel exposed to static and 70 ⁰ C conditions ...	193
Figure 11-4: FIB etched cross-section of the weld metal under static and 70 ⁰ C conditions....	193
Figure 11-5 : Higher magnification of FIB etched cross-section for the weld metal.....	194
Figure 11-6 : Corresponding EDX spectrum of the corrosion products film.....	194
Figure 11-7: FIB cross section of welded X65 c-steel exposed to RCE: 5000 rpm and 70 ⁰ C. (A) Parent metal. (B) Weld metal. (C) HAZ	196
Figure 11-8: EDX spectra showing the elements for the A) Parent metal, B) Weld metal and C) HAZ.....	198
Figure 11-9: Initial high resolution XPS scan of the films found on the corrosion specimen at 70 ⁰ C under inhibited and turbulent flow of 5000 rpm.	200
Figure 11-10: High resolution XPS scans after 6 etches showing the sulfur element detected at 70 ⁰ C under inhibited and turbulent flow of 5000 rpm.	201
Figure 11-11 (A-B) : High resolution XPS scans of the films found on the corrosion specimen at 70 ⁰ C under inhibited and turbulent flow of 5000 rpm after 25 and 75 etches.....	203
Figure 11-12: XPS depth profile for inhibited weldment under flowing (5000 rpm) and 70 ⁰ C conditions	203
Figure 15-1: LPR result for carbon steel under static conditions.....	219

List of Tables

Table 1 : Mass Transport Relationship for Important Flow Regimes [71]	30
Table 2: Common Circuit Elements, Symbols and their Impedance	66
Table 3 : Chemical Composition of X65 Pipeline Steel	73
Table 4 : Summary of the Test Parameters	89
Table 5: Flow parameters.....	126

Appendix

Appendix (1).....	
Appendix (2).....	
Appendix (3).....	
Appendix (4).....	
Appendix (5).....	
Appendix (6).....	

THE THESIS

CHAPTER 1 INTRODUCTION

1.1 Background to this study

According to Fontana [1], “Corrosion is defined as destruction or deterioration of the material by chemical or electrochemical attack because of reaction with its environment”. Corrosion has a very important economic impact in the petroleum industry. Oilfield production environments can range from practically zero corrosion to extremely high rates of corrosion.

Corrosion cost has been evaluated in sectors such as power plants where the cost of corrosion in 1988 was estimated at 5.37 billion €. The latest study was carried out in the UK with an annual cost for the chemicals and petrochemical sectors of 2720 million €. In the USA, the direct cost of corrosion was 36 billion \$ in 2002. The corrosion-related cost to the gas and liquid transmission pipelines industry is 504\$ - to 608\$ billion annually [2].

Internal corrosion of carbon steel pipelines is a common and serious problem in oil and gas production, which are designed for long-term operation. It involves an interaction between the metal wall and the flowing fluids. This problem has caused the consideration of many corrosion control programmes and research in various oilfields around the world.

There is extensive use of carbon steels as materials of construction for pipes in the oil and gas industries. These steels are relatively inexpensive construction materials for many applications and therefore involve less capital investment, but they usually exhibit poor corrosion resistance properties and as a result there is internal corrosion.

The process fluid in oil and gas production contains a range of dissolved salts and gases. The major factors controlling corrosion rates are CO_2 , H_2S , S, polysulfide, organic acids, composition of liquids, flow conditions, inorganic anions, such as chlorides, oxygen and temperature.

Sweet corrosion is the most predominant form of corrosion encountered in oil and gas production due to the presence of carbon dioxide (CO_2) in combination with water. CO_2 is a naturally occurring component in many oil and gas fields. Although dry CO_2 is non corrosive to metal and alloys, in combination with water in the produced brines, CO_2 forms weak carbonic acid (H_2CO_3) which is corrosive and can severely damage downhole and surface production facilities [3].

Water may be present either as an aqueous phase or by re-injected production water down hole to maintain the reservoir pressure and stability as well as perform water flooding to drive oil out of the formation. In reservoirs, connate water is gathered below the hydrocarbon layer and thus water increases with well age. As the field ages, the ratio of water: oil in the produced fluid increases and can reach levels of 95% or higher; this rise in water content implies an increase of corrosion problems [4].

Approximately 60% of oilfield corrosion problems are related to the presence of CO_2 , mainly due to insufficient knowledge as well as predictive capability and poor resistance of carbon and low alloy steels to this type of corrosion attack [5].

Pipeline failures usually occur not as a result of uniform corrosion but from localised attack, generally as pitting or galvanic corrosion of welds. These forms of attack are much more damaging and difficult to predict. They place high demands upon the corrosion inhibitors, which need to remain effective under high flow rates and turbulent operating conditions.

A new chemical family of corrosion inhibitors has been developed. These products were designed as green corrosion inhibitors to mitigate corrosion in the presence of carbon dioxide. Green inhibitor is not an absolute goal or destination, but a dedication to a process for continual improvement, where the environment is considered along with the chemistry. Chemical products should be designed to preserve the efficiency of function, while reducing the impact on the environment [6].

The selection of corrosion inhibitors for oil and gas pipes lines starts with evaluation in the laboratory and is followed by testing and/or use in the field. The test methods available for evaluating inhibitor performance in flowing conditions sometimes use rotating cylinder electrodes (RCEs), which can achieve the required hydrodynamic conditions on the metal surface. However, the technical difficulties of making multiple electrical connections to rotating electrodes must be overcome by the design of suitable electrode assemblies.

The benefit of using RCE is that the hydrodynamic conditions are very well defined. It is feasible to translate the conditions that are known to exist in a production pipeline to those that should be used in laboratory tests with an RCE. Shear stress in the fluid at the metal surface was taken to be the important parameter for comparison but a more modern approach is to use the Sherwood number as this defines the rate of mass transfer that is important in controlling many corrosion reactions.

In this project it is intended that the advances already made in understanding the interrelationships between corrosion and hydrodynamics were extended to the study of weld corrosion using the RCE test method.

1.2 Objectives of this study

- Develop and improve the use of the RCE test method for the study of weld corrosion in steel exposed to brines saturated with CO₂, under conditions that simulate typical pipeline flow, with an investigation of their corrosion behaviour by computer-controlled electrochemical means using accelerated corrosion techniques.
- Compare the results obtained from the RCE with those for welds that will be tested under similar conditions using a flow channel that was developed in an earlier project at Cranfield.
- Study the influence of hydrodynamics on the effectiveness of a new green inhibitor, supplied by Clariant Oil Services, on preferential weld corrosion.
- Study the film formed on the metal surface as the inhibitor develops.

- Investigate the causes and incidence of polarity reversal of the weld components after inhibitor application.

1.3 Scope of this study

It was proposed that the RCE experiments be carried out using existing equipment (Thompson Electrochem Ltd), which is rated for speeds up to 10,000 rpm, with modifications that would be carried out to incorporate the multi-channel electrical connections required for the study of weld corrosion.

A sample of welded X65 plate was polished and etched to identify the parent material, weld metal and heat affected zone. Sections were machined from each region, electrical connections were attached and the three different parts were mounted in resin and re-machined to form cylindrical specimens. In this way, the three regions of the weld were electrically isolated from each other. A set of high quality, multi-element slip rings was mounted on the motor driven spindle of the test equipment to take the electrical signals from the weld sections to the electrochemical instrumentation.

The corrosion behaviour of each weld component in the rotating cylinder electrode was measured using a range of electrochemical methods. Corrosion rate measurements were carried out using the linear polarisation technique (LPR), which can be repeated over long periods without changing the steel from its freely corroding condition. Similarly, open circuit potential measurements were recorded as an important indication of the activity of the corroding surface and the influence of inhibitor additions.

The galvanic currents between each weld component were recorded during the test using a multi-channel zero resistance ammeter and data logging PC. In this way, the influence of the hydrodynamic condition on the galvanic corrosion of the weld was studied, together with the effectiveness of the corrosion inhibitor. In some tests, the influence of surface films caused by prior corrosion of the steel was investigated as this is known to affect inhibitor efficiency and lead to current reversal in some cases.

The total corrosion rate of the material was found from the sum of the self corrosion rates (LPR measurements) and galvanic corrosion. This work has been presented at the NACE 2008 conference [7].

Alawadhi, K., M. Robinson, G. Winning; A. Chalmers (2008). Inhibition of Weld Corrosion in Flowing Brines Containing carbon dioxide. Corrosion, conference and Expo (March 16-20), paper 08622.

Tests were carried out in artificial seawater, saturated with CO₂ and containing CORRTREAT 05-193, supplied by Clariant Oil Services. The majority of the work was at ambient temperature but some tests were conducted at a higher temperature.

1.4 Overview of this thesis

Briefly, the structure of this thesis is as follows: In Chapter 2, the current understanding of CO₂ corrosion, experimental studies on corrosion, electrochemical methods of evaluating inhibitors and the behaviour of inhibitors on preferential weldment corrosion with the effects of various parameters are reviewed. Chapter 3 describes the experimental setup, test procedures and the tool used in the present study for turbulence, mass transport and corrosion rate. In chapter 4, experimental results are presented. Chapters 5, 6, 7, 8 and 9 provide analysis and discussion of the research findings. Discussions, conclusions and recommendations for future work of the present study are outlined in chapters 10, 11 and 12 respectively.

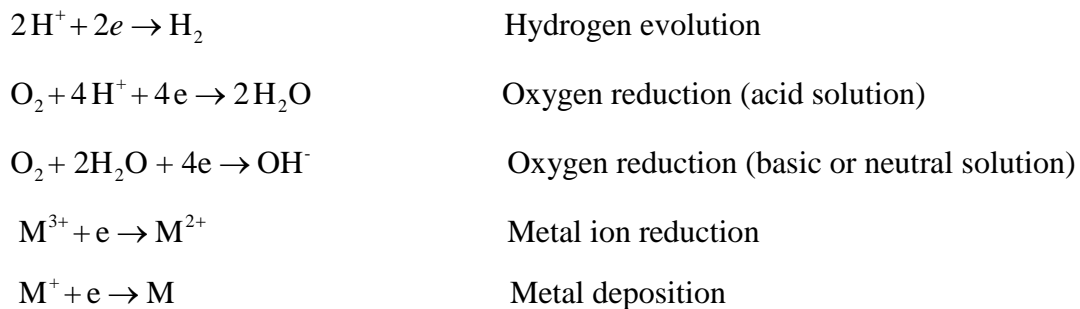
CHAPTER 2 LITERATURE REVIEW

2 CORROSION

2.1 Basic Concept of Corrosion

Corrosion has been classified as low and high temperature, wet and dry corrosion. Carbon and low alloy steel are widely used, mainly for economic reasons. Nevertheless their corrosion resistance is limited in certain environmental circumstances. Moreover, they may have different microstructures which influence their mechanical properties and corrosion resistance in certain environments.

Corrosion consists of an oxidation reaction (anode) and a reduction reaction (cathode) at the surface of the corroding material. The oxidation reaction generates metal ions and electrons, where electrons are then consumed in the reduction reaction. There are several common cathodic reactions that are frequently encountered in metallic corrosion. The most common are [1]:



For environments with water present, including moisture in the air, the electrons are consumed by converting oxygen and water to hydroxide ions. In iron and many iron alloys these hydroxide ions in turn combine with iron ions to form ferrous hydroxide ($\text{Fe}(\text{OH})_2$). Subsequent reactions form a mix of magnetite (Fe_3O_4) and hematite (Fe_2O_3). This red-brown mixture of iron oxides is rust. This is illustrated schematically in Figure 2-1.

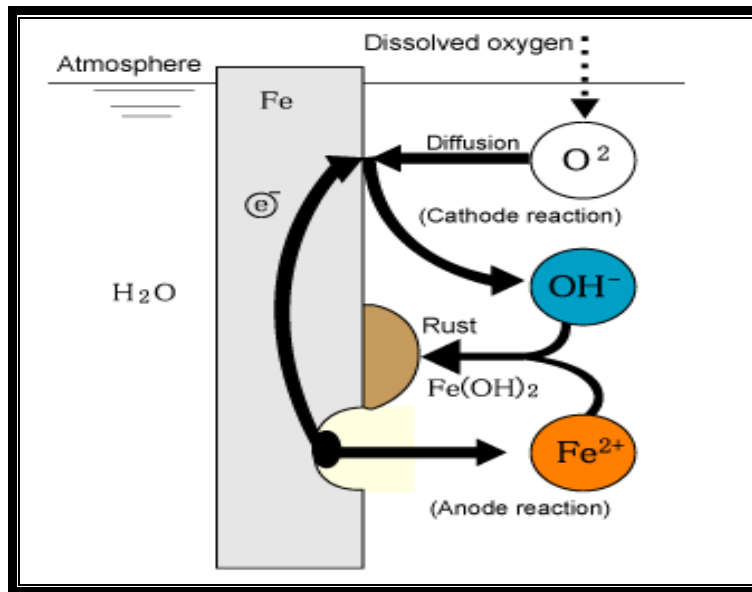


Figure 2-1: A schematic of electrochemical mechanism of iron corrosion [2]

2.2 Types of Corrosion

Corrosion occurs in several forms, depending upon the metal involved, its size and shape, specific function, atmospheric conditions, and the corrosion producing agents present. The corrosion types described in this section are the most common forms found in pipeline weldments which have caused numerous failures in the oil and gas industries.

2.2.1 Localized Corrosion

Localised corrosion is defined as the selective removal of metal by corrosion at small areas or zones on a metal surface in contact with a corrosive environment, usually a liquid. It usually takes place when small local sites are attacked at a much higher rate than the rest of the original surface. In order to operate the oil and gas pipelines under safe and reliable conditions, it is important to predict the internal corrosion that occurs in an environment containing CO₂. In oil and gas industry, localised corrosion is the most serious and frequent cause of pipeline failure. Therefore, it is necessary to predict the occurrence of localized CO₂ corrosion of carbon and low alloy steel materials.

The key factor contributing to localised CO₂ corrosion is the corrosion product scale with its non uniform formation and localised breakdown. Studies covering localised CO₂ corrosion of carbon steels have been conducted in single-phase flows where the localised attack is always associated with the formation or breakdown of iron carbonate films. Only a few corrosion studies have been performed in multi-phase flows, although in field applications multi-phase flows prevail [8].

It is believed that two main steps are involved in the localised corrosion process: initiation, and propagation. In CO₂ environments, a protective iron carbonate (FeCO₃) scale may form on the steel surface as a by-product of the corrosion process. Any localised damage to this scale may be one of the ways to initiate localised corrosion. However, in some cases localised corrosion is initiated but does not propagate [9].

Some initial work has been done in rotating-cylinder glass-cell experiments on scale removal mechanisms which were found to be associated with hydrodynamic forces and chemical dissolution [10]. Recently, an independent study by Sun and Netic [11] has suggested that localised attack can occur when partially protective scales form. It is well known that when fully protective scales form, low corrosion rates are obtained and vice versa i.e. when no protective scales form a high rate of general corrosion is seen. Whenever the corrosive environment is an in-between situation, localised attack is initiated due to the stochastic nature of the processes underlying corrosion.

As it is difficult to assess the number, size and distribution of pits, a single parameter such as supersaturation or pitting factor can provide an easily understood representation of localisation. Pitting factor: ratio of the depth of the deepest pit resulting from corrosion ($CR_{max}-CR_{ave}$) divided by the average penetration as calculated from weight loss (CR_{ave}). A low value, close to zero, represents general corrosion while a high value, closer to 1 indicates localised corrosion accruing as shown in Figure 2-2. Where the hollow symbols denote supersaturation at the beginning of the experiments and red filled symbols denote the end of experiments.

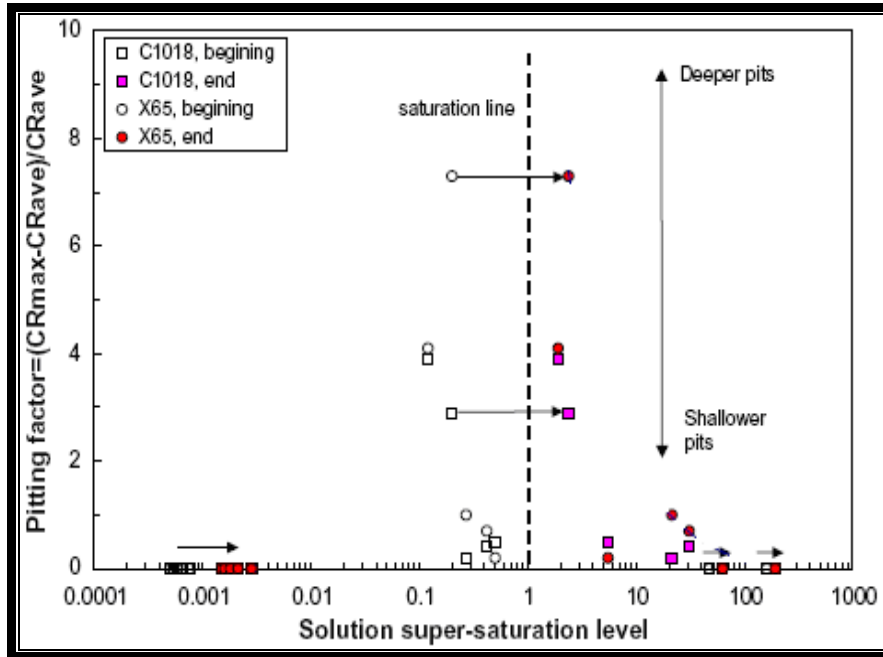


Figure 2-2: The effect of iron carbonate supersaturation on localised attack as quantified by the pitting factor, showing that the most severe pitting is obtained for relatively small supersaturation when partially protective films are formed [11]

More specifically, a relationship between localised corrosion susceptibility and the presence of pearlite bands in the steel microstructure was found. However, no correlation was evident between minor elemental concentrations (i.e., Ni, Cr, Mo) and corrosion resistance. It has been proposed that the corrosion susceptibility of the various microstructures may arise from variations in the distribution of carbon bearing phases within the steel. In the lined ferrite/pearlite structure, the carbon-bearing phase (pearlite) is distributed in layers whereas in the other structures the carbon-bearing phases are much more consistently distributed. It was found that steels with a lined ferrite/pearlite structure perform poorly in terms of localised corrosion and this was attributed to a segregated distribution of the iron carbide phase cementite (Fe_3C) [12].

It is well known that flow can accelerate corrosion of mild steel by increasing the mass transfer rates of corrosive species and/or by damaging the protective films formed on the steel surface. Schmitt et al. [13] performed numerous experiments and concluded that the beginning of localised attack was related to high near-wall levels of turbulence and the intrinsic growth stresses in the corrosion product scale.

Jiabin et al. [14] provided further information on the localized CO₂ corrosion on mild steel. Their results show that the iron carbonate scale can be partially removed by mechanical stresses, chemical dissolution or by both mechanisms acting simultaneously. The scale breakdown can happen for a variety of reasons, many of them related to fluid flow. It is hypothesised that following the scale damage, a galvanic effect is established between the scale covered surface (cathode) and the scale free surface (anode) leading to propagation of localised attack.

2.2.2 Galvanic Corrosion

The effect of coupling two different metals/alloys together, either directly or through an external path, increases the corrosion rate of the anodic alloy (the material with the more electronegative potential) and reduces or suppresses the corrosion rate of the cathodic alloy (the material possessing the more electropositive potential). The electrochemical degradation derived from joining two or more different or dissimilar alloys is termed galvanic corrosion [15]. This is illustrated schematically in Figure 2-3

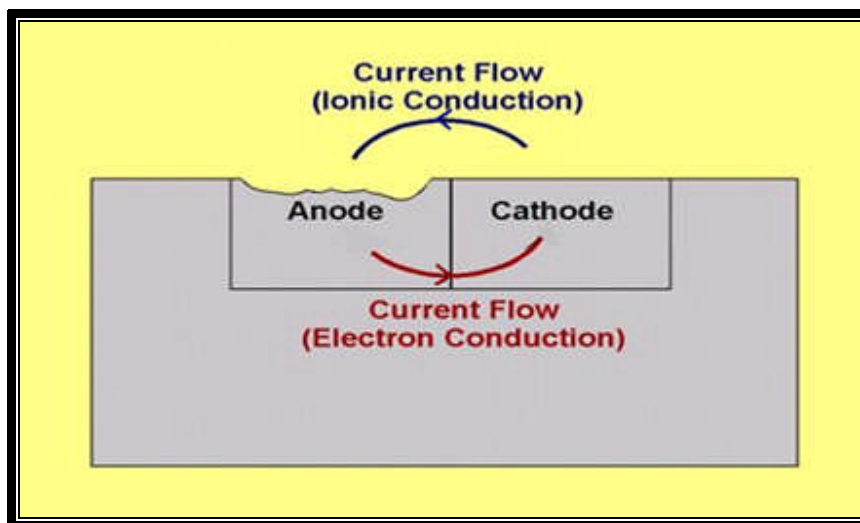


Figure 2-3: Galvanic corrosion [15]

The magnitude of the potential difference between the dissimilar materials cannot necessarily be used to predict the severity of galvanic corrosion because electrochemical potentials are a function of thermodynamics, not of the reaction kinetics that may occur. It is the surface kinetics that determines the severity of galvanic corrosion.

The extent of galvanic corrosion depends on many factors as shown in Figure 2-4. Standard test methods for galvanic corrosion are provided in ASTM G-71, G-82 and G-104

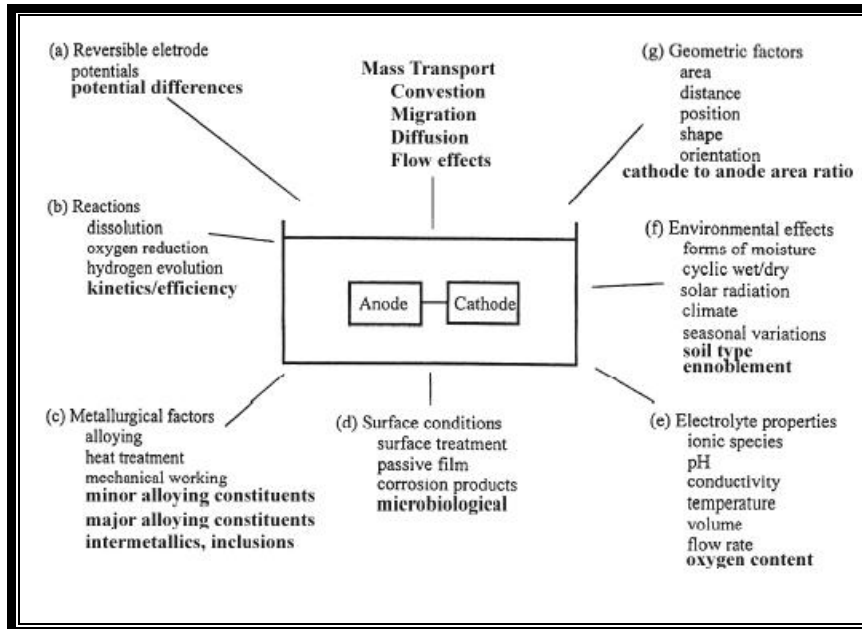


Figure 2-4: Factors affecting galvanic corrosion [16].

Flow can destroy the passive film of the more anodic member and expose the bared substrate to greater galvanic corrosion. Then galvanic corrosion can attack synergistically to remove the passive films of susceptible alloys. Surface shear stress is one measure of the force applied by fluid flow to the corrosion product film. For seawater, this takes into account changes in seawater density and kinematic viscosity with temperature and salinity [17].

2.2.2.1 Preferential Weld Corrosion (PWC)

Preferential Weld Corrosion (PWC) of carbon and low alloy steels used for pipelines and process and piping systems in CO₂ containing media has been observed increasingly. Although much of the PWC experience has been in the UK, including central, northern and southern sectors of the North Sea, and gas reception facilities on-shore, it has been also been experienced in the Gulf of Mexico. Preferential Weld Corrosion occurs by a galvanic corrosion mechanism.

The weld metal, heat affected zone (HAZ) and parent metal of the weldment present different metallurgical zones, with a different microstructure and also compositional differences. However, the composition of the parent metal and HAZ may be very similar. The term PWC usually describes the localised dissolution of metal associated with welds. It is a selective form of attack, which corrodes either the weld metal and/or the HAZ rather than the adjacent parent metal [18].

In the late 1980s, studies of carbon steel weld corrosion under simulated seawater injection conditions concluded that up to '1%w nickel containing' weld consumable, with beneficial to strength and toughness properties, should be used to minimise the risk of PWC. However, there have been instances where severe preferential weld metal corrosion has been reported in sweet environments under certain conditions combined with an adverse anodic to cathodic ratio [6]. An example of this type of problem is illustrated in Figure 2-5, in which preferential attack of the weld metal occurred.

From an inhibition point view, failures of nickel containing weldments in sweet service are now thought to be primarily a consequence of the inability of some inhibitors to penetrate a nickel-rich corrosion product on the weld metal in comparison to effective protection of the unalloyed parent pipe. The consequent potential difference between the unprotected weld and the adjacent inhibited parent material can lead to rapid localised attack of the weld metal [19].

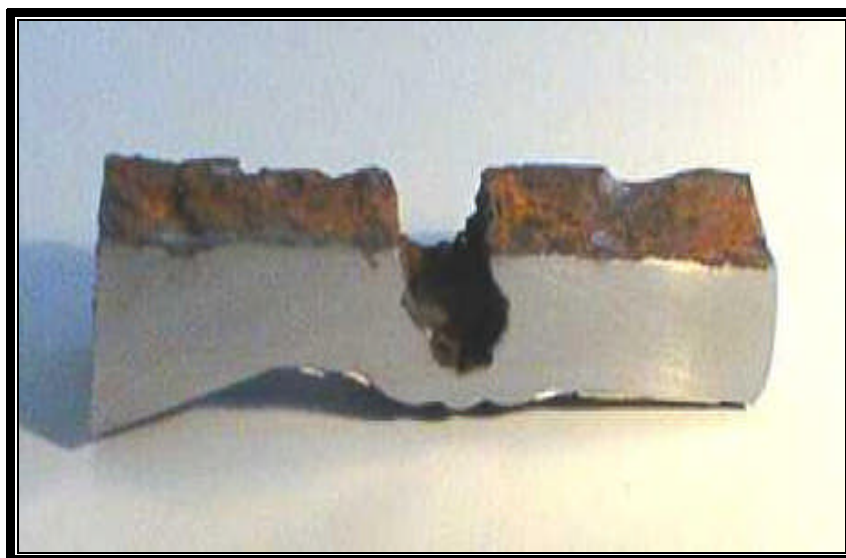


Figure 2-5: Preferential weld attack of 1% nickel weld consumable [6]

Studies have shown that PWC is influenced by several parameters including the environment (temperature, pH, partial pressure of CO₂, water composition), flow conditions, scaling effects, parent steel and weld composition, pre-corrosion times, inhibitor effectiveness and welding procedures.

Attempts to control PWC have previously involved making minor additions of noble metals (Ni, Cr, Mo, and Cu) in order to make the weld metal cathodic with respect to the adjacent parent metal and HAZ. Nevertheless, these additions must be made with caution since over-alloying can result in enhanced HAZ corrosion. According to reviews, the highest effect is encountered with additions of chromium. The corrosion rate is significantly decreased with an increasing Cr content [20].

Nose et al. [21] showed that using steels with 3% and 5% Cr gave better protection compared to chromium-free carbon steel, but 5% chromium steel suffered deeper localised attack than 3% chromium steel. On the other hand, Nice et al. [22] have presented results in a 5 months' field test exposure where 5% chromium steels showed superior corrosion resistance to general and localised corrosion compared to steels with 0.2-3% Cr.

Queen et al. [23] reported that 1% Ni showed the poorest resistance to PWC. Furthermore, silicon additions to the weld metal also produced detrimental results, whilst Mo had little effect, and Cr showed no benefit. They have suggested that welding consumable deposition giving weld metal with a composition matching the unalloyed parent metal was found to be the least prone to PWC attack.

Recent studies by Turgoose et al. [24] in a high pressure flow loop at 60⁰C, pH 4-6, 0.2 Mpa CO₂ showed that steels with the addition of nickel (1.4% Ni and 3.35% Ni) corroded faster than steel with low Ni and similar Cr contents in environments without the presence of chlorides.

Similar findings were reported by Denpo and Ogawa [25] who found that nickel addition up to 1.7%Ni also increased the corrosion rate relative to nickel free gradeX65 steel by 1.5-2X in 10% NaCl solutions, 1 bar CO₂, 80⁰C as shown in Figure 2-6.

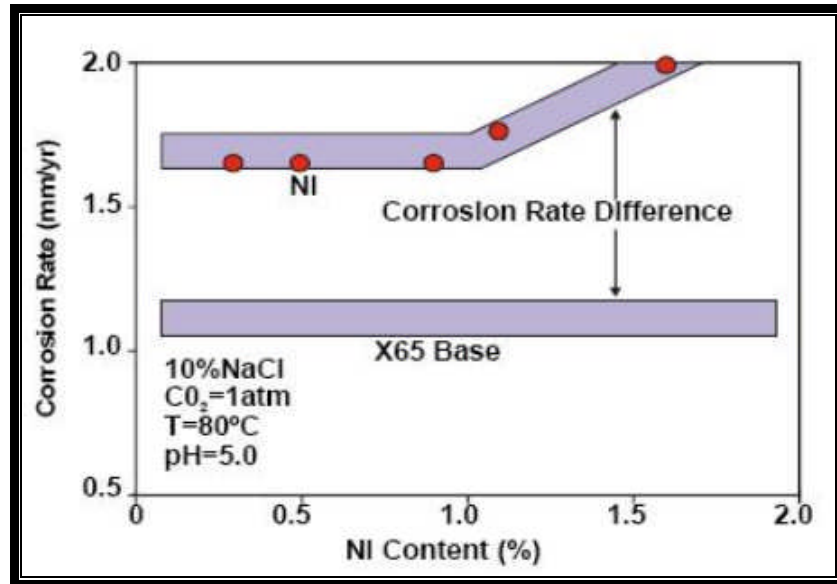


Figure 2-6: The effect of nickel on the corrosion rate of steel in a sweet environment [25]

In order to understand the effects of the pipe materials, welding process and weld consumables, Lee and Woolline [26] examined three different materials, API X52, X60, X65 with two different welding processes (MMA & TIG). They observed a strong link between PWC and composition but no distinct difference between MMA and TIG. The examination revealed that microstructures played an important role in PWC, with an increase in PWC by increasing hardness, grain size, and level of aligned second phase and a decreasing level of microstructure refinement of the root by subsequent passes.

Nowadays, significant effort has been devoted to control PWC by using inhibitors which are considered by some as a way to solve this problem if correctly applied, whereas there was some evidence to suggest that some corrosion inhibitors may increase PWC. As a result of the more strict environmental regulations that have been implemented in recent years, inhibitor use in oil and gas productions is required to have an environmentally friendly profile such as to be non bioaccumulative, biodegradable and have a low toxicity level [27].

The study of Winning et al. [6] revealed that both conventional and environmentally friendly inhibitors have been effective in reducing corrosion of the weld, and the weldment as a whole, if the correct dose is applied.

Furthermore, Alison et al. [28] showed that environmentally acceptable corrosion inhibitors are as effective, at the same dose, as conventional corrosion inhibitors and can provide the same protection against general corrosion and preferential weld corrosion of weldments. This contradicts the misunderstanding that environmentally acceptable products need to be used at higher doses.

Studies by D'Arcy et al. [29] stated that applications of corrosion inhibitors can have the effect of reversing the polarity from cathodic to anodic behaviour of the weld metal with respect to parent metal and HAZ.

There have been a number of laboratory as well as field studies of this reversal phenomenon when an inhibitor was applied. Valuable experimental data have been collected. However, the underlying mechanism of this reversal is still not yet well understood.

In Research at Cranfield University, Omonua [30], investigated the effects of environmentally-friendly inhibitors under stagnant conditions. The study showed a change in the direction of corrosion current flow when inhibitor was added to polished and pre-corroded surfaces, leading to PWC of the weld metal and HAZ with respect to the parent metal. He suggested that the change in polarity can be attributed to the nature of the corrosion product from general and galvanic corrosion, where the inhibitor adsorbed strongly on the parent metal making it cathodic with respect to other regions.

In a previous study at Cranfield University, Strutt et al. [31] indicated a danger when strongly cathodic weld sections were associated with rapid attack in adjacent anodic HAZ regions. The influence of the coupling is accentuated by a poor area ratio with a small anodic weld/large cathodic base metal.

Using cell to simulate flow in channel, Otu [32] studied the inhibition mechanism of welded carbon steel X65 types. The study showed that HAZ under flowing conditions was protected when compared to stagnant conditions; the reason for that may be as a result of flow of electrolytes in the cell (mass transport) assisting the films formed during the corrosion process to be displaced to the HAZ region preventing the decrease in the mass transfer of the inhibitors to the surface that slows down the inhibitor process.

Corrosion inhibitors may have different (adsorption) efficiencies on the parent material and the weld metal. This may be related to differences in alloying and microstructure, and to differences in the corrosion product films. In addition, different shifts in corrosion potential between parent and weld metal upon inhibition may give rise to galvanic corrosion of the weld metal, and localised corrosion of the weld can occurred [33].

Olsen et al. [34] studied the interaction between inhibitors and the different surfaces of the constituents of a weld. They reported that different adsorption characteristics can lead to inhibitor filming on the parent metal but not on the weld metal, resulting in a galvanic effect and causing PWC attack instead of preventing it.

The studies of Gulbrandsen and Dugstad [35] provide further information on the inhibitor polarity by carrying out tests in high and low conductivity (0.35 and 35 g/L) at 60⁰C, 1 bar CO₂ and pH 5-6. They suggested that the polarity reversal was caused by low concentrations of the inhibitor leading to galvanic corrosion of the weld and accelerating preferential corrosion.

2.3 CO₂ Corrosion

Carbon dioxide corrosion (sweet corrosion) is a very serious problem in the oil and gas industry and often results in severe damage by affecting the materials used in production and processing facilities. The presence of CO₂ is due to gas production from increasing well depths and the use of enhanced oil recovery techniques based on CO₂

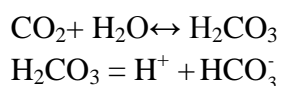
injection into reservoirs. Low cost carbon steels, which are more susceptible to corrosion in CO₂ environments, are generally used as construction materials in these facilities. The severity of corrosion depends on temperature, fluid characteristics (CO₂, partial pressure, gas/liquid ratio, formation water composition, water-to-oil ratio, and pH), flow characteristics, and material characteristics [1].

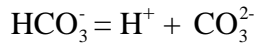
CO₂ corrosion has been the subject of numerous studies over the years. The mechanism of CO₂ corrosion has been investigated by many researchers, and predictive procedures for CO₂ corrosion of carbon steels have also been proposed by many researchers. These include multiphase flow, corrosion mechanism, inhibition performance, as well as all kinds of corrosion monitoring techniques [36, 37, and 38]. Most of the studies on CO₂ corrosion and inhibition have been done in stirred beakers, Rotating Cylinder Electrode (RCE) cells, jet impingement systems, and small-scale single-phase flow loops.

The basic CO₂ corrosion reaction mechanism has been well understood and accepted by many researchers through work done by De Waard and Milliams for Shell Research [39] which can be classified into four steps: dissolution of carbon dioxide in the aqueous solution to form the various reactive species; transportation of these reactants to the metal surface; the electrochemical reactions (anodic and cathodic) taking place at the metal surface; and the transportation of the products of the corrosion reaction to the bulk of the solution. These steps are listed below:

2.3.1 Formation of reactive species in the bulk

The chemistry of the corrosion process for carbon steel in brine conditions is due to the carbon dioxide gas dissolving in the saltwater and forming weak carbonic acid. Three species present in a CO₂ containing aqueous solution, H₂CO₃, HCO₃⁻, and H⁺, contribute to the electrochemical cathodic reduction reactions in the CO₂ corrosion process. These three species have different mass transfer and reaction kinetics and contribute to different extents to the corrosion:

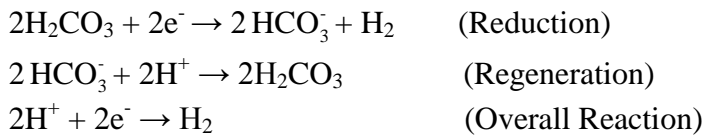




It was proposed that carbonic acid supplies a reservoir of H^+ ions at a given pH value of solution. Therefore, hydrogen ion reduction or hydrogen evolution is thought to be the dominant cathodic reduction.

2.3.2 Electrochemical Reactions (At the surface)

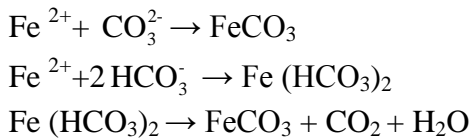
Cathodic Reactions



Anodic Reaction



Due to these processes, a corrosion layer is formed on the steel surface. Iron carbonate, FeCO_3 is formed on the steel surface where the protective nature of the film plays an important part in the corrosion process, and also depends on environmental factors and characteristics of the carbon steel. Its formation can be explained by the following electrochemical reactions:



Investigation of the mechanism of the CO_2 corrosion process have been done with a Rotating Cylinder Electrode, illustrated in Figure 2-7, which is a schematic diagram that indicates the mass transport of protons and carbonic acid in the diffusion layer and cathodic reactions at the metal surface. The protons have to diffuse from the bulk region through the boundary layer to the metal surface, while the transport flux of carbonic acid needs to reflect the diffusion of H_2CO_3 .

In corrosion, certain species in the solution are produced at the steel surface (Fe^{2+}) while others are depleted (H^+). This leads to concentration gradients and diffusion of these species towards and away from the surface. On the other hand the rate of the electrochemical reactions depends on the species concentrations at the steel surface.

Therefore, there exists a two-way coupling between the electrochemical processes at the metal surface (corrosion) and transport processes in the adjacent solution layer (diffusion in the boundary layer). Turbulent flow can penetrate deep into the boundary layer and extensively improve the rate of species transport to and from the surface, hence leading to a higher corrosion rate. On the other hand, when protective films form on the steel surface, they may slow down the diffusion of species and can reduce the corrosion rate [40].

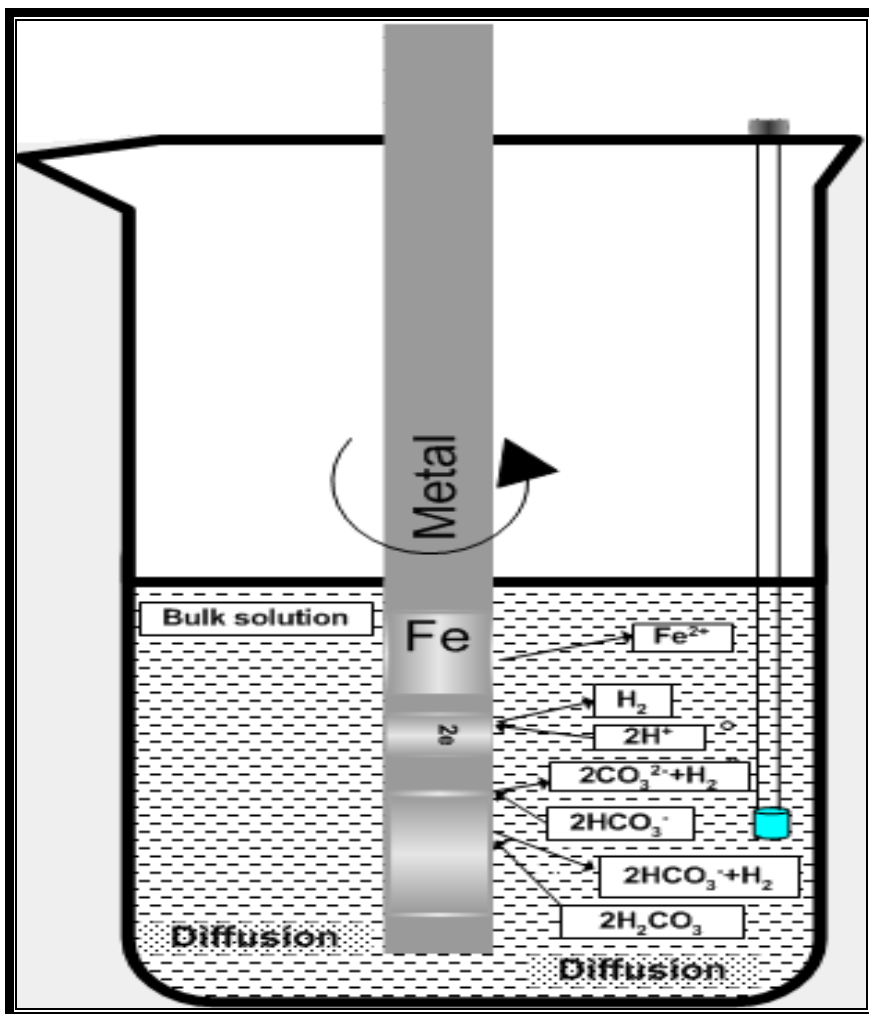


Figure 2-7: CO_2 corrosion process for carbon steel under sweet corrosion conditions

2.4 The Corrosion Product Film

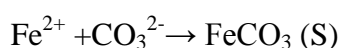
CO₂ corrosion is strongly dependent on the type of corrosion product film formed on the metal surface during the corrosion process. The stability, protectiveness and adherence of these films determine the nature and the rate of corrosion. When there is no film forming on the metal surface, most of the corrosion attack is general corrosion. Localised corrosion, which is more severe, normally happens when the corrosion film forms on the metal surface during the corrosion process.

A study by Palacios [41] stated that there are two types of corrosion product film established on the metal surface. The first is known as the primary scale which is porous, large in crystals, well adhered and has black colour characteristic. However, the secondary film is compact, small in crystals, nonporous, forms a uniform scale throughout the specimen surface, and is brown in colour. For some specimens, the bond between the two scales is not as strong as the bond between the primary scale and the metal surface.

Many studies [42, 43] have pointed out that the main components of the film are iron carbonate (FeCO₃) and iron carbide (FeC₃). In flow systems corrosion films can obviously grow for months without giving protection unless the steel is exposed to stagnant or “wet” conditions. During a few days stagnation, corrosion products can accumulate on the steel surface and form protective films [44]. Depending on the compositions, the corrosion film can be classified as follows:

2.4.1 Iron Carbonate (FeCO₃)

In CO₂ corrosion, which is being considered here, when the concentrations of Fe²⁺ and CO₃ ions exceed the solubility limit, they combine to form solid iron carbonate (FeCO₃) films according to:



Iron carbonate film growth depends primarily on the precipitation rate, (R_{FeCO_3}). As more iron carbonate precipitates, the film can grow in density as well as thickness. The rate of participation of iron carbonate can be described as follows [45]:

$$\text{Eq.1} \quad R_{FeCO_3} = \frac{A}{V} \cdot f(T) \cdot K_{sp} \cdot f(SS)$$

Where the rate of participation of iron carbonate can be described as a function of supersaturation SS , the solubility limit K_{sp} , T temperature and surface area –to– volume ratio $\frac{A}{V}$.

Super saturation is defined as:

$$\text{Eq.2} \quad ss = \frac{C_{Fe^{2+}} C_{CO_3^{2-}}}{K_{sp}}$$

Where $C_{Fe^{2+}}$ is the iron ions concentration and $C_{CO_3^{2-}}$ is the carbonate ions concentration. Supersaturation and temperature are the most important factors affecting the rate of corrosion where at high temperature the bicarbonate ions (HCO_3^-) formed on the surface give more carbonate ions (CO_3^{2-}) which results in the formation of more insoluble iron carbonate which increases the solutions pH and corrosion rates decrease significantly.

Precipitation of iron carbonate on the surface of the metal decreases the corrosion rate by acting as diffusion barrier for the corrosive species to travel to the metal surface by blocking a small number of areas on the steel surface and preventing electrochemical reactions from happening on the surface [46].

2.4.2 Iron Carbide (Fe₃C)

Fe₃C is part of the original steel in the non-oxidised state that accumulates on the surface after the preferential dissolution of ferrite (α -Fe) in to Fe²⁺ [47]. As Fe₃C is an electronic conductor, FeC₃ is cathodic to the ferrite in CO₂ environments and all the cathodic corrosion reactions occur readily on its surface as on the surface of the steel itself. This type of film could result in galvanic coupling of the metal inside the corrosion product film which might play an important role in the risk of uniform corrosion degenerating into localised attack. Fe₃C can be seen as the skeleton of the metal that is leftover after the corrosion process has removed the rest of the metal [48].

2.5 Factors Affecting CO₂ Corrosion

There has been a great interest in understanding the effect of different factors on the mechanism of CO₂ corrosion and surface film formation, because they determine the resulting corrosion rate. From the materials cost point of view, the use of carbon and low alloy steel for tubing and pipelines is the most convenient option and, therefore, considerable efforts have been made in order to increase their corrosion resistance. Moreover, many complicated environmental parameters affect general CO₂ corrosion, such as partial pressure of carbon dioxide, temperature, pH, flow velocity, the formation of the corrosion product scale, etc. These effects will be discussed in the following paragraphs.

2.5.1 Effect of Pressure

The CO₂ partial pressure plays an important role in CO₂ corrosion under both film-free and film-forming conditions. The studies of DeWaard and Milliams [49], have found the relationship between corrosion rate and CO₂ partial pressure at the temperatures studied (15, 25, and 60°C) to be exponential and the exponent is 0.67.

$$\text{Eq.3} \quad CR = \text{const} \times (p_{\text{CO}_2})^{0.67}$$

Other authors have found similar power laws between corrosion rates and CO₂ partial pressure with the exponent in the range of 0.5 to 0.8 [50].

Higher CO₂ partial pressure does not necessarily mean higher corrosion rates. This is a matter of environmental conditions. Generally, in the case of scale-free conditions as illustrated in Figure 2-8, higher CO₂ partial pressures leads to higher corrosion rates by reducing the pH as well as increasing the rate of carbonic acid reduction. Corrosion rates were experimentally measured by linear polarisation measurements (LPR) and weight loss (WL). While the predicted corrosion rates were measured by OUV 3.0 and electrochemical models [51].

The generally accepted explanation is that with P_{CO2} the concentration of H₂CO₃ increases and accelerates the cathodic reaction, and eventually the corrosion rate. This agrees with the study proposed by Wang et al. [52], that the anodic reaction is practically unaffected when the CO₂ partial pressure increased from 3 to 20 bars while the cathodic limiting current density increased due to a large reservoir of carbonic acid.

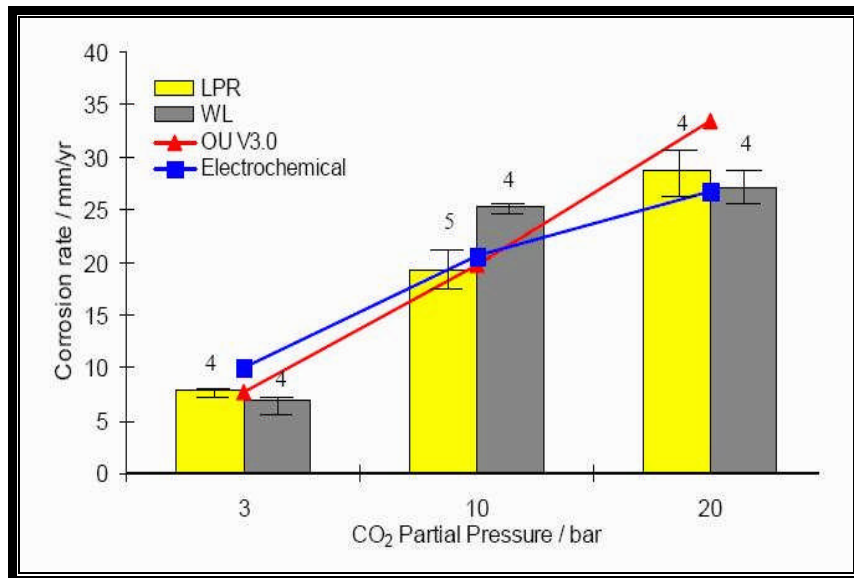


Figure 2-8 : Predicted and experimental measured corrosion rates showing the effect of CO₂ partial pressure in those experiments no protective films formed [51]

However, under film forming conditions, a study by Sun and Netic [53] in a horizontal wet gas flow stated that under protective film formation, high CO₂ partial pressure with a pH range below 5.2 can reduce the corrosion rate due to a lower availability of cathodic sites leading to an increase in bicarbonate and carbonate ion concentration and a higher supersaturation.

2.5.2 Effect of Temperature

Temperature has a significant influence on corrosion rates. It is generally agreed that under a given CO₂ partial pressure the corrosion rate increases with increasing temperature until a certain temperature is reached. Beyond this temperature protective surface films are formed and the corrosion rate actually decreases with increasing temperature.

Two distinct mechanisms of carbon dioxide corrosion were recognised from research and technology development i.e., low temperature (<60°C) and high temperature (60-150°C). At low temperature CO₂ corrosion is a function of pH, salt concentration, temperature, P_{CO_2} and metallurgy of the low alloy steel. However, at high temperature, CO₂ corrosion is influenced by system hydrodynamics because of a change in the surface electrochemistry [54].

A number of authors have found that the temperature strongly influences the conditions needed to form protective iron carbonate layers. At lower temperatures (<60°C) the solubility of FeCO₃ is high and the precipitation rate is slow, and protective films either will not form or may still build up but are not protective due to their open porous structure and poor bond with the substrate metal. This may have been influenced by the experimental conditions under which the films were formed unless the pH is increased. In this temperature range, the corrosion rate increases with temperatures up to an intermediate range of 60-80°C.

It was reported that above 60°C the protectiveness of the iron carbonate layer increases with temperature due to the decrease of iron carbonate solubility and, thus, the corrosion rate is increased, as shown in Figure 2-9 [55].

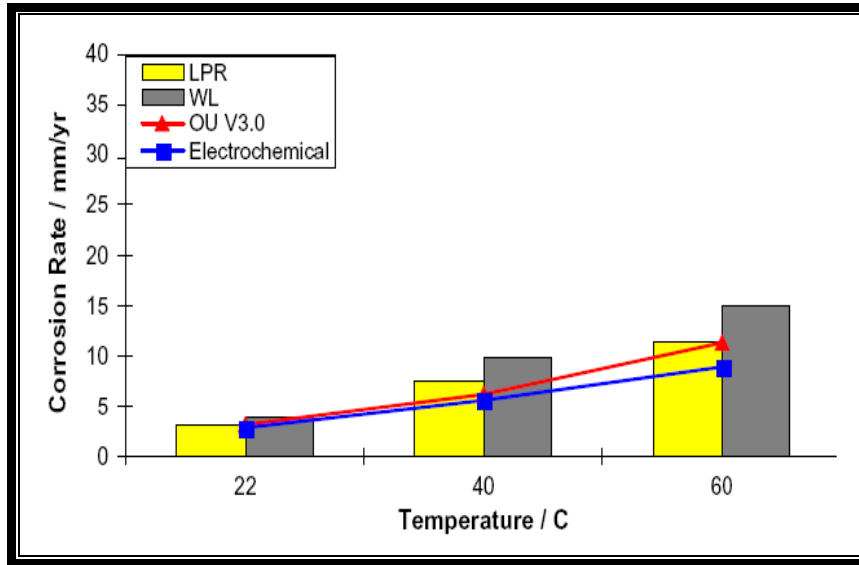


Figure 2-9: Predicted and experimentally measured corrosion rates showing the effect of temperature [55]

Studies by Munoz et al. [56] found that on ferritic-pearlitic steels surface scales formed below 40°C mainly consist of iron carbide (Fe_3C) with some FeCO_3 and carbonates of alloying elements of the steel. It is suggested that Fe_3C , which is considered as a part of the original steel microstructure may become sites of cathodic reaction. They found that at higher temperatures the FeCO_3 solubility is reduced and the precipitation rate is greatly faster, thus allowing the formation of iron carbonate films.

Protective carbonate scales can be recognised by their morphology and crystallinity. From scanning electron microscopy (SEM), Dugstad [57] found that at low temperatures (20 and 40°C) mainly iron carbide was formed but protective films were formed at 80°C after 20-40 hours. In these tests, the corrosion rate increased with temperature and reached a maximum in the temperature range 60-90°C. The reason was attributed to the higher precipitation rates of iron carbonate at elevated temperatures.

Moreover, study showed that by using X-ray diffraction (XRD), at a low temperature (30°C) and pressure conditions (1atm partial pressure) that the morphology of the scale associated strongly with the degree of protection and that the large crystal structure of the film provided little protection, hence causing the corrosion rates to increase with time [58].

An experiment was carried out by Olsen under water condensing conditions to study the CO₂ corrosion of carbon steel. In the absence of the corrosion inhibitor, black corrosion film consisted primarily of Fe₃C and FeCO₃ was formed. At high temperature (70°C), the films were thin and not easy to remove, and resulted in a reduction of the corrosion rate [59].

In general, a calibration of corrosion rates (mm/y) as a function of both CO₂ pressure (bar) and temperature (°C) can be represented in a simple nomogram shown in Figure 2-10 [60].

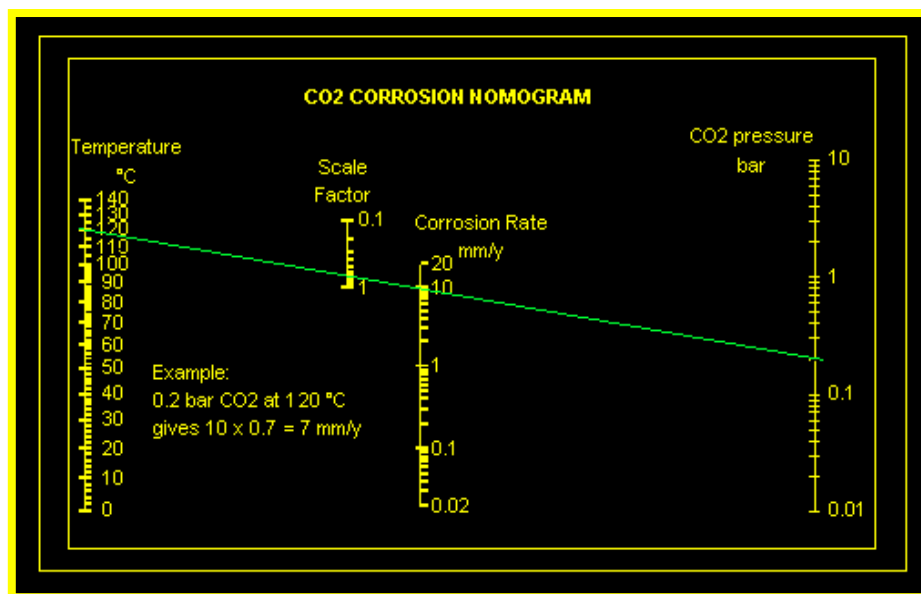


Figure 2-10: Nomogram for predicting CO₂ corrosion of carbon steel is based on the DeWaard- Milliams equation [60]

2.5.3 Effect of Velocity

Flow plays an important role in a process with complete or partial mass transfer control. So far it has been established that in CO₂ corrosion, at higher current densities where Tafel behavior is no longer observed, H⁺ reduction is mass transfer (diffusion) controlled and H₂CO₃ reduction is controlled by the interaction between mass transfer and chemical reaction at higher velocities. Therefore it is expected that flow will affect the CO₂ corrosion rates [61].

There are two main ways in which flow may affect CO₂ corrosion which can be notable based on whether or not other conditions are favorable to protective scale formation or not. In the case of corrosion where protective scales do not form (usually at low pH as found in condensed water and in the absence of inhibitors), the main role of turbulent flow is to enhance transport of species towards and away from the metal surface. This may lead to an increase in the corrosion rate as illustrated in Figure 2-11.

Conversely, when protective iron carbonate scales form (typically at higher pH in produced water) or when inhibitor films are present on the steel surface, the above mentioned effect of flow becomes unimportant as the main resistance to corrosion is now in the surface scale or inhibitor film. In this case, the effect of flow is to interfere with the formation of surface scales/films or to remove them once they are formed, leading to an increased corrosion rate [40].

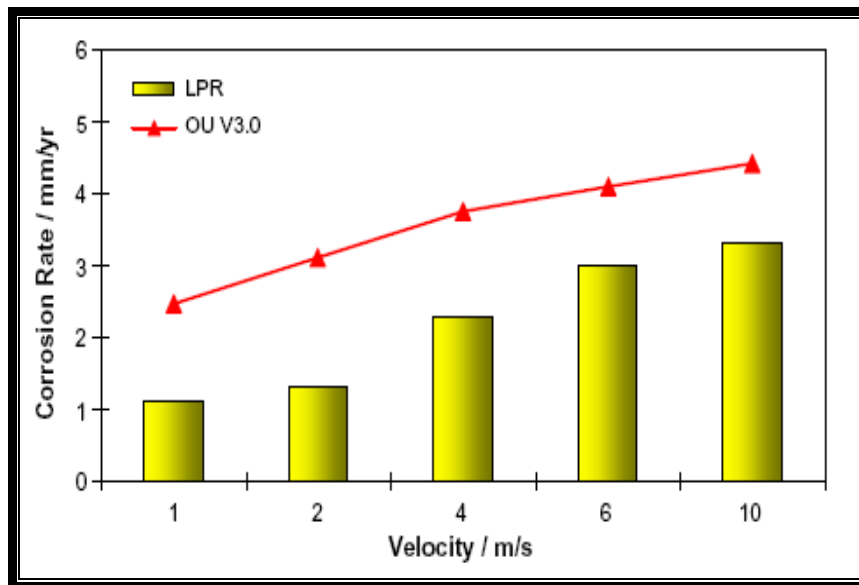


Figure 2-11: Predicted and experimentally measured corrosion rates showing the effect of velocity in the absence of iron carbonate scales [40]

Flow affects the metal dissolution rate in different ways. Figure 2-12 shows that below a critical flow velocity, the corrosion rate increases only gradually with increasing flow intensity. While above the critical flow velocity the interaction between the fluid and the wall becomes so intense that protective films or scales are destroyed by near-wall turbulence elements which also prevent re-formation of the protective film [61, 62].

Several authors have studied the influence of the flow velocity in the presence of protective CO₂ corrosion product films. Their studies have shown that the flow velocity can influence to a certain extent the transport of cathodic species towards the steel surface, yielding an increase of metal dissolution rates at high flow velocities [63, 64]. At the same time flow may stimulate the removal of Fe²⁺ ions from the steel surface at the bottom of pores and may cause lower surface supersaturation and slower precipitation rates. This in turn yields less protective films and, hence, higher corrosion rates [65].

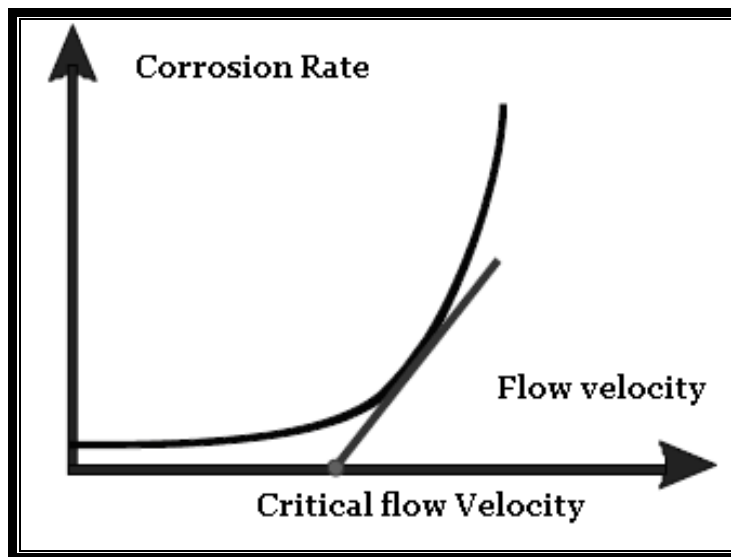


Figure 2-12: Effect of flow on corrosion rate [65]

2.6 Laboratory Test Method and Hydrodynamics Relationships

Corrosion is not the result of chemical processes alone but is also affected by fluid flow at the solid/liquid interface. Fluid flow causes an increase in the rate of the transport of chemical species to/from the metal surface, resulting in an increase of the corrosion rate [66].

Many industrial processes involve movement of corrosive liquids in metallic structures; for example, in oil and gas production environments, material transported in oil and gas pipelines are multiphase in nature, contain oil, aqueous (brine), and gas phases. The corrosion rate, and hence inhibitor performance are influenced by composition, temperature, flow and pressure.

A moving fluid can lead to accelerated corrosion because of the flow induced removal of protective corrosion by-products from the metal layer [67]. The influence of the flow on the corrosion process is an important issue to be considered during design and operation.

It has been detected that corrosiveness is exacerbated by flowing environments containing CO₂ and can produce severe damage to carbon steel structures in contact with them. Some data reported in the literature indicate that the damage produced by these flowing environments can be 10mm/y of penetration [68].

Earlier studies concentrated on understanding the influence of the flow on the corrosion process by using metallic discs rotating at a constant rate immersed in different corrosion environments and conditions. The evaluation of the influence that flow had on the corrosion of these metallic disks was made by visual and weight loss determination and no electrochemical measurements were used. Therefore, these studies raised several ideas for predicting the effect of hydrodynamics flow parameters on corrosion rates under all types of fluid velocity conditions [69].

Years later, there has been development of electrochemical theories as well as techniques. The rotating disc electrode has been used extensively in corrosion studies, but it is limited in practice because of the flow being quite different from that of the industrial transport process. Moreover, the RDE usually operates under laminar flow, while most of the industrial process operates in turbulent flow [67, 70].

A variety of approaches have been used in the development of hydrodynamic systems with different degrees of accomplishment especially metal corrosion in turbulent flow conditions. Among these hydrodynamic systems, jet impingement, RCE, RDE, closed-circuit loops and pipe flow are systems that have been used widely during recent years in the corrosion community for fluid flow corrosion studies which simulate reliably and repeatedly under turbulent conditions. For most experimental tools, the known power laws for mass transport relationships, with their range of validity and the equations to quantify wall shear stresses, are given in Table (1) [71].

Table 1 : Mass Transport Relationship for Important Flow Regimes [71]

Flow System	Power Law $Sh = a \cdot Sc^b \cdot Re^c$	Internal of validity	Wall Shear Stress	Reynolds Number
Free Rotated Disc <i>Laminar flow</i> <i>Turbulent Flow</i>	$0.60 \cdot Sc^{1/3} \cdot Re^{1/2}$ $0.011 \cdot Sc^{1/3} \cdot Re^{0.87}$	$10^2 < Re < 10^5$ $Re > 10^6$	$\tau = 6.302 \cdot \nu \cdot \rho \cdot \omega \cdot \sqrt{Re}$	$Re = \frac{2 \cdot \omega \cdot r^2}{\nu}$
Free Rotated Cylinder <i>Turbulent Flow</i>	$0.079 \cdot Sc^{0.35} \cdot Re^{0.7}$	$10^2 < Re < 4 \cdot 10^5$	$\tau_{RCE} = 0.0791 \cdot Re^{-0.3} \cdot \rho \cdot r^2 \cdot \omega^2$	$Re = \frac{2 \cdot \omega \cdot r^2}{\nu}$
Coaxial Cylinder	$0.0027 \cdot Sc^{1/3} \cdot Re$	$Re > 2.7 \cdot 10^5$	NA	$Re = \frac{2 \cdot \omega \cdot r^2}{\nu}$
Rotating Cage <i>Turbulent</i>	NA	NA	$\tau_{RC} = 0.0791 \cdot Re^{-0.3} \cdot \rho \cdot r^2 \cdot \omega^{2.3}$	$Re = \frac{2 \cdot \omega \cdot r^2}{\nu}$
Impinging Jet <i>Region (A) Laminar</i> <i>Region (B) Transition</i>	$Sh = 1.51 \cdot Re^{0.5} \cdot Sc^{0.33} \cdot \left(\frac{H}{d}\right)$ $Sh = 1.12 \cdot Re^{0.5} \cdot Sc^{0.33} \cdot \left(\frac{H}{d}\right)$	$Re < 2000$ $4000 < Re < 16000$	$\tau_{ij} = 0.0447 \cdot Re^{-0.182} \cdot \rho \cdot u^2 \cdot \left(\frac{x}{d}\right)^{-2}$	$Re = \frac{d \cdot u}{\nu}$ d= nozzle diameter U=Nozzle flow velocity L = d
Flat plate in channel and Tube Flow <i>Laminar Flow</i> <i>Turbulent Flow</i>	$2.54 \cdot Sc^{1/3} \cdot Re \left[\frac{d_e}{l}\right]^{1/3}$ $2.54 \cdot Sc^{0.35} \cdot Re^{0.7}$	$Re < 2300$ $Re > 2300$	$\tau = \left(\frac{\Delta p}{\Delta L}\right) \cdot \left(\frac{d}{4}\right)$	$Re = \frac{d_e \cdot u}{\nu}$ $d_e = \frac{4 \times \text{Cross section area}}{\text{perimeter}}$

2.6.1 The Rotating Cylinder Electrode (RCE)

One very convenient laboratory hydrodynamic test system is the rotating cylinder electrode (RCE). The popularity of using the RCE in corrosion studies in recent years, is due to some of its characteristics, such as compactness, relatively inexpensive, easily controlled and its well understood mass transfer properties [72].

It has been found that for the RCE enclosed in a concentric cell, the flow remains laminar when the rotating speed of the inner cylinder is low. However, when the rotating speed exceeds a critical value, instability sets in and rows of cellular vortices, known as Taylor Vortices are developed. These vortices enhance the rate of mass transport to and from the metal surface, momentum and heat transfer characteristics. As the rotation rate of the cylinder increases, the solution flow transition undergoes from laminar to turbulent flow. The transition from laminar to turbulent is often characterised using the Reynolds number (Re) to quantify the ratio between inertial forces and viscous forces in a solution. This transition has been suggested to occur at values of $200 < Re < 2000$ [73].

In laboratory corrosion studies, RCE was the second-ranked methodology compared to jet impingement after that simulates different regimes of fluid flow. It is a useful tool in order to understand the mass transfer process, inhibition mechanism, effects of surface films, etc. especially in turbulent flow conditions. However, in CO₂ corrosion studies an argument about the validity of using RCE was raised due to the differences of the measured corrosion rate values in pipe flow studies and in the RCE. When the RCE is immersed and rotated in a test solution, the hydrodynamic conditions generated, even at low rotational speeds, are generally quite turbulent. This makes the RCE an ideal probe for studying corrosion process in turbulent conditions with low velocity [74].

2.6.2 Hydrodynamics Parameters of the RCE (Re , Sc , Sh)

The flow regimes in pipelines are more difficult to simulate directly in the laboratory. For this reason, the hydrodynamic flow parameters are determined, and then the laboratory corrosion tests are conducted under calculated hydrodynamics' parameters.

A variety of approaches have been used in development of the most common hydrodynamic parameters such as mass transfer coefficient and wall shear stress with several approximations to develop the hydrodynamic equations.

One very convenient laboratory methodology test system is the use of the rotating cylinder electrode (RCE). In RCE turbulent flow, materials can be transferred from the solution to the cylinder surface, and it can also carry material away from the surface. This rate of mass transport plays a major factor on the rate of corrosion.

Due to the difficulties found in the theoretical explanation of the mass transfer process taking place in turbulent flow, a different approach is used based on the analysis of experimental data, in order to study the turbulent flow by using empirical relationships and dimensionless numbers.

The dimensionless numbers are groups of variables that can be considered as illustrative of certain characteristics of a fluid flow. The most common dimensionless numbers used in corrosion studies, especially under flowing environment conditions, are Reynolds number (Re), the Schmidt number (Sc) and Sherwood number (Sh) [75].

Re is an important dimensionless number associated with fluid flow and used to identify the type of flow in a system as well as determining the transition point from laminar to turbulent flow. It represents the ratio of the momentum forces to the viscous forces in the fluid flow. It is defined as:

$$\text{Eq.4} \quad Re = \frac{v d_{RCE}}{\nu}$$

Where (v) is the mean velocity of the fluid and (ν) is the kinematic viscosity of the fluid.

The kinematic viscosity can be written as:

$$\text{Eq.5} \quad \nu = \frac{\mu}{\rho}$$

Where μ and ρ are the viscosity and density of the fluid respectively.

Sc is a dimensionless number describing the mass transport properties of the fluid in which there are simultaneous momentum and mass diffusion convection processes. It is defined as:

$$\text{Eq.6} \quad Sc = \frac{\mu}{\rho D} = \frac{\nu}{D}$$

Where D is the diffusion coefficient of the species in the fluid. Sh is a dimensionless number associated to the mass transfer coefficient of a specific species in the fluid. It is defined as:

$$\text{Eq.7} \quad Sh = \frac{K_m d_{RCE}}{D}$$

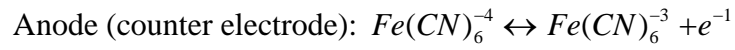
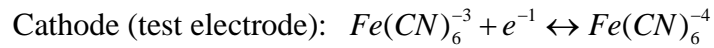
Where K_m is the mass transfer coefficient, d is the diameter of the rotating cylinder electrode and D is the diffusion coefficient.

A review by Gabe [76], noted that the mass transport to a RCE in turbulent flow may be described by empirical dimensionless correlation using the following expression:

$$\text{Eq.8} \quad Sh = K Re^a Sc^b$$

Where K , a and b are experimentally determined constants. K depends on the type of surface, the degree of roughness and the electrolyte composition. The value for b was derived experimentally as 0.356.

Early reports by Silverman [77], provided the most commonly accepted description for the RCE mass transport as well as the mass transfer coefficient based on the electrochemical study of the reduction – oxidation reaction:



He obtained the relationship between the measured limiting current density of the species in the solution and the rotation rate of the cylindrical electrode at constant temperature.

The linear relationship between calculated mass transport and the rotation rate of the electrode to the power of 0.7 is shown by the following relationship:

$$\text{Eq.9} \quad K_m = 0.0791(d_{RCE})^{-0.3}(v)^{-0.344}(D)^{0.644}(u_{RCE})^{0.7}$$

Where u_{RCE} is the velocity, d_{RCE} is the diameter of the electrode, v is the kinematics viscosity, and D is the diffusion coefficient.

The flow analysis studies of the RCE point out that the characteristic length L used in the calculation of the Re and Sh dimensionless numbers is equal to the diameter of the cylinder (d_{cyl}), hence equation (8) can be expressed in terms of a dimensionless number as:

$$\text{Eq.10} \quad Sh_{RCE} = 0.0791 Re_{RCE}^{0.7} Sc^{0.356}$$

The mass transport coefficient of the RCE is given by the following relationship:

$$\text{Eq.11} \quad K_m = \left(\frac{D}{d_{cyl}}\right)Sh = \left(\frac{D}{d_{cyl}}\right)(0.0791\text{Re}_{RCE}^{0.7} Sc^{0.356})$$

Therefore from a combination of equations (9) and (11), the overall K_m can be expressed in one of the three forms depending on whether the rotation speed is expressed in terms of linear surface velocity, angular velocity or rotation per minute [72].

$$\text{Eq.12} \quad K_m = 0.0791(d_{RCE})^{-0.3}(v)^{-0.344}(D)^{0.644}(u_{RCE})^{0.7}$$

$$\text{Eq.13} \quad K_m = 0.0487(d_{RCE})^{+0.4}(v)^{-0.344}(D)^{0.644}(\omega)^{0.7}$$

$$\text{Eq.14} \quad K_m = 0.0051(d_{RCE})^{+0.4}(v)^{-0.344}(D)^{0.644}(F)^{0.7}$$

Wall shear stress and mass transfer for the turbulent flow are closely associated and cannot be separated mathematically or experimentally. However, different geometries can have more of an effect on one of these two parameters than the other or vice versa.

The turbulent flow at the RCE induces a wall shear stress on the surface of the cylinder. Wall shear stress is a direct measure of the viscous energy loss within the turbulent boundary layer, and is related to the intensity of turbulence in the fluid acting on the wall. It is not a force/unit area on the wall from the fluid, but a force/unit area in the fluid at the wall [75].

The general equation for the flow accelerated corrosion of carbon steel based on the inter-relationship of the hydrodynamics parameters, solution chemistry and environment variables for single phase, sweet, aqueous system for wall shear stress range 0.2-100 Pa is expressed by:

$$\text{Eq.15} \quad R_{corr} = a \cdot \tau^b$$

Where,

R_{corr} = corrosion rate in mm/year

τ = wall shear stress in N/m^2

a & b = constants

The coefficients “a” and exponent “b” are functions of solution chemistry (Fe^{++} , pH, O_2 , P_{CO_2} etc) and other environmental parameters (total pressure and temperature).

In order to calculate the value of the wall shear stress (τ_{RCE}) for the RCE the following equation is assumed to be valid [75].

$$\text{Eq.16} \quad \tau_{\text{RCE}} = \frac{f}{2} \rho u_{\text{RCE}}^2$$

$$\text{Eq.17} \quad \text{Re}_{\text{RCE}} = a \cdot \tau^b$$

Where (f) is the friction coefficient, (u) is the peripheral velocity and (ρ) is the density.

For a smooth RCE, the friction factor has been found to be related to the Re according to the following expression [78]:

$$\text{Eq.18} \quad \log \text{Re}_{\text{RCE}} = 0.1737 \left\{ \frac{f}{2} \right\}^{-0.5} - \log \left\{ \frac{f}{2} \right\}^{-0.5} + 0.2979$$

Turbulent flow regimes between $10^3 < \text{Re}_{\text{RCE}} < 10^5$, Eq (18) can be approximated to the following empirical expression:

$$\text{Eq.19} \quad \frac{f}{2} = 0.0791 \text{Re}^{-0.3}$$

By combining Eq.16 and Eq.19, the shear stress equation for the hydraulically smooth cylinder can be written as:

$$\text{Eq.20} \quad \tau_{RCE} = 0.079 \text{Re}_{RCE}^{-0.3} \rho u_{RCE}^2$$

Equation (20) can be expressed in terms of angular velocity that was derived by [77] to give the following equation by solving for the rotation rate:

$$\text{Eq.21} \quad \omega = \left(\frac{2\pi}{60} \times rpm\right)$$

$$\text{Eq.22} \quad \tau_{RCE} = 0.079 \text{Re}_{RCE}^{-0.3} \rho \omega_{RCE}^2 r^2$$

2.6.3 RCE Flow Domain and Boundary Conditions

The flow domain consists of an inner rotating cylinder electrode and an outer stationary cell filled with (3.5 %) artificial seawater up to a given height. The inner solid cylinder electrode is concentric with the axis of the cell rotating at different angular velocities. No slip boundary conditions are imposed, thus the constant tangential velocities are specified at the inner cylinder, and a zero velocity is specified on the outer cylinder (the cell) as shown in Figure 2-13 [79].

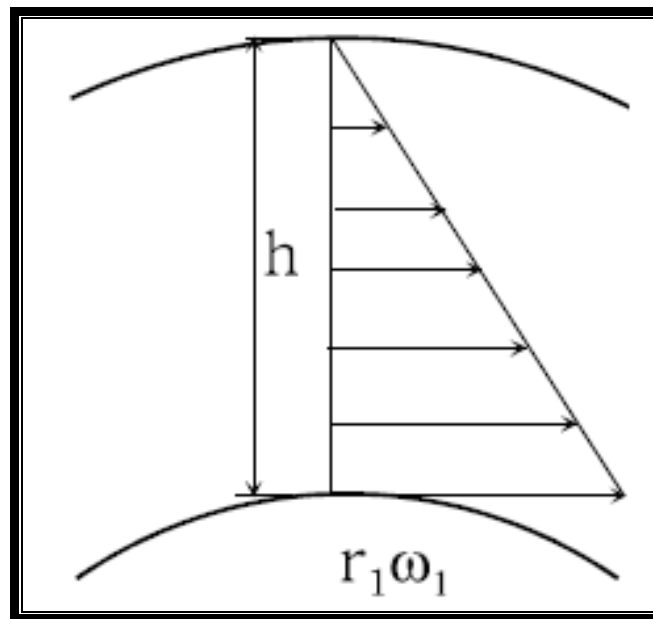


Figure 2-13: Velocity profile for inner cylinder rotating and the outer cylinder at rest [79]

The rotational motion of the inner cylinder induces a primarily circumferential flow in the annular region between the inner and the outer cylinder (the cell). If the rotational speed is high, then large scale secondary flows, typically the size of the gap width will be established. The presence of these Taylor vortices has a strong effect on the mass-transfer rate from the cylinder [80].

The presence of the fluid viscosity slows down the fluid particles close to the solid surface and forms a thin slow-moving fluid layer called a boundary layer. The flow velocity is zero at the surface to satisfy the non-slip boundary condition. Inside the boundary layer, flow momentum is quite low since it experiences a strong viscous flow resistance. Therefore, the boundary layer flow is sensitive to the external pressure gradient (as the form of a pressure force acting upon fluid particles). When vortices shed from the cylinder, uneven pressure distribution develops between the upper and lower surfaces of the cylinder, generating an oscillatory aerodynamic loading (lift) on the cylinder. This unsteady force can induce significant vibrations on a structure [80].

2.7 Correlation of the RCE Test Method and Pipe Flow

Fluid velocity is considered as the primary parameter used to correlate, compare or predict laboratory corrosion test results with field applications. But, this idea has begun changing recently. Corrosion researchers understand that flow-accelerated corrosion must be expressed in terms of geometry-independent fluid flow parameters common to all hydrodynamic systems to match or mimic field corrosion conditions.

When the hydrodynamics parameters, especially shear stress of different geometrics (RCE and Pipe), are the same, then the corrosion mechanism (not the rate) is hypothesised to be the same. However, shear stress in RCE and the pipe system does not result in an equal mass transfer coefficient, but relationships do exist between the mass transfer coefficient and wall shear stress [79]. Under these conditions, the corrosion rate and the efficiency of corrosion inhibitions in the laboratory and in the field are similar.

An important issue when attempting to use the RCE to match the field corrosion condition is to choose the proper rotation rate at which to perform electrochemical measurements. Several solutions to this problem have been proposed over the years. Most involve operating the RCE at a rotation rate where the wall shear stress and the mass transport coefficient match that found in the field. When an RCE is operated at a rotation rate which produces similar mass transport conditions to those found in the field, it is assumed that the corrosion mechanism occurring in the field will be reproduced in the laboratory.

There have been specific cases where the RCE failed [75] to reproduce the field corrosion condition, and particular attention needs to be paid to those situations where surface roughness plays a role in mass transport.

Turbulent flow in the two geometries RCE and pipe flows has many similarities. Fully developed turbulence is encountered in the bulk liquid. As solid walls are approached, the turbulent fluctuation is damped so there exists a layer near the metal surface where a viscous force dominates and any turbulence is dissipated rapidly. Between this so-called viscous sublayer and the turbulent core, there is a transition layer, called the buffer sublayer where the viscous and turbulent forces are of the same order of magnitude [79].

Data presented by Chen et al. [81], concluding that the corrosion rate measured in all hydrodynamic systems is independent of the geometry, involved pointing out that the transfer of corrosion data from one geometry to another can be obtained based on the mass transfer coefficient even with the absence of a surface film in the diffusion boundary layer.

A study proposed by Chesnut et al. [82] obtained a good correlation between RCE and flow loop tests at a shear stress of about 40Pa. Their study showed that the ranking of the inhibitors at shear stress less than 40Pa can be different from the ranking at higher shear stresses.

An investigation by Nestic et al. [83] found that, in the absence of the surface film, corrosion rates measured in flow loop and RCE experiments correlate under the same mass transfer conditions at room temperature. For similar experiments at higher temperature, corrosion rates in the RCE experiments were higher than those measured in the flow loop.

A comparison between flow loop and RCE tests has been done for two inhibitors. The ratio between the RCE results and flow loop results under similar shear stress was 0.3 for the blank and water soluble inhibitor. However, under the oil soluble inhibitor, the ratio of RCE to flow loop varied wildly compared to the results obtained under water soluble inhibitor. Results show that the test incorporating high flow rates and high shear stress levels will differentiate between the performances of different inhibitor formulations [84]

Corrosion rate comparison of the steel pipe with different RCE speeds was done by Denpo and Ogama [85]. The diameter, test solution, temperature and dissolved oxygen content were identical in both experiments. Based on the similarity of solution obtained for mass transfer with pipe flow and rotating electrode, the rotating velocity was converted to the equivalent velocity in the pipe. The corrosion rate of the rotating cylinder electrode obtained electrochemically was used to predict the corrosion rate of the pipe at the equivalent velocity. The predicted corrosion rate was in agreement with the measured corrosion rate.

Based on the data from a RCE and a pipe of carbon steel in brines containing CO₂, under conditions where a protective scale was not formed, Efird et al. [75] concluded that the RCE did not correlate with the pipe flow as a function of wall shear stress or mass transfer.

Dawson et al. [86] obtained identical results from the RCE and from the jet impingement for the same wall shear stress. Based on the results, shear stress can be used as a fundamental test parameter for inhibitor evaluation under turbulent flow conditions.

They emphasised that the use of the fluid velocity to describe the hydrodynamics conditions is inadequate unless the geometry or test apparatus dimensions are also specified. In addition they recommended that the actual hydrodynamic conditions in the tests must be known in order to compare with other tests and to predict inhibitor performance in practical rotating systems. The maximum wall shear stress achieved in RCE and jet impingement was 28 Pa, and 1300 Pa respectively.

2.8 Corrosion Inhibitors

Inhibitors are chemical substances which can retard the corrosion of metals when added in small concentrations to the fluids in contact with the metal. When the environment is too aggressive for unprotected carbon steels, the option to reduce corrosion problems is with the use of inhibitors [87].

Corrosion inhibitors used in oil and gas production are usually applied either by continuous injection into the produced fluids or by batch treatment at regular intervals. Continuous injections are used for oil or gas wells by continuously injecting a liquid inhibitor of dilute concentration. Alternative methods include, batching and the squeeze method. Batch treatment is used where an inhibitor is diluted with appropriate solvent and injected into the annulus of an open hole well. However, in squeeze treatment a quantity of inhibitor is pumped into the well, followed by sufficient solvent to force the inhibitor into the formation. The inhibitor is absorbed by the formation where it slowly escapes to inhibit the produced fluid [88].

Based on laboratory test results, it is not possible to say what actual dose rate of inhibitor should be applied to give the promised corrosion protection. Laboratory tests only give an estimate of the inhibitor dose rate required. Inhibitor dose rates may be more or less than the required dosage predicated in laboratory tests to achieve a required corrosion rate. It is imperative that inhibitor injection in the field be optimised based on corrosion monitoring to give acceptable corrosion rates [89].

Most of the inhibitors used in the oil industry are organic chemicals which adsorb strongly on the surface of the metal and support the formation of a protective film on the metal. Organic compounds containing nitrogen include amines, amides, quaternary, ammonium salt and specially imidazolines and their derivatives. Most commercially available inhibitors are proprietary formulations which may contain additives in addition to the inhibiting compound or a mixture of inhibiting compounds [90].

Corrosion inhibitors that are classified nowadays as green (environmentally friendly inhibitors) have been developed and are required to provide adequate protection in a CO₂ environment operated in particular under extremely high wall shear stress conditions. The development of green corrosion inhibitors requires the knowledge of the pertinent country's regulations, evaluation of the environmental performance for the environment in which the product will be exposed, and the excellent corrosion protection in the applications for which this inhibitor is designed. These products should be designed so that at the end of their application, the product does not persevere in the environment, and it should break down into innocuous degradation products [91].

Organic corrosion inhibitors are the most common and effective commercially in order to minimise carbon dioxide induced corrosion in carbon steel pipelines. Most CO₂ inhibitors are nitrogen, sulphur, or phosphorus-containing organic compounds, such as imidazolines, quaternary amines, and phosphate esters.

Quaternary compounds have become popular and effectively prevent corrosion of iron and steel in acid solutions. The well accepted explanation for these inhibitive properties of quaternary amines with straight chains is electrostatic interaction of the positive ions to the negatively charged metal. These inhibitive properties improve when organic groups are added that contain a lone pair of electrons or electron system with multiple bonds or aromatic rings which bond to a metal surface by electron transfer to the metal [92].

Changes in corrosion potential after the addition of the inhibitor are a useful indication of whether the anodic or cathodic reaction is retarded. When an inhibitor affects the anodic process, it is referred to as an anodic inhibitor. However, when the cathodic kinetics is affected, the inhibitor is described as a cathodic inhibitor. When the inhibitor affects both the anodic and cathodic electrochemical processes it is referred to as a mixed inhibitor. A plot of the current versus potential in the absence and presence of an inhibitor shows the effects of the inhibitor on the polarisation characteristic of steel as shown in Figure 2-14 [93].

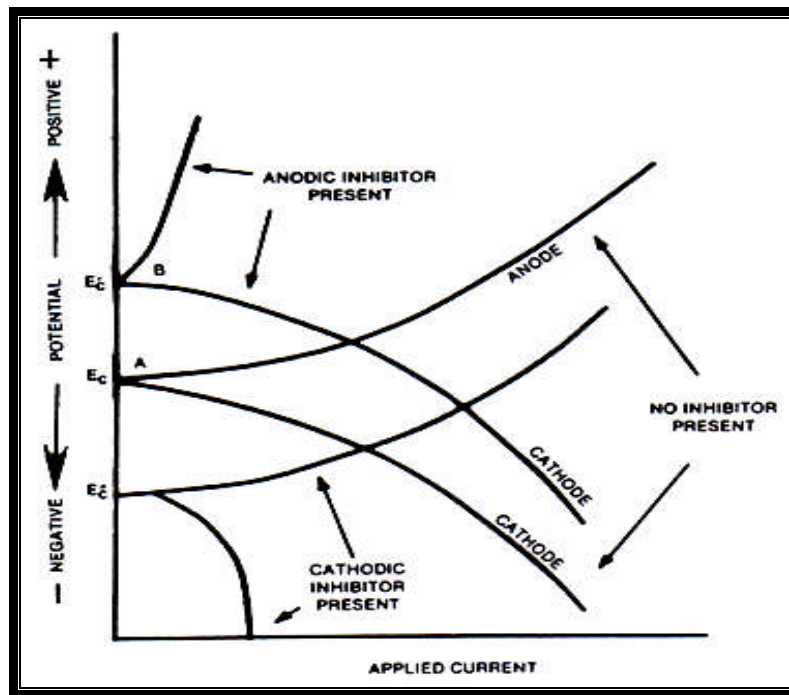


Figure 2-14: Effect of inhibitors on polarisation curves [93]

If the polarisation curve is displaced with no change of Tafel slope, it may be assumed that the inhibitor is blocking the active sites. However, when there is an increase in the Tafel slope, this indicates that the inhibitor affects the mechanism of reaction. The interaction between inhibitors and the different surfaces of the constituents of a weld is important.

Different adsorption characteristics may lead to inhibitor filming on the parent metal but not on the weld metal. This can create galvanic effects and cause preferential attack instead of preventing it. Moreover, due to environment changes and the use of some types of inhibitors, weld localised corrosion can be predicted due to anodic weld metal with respect to the parent metal. It is therefore extremely important to make a careful selection of an inhibitor formulation which is compatible with the pipeline weld under the conditions of operation in service [94].

Inhibitor addition strongly decreases the corrosion rate dependent on both steel structure and pre-corrosion period length. It is worth noting that pre-corrosion time decreases inhibitor efficiency, where the longer the pre-corrosion time, the thicker the iron carbide will grow as a result of the efficiency decrease. In some cases failure of the inhibitor occurs as a result of high metal dissolution rates preventing the slowly adsorbing inhibitors from adsorbing on the metal surfaces and protecting them from corrosion [6].

Inhibitor concentrations vary from a few parts per million in continuous injection application to several thousands parts per million. In some cases, an insufficient inhibitor can lead to corrosion that is more severe than if no inhibitor was present, such as anodic inhibitors if they were used at too low a concentration, where they can actually aggravate pitting corrosion [95].

Reduction of inhibitor concentration was noticed during the initial stages of use due to its reaction with contaminants, as well as protective film formation. Clean and smooth metal surfaces usually require lower inhibitor concentration than do rough and dirty surfaces. In some cases, depletion of the inhibitor occurs due to the presence of grease and oil on the metal surfaces [96].

2.8.1 Types and Mechanisms of Inhibitors

Inhibitors are classified in Figure 2-15 according to their mechanism and composition. However, some authors may use slightly different classes. Inhibitors fall into several types.

Generally, inhibitors slow down the corrosion process in three ways:

- Increased polarisation of the anodic reaction (anodic inhibition)
- Increased in polarisation of the cathodic reaction (cathodic inhibition)
- Increase in the electrical resistance of the circuit by forming a deposit on the surface of the metal.

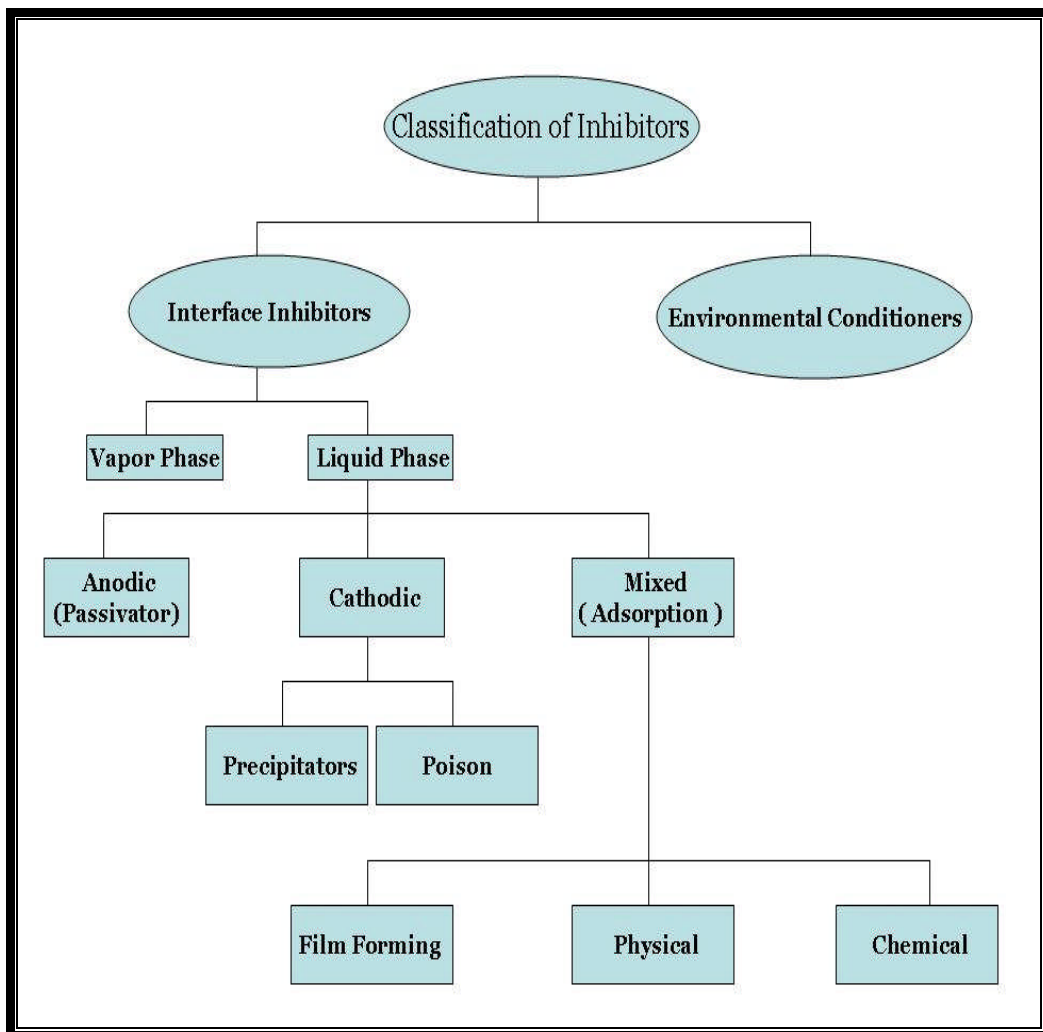


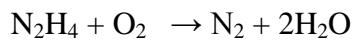
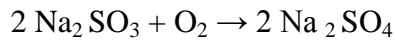
Figure 2-15: Inhibitor classification [97]

2.8.1.1 Environmental Conditions (Scavengers) [98]

These chemicals act by removing corrosive reagents. For example, by preventing cathodic depolarisation due to oxygen in the solution as well as reducing the current and potential, and hence the corrosion rate.

Oxygen scavengers are added to water, either alone or with another inhibitor to retard corrosion. One of the most common oxygen scavengers is sodium sulphite (Na_2SO_3). At elevated temperature, hydrazine has been used to remove oxygen.

A reaction typical of a scavenger is indicated in the following equations



Interface Inhibitors

Interface inhibitors form a diffusion barrier on the metal/environment interface to give rise to resistance of the anodic and cathodic reactions. They can be classified into liquid and vapour-phase inhibitors.

A- Liquid phase Inhibitors

These can be classified as anodic, cathodic or mixed, depending on the change in corrosion potential after the addition of the inhibitor.

• Anodic Inhibitors

The anodic inhibition mechanism is illustrated in Figure 2-16 which shows an increase in the polarisation of the anode where a large potential change results in a small current flow, which causes the corrosion potential to shift in the noble direction. In the case of stainless steel, the cathodic curve may then intersect the anodic curve in the passive region. Adsorption of the inhibitor on the anodic areas also plays a part in the process because it decreases the current density required for the anode to reach the critical passive potential. The most effective and widely used anodic inhibitors are:

- Oxidising anions, such as nitrite, chromate and nitrate, which can passivate steel in the absence of oxygen.
- Non-oxidising ions such as phosphate and molybdate that require the presence of oxygen to passivate steel.

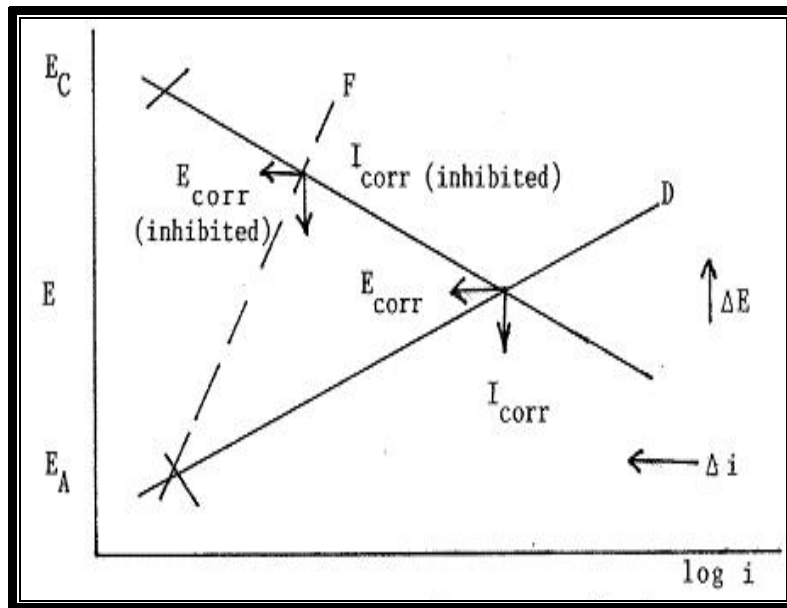


Figure 2-16: Evans type diagram showing corroding system under anodic inhibition [98]

• Cathodic Inhibitors

The effects of the cathodic inhibitor on cathodic polarisation are shown in Figure 2-17. In this case the corrosion potential is shifted to more negative values. The cathodic reaction is either used for hydrogen ion reduction to form hydrogen gas, or reduction of oxygen. Both these phenomena cause the environment immediately adjacent to the cathodes to become alkaline. Therefore ions such as zinc, magnesium and calcium may be precipitated as oxides to form a protective layer on the metal.

Inhibition by polarisation of the cathodic reaction can be achieved in several ways such as oxygen scavengers, cathodic poisons and cathodic precipitates. A serious drawback of using cathodic poisons is that they sometimes cause hydrogen blistering and an increase in hydrogen embrittlement, especially in acid solutions.

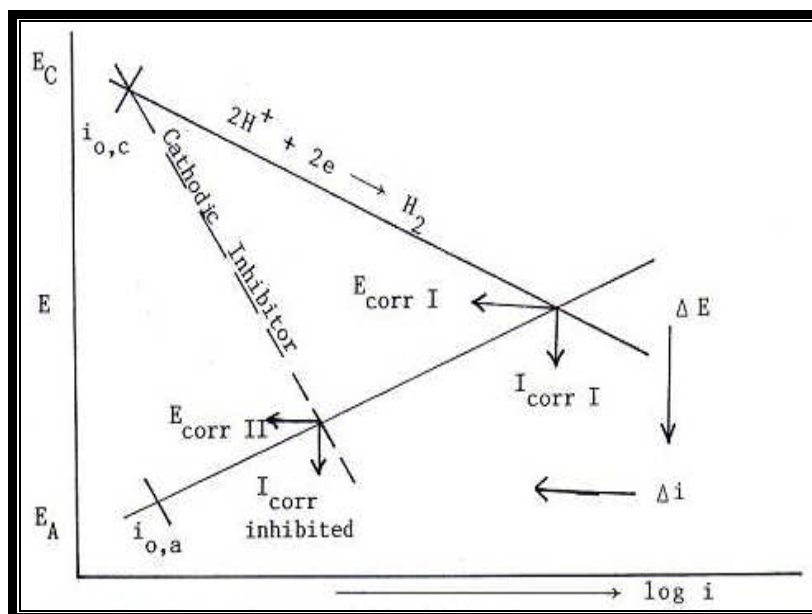


Figure 2-17: Evans type diagram showing corroding system under cathodic inhibition [98]

- **Mixed inhibitors**

This type of inhibitor controls both anodic and cathodic reactions, as illustrated in the Evans diagram, Figure 2-18. Organic inhibitors affect the entire surface of a corroding metal when present in sufficient concentration by forming an adsorbed film on the metal surface. Their effectiveness depends on chemical composition, molecular structure and their affinities for the metal surface. Inhibition of metal corrosion by organic compounds is a result of adsorption of organic molecules or ions at the metal surface forming a protective layer. This layer reduces or prevents corrosion of the metal.

The extent of adsorption depends on the nature of the metal, the metal surface condition, the mode of adsorption, the chemical structure of the inhibitor, and the type of corrosive media. Mixed inhibitors protect the metal in three possible ways: Physical adsorption, chemisorptions and film formation. Physical (electrostatic) adsorption may be due to the electrostatic attractive forces between ionic charges or dipoles of the adsorbed species and electric charges on the metal at the metal solution interface.

Organic inhibitors will be adsorbed according to the ionic charges of the inhibitors and the charge on the metal surface. Cationic inhibitors (positively charged) such as amines, or anionic inhibitors (negatively charged) such as sulfonates, will be adsorbed preferentially, depending on whether the metal is charged negatively or positively (Opposite sign charges attract). The charges on the metal can be expressed by their potential with respect to the zero-charge potential. As the potential becomes more positive, the adsorption of anions is favoured and as the potential become more negative, the adsorption of cations is favoured [96].

Besides electrostatic interaction, inhibitors can bond to metal surfaces by electron transfer to the metal to form a link. Electron transfer is from the adsorbed species by the presence of loosely bound electrons that can be found in anions and neutral organic molecules containing lone pair electrons or π -electron system associated with multiple, triple bonds or aromatic ring. In organic compounds, suitable lone pair electrons for bonding occur in functional groups containing elements of groups V and VI from the periodic table. The tendency for stronger bond formation as well as stronger adsorption by these elements increases with decreasing electro negativity in the order oxygen (O) < nitrogen (N) < sulphur (S) < (Se) [99].

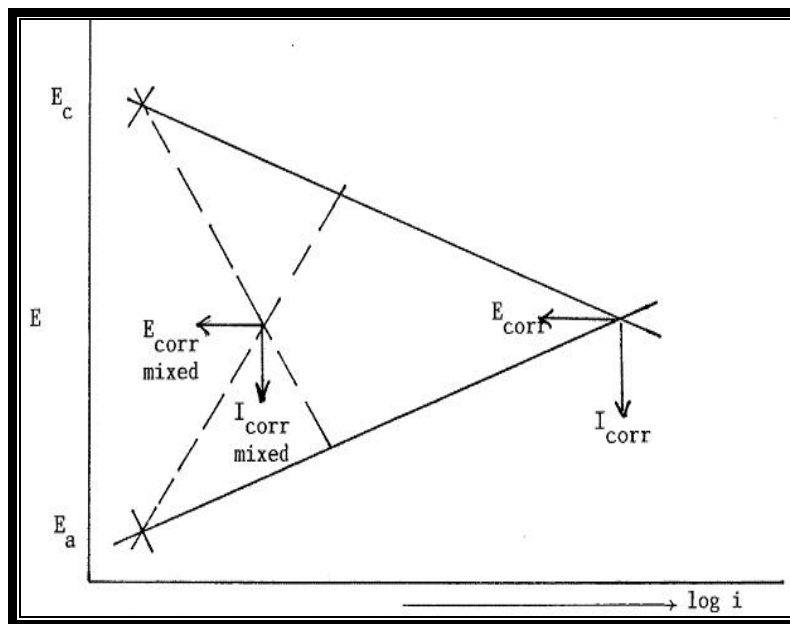


Figure 2-18: Evans Type diagram – showing corrosion kinetics for mixed inhibition [98]

B- Vapour-Phase Inhibitors

These are similar to the organic adsorption-type of inhibitors and possess a very high vapour pressure. They are also called (VCIs), volatile corrosion inhibitors which are transported in a closed system to the site of corrosion by volatilisation from the source. When in contact with a metal surface, the inhibitor vapour condenses and is hydrolysed by any moisture present to liberate nitrite, benzoate and bicarbonate ions. They are usually effective in closed vapour spaces such as shipping containers and boilers because they would be lost rapidly through any leaks in the package or container

2.9 Factors Affecting Inhibitor Performance

2.9.1 Effect of Carbon Steel Microstructures, Chemical Composition and Pre-corrosion

The importance of carbon and low alloy steel chemical composition and microstructure on the inhibition of CO₂ corrosion has been widely recognized, but different aspects are still uncertain. Several authors have studied the influence of steel microstructures on the corrosion process in aqueous solutions containing CO₂, although there is no general agreement on this issue. The effect of these variables on the corrosion product film formation and properties on inhibitor efficiency are far from being understood. This is mainly due to the complexity of the problem and the difficulty of describing the mechanisms involved. In addition, test conditions also vary widely, making them almost impossible to compare [100].

Steels may have different microstructures depending on the chemical composition and on the fabrication process. These various microstructural components (ferrite, pearlite, bainite, martensite) could affect not only the mechanical properties but also the corrosion resistance of the material as well as inhibitor efficiency [101].

Oblonsky et al. [102] showed the effectiveness of the surface conditions and microstructure. They studied the adsorption of octadecyldimethylbenzylammonium chloride (ODBAC) to carbon steel with two different microstructures. They found that ODBAC physisorbs strongly to the ferritic-pearlitic microstructure and weakly to the martensitic microstructure. They attributed the differences to the persistency of the passive films on the two microstructures, with further stable passive film on the martensitic steel preventing most favourable adsorption of the inhibitor.

French et al. [103] produced SEM results showing that the structure of the corrosion product layer is adapted by the inhibitors. They suggested that the structure of the inhibitor must be the appropriate one to interrelate with the corrosion products and that they can be effective on iron carbonates or sulphides, but not effective on oxides.

Malik [104] studied the influence of pre-corrosion on the performance of a C16 quaternary amine as inhibitor for CO₂ corrosion of carbon steels. He found that the improved inhibition on a pre-corroded surface was related to the concentration of the inhibitor and to its blocking effect on CO₃²⁻ entry into regions of high Fe²⁺.

Numerous studies have been carried out to show that for C-Mn steels, inhibitor efficiency is affected by microstructure and that this effect could be specific to inhibitor molecular structure

Lopez et al. [105] studied the influence of microstructure on inhibitor performance. Using electrochemical measurements, they evaluated the effect of the addition of 100 ppm of benzimidazole on the corrosion layers for two different microstructures. The presence of the inhibitor improved the corrosion resistance for the annealed samples, while for the Q and T samples, the opposite effect is observed, despite benzimidazole not being particularly efficient in the experimental conditions studied.

From scanning electron microscopy (SEM), electron dispersive X-ray (EDX) and X-ray photoelectron spectroscopy (XPS), a study by Lopez [106] analysed characteristics such as morphology, thickness and composition of corrosion layers formed on carbon steel with two different microstructures (annealed, and quenched and tempered). The author concluded that the microstructure of steel influences inhibitor efficiency, the properties of the corrosion layers, such as morphology, and the quantity of the various chemical compounds that are present

Having studied two steel compositions with the same microstructures and keeping the experimental conditions constant, Lopez [100] demonstrated that not only the molecular structure of the inhibitor molecule is important when determining its performance in chloride media containing deoxygenated CO₂, but also the microstructure of the steel to be used as the working material. Also in his study, he concluded that the presence of a long hydrocarbon chain with hydrophobic properties could be linked with the formation of a protective, yet porous, film that reduces thoroughly the corrosion process.

Numerous studies have been carried out to show the effect of microstructure on the detrimental effect of pre-corrosion on inhibitor efficiency. Paolinelli, [107] studied the effect of pre-corrosion and steel microstructure on inhibitor performance under flowing conditions (laminar flow) with two different microstructures (ferrite-pearlite and tempered martensite). The inhibitor was added after different pre-corrosion periods: 24, 48 and 72 hrs. Studies showed that the properties of surface films and the efficiency of the inhibitor depend on microstructure, being greater for tempered martensite than for ferrite-pearlite. In addition, pre-corrosion decreases efficiency and its impact is also microstructure dependent.

With the same heat treatments and microstructural characteristics of both steel samples having been reported previously in [109], Paolinelli, [108] studied the influence of steel microstructure, pre-corrosion period of 72 hrs and 1%Cr content addition on CO₂ corrosion susceptibility of C-Mn steels and on the inhibitor performance that has been studied. The results show the detrimental effect of pre-corrosion and Cr addition, due to the presence of chromium-rich compounds, slows down the inhibitor adsorption and inhibitor efficiency.

It is also shown that the pre-corrosion impact depends on microstructure and chemical composition. More recently, the same author has shown that the addition of 1%Cr has a remarkably detrimental effect on a commercial inhibitor performance when samples are pre-corroded for 24 hours [109].

These results show that a clear Cr enrichment in the corrosion product for both microstructures has a detrimental effect on the performance of the inhibitor used. This is in agreement with an earlier study of Kapusta and Canter [110] who studied the effect of the steel composition on inhibitor efficiency. They used two steel types– tempered martensite and ferritic-pearlitic with two different inhibitors. They concluded that Cr enrichment takes place in the corrosion product scale. They suggested that the presence of this scale, which increases the corrosion resistance in inhibitor free brines, also reduces the effectiveness of the inhibitors due to the poor adsorption of the inhibitor molecules on a Cr rich scale.

Gulbrandsen et al. [111] studied the influence of pre-corrosion on the performance of inhibitors for CO₂ corrosion of carbon steel. The tests were performed at 20-50°C, pH 5, 1 bar CO₂, and 1-3 wt. % NaCl solution. They used generic inhibitor compounds and the test specimens were pre-corroded for six days in the corrosive media prior to the inhibitor addition. They reported results from four different commercial inhibitors and three different steels: X65, St52 and Cr0.5. They concluded that the negative effect of pre-corrosion in ferritic-pearlitic steels could be related to differences in the cathodic reaction inhibition efficiency on cementite and on ferrite

Mora-Mendoza et al. [112] studied the influence of cementite on the corrosion rate of mild steel under turbulent flow conditions at different pH. The experiments were carried out in 3% NaCl solutions saturated with CO₂ at 25°C. They found that when a quaternary amine inhibitor was added, the corrosion rate was lower as the pre-corrosion time was minimal. They reported the effect as either an increase in cathodic area or an electrochemical potential gradient between the Fe₃C pores that prevented positively charged inhibitor ions from reaching all anodic sites.

Turgoose and his co-workers [24] pointed out that the major factor affecting the inhibitor performance on the weld metal is the pre-corrosion time, not the test geometry. The experiments showed very different behavior for 4 days of pre-corrosion in the thin film set-up and for 4 hours of pre-corrosion in a bubble test cell. The results showed that after four days of pre-corrosion, in thin film tests, the inhibitor did not protect the weld. However, bubble tests with only a few hours of pre-corrosion did give protection of the weld metal. To clarify the cause of this, the authors carried out bubble tests with long-term pre-corrosion, and again the inhibitor failed to sufficiently protect the weld metal. Severe selective attack of the weld metal occurs when the other components of the weld are well inhibited, but the weld poorly so. This can occur with under dosing of the inhibitor, and this is significantly affected by the extent of pre-corrosion of the weldment before inhibitor addition.

Winning and McNaughtan [6] reported that the length of time of pre-corrosion had a significant influence on the time required for the corrosion inhibitor to reduce corrosion. They also stated that the rate of inhibition could be controlled by application of the appropriate amount of synergist as well as using an organic synergist.

2.9.2 Effect of the Temperature

Temperature was regarded as a significant and field proven parameter. Changes in temperature may affect several factors. For example the chemical structure of the inhibitor compound, the physical properties of the inhibitor film and the chemisorption process taking place on the steel surface. At elevated temperature, inhibitor solubility may be affected in an unexpected way; for example, some inhibitors have lower solubility in brine at elevated temperature than with the ambient temperature. Elevated temperature can also polymerise some inhibitors which sometimes cannot be tolerated, since plugging can take place. The metal surface can change according to the temperature; for example, in a CO₂-H₂O system at < 60°C, iron carbonate forms, on which some inhibitors fail to perform well. [113].

The performance of various corrosion inhibitors has been tested in a flow loop at high temperature. The experimental conditions were 60-150°C, 1 bar CO₂, pH 5 and 0.1-1% NaCl. The inhibited corrosion rate generally increased with increasing temperature. The effect of the temperature was dependent on the inhibitor formulation [114].

Gulbrandsen et al. [94] observed that inhibitor performance was impaired with increasing pre-corrosion time and increasing temperature. The commercially available water soluble corrosion inhibitors for CO₂ corrosion, have been tested in the laboratory on carbon steel specimens that were corroded for up to 18 days in the medium prior to inhibitor addition. The tests were performed at 20-50°C, pH 5, 1 bar CO₂, 1-3 wt% NaCl in glass cells and a glass loop. The results show that inhibitor performances were impaired with increasing pre-corrosion time and increasing temperature.

2.9.3 Effect of Flow

The flow effect on CO₂ corrosion is mainly about the effect on mass transfer involved in the corrosion process. Higher flow velocity usually means high turbulence and effective mixing in the solution. Increased turbulent flow accelerates the corrosion species both towards and away from the metal surface. This may result in an increase of corrosion rate when the mass transfer is the rate controlling factor and no corrosion film forms at the metal surface. If the corrosion reaction appears to be under activation control, there is no significant effect of liquid flow velocity on CO₂ corrosion. On the other hand, at higher flow velocity, less protective corrosion film will form at the metal surface. In some cases with enormously high flow velocity, the flow can even mechanically remove the protective film, resulting in an increase of corrosion rate, sometimes even localised corrosion [46].

The effectiveness of inhibitors for use under normally occurring flowing conditions is highly dependent on fluid velocity. Fluid velocity is widely believed to be an important factor in the removal of inhibitor films especially at high velocities where the hydrodynamics such as shear stress and mass transfer, considered to be the fundamental hydrodynamic factors that describe the effect of flow on corrosion, will increase the fluid to wall shear stress so that the film of corrosion product or inhibitor, which normally provides protection, is thinned or even removed causing a high corrosion rate [86].

In general, the efficiency and persistency of an inhibitor film under flowing conditions probably depend on four major factors: the type of adsorption of the inhibitor film (physisorption, chemisorption, composition and roughness of the substrate), the chemical composition of the flow, the wall shear stress/mass transport coefficient, and the erosive nature of the flow [84].

Laboratory tests have been developed by Turgoose et al. [24] to ensure that corrosion inhibitor treatments are compatible with weld metallurgies. It was concluded from their work that under high flow rate conditions, less compact/adherent inhibitor films/scales on the weld metal might be removed while films on the parent pipe remained intact leading to a switch from cathodic to anodic weld metal behaviour.

Corrosion rates in flowing media containing inhibitors depend on flow intensity. Here, the flow rate refers to the effects of a combination between flow velocity and pattern, sand content and particles size, as well as many other flow influenced parameters as has been mentioned earlier. As shown in Figure 2-19, corrosion rate increases sharply beyond a critical flow rate and below the critical flow rate an almost steady corrosion rate is observed. Critical flow intensities can be quantified in terms of critical wall shear stresses which are defined as the highest wall shear stress up to which no flow induced localised corrosion occurs under specific system conditions. The critical flow intensity varies from one inhibitor to another depending on the adsorption strength of the inhibitor to the metal surface [116].

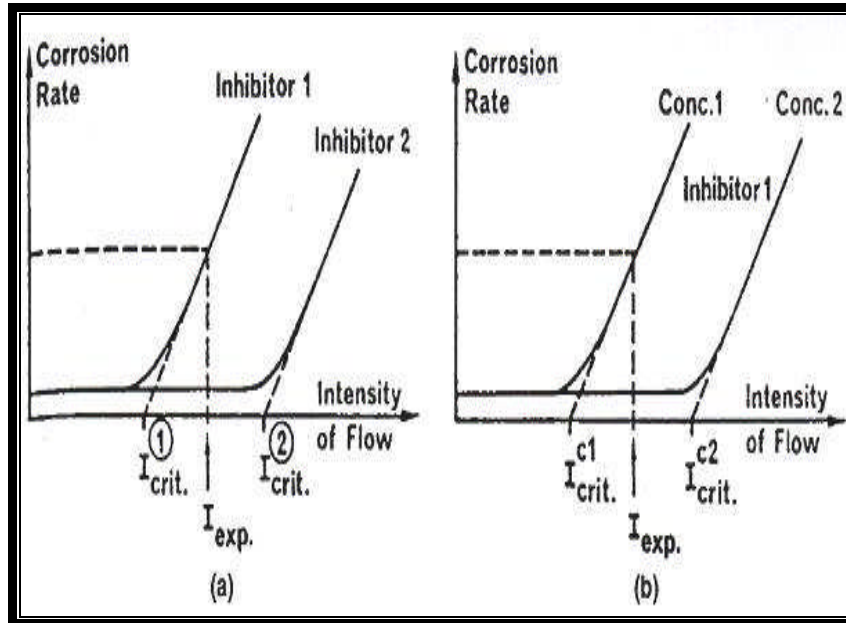


Figure 2-19: Effect of flow intensity on corrosion rate for different inhibitors (a) and same inhibitor different concentration (b) [116]

A study by Chen [117] used electrochemical techniques including EIS and DC, on the Rotating Cylinder Electrode (RCE). They found that the effectiveness of inhibitors for use under normally occurring flowing conditions is highly dependent on the fluid velocity. At high velocities, the fluid-to-wall shear stress increases so that films of corrosion product and/or inhibitor, which normally provide corrosion protection, are thinned or even partially removed, causing high rates of corrosion.

Research by Mendoza et al. [118] reported higher corrosion rates when flow velocity was increased using a RCE in the presence of an inhibitor. They concluded that when the rotation speed increases, changes in E_{corr} to more positive values could create a positive charge on the metal surface that forces the inhibitor to be removed, especially if the inhibitor was adsorbed by electrostatic attraction.

In contrast, a study by Kvarekval et al. [114] in flow loops at high flow velocity, the flow velocity was varied between 1 and 9 m/s, corresponding to wall shear stress values between 5 and 135 Pa respectively. The inhibited corrosion rate showed little dependence on the flow velocity. No inhibition failure related to flow was observed. SEM inspection showed that rather thick corrosion product layers had formed on the

specimens. The results indicate that the inhibitor adsorption works in interaction with the corrosion product film and may have strengthened the corrosion product films and made them less susceptible to removal at high flow velocities

There has been considerable debate over the past 10-15 years with regard to the effects of flow on inhibition both in terms of adsorption/desorption effects under highly turbulent conditions and inhibitor transport issues. Over recent years, it has become apparent that many inhibitors are actually considerably more resistant to flow effects than was perhaps thought 10-15 years ago. A number of studies have demonstrated that at moderate ranges of flow (10-15 m/s), inhibitor performance has been found to be essentially independent of velocity [119].

The persistence of the inhibitor film assessed in CO₂ containing media, using RCE and RDE as a function of hydrodynamics flow conditions with electrochemical impedance spectroscopy as an electrochemical method, was studied by Altoe et al. [120]. They concluded that the stability of the inhibitor film is flow dependent and is strongly affected by the residual concentration of the inhibitor in the solution. This latter case was essential to regenerate the inhibitor film, especially at high flow velocities.

2.10 Evaluation and Selection of Inhibitors

In oil and gas exploration and production, the use of corrosion resistant alloys for pipe line construction is often cost-prohibitive. For this reason the selection of appropriate corrosion inhibitors for any field conditions is an extremely important process. The selection is usually based on comprehensive laboratory and field testing.

Therefore it is important to understand the key process parameters that depend on inhibitor selections such as operational conditions, solution chemistry and flow conditions (water cut, flow velocity and flow pattern) [35]. For laboratory methodology to be useful, it is extremely important to simulate the combined effect of parameters such as pressure, temperature and the compositions of steel, gas, oil and water that influence corrosion inside an actual pipeline.

The inhibitor selection process consists of a series of laboratory tests before they can be qualified for field trial and eventually applied for field use. The preliminary performance test undertaken may include the wheel test, kettle test and partitioning test. Additional tests may simulate more closely the field operating conditions, such as rotating cylinder electrode (RCE), jet impingement equipment, and high shear autoclave and flow loop [121].

2.10.1 Inhibitor Efficiency

Ranking and selection of corrosion inhibitors is generally based on percentage inhibition where the inhibitor with highest inhibition is usually selected. Inhibitor efficiency depends on a number of factors such as molecular size and mode of interaction with the metal surface, temperature, pressure, number of adsorption sites and their charge density and flow parameters such as velocity and shear stress. Efficiency of the inhibitor can be expressed based on the formula shown below.

$$\text{Eq.22} \quad \text{Inhibitor Efficiency (\%)} = \frac{(\text{CR}_{\text{Uninhibited}} - \text{CR}_{\text{Inhibited}})}{\text{CR}_{\text{Uninhibited}}} \times 100$$

Where:

$\text{CR}_{\text{uninhibited}}$ = corrosion rate of the uninhibited system

$\text{CR}_{\text{inhibited}}$ = corrosion rate of the inhibited system

In general, the efficiency of an inhibitor increases with an increase in inhibitor concentration, e.g. a typically good inhibitor would give 95% inhibition at a concentration of 0.008% and 90% at a concentration of 0.004% [122].

CHAPTER 3 ELECTROCHEMICAL TECHNIQUES FOR CORROSION RATE MEASUREMENTS

3 Introduction

Corrosion monitoring techniques can be classified into two major categories: non electrochemical techniques and electrochemical techniques. Traditionally the non electrochemical techniques are widely used through the industry due to their simplicity, robustness and reliability. However, the drawback of these techniques is that they do not reveal any details about corrosion mechanisms. On the other hand the electrochemical measurements provide a great deal more with regard to the corrosion mechanism. Corrosion is an electrochemical process, therefore electrochemical methods were designed as a preliminary investigation into the applicability of each technique for more detailed research into weld corrosion. Laboratory studies using electrochemical techniques such as galvanic current measurements and linear polarisation resistance tests have been used in static and flowing conditions with and without inhibitor to identify the corrosion rates of each region of the weld. The main advantages of the electrochemical methods are short measuring times, high measurement accuracy, and the possibility of continuous corrosion monitoring.

3.1 Linear polarisation resistance

One of the main advantages of this technique is that it enables corrosion rates to be obtained relatively fast (2-10 minutes) compared to non-electrochemical techniques. However, the drawback of this technique is that it gives no information about the corrosion mechanism.

This technique is based on the fact that the quantity of free electrons required to produce a small shift in the potential of the corroding electrode are proportional to the corrosion current density, which can be converted to a corrosion rate. A potential (typically of the order of 10-20 mV) is applied to a freely corroding element and the resulting linear current response is measured.

This small potential perturbation is usually applied step-wise, starting below the free corrosion potential and terminating above the free corrosion potential. The polarisation resistance (R_p) is the ratio of the applied potential and the resulting current response. This resistance is inversely related to the uniform corrosion rate. The output data shown in Figure 3-1, is used to calculate both the polarisation resistance R_p and the corrosion current (i_{corr}). The slope of a line is the change in its Y-values divided by the change in its X-values. Hence the slope for a linear polarization curve is the change in potential divided by corresponding change in current density. This relationship is written mathematically as:

$$\text{Eq.23} \quad R_p = \frac{\Delta E}{\Delta I}$$

Once the R_p has been estimated, the corrosion rate can be obtained from the Stern-Geary equation which assumes the polarisation current changes linearly with a change in the potential. From this linear approximation, the corrosion current can be estimated as shown below:

$$\text{Eq.24} \quad i_{corr} = \frac{b_a \cdot b_c}{2.3(b_a + b_c)} \cdot \frac{1}{R_p}$$

$$\text{Eq.25} \quad i_{corr} = \frac{B}{R_p}$$

Where B [Stern -Geary Constant (mV)] = $\frac{b_a \cdot b_c}{2.3(b_a + b_c)}$

i_{corr} = corrosion current density ($\frac{A}{cm^2}$), R_p = Polarisation Resistance (Ωcm^2)

b_c = the cathodic Tafel slope ($\frac{V}{decade}$)

b_a = the anodic Tafel slope ($\frac{V}{decade}$)

An example of this calculation is available in Appendix 1

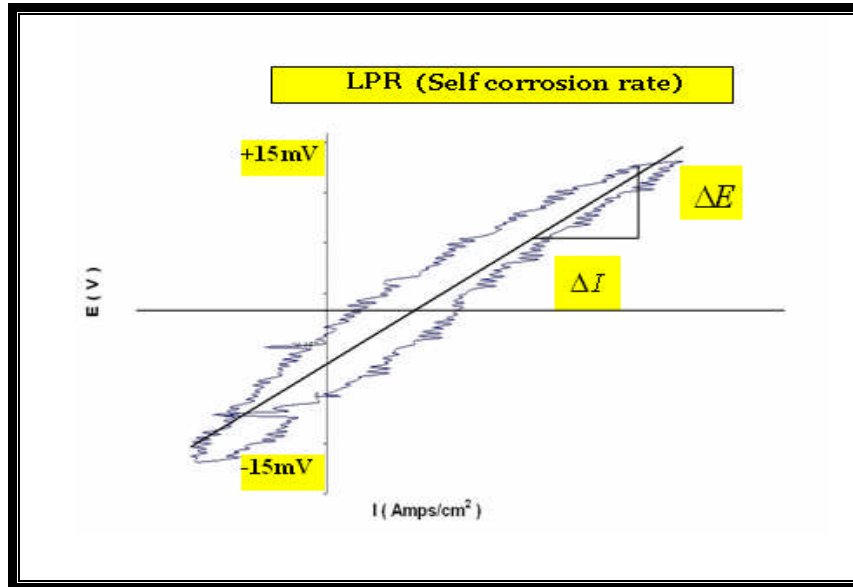


Figure 3-1: Obtaining R_p from applied – current linear polarisation curve.

3.2 Zero Resistance Ammeter

Scientific studies, using artificial corrosion conditions to predict the specific corrosion behaviour of metal/alloy couples, require the measurement of the small current of the short circuit without introducing an additional resistance which polarises the system either cathodically or anodically and causes erroneous results. For this reason, the so called Zero-Resistance Ammeter (ZRA) can be used to permit coupling or galvanic current measurements to be made with zero resistance in the measuring circuit.

The electrical connections permitted galvanic current to be monitored between samples. Wires were connected to the Galvo-gill 12 (Zero Resistance Ammeter) machine using different channels with HAZ as the common terminal for both parent and weld metal in order to measure the current flow from each of weld components. Measurements of the current flowing in an electrochemical couple are a direct measure of the increase of the corrosion rate of the anodic element by measuring galvanic current. The ZRA directly measures the galvanic current and the effect of parameters, such as flow.

Electrical connection to the Zero Resistance Ammeter (ZRA) is shown in Figure 3-2. The electrode connected to the cathodic terminal was the HAZ which was the common terminal for both the parent metal and weld metal. In the first channel, the parent metal and HAZ formed first couple. The second channel had the second couple formed between weld metal and HAZ. When the current registered by the ZRA was positive, it meant the element connected to the anodic terminal was corroding preferentially to the element on the cathodic terminal, and vice versa.

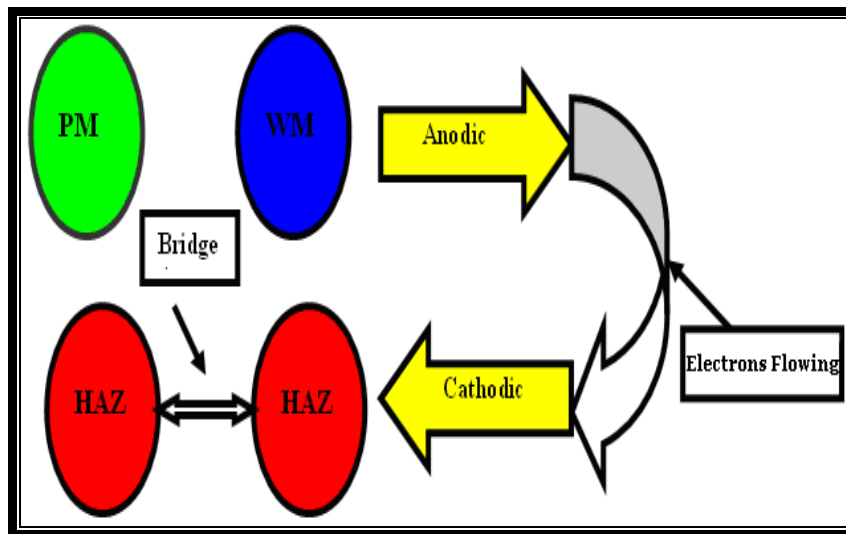


Figure 3-2: Schematic diagram of sample connection to Zero Resistance Ammeters

3.3 AC Impedance

In the oil and gas production industry, internal corrosion of carbon steel pipelines is a well known phenomenon and a serious problem. Inhibition is the most cost-effective and flexible method of corrosion control. Therefore, knowledge of the mechanism of a corrosion inhibition process is highly desirable in the design and proper selection of inhibitors.

In the past two decades, pipeline corrosion investigations and prediction have generated an extensive literature on “sweet” CO₂ corrosion, but few studies have dealt with the influence of the hydrodynamic conditions on inhibitors performance in laminar and turbulent flows [123, 124]. Some authors have recently been studying the inhibitor behaviour under multiphase turbulent flow [125].

However, very little is known about the inhibitor film formation mechanism as well as the porosity and thickness of the inhibitor film. For corrosion of welded carbon steel pipelines electrochemical impedance spectroscopy (EIS) is promising method and hence, more emphasis has been placed on its use for studying weld corrosion.

EIS has been used to study the corrosion product film and inhibitor performance during last twenty years. Generally, the application of the EIS technique has been used by researchers for the evaluation of the inhibitor, anodic coatings and polymer coatings [126,127].

EIS data was most commonly analysed by researchers by fitting the data to an equivalent circuit model. The elements in the model are common electrical elements such as resistors and capacitors; for example, the solution resistance was substituted by resistor and the electrochemical double layer by non ideal capacitor (constant phase element). A brief introduction to the measurement technique is given below:

3.3.1 Concept of A.C. Impedance

EIS has been adopted by corrosion scientists, particularly in the last decade, due to its ability to separate out various processes occurring at a corroding electrode. It has been employed in aqueous solution, non aqueous, organic and inorganic electrolyte, molten salts, for organic coating, with and without inhibitive pigments, as well as for reinforced concrete etc. This technique appeared in the 1920's, and developed rapidly since Randles suggested the equivalent circuit for the electrochemical interface. Since the 1970s extensive studies have been carried out on various systems by the use of the A.C. impedance technique. These studies emphasised active-passive transition, mechanism of iron dissolution and the influence of diffusion on the impedance data [128].

Figure 3-3 shows the simple electrochemical circuit with a pure charge transfer process and the most common cell elements proposed by Randles. The circuit includes a solution resistance, double layer capacitance and a charge transfer resistance.

The double layer capacitance is parallel to the impedance due to charge transfer reaction.

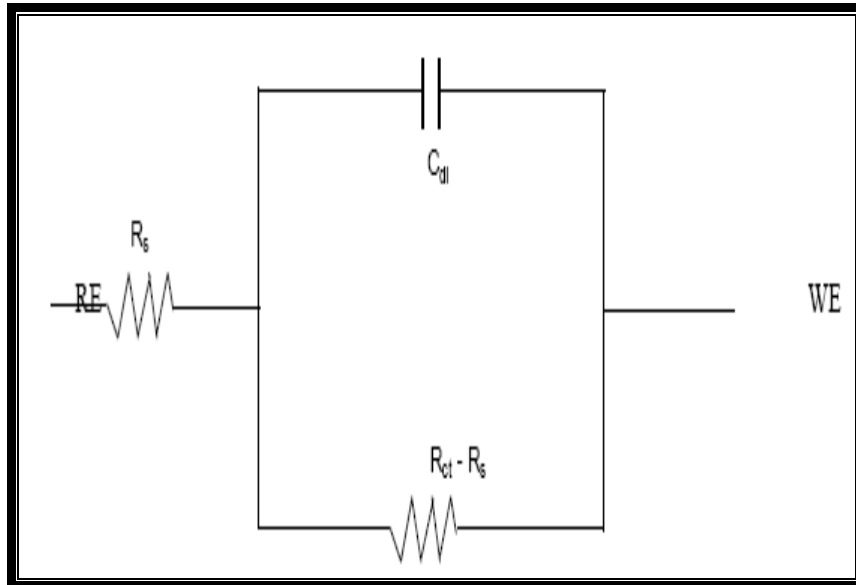



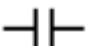

Figure 3-3: Randles type equivalent circuit components [128]

The basic concept of the technique is that the electrochemical interface of the corrosion electrode can be viewed as a combination of the passive electrical circuit elements such as resistance, capacitance and inductance. An arrangement of such a set of components will respond to an applied AC signal, and the resultant current passing in the circuit can be determined by Ohm's Law:

$$\text{Eq.26} \quad V = R \times I$$

Table 2 shows a list of circuit elements where some have no imaginary components (frequency independent) at all such as resistor. However, the capacitor has no real component and an imaginary component which is a function of its capacitance at AC frequencies, where ω is the angular frequency ($2\pi f$) and j a complex number $= (\sqrt{-1})$.

Table 2: Common Circuit Elements, Symbols and their Impedance

Circuit Elements	Symbol	AC Impedance Equations
Resistor		$Z = R$
Capacitor		$Z = \frac{1}{jC \omega}$
Inductor		$Z = j \omega L$

The most components are : The solution resistance: R_s (ohm.cm^2), the charge transfer resistance : R_t (ohms.cm^2), the substrate double layer capacitance: C_d (F), the Warburg diffusion impedance: Z_w (ohms.cm^2),the film resistance, R_f (Ohm.cm^2), and the film capacitance C_f (F) .

There are three fundamental ways (Nyquist plot, Bode plot, Equivalent circuit) commonly used for the graphical presentation of impedance data obtained over a wide frequency range. By plotting the impedance data in different forms, individual components can be obtained, which make up the electrochemical system under test, which in turn supplies valuable mechanistic information on corrosion degradation of the metal

3.3.2 NYQUIST PLOT

Analysis of impedance data is commonly carried out over a wide frequency range with the aid of the Nyquist complex plane plots in order to determine the individual components of the equivalent circuit model parameters (R_s , R_p and C) from a complex impedance plot, as shown in Figure 3-4.

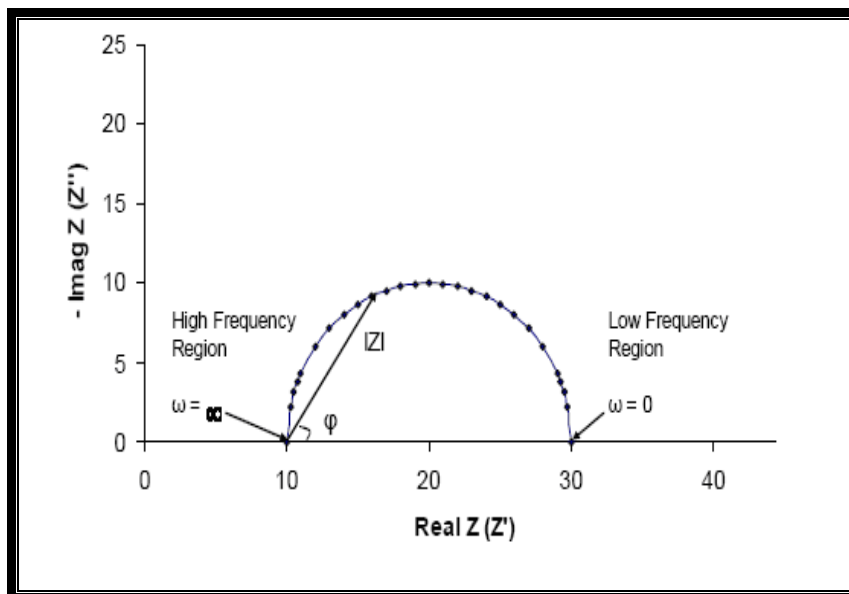


Figure 3-4: Nyquist plot for a simple electrochemical one time constant system [128]

The Nyquist plot represents a series of vector points reflecting the impedance of the circuit at particular frequencies. The real part of the impedance response represents the resistive part. However, the ordinate as the imaginary part (the capacitance) is frequency dependent and its value varies along the curve.

In the monitoring technique, based on the theory of Ac impedance, the solution resistance is estimated from impedance measured in the high frequency range, while the sum of the polarisation resistance and solution resistance is estimated from the impedance in the low frequency range.

At high frequencies the capacitor conducts easily and the only resistances are those of the solution and film resistance which appear on the left hand intercept of the semi circle on the Z' - real axis. As the frequency drops the capacitor conducts less and less and the plot follows a semi circle until the capacitor stops conducting current and the cell impedance becomes R_s and R_{ct} which correspond to the right hand intercept with the Z' -real axis.

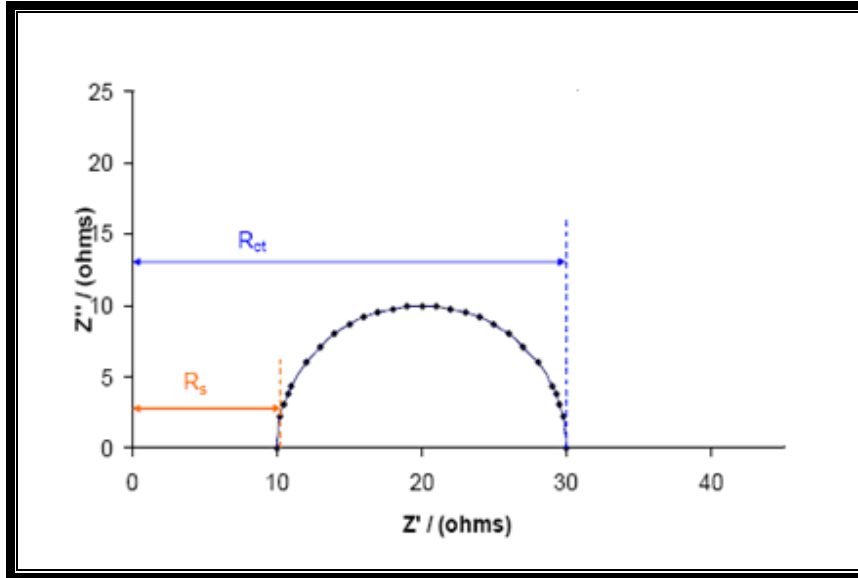


Figure 3-5: R_{ct} & R_s measurements in a pure charge transfer controlled situation [128]

In Figure 3-5, the parallel combination of the resistor R_{ct} (charge transfer resistance) and capacitor represents the corroding interface where the Cdl represents the capacitance of the double layer, which is formed by adsorption of ions and water molecules. The charge transfer resistance in an activation controlled system is equivalent to the linear polarisation resistance and is a measure of the electron transfer and hence the corrosion rate.

The value of R_{ct} can be used to calculate the corrosion rate current I_{Corr} from the Stern-Geary relationship:

$$\text{Eq.27} \quad I_{Corr} = \frac{Const}{R_{ct}}$$

Few reactions involve pure activation control and with iron in seawater, diffusion control plays an important part. In practice diffusion controlled processes occur frequently and as a result, an additional circuit element (Warburg impedance) is included in the equivalent circuit and combined in series with R_{ct} and can be represented on a Nyquist plot by a line at 45° to the axis.

Warburg impedance appears at low frequencies and since the diffusion is a slow process, it is unperturbed by high frequencies. Therefore, with decreasing frequencies, the contribution from a diffusion process to the total impedance increases. The curve (Nyquist plot) is no longer a semi circle, as shown in Figure 3-6 [128].

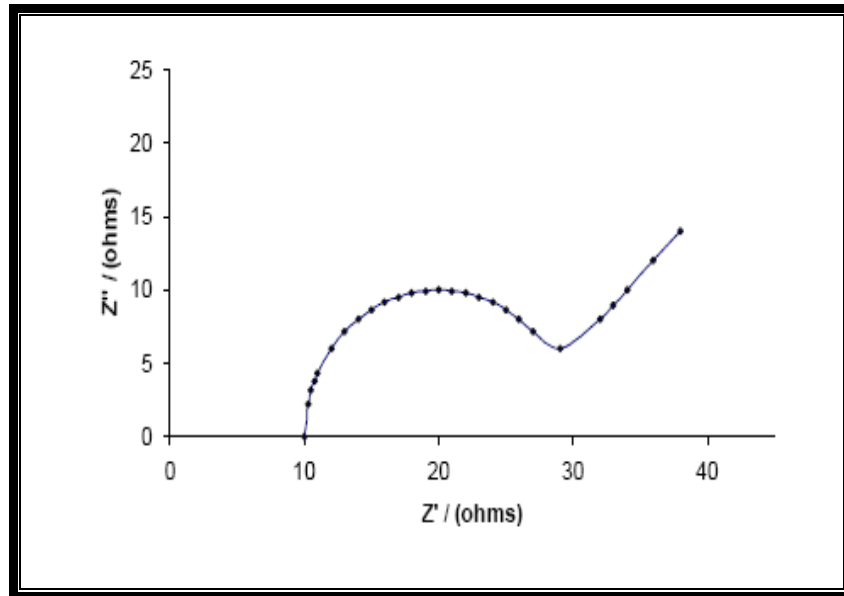


Figure 3-6: Shape of the Nyquist plot when it changes from charge transfer control to diffusion control [128]

3.3.3 Equivalent Circuit Models

EIS data is commonly analysed by fitting to an equivalent electrical circuit, which can then be used to model the various phenomena going on at the interface. The equivalent electrical circuit can behave in a similar way to an electrochemical process. This concept has since been expanded to the corrosion process where the combination of a resistor to simulate the solution and corrosion film resistance in the cell, coupled to a second or charge transfer in parallel to the double layer capacitor, will reproduce the behaviour observed by a corrosion process under activation control.

Some common equivalent circuit models which can be used to interpret simple EIS data with their Nyquist plots, Bode plots and impedance plots are shown in Figures 3-7, 3-8, 3-9 and 3-10 respectively [129].

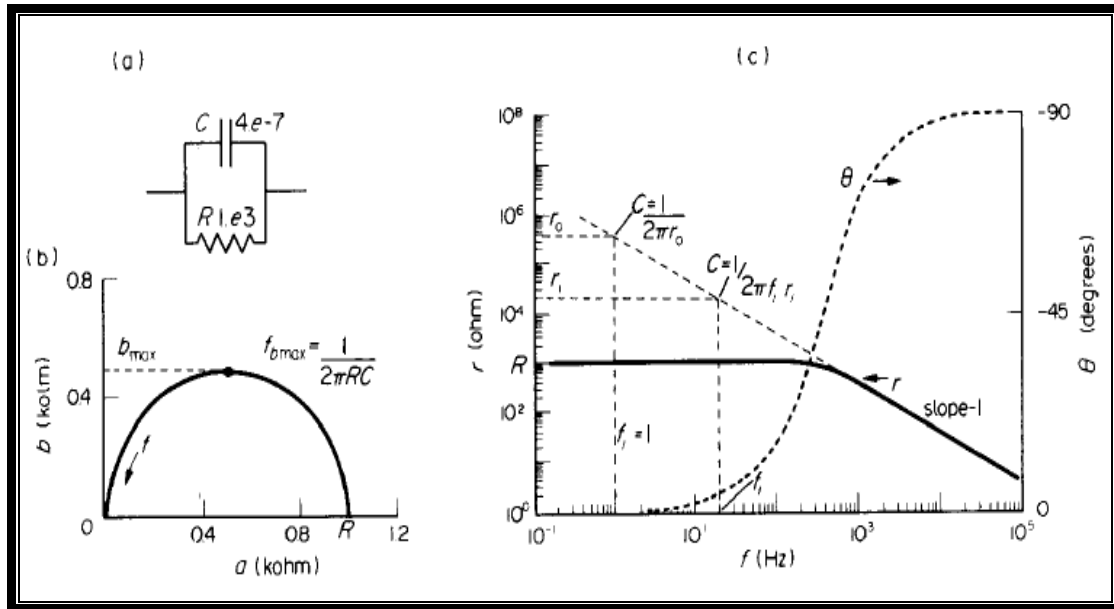


Figure 3-7: Equivalent electrical circuit used to represent a parallel resistor, R and capacitor, C , combination (a) and its Nyquist (b) and Bode (c) impedance plots [129]

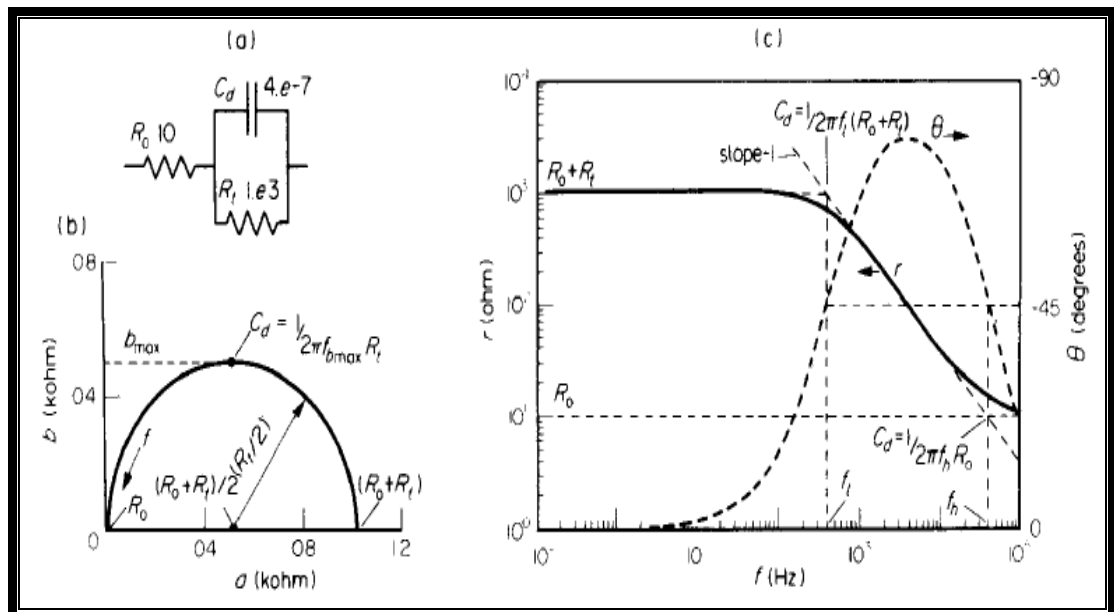


Figure 3-8: Equivalent electrical circuit used to represent the unpainted metal/solution interface (a) and its Nyquist (b) and Bode (c) impedance plots [129]

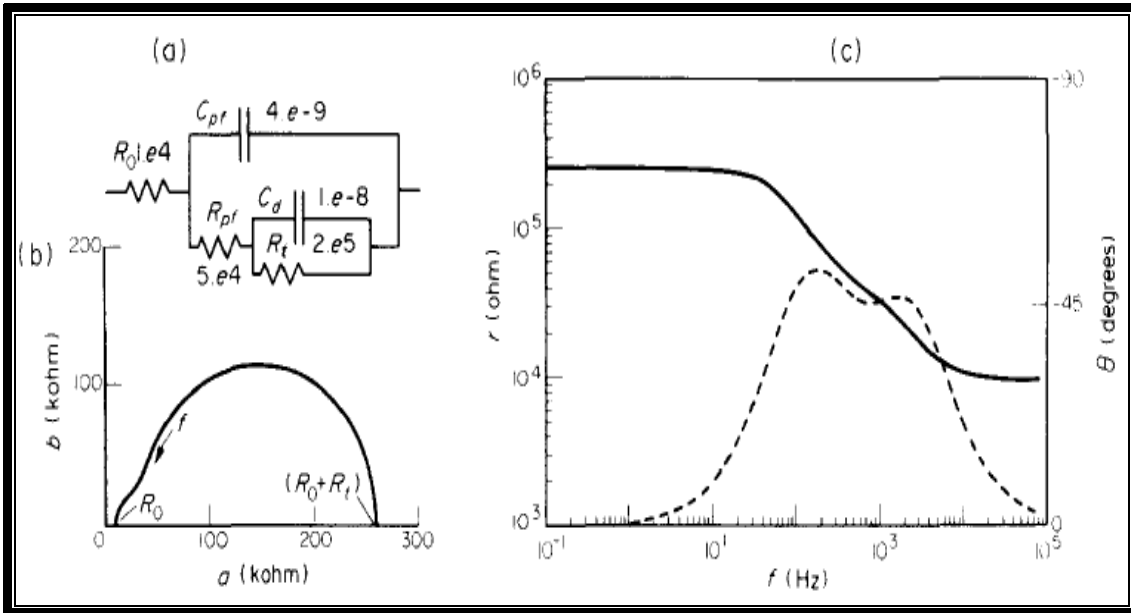


Figure 3-9: Equivalent electrical circuit used to represent the painted metal/solution interface in the absence of diffusion (a) and its Nyquist (b) and Bode (c) impedance plots [129]

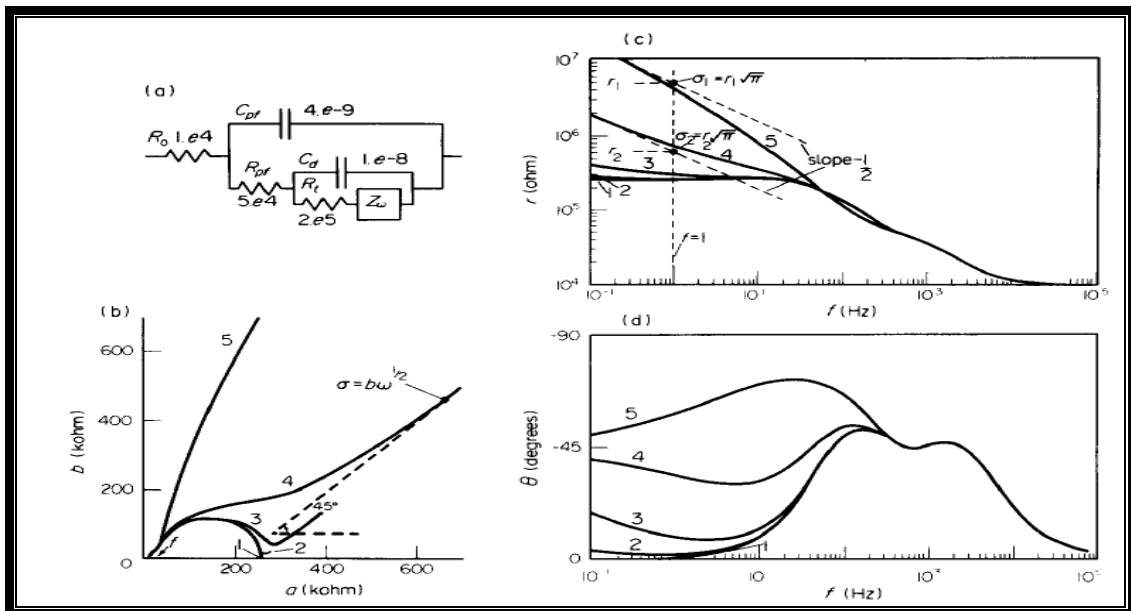


Figure 3-10: Equivalent electrical circuit used to represent the painted metal/solution interface in the presence of diffusion (a) and its Nyquist (b) and Bode (c) impedance plots [129]

CHAPTER 4 EXPERIMENTAL WORK

4 SUMMARY

The aim of the experimental work was to study the effectiveness of typical oilfield corrosion inhibitors in controlling the internal corrosion of welded X65 pipeline steel in brines saturated with carbon dioxide at one bar pressure, under static and dynamic flowing conditions, at a range of temperatures. The experimental work was carried out in several stages.

The first stage of the experimental work was concerned with the generation of a preliminary sweet corrosion test for the weldment in a glass cell under stagnant conditions.

The second stage of the work included a set of results obtained for the welds by using the flow channel developed in an earlier project at Cranfield University, with the associated corrosion monitoring systems such as LPR, Zero Resistance Ammeter and AC impedance. The electrochemical measurements described in this section were designed as an investigation into the applicability of each technique for more detailed research into weld corrosion.

The third stage of experimentation was the construction of the rotating cylinder electrode and related to the inhibitive effect of a commercially available green inhibitor on the sweet corrosion of X-65 carbon steel. These experiments were carried out in glass cells for stagnant conditions in addition to the flow channel and rotating cylinder electrode for flowing conditions.

The majority of the experiments were carried out at ambient temperature and a pressure of 1 bar in a cell containing artificial seawater (Tropic Marine Sea salt), saturated with CO₂. Some results for tests at 50°C and 70°C are also reported

Experiments were performed in order to follow the procedural requirements of the ASTM G170-01a standards guide to ensure the selection of the appropriate corrosion inhibitor for a given set of experimental data in the laboratory under high shear conditions. Prior to initial work in the laboratory, an assessment control of substances hazardous to health (COSHH) was carried out.

4.1 Specimen characteristics and preparations

Samples were machined from welded X65 steel pipe with a composition of 0.08% C, 1.6% Mn & 0.3% Si, the remaining being iron (Fe) as shown in Table 3. The steel had been thermomechanically controlled rolled to give a 32mm thickness with a fine-grained ferritic microstructure and a hardness of 200-210 Hv. The double-vee weld had been produced by the submerged arc process, with a relatively high heat input (5-10 J/mm) and a hardness of 220-260 as shown in Figure 4-1.

Table 3 : Chemical Composition of X65 Pipeline Steel

Chemical composition	C	Ni	Cr	Mo	Si	Mn	Al	P	Cu	V	S
(%)	0.08	0.04	0.02	0.01	0.3	1.6	0.04	0.009	0.02	0.05	0.006

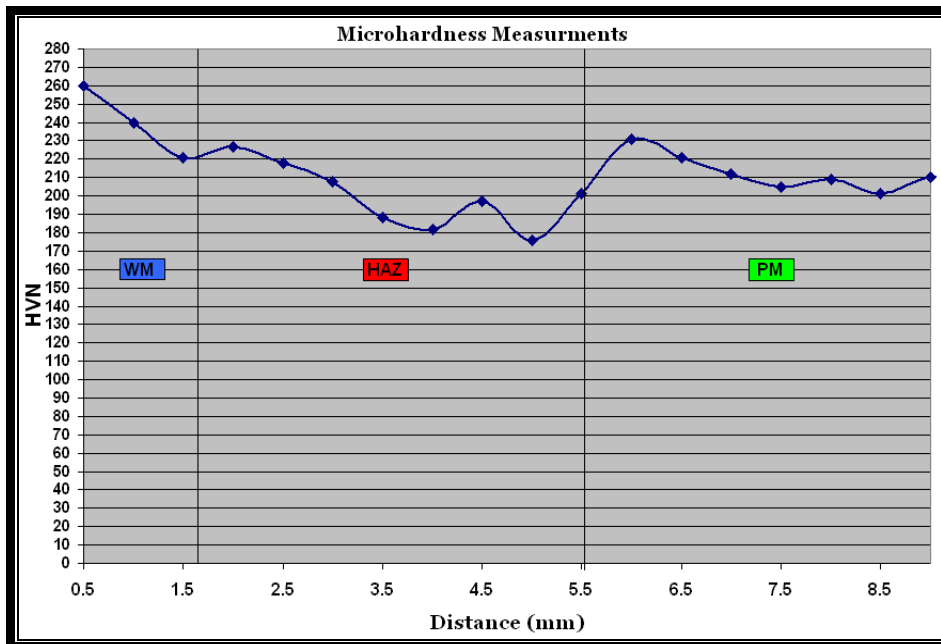


Figure 4-1: Typical microhardness profile over a weldment of PM, WM and HAZ

Weldments of ferritic steels are found to have distinct microstructural variations as one traverses from the weld metal to parent metal through the heat affected zone (HAZ). The nature of the structures in the three weld regions will depend on the peak temperatures experienced by different regions of the weldment during the welding process. A controlled thermal process is important to avoid producing local microstructures, which are susceptible to localized corrosion. Figure 4-2 shows a continuous cooling time (CCT) diagram which shows some of the possible structures formed during a welding process. Cooling curve 1 is slow enough to give complete transformation from austenite to ferrite and pearlite, curve 2 gives a mixture of ferrite, bainite and martensite, curve 3 gives bainite or martensite, while curve 4 gives only martensite. Thus, the heat affected zone (HAZ) and weld zone (WZ) may contain a mixture of ferrite, pearlite, bainite and martensite. Low transformation temperature products like martensite and upper and lower bainite have a higher tendency to corrode than other microstructures [130].

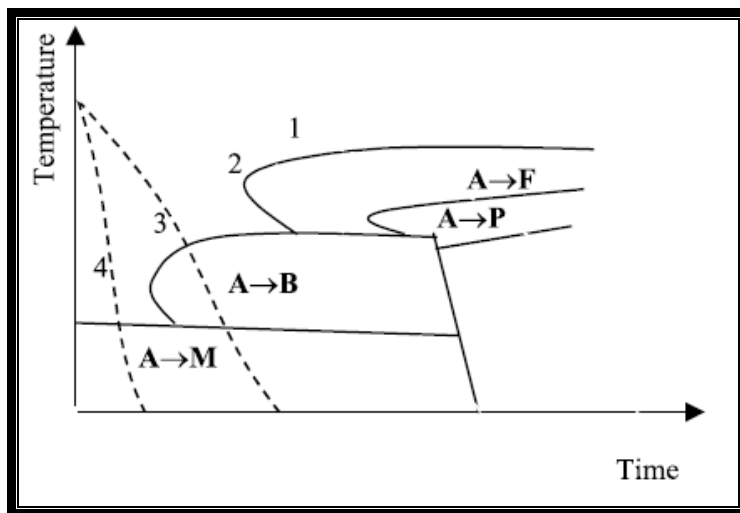


Figure 4-2: CCT Diagram with four cooling rates including the phases (A) austenite, bainite (B), ferrite(F), Pearlite (P) and martensite (M) [130]

A sample was cut from the weld, polished along the long transverse section and etched in 2% Nital for 20 seconds to reveal the positions of the parent metal, weld and HAZ zones before they were examined by optical microscopy, as shown in Figure 4-3. A detailed description of the microstructure of the three weld regions for the present study can be shown from the metallographic photographs taken as shown in Figure 4-4. It can be seen that there was a distinct microstructure variation, even within in the HAZ. In the region close to the parent metal, the microstructure consists of uniformly distributed

carbides in a ferritic phase where the white areas are an iron rich grain, while the dark areas are a mixture of ferrite and iron carbide

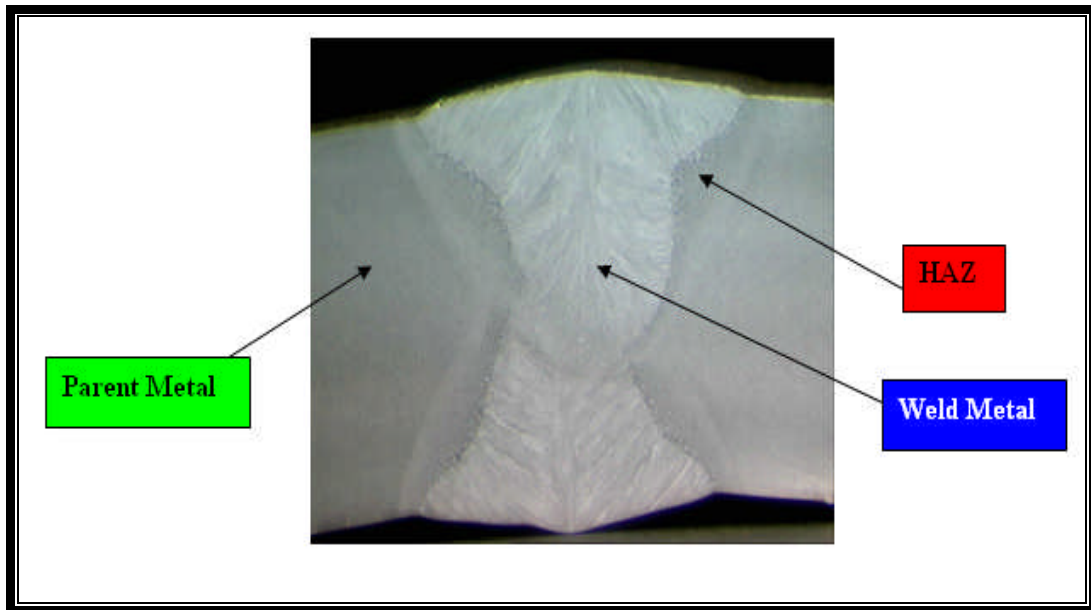


Figure 4-3: Diagram showing the weldment sectioning

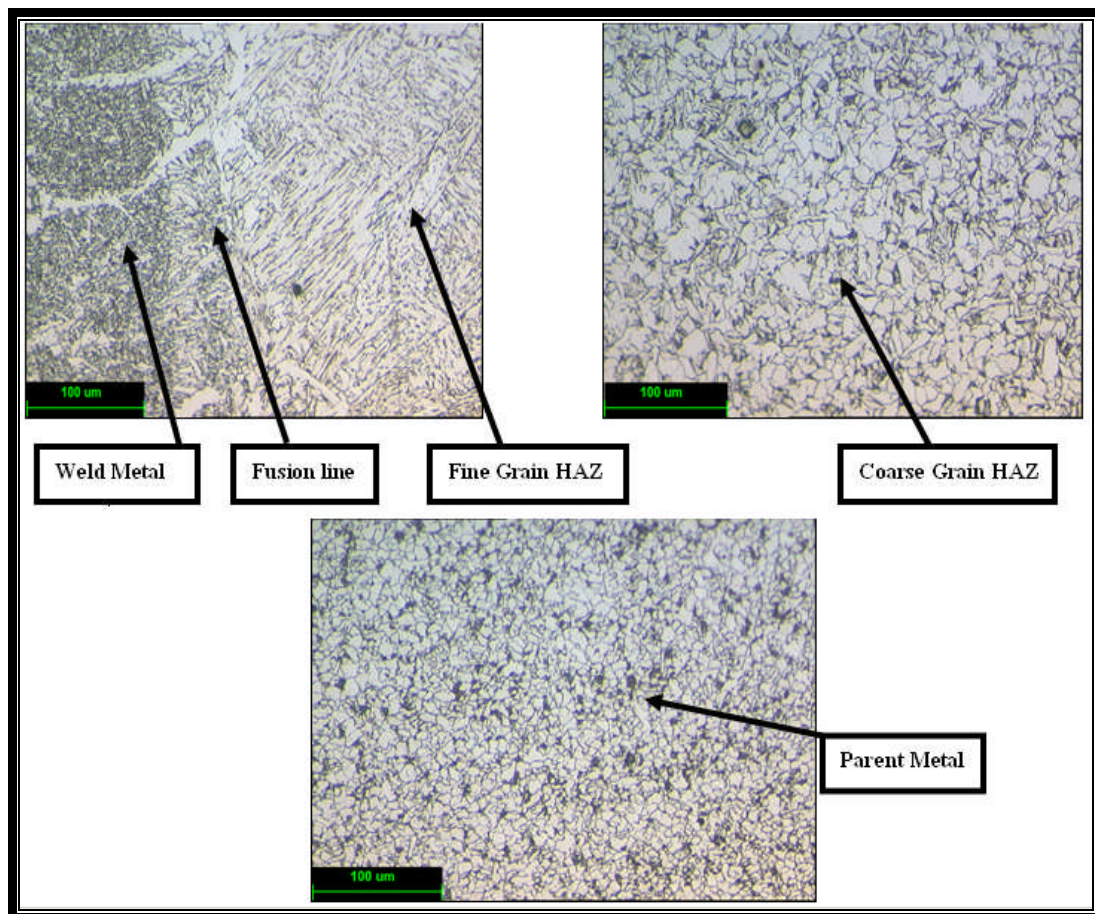


Figure 4-4: Parent - Weld - HAZ metallography

4.2 Preliminary electrochemical measurements (Stagnant conditions)

A series of sweet corrosion tests were carried out in a glass cell under stagnant conditions. The working electrodes were machined out from commercial steel pipe grade API X65. The surface preparation was carried out by grinding/polishing with 1200 grit of silicon carbide paper then degreasing with iso-propanol to remove any dust and scratches so that only the corrosion examined is that which occurred in the cell. The ratio of exposed surface area for the PM, WM and HAZ was approximately 8:2:1 respectively. The three regions were then separated by carefully cutting along the boundaries and they were reassembled by mounting in epoxy resin. Electrical connections were attached to each component in order to carry out electrochemical measurements as shown in Figure 4-5.

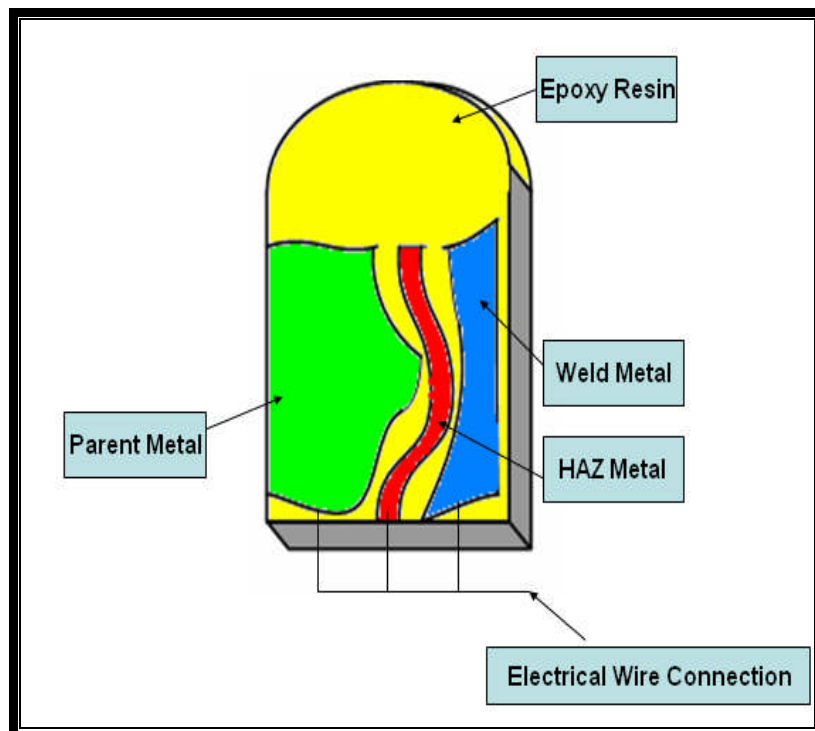


Figure 4-5: Shows a view of the sample in epoxy mount

4.2.1 Experimental setup and procedures

Under sweet corrosion conditions, artificial sea water (3.5%) was used in a glass cylinder and a polypropylene lid with four inlets for saturated calomel as reference electrode (SCE), platinum counter electrode (PCE), working electrode and CO₂ gas inlet. The electrolyte was saturated with CO₂ by continuous sparging with CO₂ under pressure of 1 bar. Constant sparging of the electrolyte with CO₂ ensured no leakage of oxygen into the cell, and this was supported by lack of any visual sign of oxygen corrosion.

The corrosion behaviour of the steel at each electrode was measured by Zero Resistance Ammeter and Linear Polarization Resistance (LPR) under static conditions as shown in Figure 4-6. For the galvanic test, each segment of the weld was coupled through a zero resistance ammeter (ZRA).

This allowed galvanic coupling currents of individual sections of the weld to be monitored during free corrosion in the test solution. The set up of the ZRA ignores the use of the counter electrode as current transfer can be measured easily between the three segments.

Once the coupling test period was completed, each section of the weld was uncoupled in turn and its self corrosion rate was found by LPR measurements. The Potentiostat was configured with the computer using the following parameters for LPR test. Scan rate = 166 μ V/s, Stern – Geary coefficient = 13 and scan range + 15 mV, -15mV.

Further experiments using the same methodology were conducted with the addition of 30 ppm by volume of the ‘green’ oilfield corrosion inhibitor CORRTREAT 05-193, supplied by Clariant Oil Services. The inhibitor was injected into the cell before starting the test.

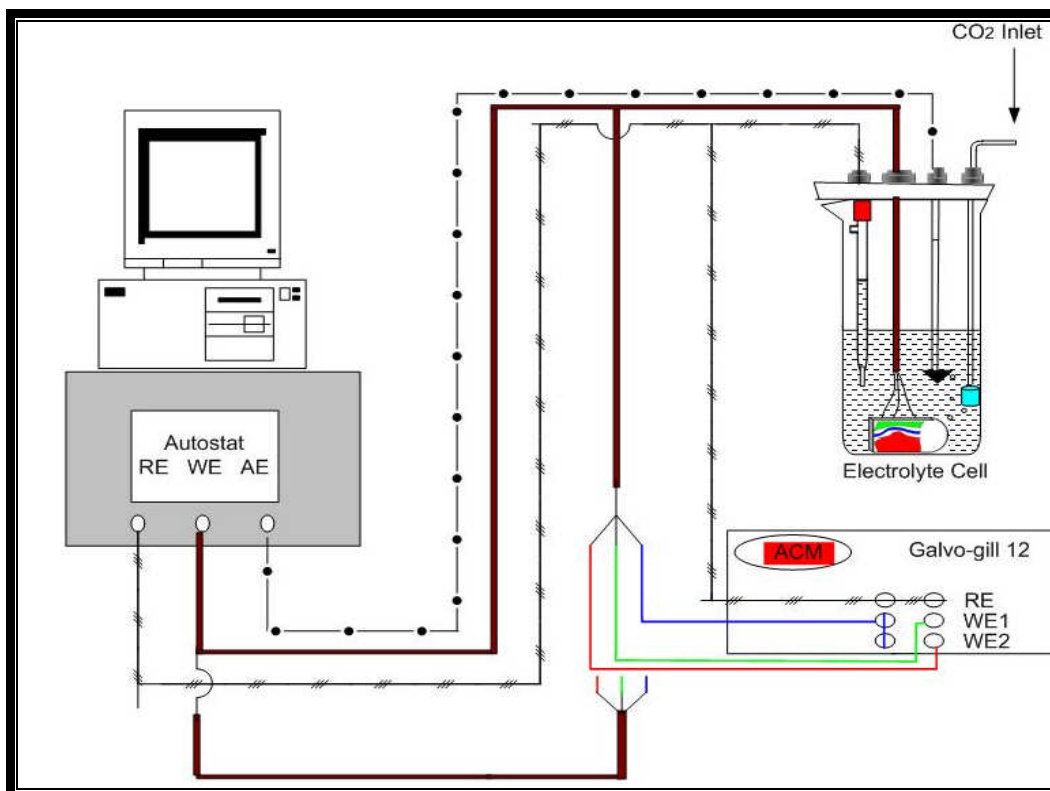


Figure 4-6: Sample under static conditions

4.3 Flow Channel experiment

Flow cell device in a closed loop condition was designed to evaluate the performance of film forming corrosion inhibitors by considering the LPR and galvanic current measurements. Flow experiments in channels are rated as the most service-related and most predictive because the flow pattern in channels is encountered in technical plants and is well defined by equations for mass, heat and momentum transfer [71].

Three physical quantities that are required in order to correlate the relation between the alloy surface and the hydrodynamic boundary layer are the friction factor (roughness measurement), the Reynolds number (defines flow regime) and the fluid velocity (rate of momentum transfer). The magnitude of the Reynolds number and shear stress are dependent on the fluid flow rate through the channel and can be easily calculated mathematically, see Appendix 2.

4.3.1 Flow Channel Apparatus

Samples were prepared from the parent metal, weld metal, and heat affected zone and assembled in epoxy resin. After grinding and polishing the electrode surfaces, a Perspex plate was attached to the sample, separated by a 2mm thick rubber gasket, to form a flow channel through which brine saturated with CO₂ was pumped using a peristaltic pump as shown in Figure 4-7.

A saturated calomel reference electrode was located over a 1 mm diameter hole above the HAZ electrode in order to measure the corrosion potential of each region of the weld. The ratio of exposed surface areas of parent, weld, and HAZ segments was 8:2:1 respectively. Before commencement of the experiment the working electrodes were polished using 1200 grit silicon carbide paper and degreased with iso-propanol to remove any surface film.

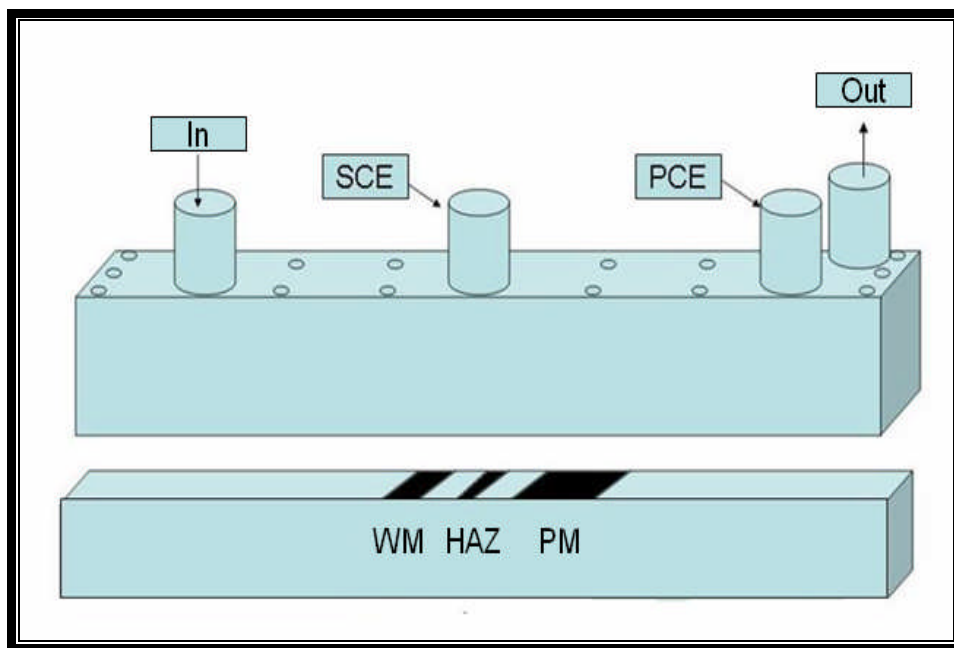


Figure 4-7: Flow channel assembly

4.3.2 Experimental setup and procedures

The effect of flow on sweet corrosion of the carbon steel weldment was studied using a flow channel. General arrangement consisted of the flow cell, the rotating peristaltic pump, potentiostat, Galvo –Gill 12 (ZRA), computer and reservoir (glass cylinder) as illustrated in Figure 4-8.

To ensure the consistency of the results obtained from these experiments, the samples were subjected to the same test conditions throughout all the experiments. The flow channel was equipped with a fixed rubber hose for inlet and outlet of flow while, the glass cell (reservoir) filled at 0.8 litre capacity of 3.5% artificial sea water and fitted with the suitable cover lid with 3 inlets to allow for the CO₂ injection as well as the discharge and suction of the solution electrolyte. Moreover, a peristaltic pump was used to maintain a uniform flow circulation and direction of 0.6 ms⁻¹, which corresponded to a shear stress of 2.56 Pa.

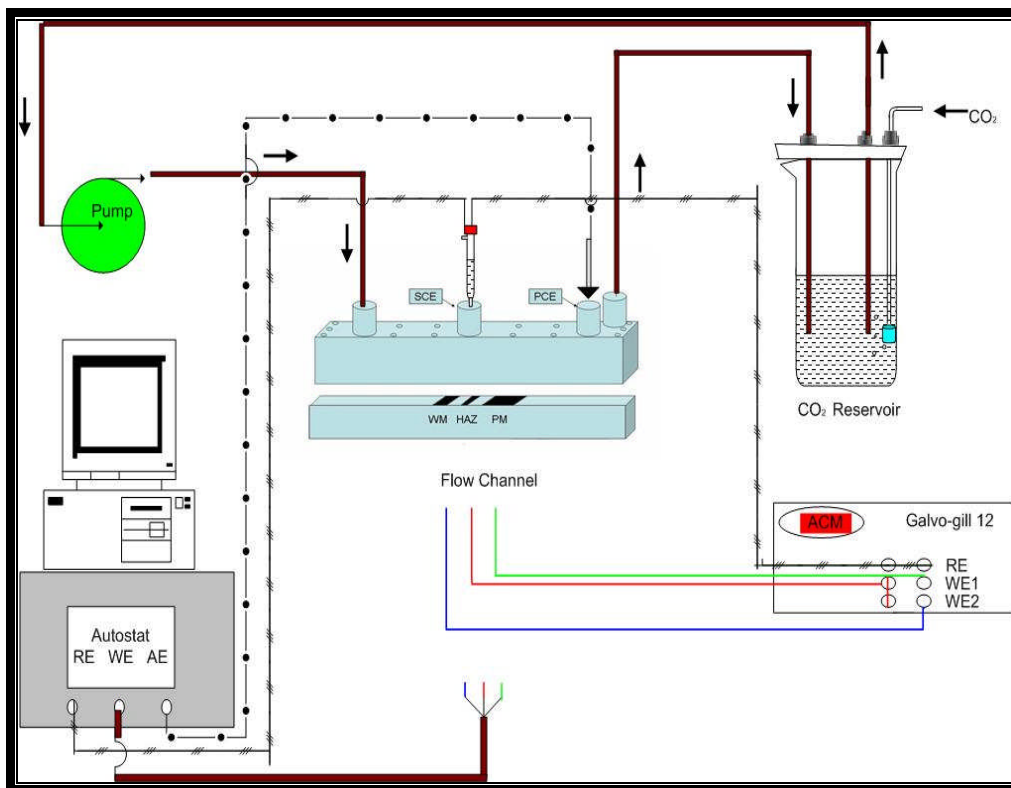


Figure 4-8: Flow loop assembly

4.4 Rotating Cylinder electrode experiments

As the recent development of the flow channel did not produce the required local turbulence and high shear stress found in practice, this part of the work was extended to develop an alternative hydrodynamic system, which allowed higher shear stresses to be achieved under more aggressive conditions. The most common hydrodynamic system that is utilised in the laboratory is the rotating cylinder electrode.

The evaluation of inhibitor performance in flowing conditions is frequently carried out using rotating cylinder electrodes (RCEs), which can achieve the required hydrodynamic conditions on the metal surface. However, there have been few attempts to use this method for investigating weld corrosion due to the technical difficulties of making multiple electrical connections to rotating electrodes consisting of three or more different regions of a weld.

4.4.1 Specimen characteristics and preparations

Hollow cylindrical samples were machined from each region of the weld and electrical connections were attached to each one from commercial steel pipe grade API X65 that had been welded. The three component parts composed of PM, HAZ and WM were mounted on the surface of an insulated stainless steel rotating shaft, separated by PTFE spacers, and secured with a retaining nut.

The samples were machined with common dimensions of 20 mm O.D and 24 mm, 6 mm and 3 mm in length for parent metal, weld metal and HAZ respectively. The parent metal exposed area to the test solution was 15 cm² while for weld metal and HAZ they were 3.7 cm² and 1.8 cm² respectively. Figure 4-9 shows the welded electrode used in the RCE testing. The area ratios for the parent metal, weld metal and HAZ were 8:2:1 signifying a condition close to a pipeline weld.

Large areas of parent material further from a weld are considered to have a lesser effect on localised corrosion due to the increased ionic path involved. Finally, the samples were polished up to 1200 grit silicon carbide, rinsed, dried and degreased with isopropanol and then were ready to be tested.

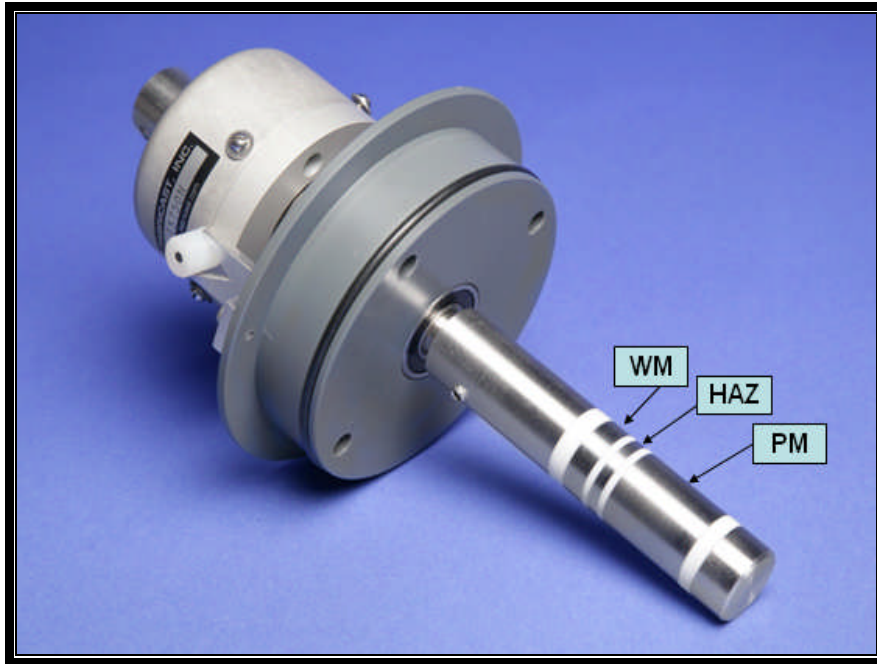


Figure 4-9: Welded cylindrical electrode sections

4.4.2 Rotating Cylinder Apparatus

The design of the RCE was devised, constructed and tested for this project. It is one of the convenient methods for rapidly rotating a sample with respect to a fluid as well as being compact, relatively inexpensive and easily controlled. The RCE system setup consists of three components. These components are the motor/frame assembly, the spindle/electrode assembly and the electrochemical cell. The RCE developed has an electrode rotator as well as control unit capable of precisely adjusting the rotation speeds up to 10,000 rpm of a vertical stainless steel shaft.

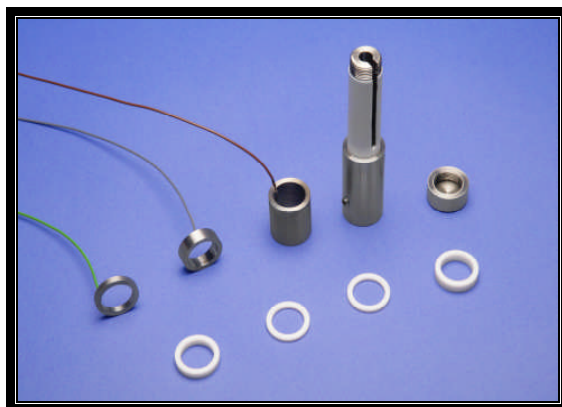
A set of high quality, multi-element slip rings was mounted on the motor driven spindle of the test equipment to take the electrical signals from the weld sections to the electrochemical instrumentation, as well as provide both mechanical stability and electrical contact with the metal cylinder sample. Electrical contact with the RCE was made using a slip-ring assembly fitted with silver-graphite bushes mounted on the top of the shaft. By means of grub screws, the electrode holder was secured to the motor shaft.

The slip rings had a maximum dynamic resistance of 10 milliohms so that electrical noise was very low and the assembly was rated for speeds of 13,000 rpm, well above the maximum of 5000 rpm used in this study.

The electrochemical cell was comprised of a standard glass cell (1L) with a polypropylene lid, and was used in all the electrochemical experiments. The polypropylene lid contained four inlets used for CO₂ gas inlet/outlet, working electrode, the reference electrode (saturated calomel electrode [SCE]) with connection into the cell through a Luggin capillary probe, temperature thermometer and the counter electrode (platinum electrode paddle type with the following dimensions: Gauze Wire 0.12mm, 250 mesh per cm² and 2.5 grams in weight and total area of 8.4 cm²).

For some tests to identify the chemical composition of the surface film, the electrode assembly needed to be modified so that each electrode could be examined by X-ray diffraction. Therefore, working electrode which comprise of the three weld regions previously were replaced with identical electrode material where each sample could be remove individually for the surface film analysis. The surface preparation for these samples was identical to that described in section 4.4.1.

A schematic of the rotating cylinder components, section through electrode, rotating electrode assembly and rotating cylinder electrode set up are shown in Figures 4-10 till 4-14 respectively.



(A)



(B)



(C)



(D)

Figure 4-10: Rotating cylinder electrode components (A) Cylindrical working electrodes, (B) Slip ring, (C) Slip ring mounted on top of the cylindrical working electrode shaft, (D) Standard glass cell

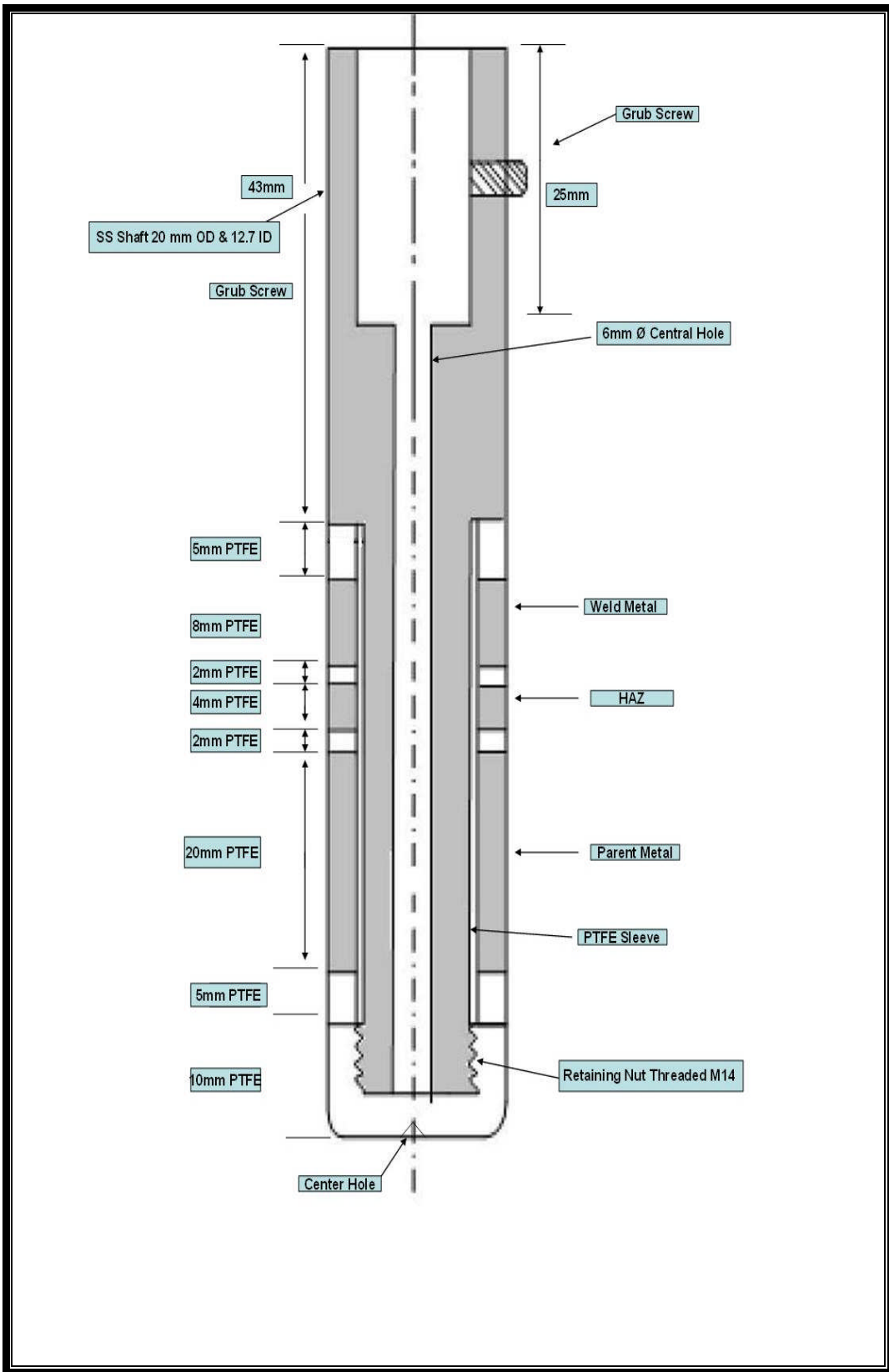


Figure 4-11: Section through electrode (Full size)

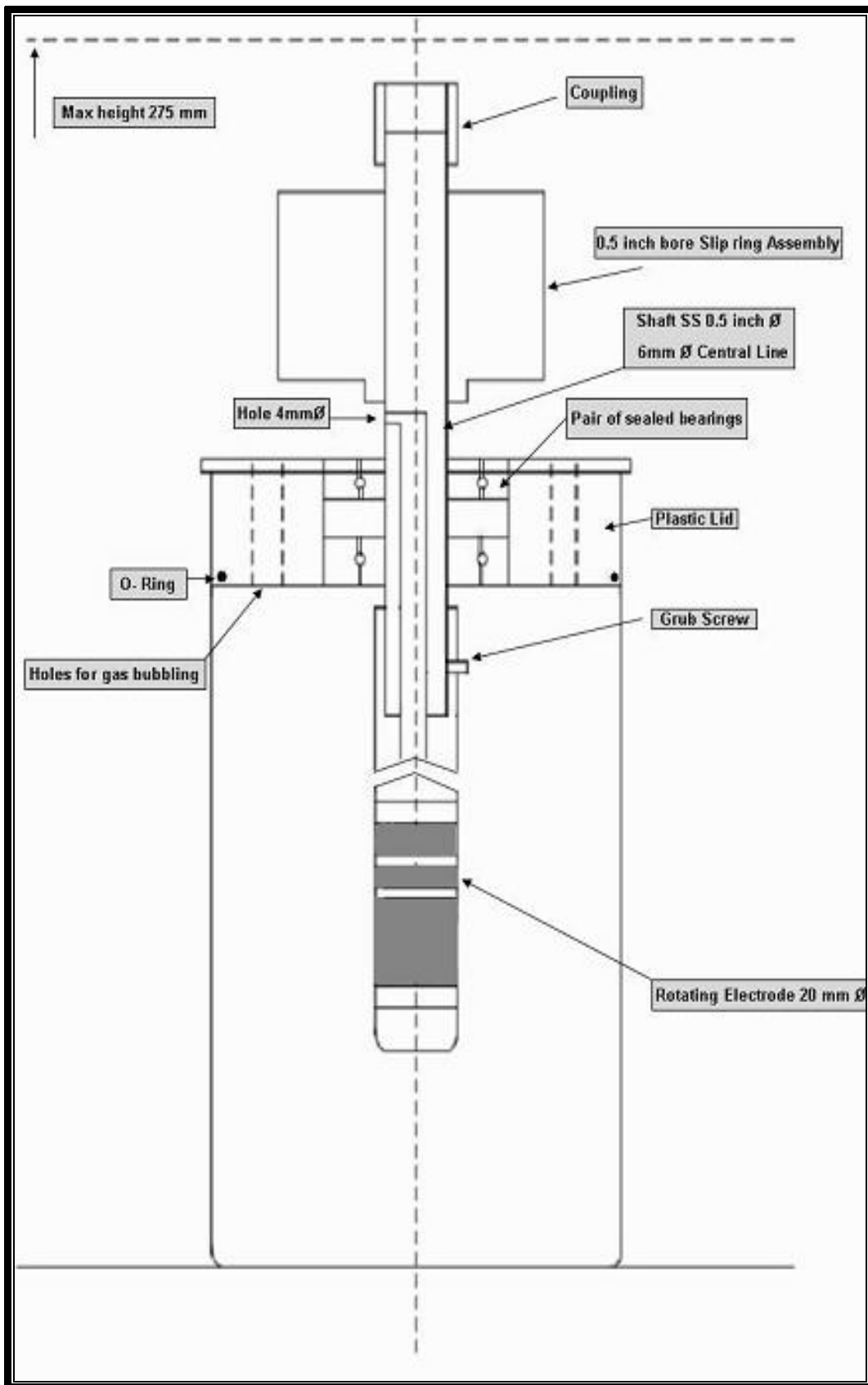


Figure 4-12: Rotating cylinder electrode assembly

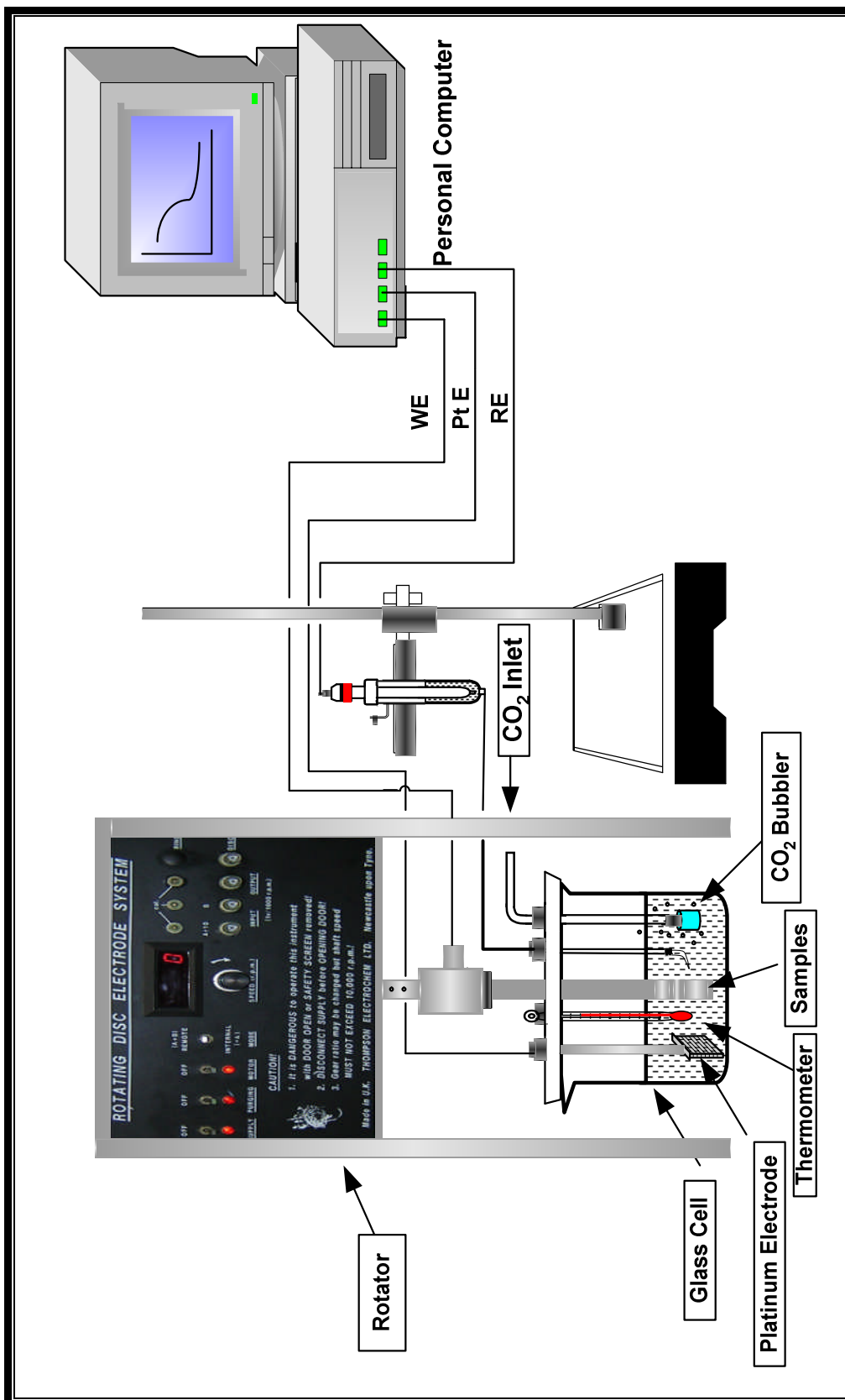


Figure 4-13: Rotating cylinder electrode setup

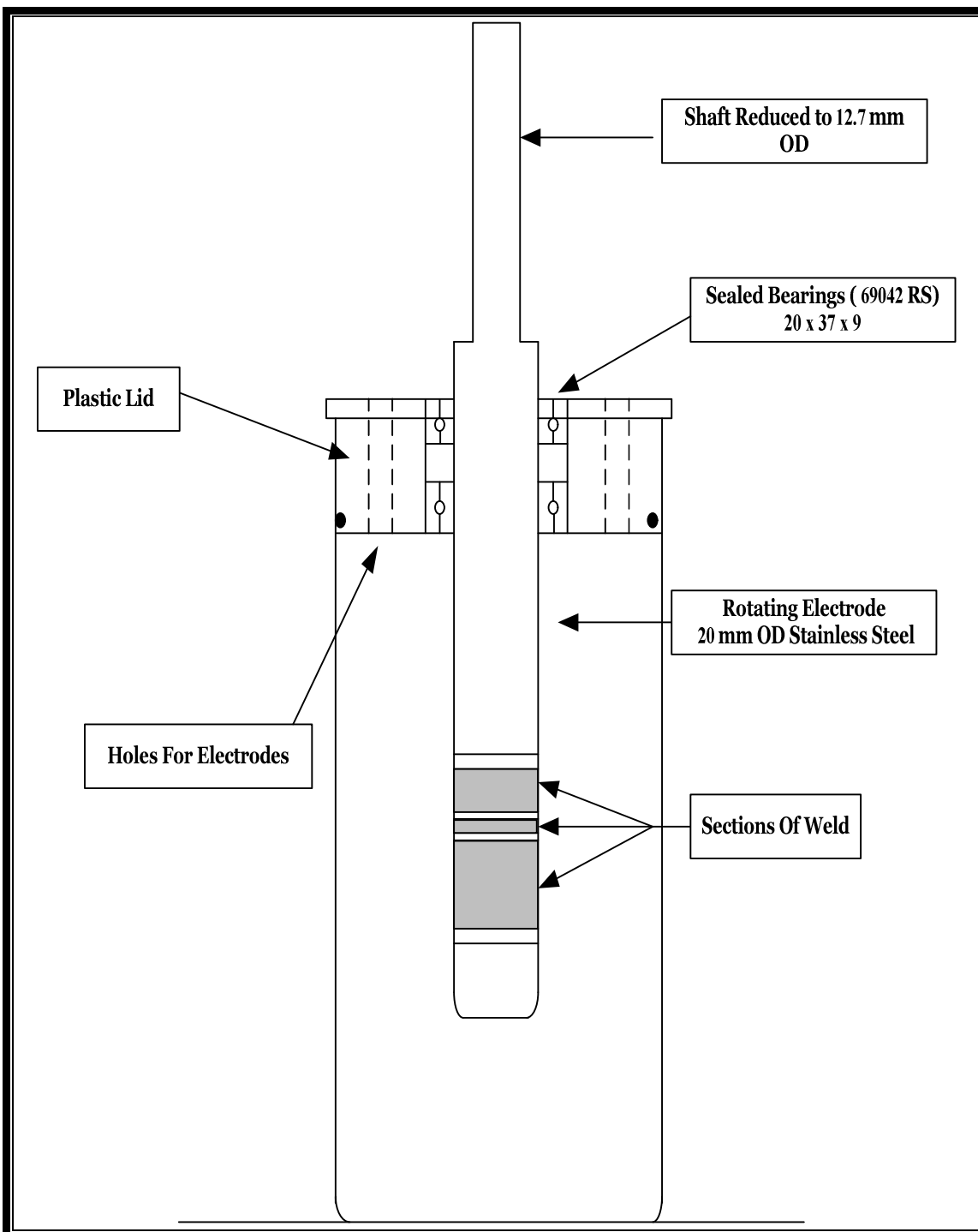


Figure 4-14: Removable working electrode assemblies

4.4.3 Experimental Parameters

Table 4 : Summary of the Test Parameters

Parameter	Condition
Test Solution	3.5 % sea water solution
Temperature °C	Room temperature, 50°C, 70°C
CO₂ partial pressure	1 Bar CO₂
Rotating Cylinder Speed	Static – 5,000 rpm
Polarisation resistance sweep limits	-10 mV to 10 mV E_O
Inhibitor	CORRTREAT 05-193
Inhibitor concentration ppm (volume)	30
Material	Carbon manganese Steel X65

4.4.4 Experimental setup and procedures

Prior to testing, the exposed surface of the test sample was polished using 1200-grit silicon carbide (SiC) metallographic polishing paper, degreased, rinsed in iso-propanol and air dried, immediately before exposure.

The experiment was carried out in a standard glass cell (1L) with lid containing four inlets filled with aqueous solutions of 3.5% artificial sea water at 0.8L capacity which was the required volume for the test.

The CO₂ gas was bubbled for 20 minutes prior to testing in order to remove the dissolved oxygen from the test solution. During the experiment, the CO₂ flow was kept constant and in this way the deaeration of the solution, the saturation with CO₂ and constant positive pressure of CO₂ were always ensured.

After bubbling CO₂ for 20 minutes, as mentioned previously, the rotation speed was set at 500 rpm as the first rotation speed, before increasing to 1000, 2000, 3000, 4000 and 5000 rpm at 20 minutes intervals.

The rotation speed of the shaft was selected to simulate typical wall shear stress conditions of the system under consideration. The sample on the RCE was immersed in the glass cell and exposed to the test environment while being rotated at the required rate.

The corrosion behaviour of each weld component in the rotating cylinder electrode was measured using a range of electrochemical methods. The electrochemical cell was electrically connected to a computer-controlled potentiostat for the linear polarisation test and ZRA (zero resistance Ammeter (ACM Gill 12) for the galvanic current measurements, both of which were operated by software.

4.4.4.1 Galvanic Corrosion Test of the Welds

The galvanic currents between the weld components were recorded at one minute intervals during the test using a multi-channel Zero Resistance Ammeter (ACM Instruments GalvoGill 12) connected to a data logging PC. The currents from the parent plate to the weld metal and from the HAZ to the weld metal were recorded on two channels and the individual currents from the three electrodes were established from the following relationship:

$$\text{Eq.26} \quad I_{PP} + I_{HAZ} + I_{WM} = 0$$

After completion of the last rotation (5000 rpm), the test was left under static conditions with each segment of the weld coupled through a zero resistance ammeter (ZRA). This allowed galvanic coupling currents between individual sections of the weld to be monitored during free corrosion in the test solution, for a period of 10 hours followed by the linear polarisation resistance test.

4.4.4.2 Linear polarisation Test (LPR) of the Welds

A series of 3 LPR tests were then performed upon each sample in order to ensure the consistency of the results. Prior to the test, the electrode free potential had been allowed to stabilise for 5 minutes, then checked by a digital multimeter and compared with the potential reading registered on the potentiostat.

The LPR measurement test is short in duration and each test was run for an approximate time of 5 minutes. Once the required rotation speed had been reached then the electrochemical measurements, typically linear polarisation resistance, were recorded periodically through the rotation period. The corrosion rate was measured whilst the rotation speed was progressively increased and then decreased.

The linear polarisation test was conducted with a -10, +10 mV maximum shift from the free corrosion potential, scanned anodically and cathodically at a scan rate of 166.7 μ V/s.

The test was then left for approximately 10 hours under static conditions to ensure that the system approached steady state conditions with each segment of the weld coupled through a ZRA.

In order to study the effectiveness of the temperature variation on the corrosion rate as well as inhibitor performance, experiments were carried out with the same method as inhibitor free experiments. For tests at temperatures above ambient, the glass cell was placed in a heated water bath with the heating coil switched on, with the temperature controller set on temperature of 50°C then 70°C, and the carbon dioxide gas was bubbled through the solutions for 20 minutes prior to the testing.

The same procedures and electrochemical methods were repeated in the presence of 30 ppm inhibitor concentration. The inhibitor was injected into the cell before starting the test. As there was not a significant difference on the density of water and the inhibitor (1.015-1.06@ 25° C), the volume of the inhibitor by using pipette was 30 μ L which is equivalent to 30ppm.

In order to ensure correct control of the sample electrode rotation rate and the correct recording of potentials, regular checking of the speed of the rotator and the potential of the reference (SCE) electrode were carried out. Significant vibration, as well as noise on the structure at particular rotation speeds, was observed during the test. This was controlled by alignment and clamping.

4.4.5 Surface Characterisation Techniques

Examination of the exposed working electrodes was performed using scanning electron microscopy (SEM) with energy –dispersive x-ray (EDX) analysis and X-ray photoelectron spectroscopy (XPS). After the examination, the specimens were prepared for the final step of cross-sectional analysis, to examine the thickness and morphology

of the corrosion product film. This was achieved by first embedding the coupon into epoxy, followed by cutting across the specimen surface. A SEM was used to examine the cross section. The cross-section analyses of the corrosion layers were performed by energy dispersive X-ray (EDX). Mapping of C, O and Fe was carried out to investigate the distribution of these elements in the surface layers and to calculate the relative concentration values of each element in the corrosion layers. Samples were prepared by etching the SEM cross-sections with a focused ion beam (FIB).

For conventional imaging in the SEM, the selected area must be electrically conductive, at least at the surface, and electrically grounded to prevent the accumulation of electrostatic charge at the surface and protect it while the cross section is being milled. They are therefore usually coated with an ultra thin coating of electrically-conducting material, commonly gold and platinum deposited on the sample.

(a) X- Ray Diffraction (XRD)

An XRD instrument model (Siemens D5005) was used for direct XRD measurements of scale on the working electrodes surfaces with Chromium wavelength of 2.291Å. The determination of chemical composition was carried out by comparison of experimental lines with standard data obtained from the XRD database.

(b) Optical Microscopy and Scanning Electron Microscopy.

A Nikon Lab microscope with Micropublisher digital camera and Synoptics “Aquis” image capture software were used to visually investigate corroded working electrode surfaces and to take microscopic photographs of typical areas of the surface of the corroded working electrode. A FEI SFEGSEM XL30 scanning electron microscope was used for SEM analysis.

(C) X-ray Photoelectron Spectroscopy (XPS)

The XPS was done on a VG ESCALab MkII. The primary electron energy was 10kV and current between 10 and 20 nA. Etching was performed using 2kV Argon ions and used several different ion intensities from 0.1 to 1 uA.

4.4.6 Rotating cylinder electrode (EIS investigations)

The goal of this work was focused on the importance of hydrodynamic effects on the formation, structure and stability of inhibitor film on the segmented weld in the presence of CO₂ corrosion, in static and flowing conditions, with or without inhibitor, using a rotating cylinder electrode with EIS as the electrochemical method. This is considered to be a very useful technique for the evaluation of inhibitor performance, and analysis of electrochemical mechanisms, using very small signals which may not disturb the freely immersed electrode and corrosion process [131].

Most of the studies have been conducted in laboratory scale systems, such as RDE or the laboratory scale flow loop and multiphase flow systems [132].

4.4.6.1 Sample Preparation

Under static conditions, a cylindrical electrode sample comprised of PM, WM and HAZ with a total area of (6.28cm²) was prepared. A hole was drilled in order to hold the samples in the cell by the use of studding, with the upper part coated with Lacomit in order to avoid any current exchange between the studding and the sample. However, under flowing conditions, details of the preparation have been detailed previously in section 4.4.1

4.4.6.2 AC Impedance System Setup and procedures

Schematic layouts of the AC impedance system under static and flowing conditions are shown in Figures 4-15 and 4-16 respectively. Prior to testing, the exposed surface of the test sample was polished using 1200-grit silicon carbide (SiC) metallographic polishing paper, degreased, rinsed in iso-propanol and air dried, immediately before exposure.

An electrochemical cell with 0.8L of 3.5% artificial sea water was de-aerated with CO₂ for 20 minutes before testing and kept under CO₂ atmosphere during testing to ensure there was no leakage of oxygen through the top of the cell. This was confirmed by a lack of any visual signs of oxygen corrosion.

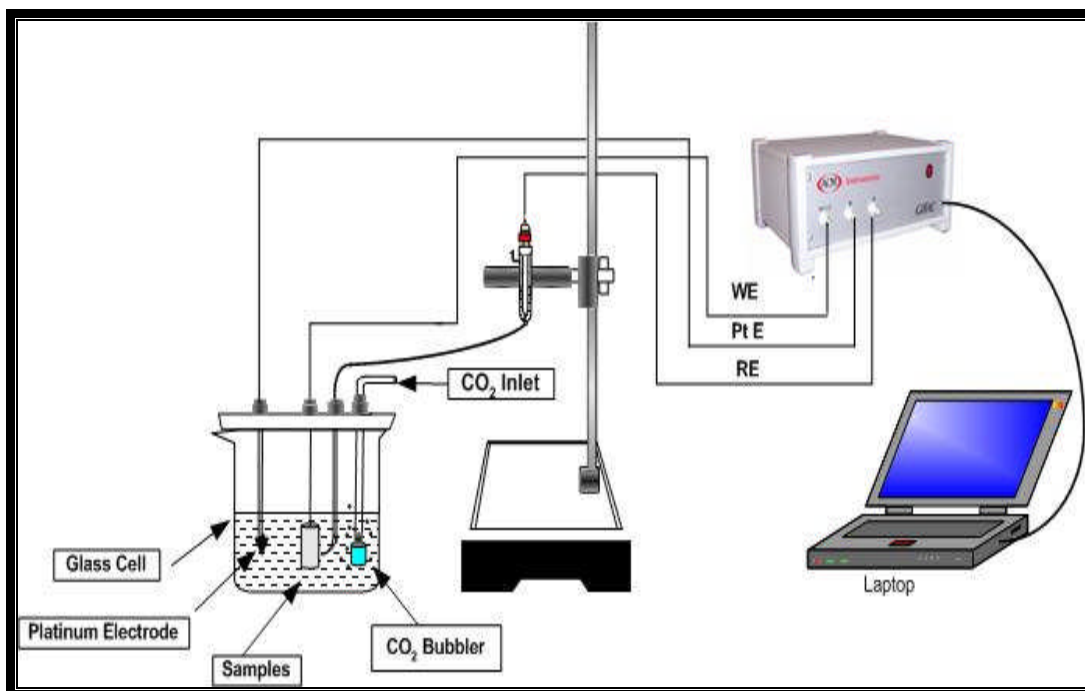


Figure 4-15: Impedance system components under static conditions

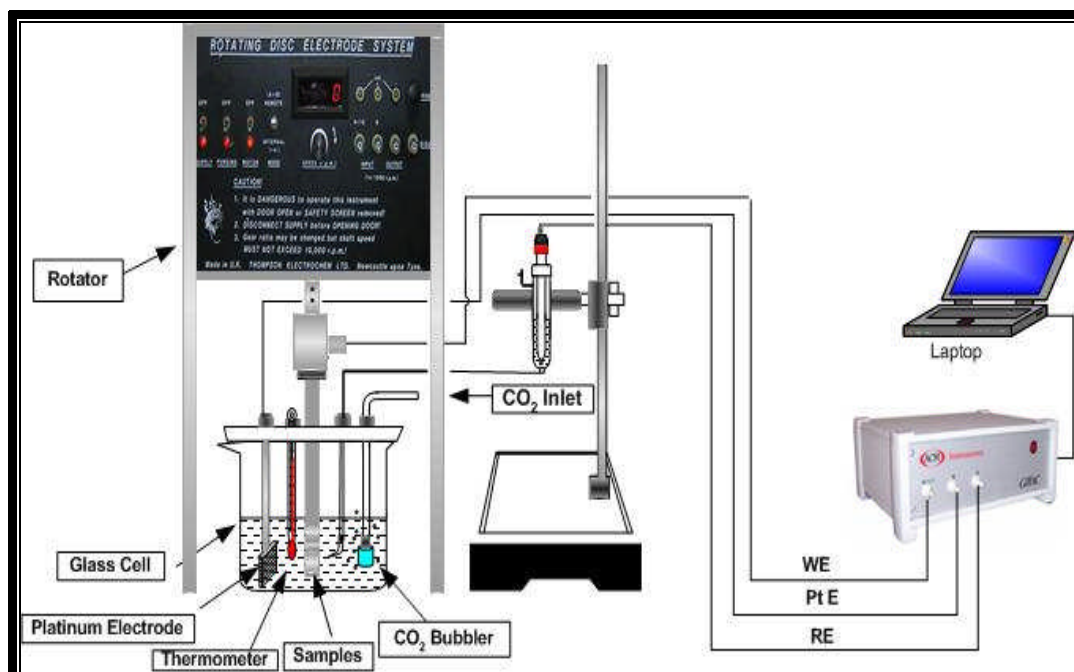


Figure 4-16: Impedance system components under flowing conditions

The electrochemical cell was electrically connected to a computer controlled Potentiostat /galvanostat (ACM Gill), which was operated by software supplied by ACM Instruments, and the EIS parameters were carried out at the open circuit potential with amplitude of 10mV AC potential in the frequency range of 0.001Hz to 20 kHz, as shown in Figure 4-17.

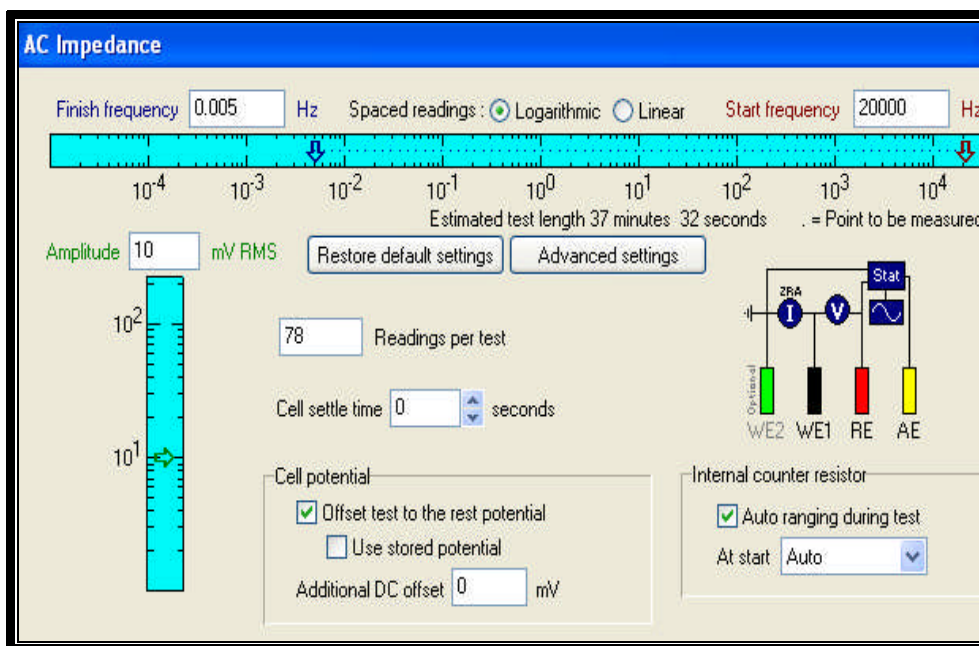


Figure 4-17: EIS parameters

The EIS measurements were taken on a polished electrode during 10 hours exposure to artificial seawater. Tests were carried out with three- electrodes configuration: platinum electrode as counter electrode, a saturated calomel electrode (SCE) as reference electrode, and a cylindrical electrode as working electrode, which were immersed in a solution saturated with CO₂ for 20 minutes prior to the test.

Experiments were performed under static and flowing conditions. The temperatures at which the experiments were done were room temperature, 50⁰C and 70⁰C, with a rotation speed of 5000 rpm. Once the required rotation speed had been reached then the electrochemical measurements, typically electrochemical impedance spectroscopy, were recorded periodically through the rotation period.

CHAPTER 5 RESULTS

Preliminary Experiments

5 Under Static Conditions

5.1 Analysis of galvanic couple tests under static & sweet corrosion (CO₂)

The basic idea for this test was to investigate the corrosion currents between the individual elements that comprise the weldment. This experiment was run for 10 days under sweet corrosion (CO₂) conditions. The variation of galvanic current over the time is shown in Figure 5-1. The corresponding current densities are given in Figure 5- 2.

The first couple of (PM-HAZ) exhibited a positive current which indicated the preferential corrosion of the parent metal with respect to HAZ. However, the second couple WM-HAZ had a negative current which meant that the HAZ corroded preferentially with respect to WM.

Figure 5-3 shows the average galvanic currents for each region of the weld and it can be seen that the sum of the anodic currents from the parent metal and the HAZ equal the cathodic current on the weld metal as the total sum of corrosion currents in the circuit is zero. It was noticed that there was a daily galvanic current fluctuation as shown in Figure 5-1, and this is due to the effect of temperature caused an increase of the galvanic current. In the case of electrochemical reactions, temperature favors the kinetics of corrosion reactions, and more specifically, the anodic dissolution of the metal [133].

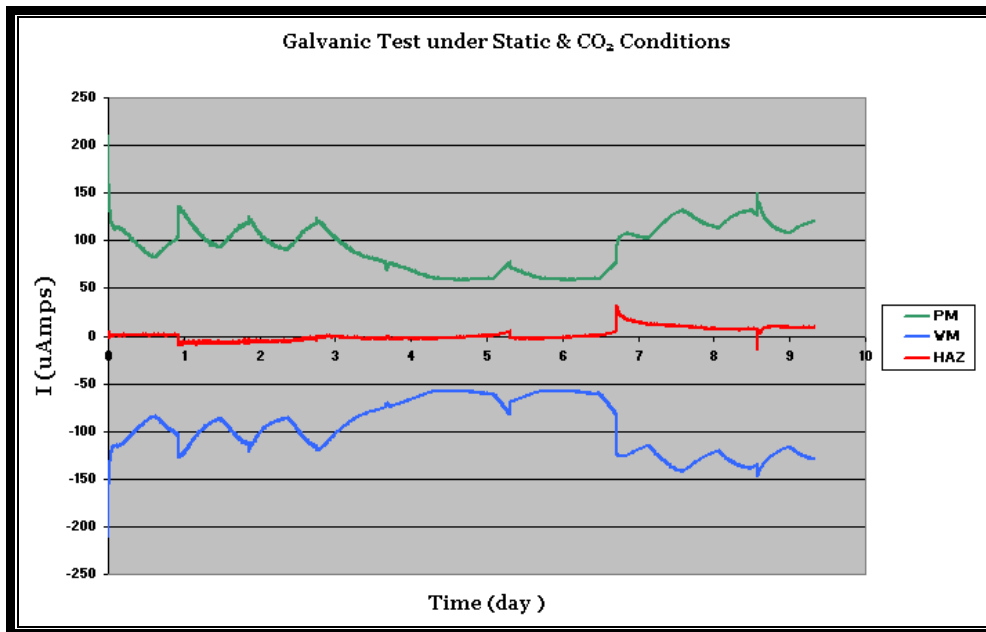


Figure 5-1: Galvanic current in static & sweet conditions

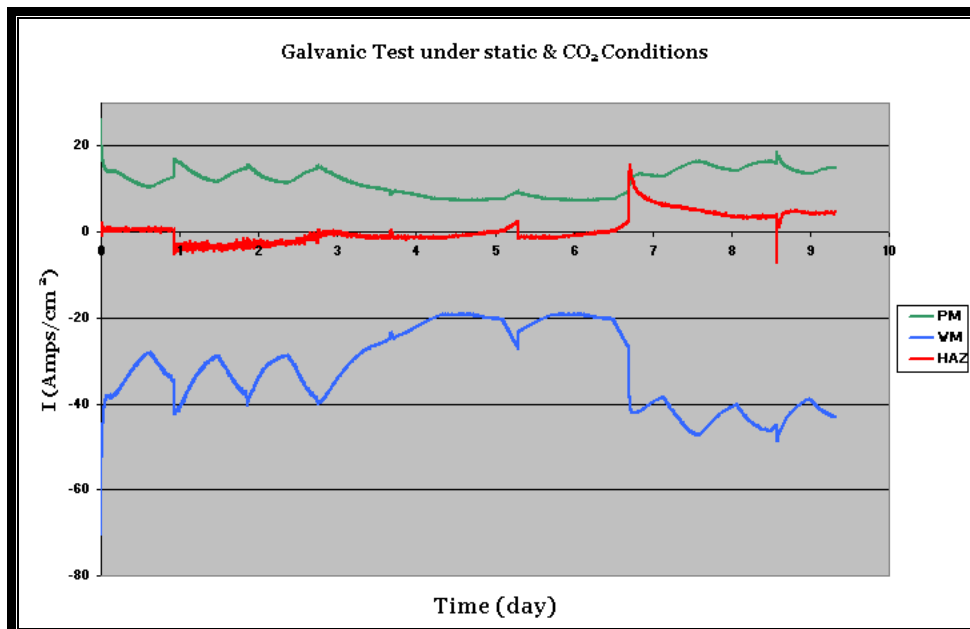


Figure 5-2: Galvanic current densities in static & sweet conditions

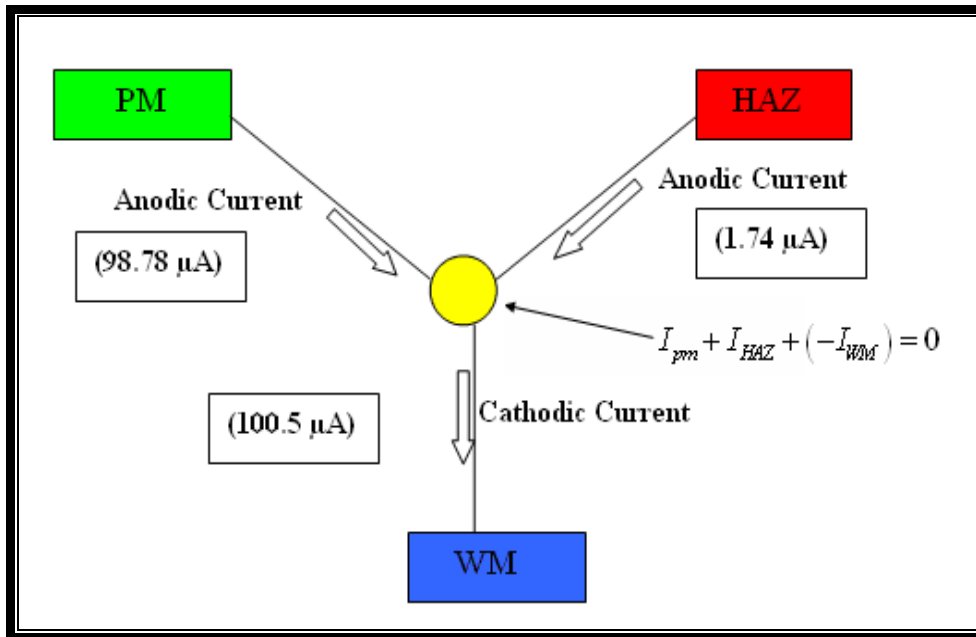


Figure 5-3: Galvanic current for repolished surface 10 days

5.2 Analysis of LPR tests under static & sweet corrosion (CO₂)

The corrosion rate of each weld region was monitored daily by linear polarization resistance (LPR) technique. A set of LPR data was obtained up to a period of 10 days, as shown in Figure 5-4 corresponding to linear polarization current density, as shown in Figure 5-5. The initial corrosion rate for WM was the highest. After one day a significant deviation of corrosion rate for all the three regions had been observed. A sharp increase was observed for HAZ in day 2 with a value of 1.14 (mm/ y), which continued to increase to the end of the experiment with maximum rate of 1.27 (mm/y).

For WM it was observed to gradually increase until day 5 then a sharp decline at the end of the test with value of 0.48 (mm/y), while PM section indicates a fairly constant corrosion rate over the test period with a value of 0.51 (mm/ y).

By the end of the experiment, a black film covered the three regions with no significant sign of localized corrosion.

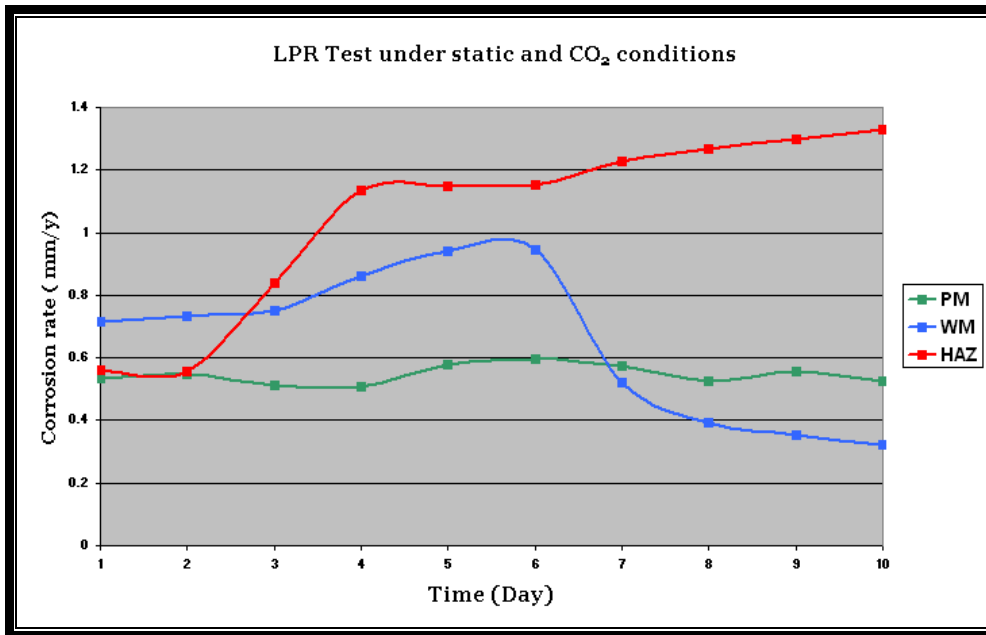


Figure 5-4: LPR test current density for polished surface under static and CO₂ conditions in 10 day

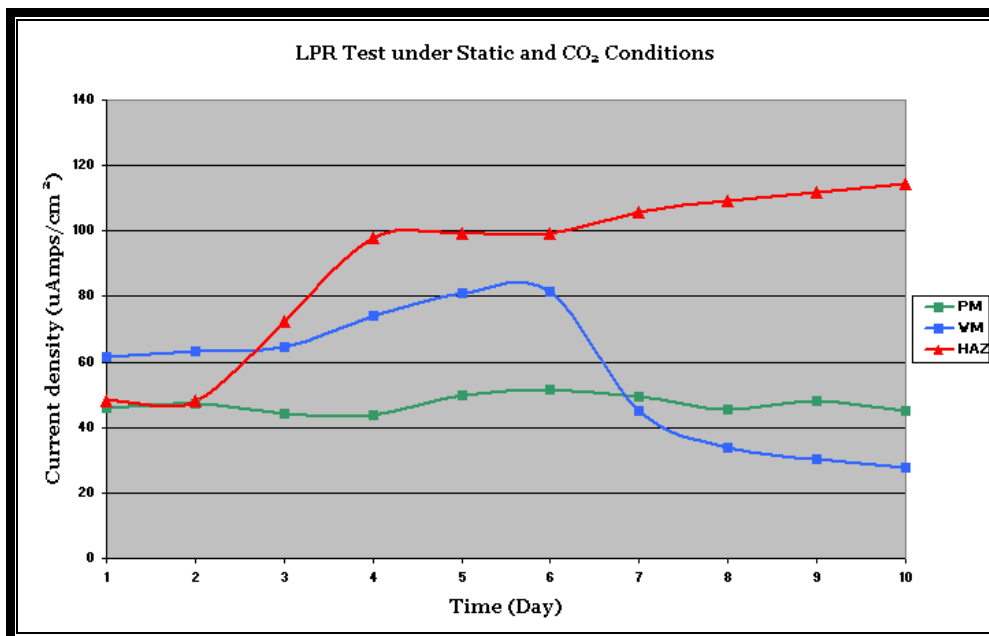


Figure 5-5: LPR Test for polished surface under static & CO₂ conditions in 10 days

5.3 Total corrosion rate of weld components in static conditions with CO₂

Figure 5-6 compares the LPR test (self corrosion) results and galvanic corrosion for the three zones. The total corrosion of the welded sections can be calculated as follows:

Total corrosion = Self corrosion + Galvanic. The corrosion rate is expressed as current density. From the graph it was noticed that the weld metal galvanic current density showed a cathodic response over the test period of 10 days. Upon initial exposure to the test conditions, the parent metal self corrosion current density recorded a magnitude of $45.95\mu\text{A}/\text{cm}^2$ and a galvanic current density of $12.34\mu\text{A}/\text{cm}^2$. The parent metal behaved as an anode, which indicates that parent metal corroded preferentially with respect to WM.

Upon the initial exposure for weld metal self corrosion, the observation indicated a rapid increase to the highest active value of $81.61\mu\text{A}/\text{cm}^2$ which was recorded through the first 6 days then gradually decreased during the rest of the test. The weld metal behaved as a cathodic and attained the minimum value especially in day 9 with magnitude of $-43.41\mu\text{A}/\text{cm}^2$. As a result of this behaviour, the total weld metal corrosion was reduced, corresponding to the reduction in the magnitude of galvanic current.

The HAZ showed a fluctuating anodic and cathodic behaviour. Upon initial exposure it was anodic behaviour. However after 8 days of the test period, a cathodic behaviour was observed. HAZ self corrosion current density started at $48\mu\text{A}/\text{cm}^2$ and gradually increased reaching maximum value of $115\mu\text{A}/\text{cm}^2$ after 10 day exposure to the test conditions. However the total HAZ corrosion rate was reduced due to the large reduction of the HAZ galvanic current density which, contributed to the total HAZ current density reduction. Results obtained on different zones of the weldment show the effectiveness and protection achieved by changes in these galvanic current readings. Moreover, it was observed that the rate of self corrosion was higher than the galvanic corrosion, which indicates that galvanic current corrosion alone was sufficiently low enough not to necessitate to corrosion mitigation measures.

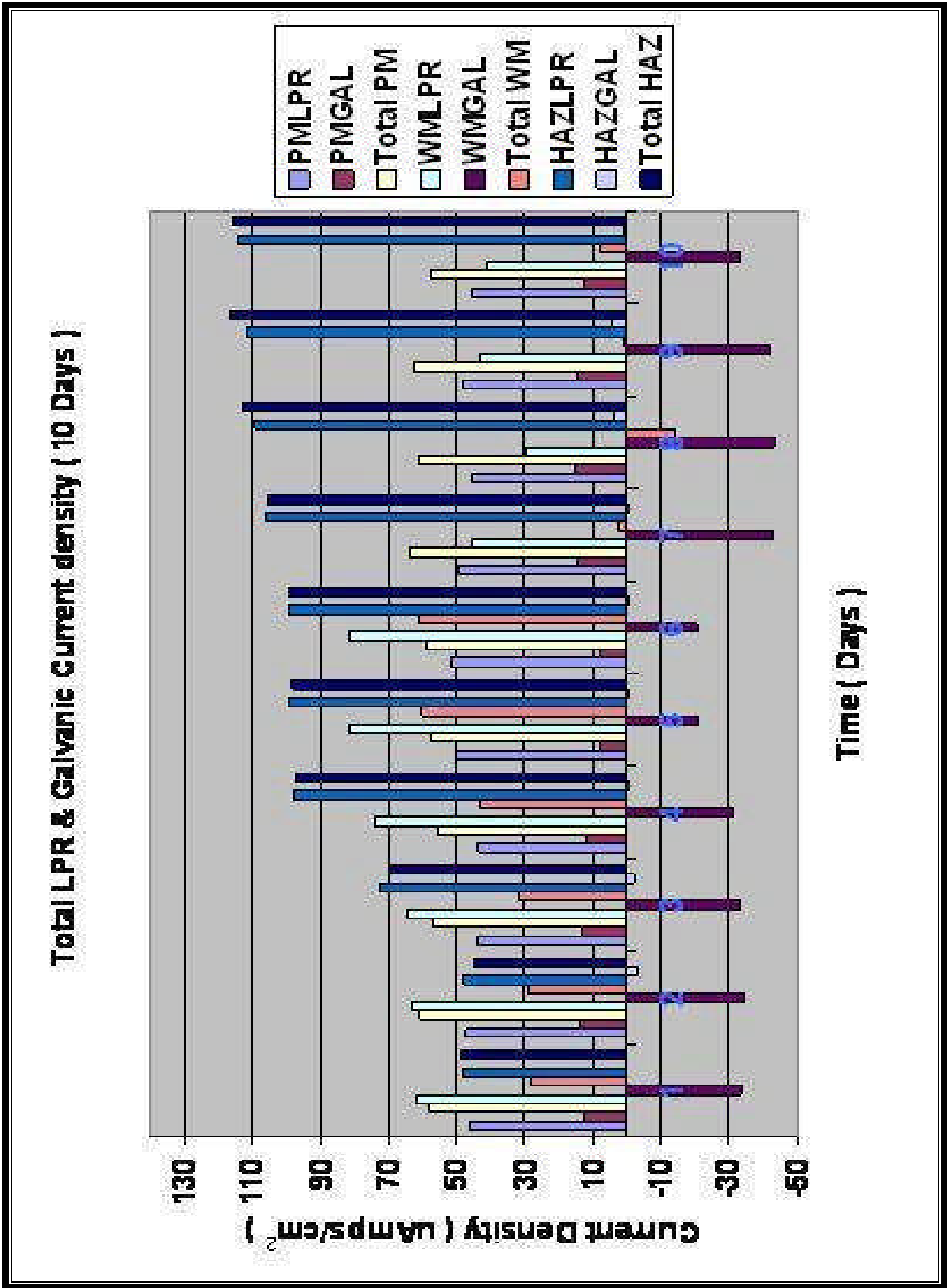


Figure 5-6: Comparison of LPR & galvanic current density for 10 days

5.4 Analysis of galvanic couple tests under static & (CO₂) with inhibitor addition

The variation of galvanic current over time was recorded for each sector and presented in Figure 5-7. The first couple of (PM-HAZ) exhibited a positive sign of flow current, which indicated the preferential corrosion of the parent metal with respect to HAZ. However, in the second couple (WM-HAZ) negative current was observed which meant that the HAZ corroded preferentially with respect to WM.

In Figure 5-8, the HAZ current density remained relatively stable for most of the 5 days and continued to be cathodic throughout the test with slight anodic behaviour in day one and day 2 before reverting to cathodic again.

In Figure 5-9 corrosion current to the HAZ (- 2.239 μA) was calculated from the corrosion currents of the parent metal (11.369 μA) and WM (- 9.039 μA), where the total current was always zero. This experiment was run for 5 days under sweet corrosion (CO₂) conditions.

The inhibitor was injected at the start of the test. It was clear that the inhibitor film formation had an effect over the first few hours as all the galvanic currents for the each region approached zero, with the weld metal remaining cathodic to the rest of the material.

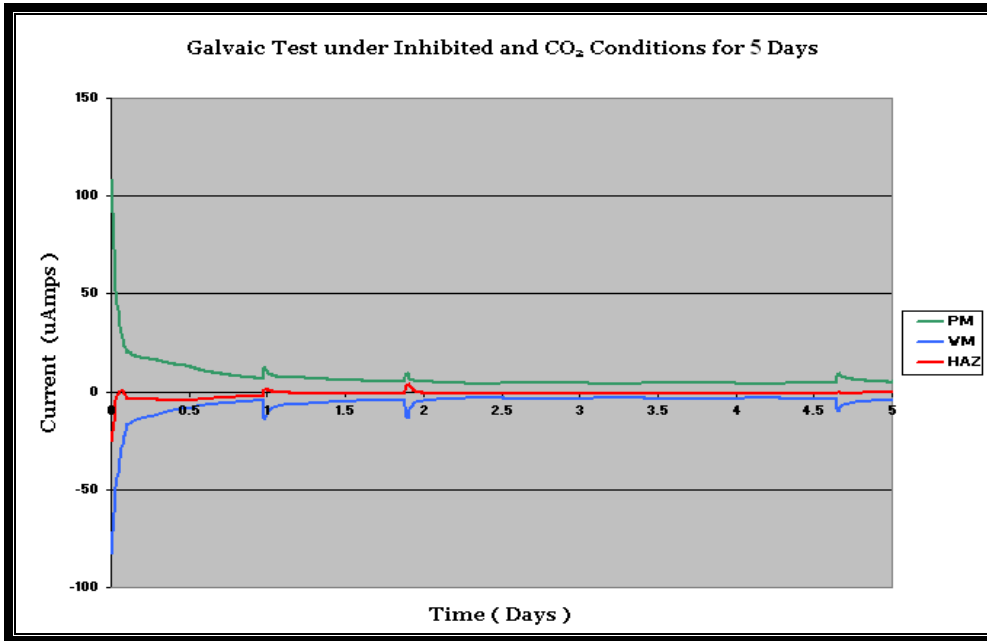


Figure 5-7: Galvanic current in static condition & inhibitor for 5 Days

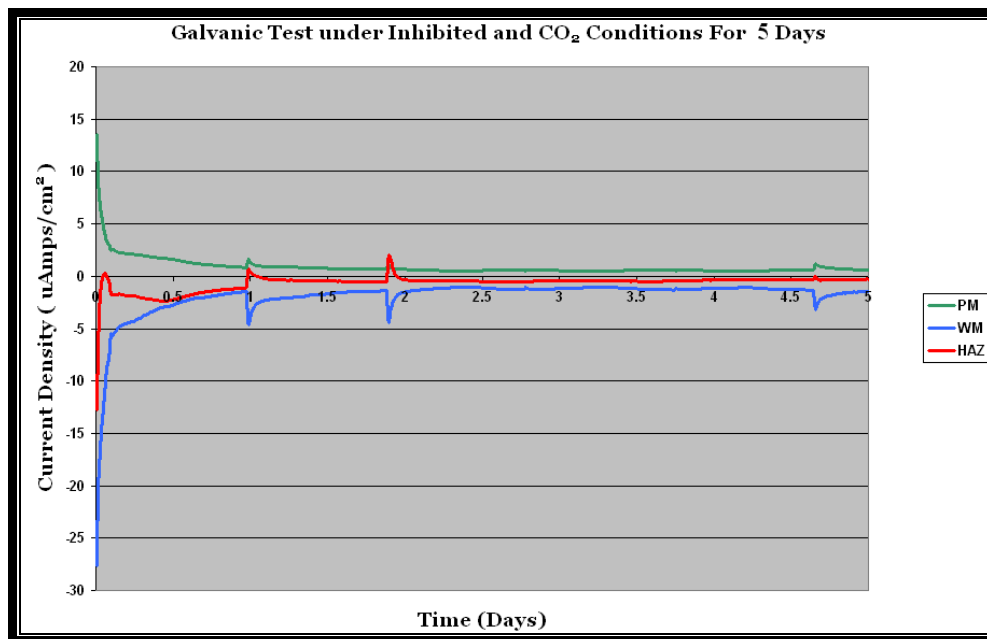


Figure 5-8: Galvanic current densities in static condition & inhibitor for 5 Days

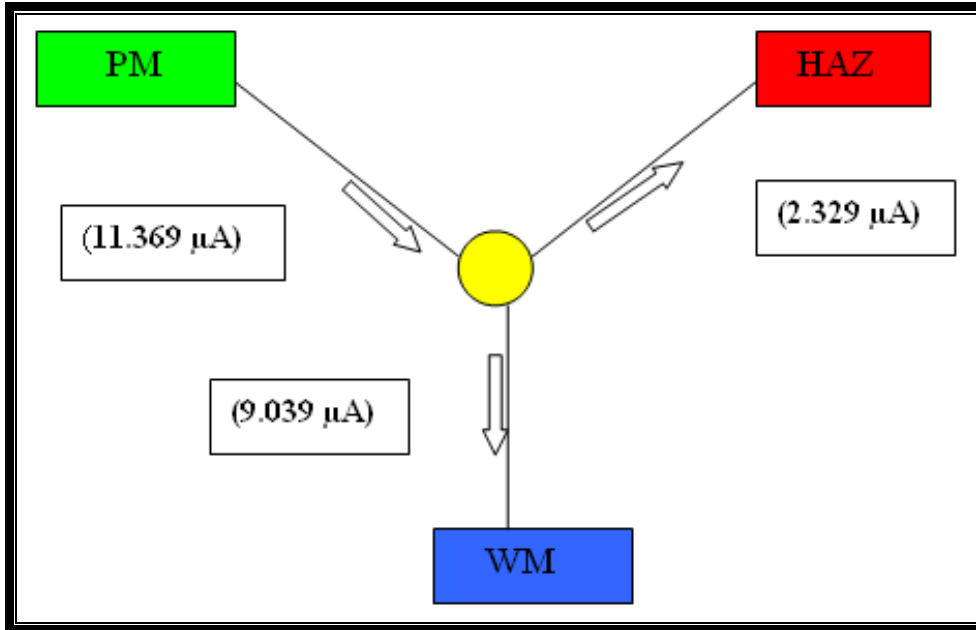


Figure 5-9: Average galvanic currents for static & inhibitor condition for 5 days

5.5 Analysis of LPR tests under static & (CO₂) with inhibitor addition

The self corrosion rates of each weld section in inhibited solution are shown in Figure 5-10. Figure 5-11 shows the same results with corrosion currents converted to metal loss. It was clear that corrosion inhibitors had an effect on all the weld segments due to a dramatic reduction in the corrosion rate of the parent metal, weld metal and HAZ. Parent metal was inhibited from 0.26 mm/ y down to 0.07 mm/y while weld metal and HAZ were inhibited from 0.67 mm/y and 1.00 to 0.16 mm/y and 0.25 respectively by the end of the experiment. It was observed from the figure that HAZ had the highest initial corrosion rate.

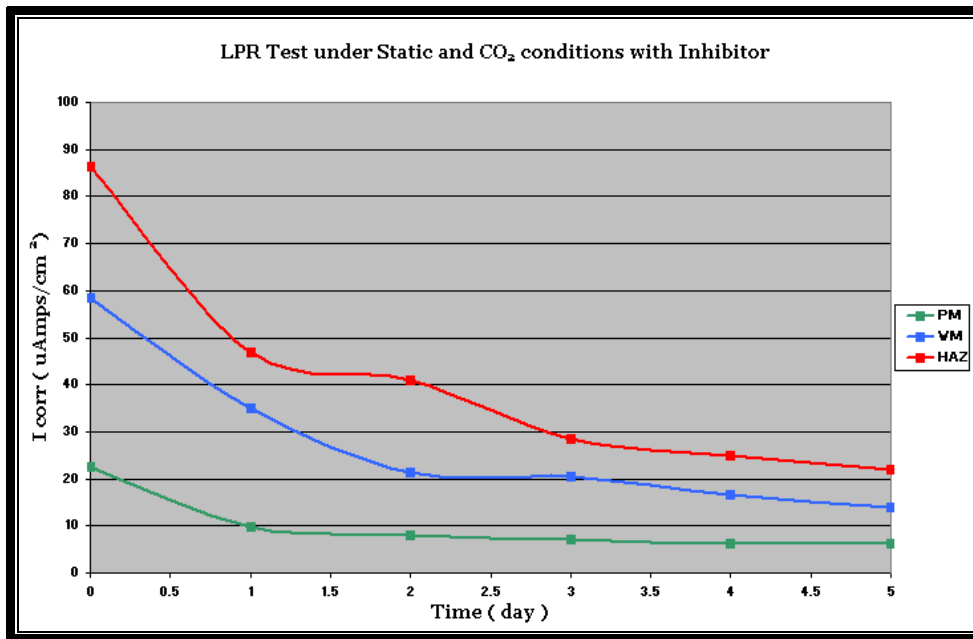


Figure 5-10: Current density for inhibited samples under static conditions for 5 days

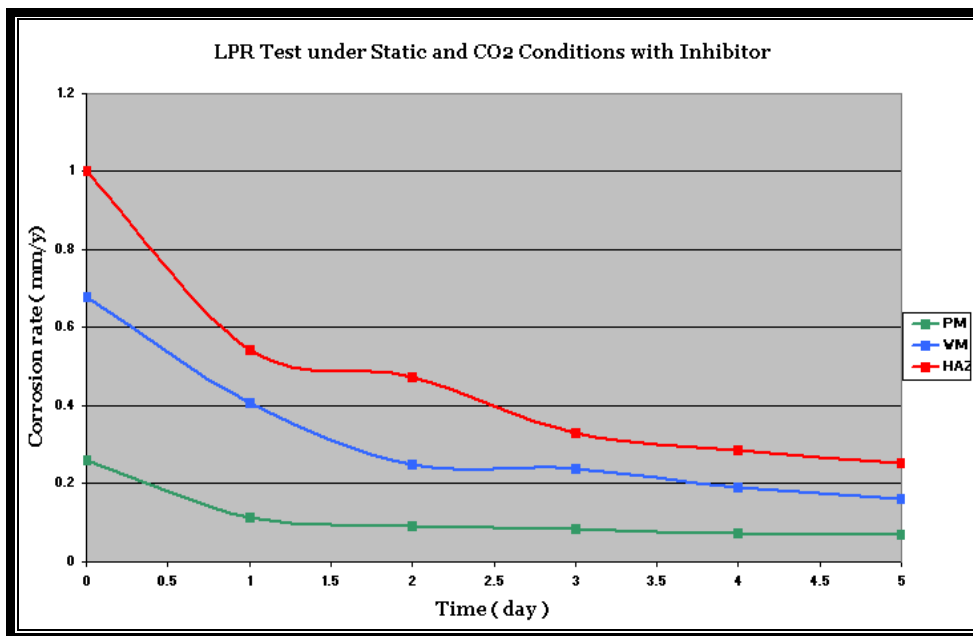


Figure 5-11: Corrosion rate for inhibited samples under static condition for 5 days

5.6 Analysis of galvanic couple tests under flowing & (CO₂) conditions

Flow was circulated by a peristaltic pump with a speed of 0.55 m/s and calculated shear stress of 2.5 Pa. Details of the shear stress calculation can be seen in Appendix 2. The first couple of (PM-HAZ) exhibited negative current upon initial exposure which then changed to positive current and indicated the preferential corrosion of the parent metal with respect to HAZ, as shown in Figure 5-12. The second couple (WM-HAZ) exhibited a positive current upon initial exposure, and then a reversal was observed to a negative current which indicated that the HAZ was corroding preferentially.

A significant switching behaviour of the weld metal and HAZ was observed in days 3 and 4 due to a pump failure, which probably affected the level of dissolved oxygen in the solution. However the switching behaviour recovered after the fourth day with the same behaviour but with higher magnitude of galvanic current density for both weld metal and HAZ, while for the parent metal for the galvanic current density was relatively low. By the end of the test, brown rust was established across the coupled surfaces, indicating that oxygen had been present, and it was later seen that there were pits on the parent metal and HAZ surfaces.

Corrosion current to the HAZ (27.51 μ A) was calculated from the average corrosion currents from PM (4.24 μ A) and WM (31.75 μ A), where the total current is always zero as shown in Figure 5-13.

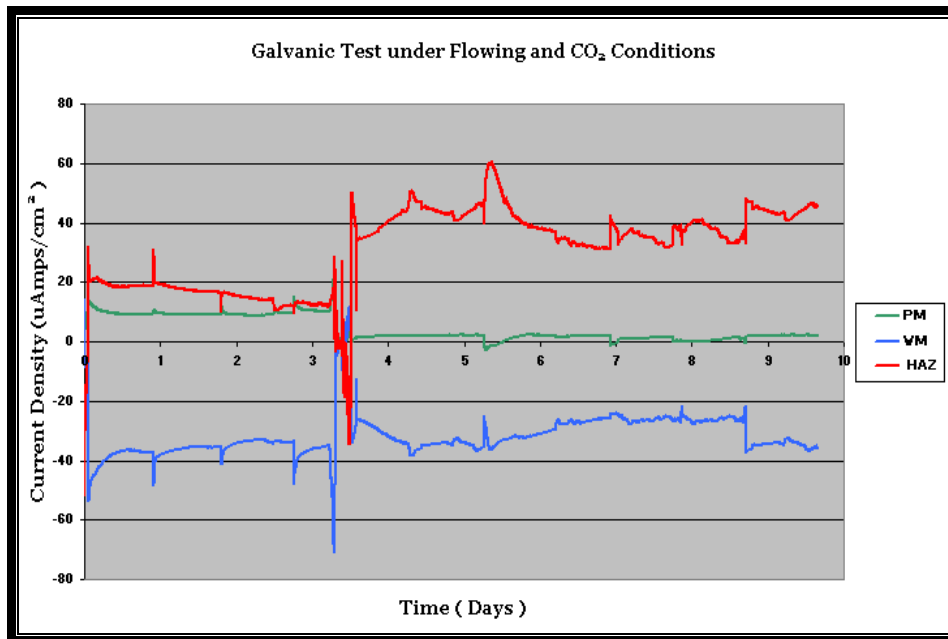


Figure 5-12: Galvanic current densities under sweet corrosion (CO_2) & flowing conditions for 10 days

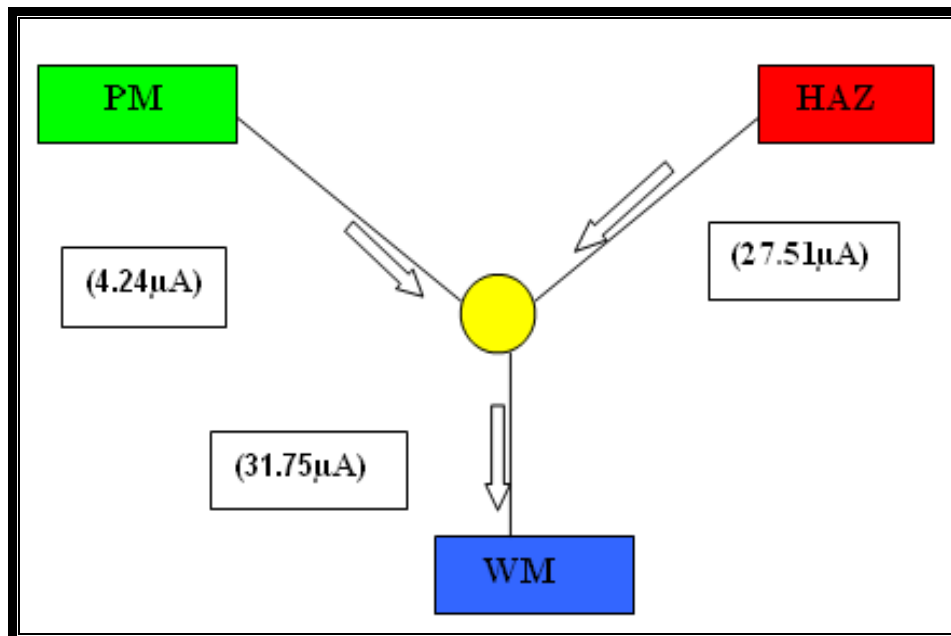


Figure 5-13: Average galvanic currents for flow & sweet corrosion over 10 days

5.7 Analysis of LPR test under flowing & CO₂ conditions

A series of LPR data was obtained up to 10 days, as shown in Figure 5-14. Corrosion rates of the three regions were fairly constant over the first two days. A significant sharp increase of corrosion rate for all the three regions was observed in day 3 due to pump failure. It was clear that this resulted in oxygen entering the flow loop as brown rust formed across the three regions and the solution became discoloured. After replacing the solution and restarting the test, the corrosion rates gradually decreased to the values on day 2. Figure 5-15 shows the same results with corrosion currents connected to metal loss.

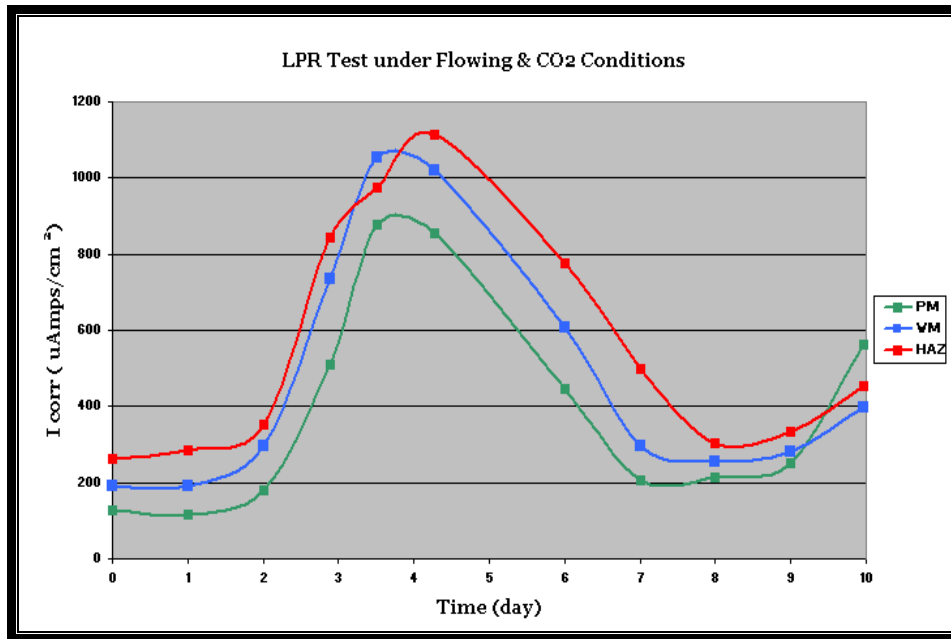


Figure 5-14: Current density under flowing & CO₂ conditions after 10 days

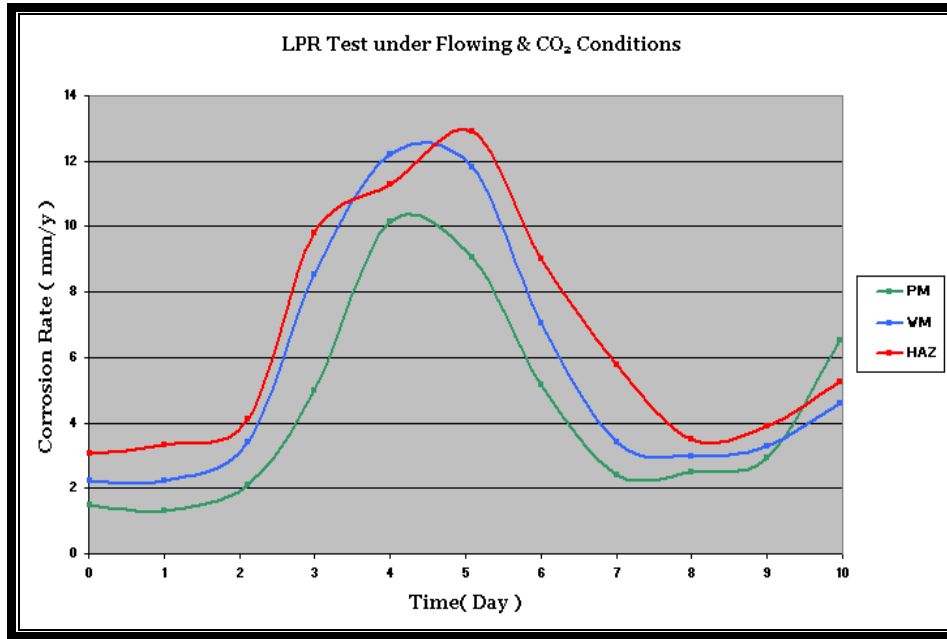


Figure 5-15: Corrosion rate under flowing & CO₂ conditions after 10 days

5.8 Analysis of galvanic couple tests under flowing & CO₂ conditions with inhibitor addition

The basic idea for this test was to investigate the galvanic corrosion currents between the individual elements that comprise the weldment under inhibited flowing conditions. This experiment was run for 10 days. The variation of galvanic current density over time is shown in Figure 5-16.

The first couple (PM-HAZ) demonstrated cathodic behaviour, although its starting response upon initial exposure was anodic behaviour which indicated that HAZ was corroding preferentially with respect to parent metal.

The second couple (WM-HAZ) exhibited an anodic behaviour response during most of the test period although its initial response was cathodic. The implication of this was that WM corroded preferentially with respect to HAZ.

The overall effect was that weld metal was anodic and corroded in preference to the HAZ and parent metal. However, it was observed that the current density was progressively reduced towards the end of the test.

An intermittent change in current density was observed on the three electrodes when the daily linear polarization test was carried out and each sample was disconnected from the ZRA for few minutes. At the end of day 1 it was observed that the weld metal current density became anodic to the other electrode with an increasing galvanic current between day 1 and day 2 before decreasing slightly towards day 8, while both parent metal and heat affected zone were relatively steady, approaching zero current density.

A switching behaviour was observed between days 8 & 9, before reverting to the original behaviour. Figure 5-17 shows the average galvanic currents for each region of the weld and it can be seen that the sum of the cathodic currents of the parent metal and the HAZ equal the anodic current of the weld metal but are in opposite in sign.

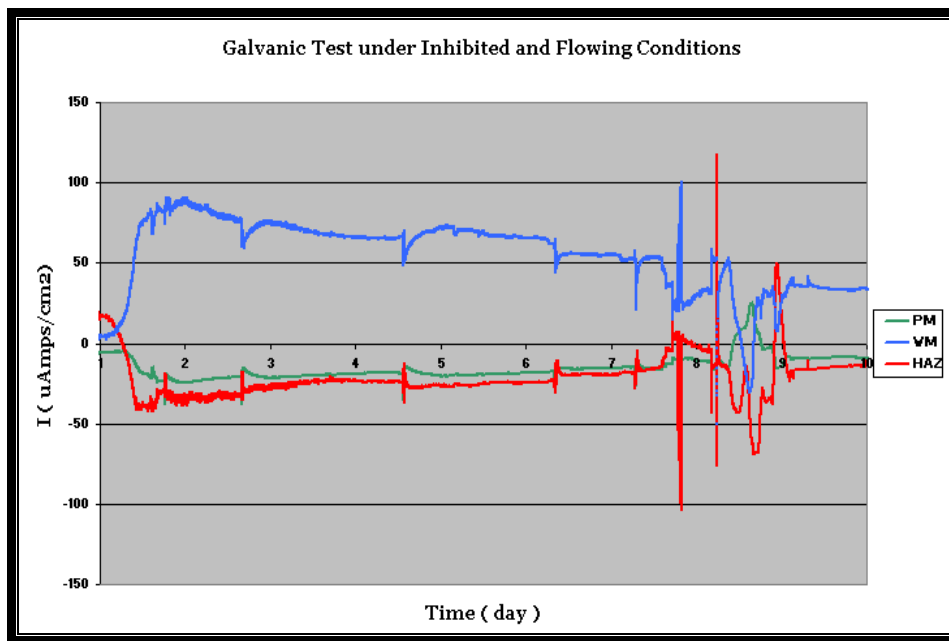


Figure 5-16: Galvanic current density under inhibited & flowing conditions for 10 Days

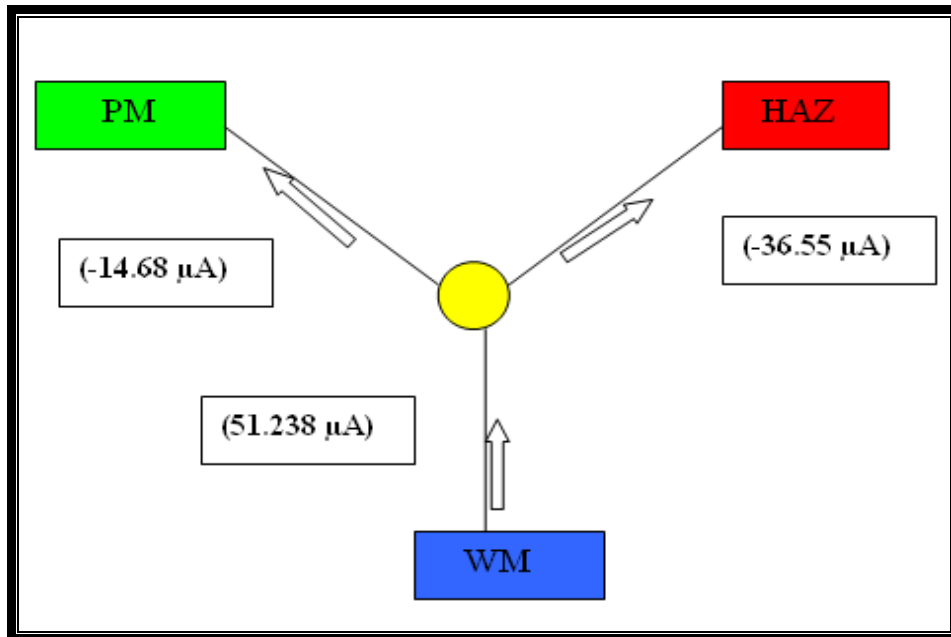


Figure 5-17: Average galvanic current densities under inhibited and flowing conditions over 10 days

5.9 Analysis of LPR test under sweet corrosion CO_2 with flow condition and inhibitor addition

The self corrosion rate measurements of each weld section in inhibited solution were run for 10 days, as shown in Figure 5-19. Corrosion inhibitor had an effect on all three weld segments and a corrosion rate reduction was observed. It was observed that the green inhibitor was quite effective at 30 ppm. However, it was less effective for WM compared to other regions. It was observed that a black layer covered all three regions. However the weld metal surface had more corrosion due to pitting. If parent metal was the most cathodic then the corrosion rate of the most anodic section would be significantly increased, and in this case it was the weld metal.

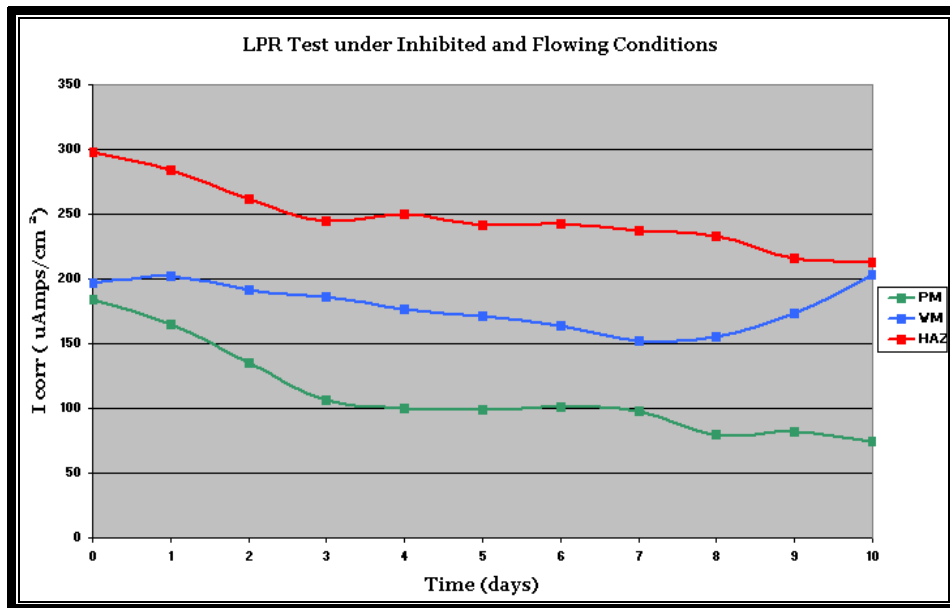


Figure 5-18 Current density for inhibited samples under flow conditions for 10 days

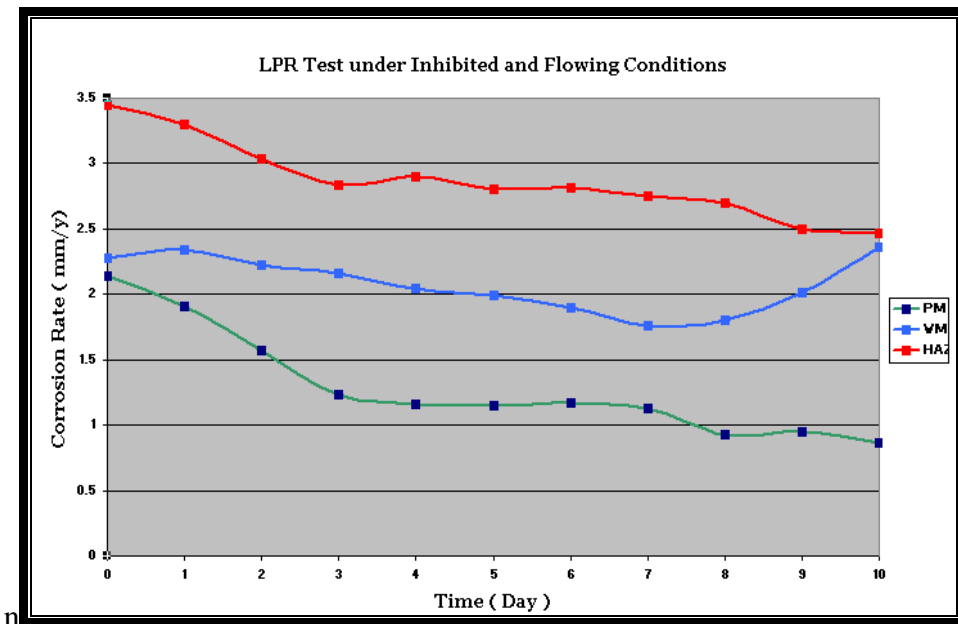


Figure 5-19 Corrosion rate for inhibited samples under flow conditions for 10 Days

5.10 Comparison of the corrosion inhibitor efficiency for the three sections under static and flow conditions

Corrosion rate comparisons of each weld section under static and flowing conditions with inhibitor and with no inhibitor are shown in Figure 5-20, Figure 5-21 and Figure 5-22 respectively.

It was clear that corrosion inhibitor had an effect on all weld regions due to a reduction in the corrosion rate, especially for parent metal. Corrosion inhibitor efficiency was calculated with the formula provided in section 2.10.1. In the static condition the calculated efficiency was at 5 days exposure. It was observed that the green inhibitor performed with relatively high average efficiency, reaching values of 88 % for parent metal, 83 % for the WM and 78% for HAZ. In contrast, the same inhibitor in flowing conditions had an efficiency of 86% for PM while efficiency for WM and HAZ were 48% and 53% respectively.

An interesting observation is that the inhibitor performance on the parent material was similar in the flowing condition and static condition. However, for WM and HAZ, a reduction of 35% and 25 % respectively were observed in flowing conditions.

The Inhibitor had a negative effect on the weld metal by making it more anodic as it was corroded preferentially to the PM. The reason for this change of behaviour may be related to film formation and this will be discussed later in the thesis.

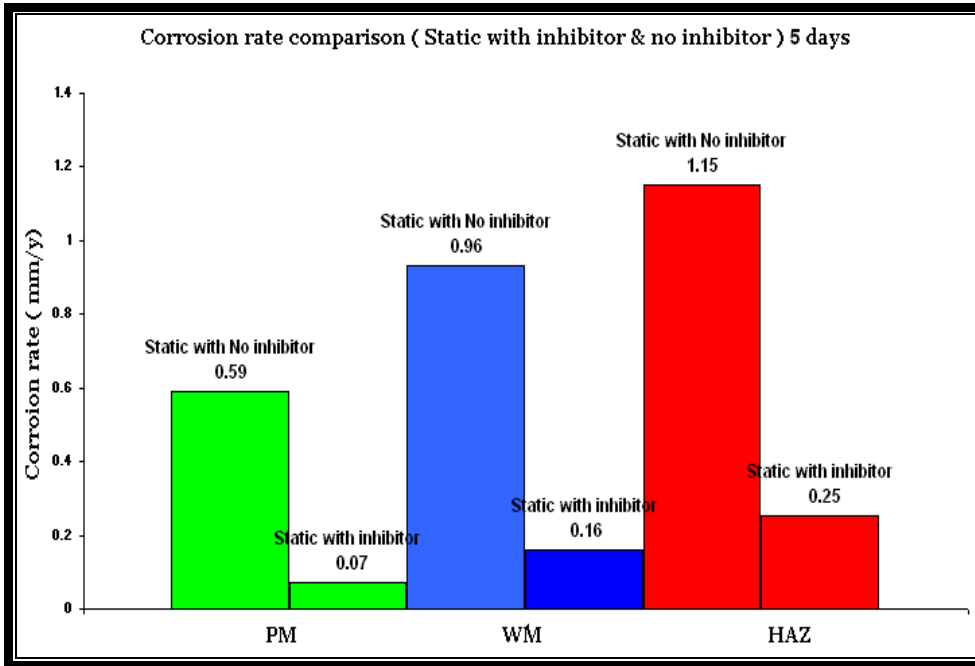


Figure 5-20: Corrosion rate comparisons for static conditions with inhibitor and no inhibitor after 5 days

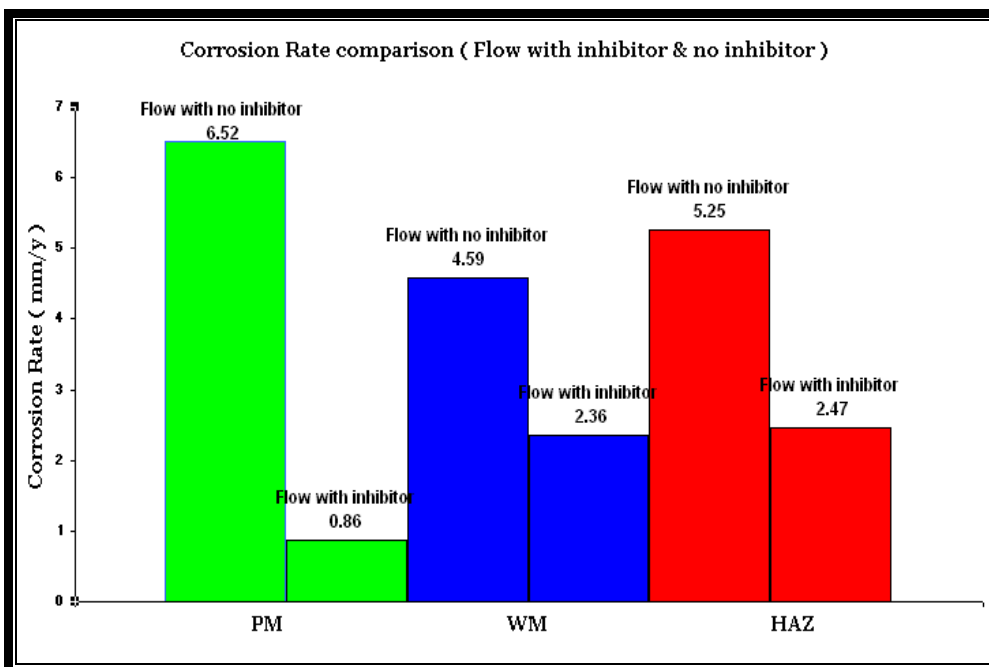


Figure 5-21: Corrosion rate comparisons under flowing conditions with inhibitor and no inhibitor after 10 days

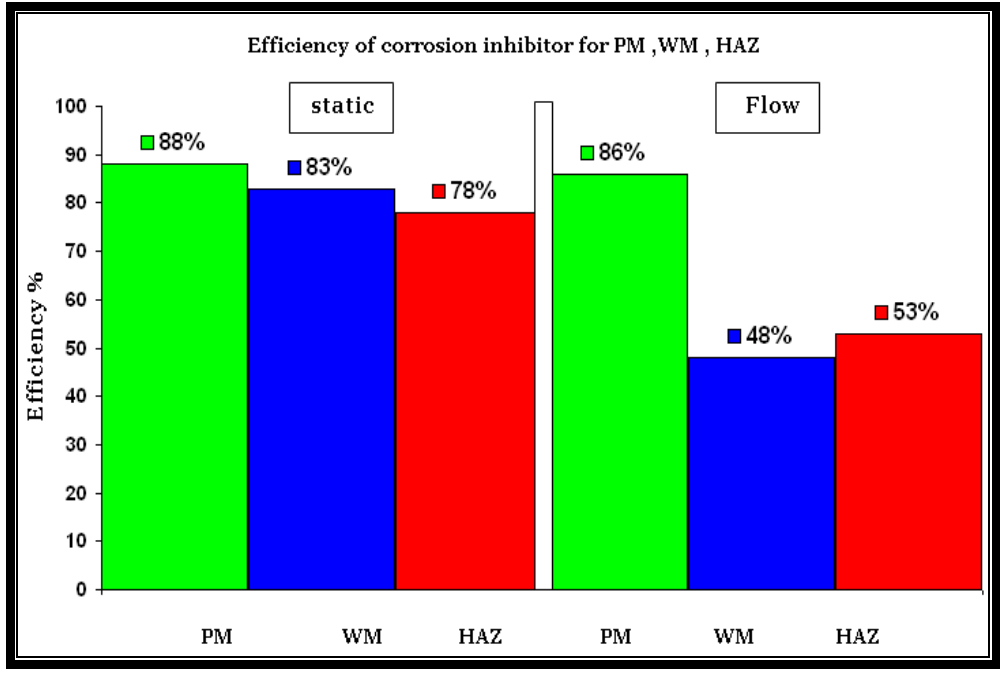


Figure 5-22: Comparisons of the inhibitor efficiency under static (5 days) and flowing conditions for 10 days

6 Rotating Cylinder Electrode Results (Part One)

6.1 Analysis of galvanic couple tests under uninhibited (static -1000 rpm) conditions for 3 Days

The basic idea for this test was to investigate the corrosion currents between the individual elements that comprise the weldment. This experiment was run for 3 days under sweet corrosion (CO_2) conditions with different rotation rates. The variation of galvanic current over the time is shown in Figure 6-1. The corresponding current densities are given in Figure 6-2.

The first couple of (PM-HAZ) exhibited a positive current which indicated the preferential corrosion of the parent metal with respect to HAZ. However, the second couple WM-HAZ had a negative current which meant that the HAZ corroded preferentially with respect to WM. Figure 6-3 shows the average galvanic currents for each region of the weld and it can be seen that the sum of the anodic currents from the parent metal and the HAZ equal the cathodic current on the weld metal.

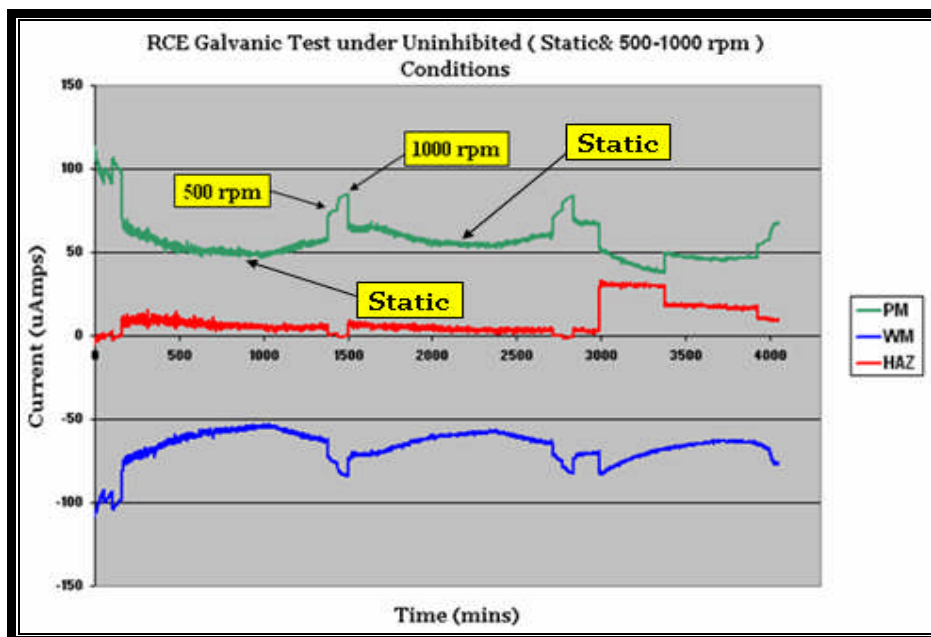


Figure 6-1: Galvanic current under uninhibited conditions

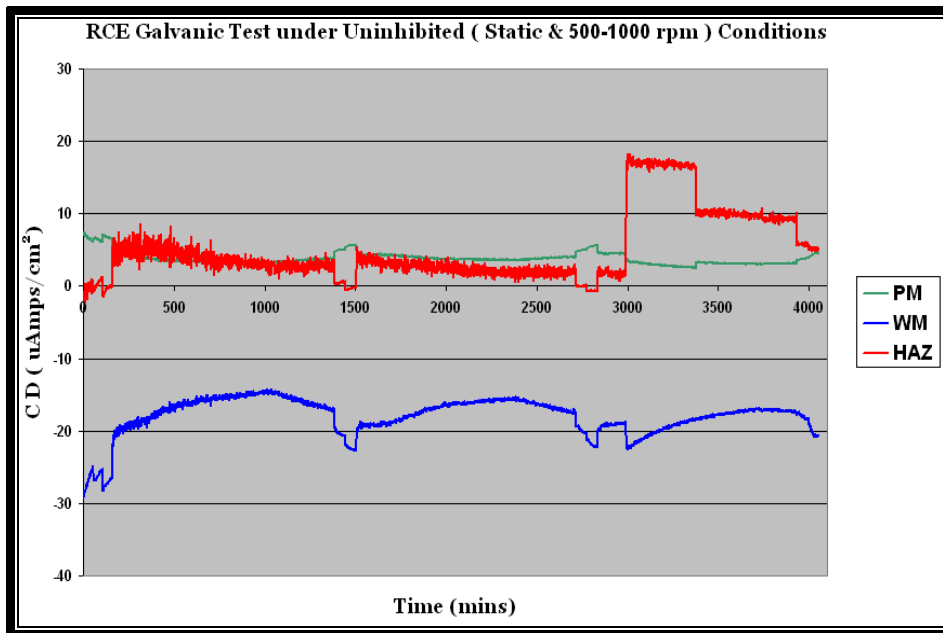


Figure 06-2: Galvanic current density under uninhibited Conditions

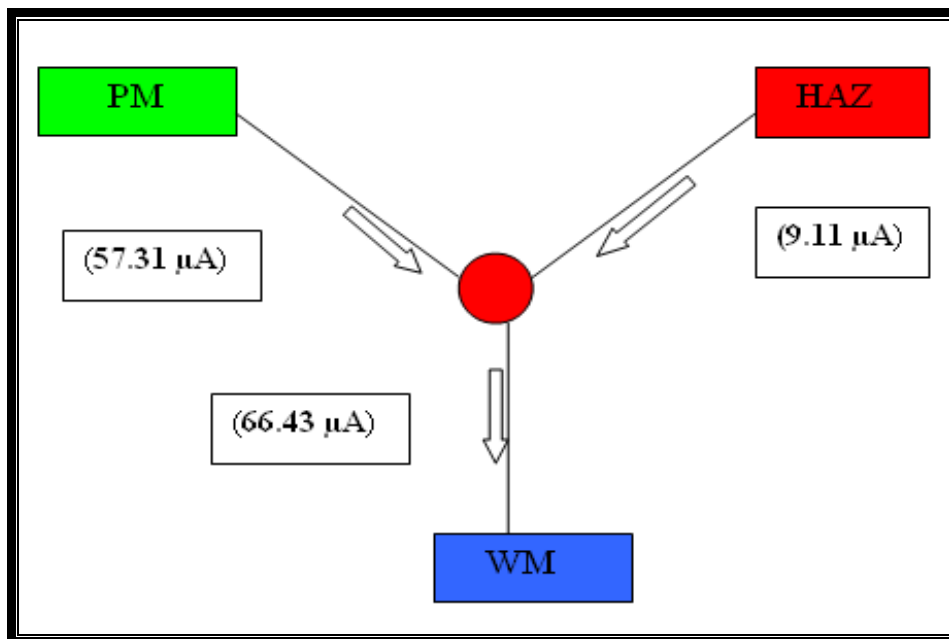


Figure 6-3: Average galvanic current under uninhibited conditions

6.2 Analysis of LPR tests under uninhibited conditions for 3 Days

The corrosion rate of each weld region was monitored daily by the linear polarisation resistance (LPR) technique. A series of LPR data was obtained up to a period of 3 days. The variation of the current density over the rotation speed is shown in Figure 6-4. While, the variation of corrosion rate with rotation speed is shown in Figure 6-5.

Typically 10 hours after the beginnings of the experiment under stagnant conditions, measurements of the LPR (corrosion rate) as a function of rotation speed were performed, in order to achieve a baseline corrosion rate. During the static conditions, a black film formed and covered all three sample surfaces. This film may represent a physical barrier which retards the diffusive transfer of corrosive species and prevents metal dissolution which may have been responsible for the low baseline corrosion rate. Indeed, presence of this film could also result in acidification under the corrosion layer, facilitating the initiation of pitting corrosion.

The presence of corrosion product was verified by visual inspection during the test with a tendency for shallow pitting after the test was completed. As expected, there was an increase in the corrosion rate for each sample tested as the rotation speed and shear stress increased, with HAZ found to have the highest corrosion rate. The LPR corrosion rate for parent metal was 0.56-1.76 mm/yr, WM 0.618-1.72 mm/y and HAZ 0.97-2.08 mm/y over the whole range of the velocities. The shear stress from the RCE was calculated by using Eq.10 $Sh_{RCE} = 0.0791 Re_{RCE}^{0.7} Sc^{0.356}$.

Due to high shear stress, especially at high rates of rotation, visual examination of samples after the test completion indicated that certain weld segments were either partially covered with the protective film or the film formed was loosely adherent to the surface and so unable to provide complete protection, as shown in Figure 6-6.

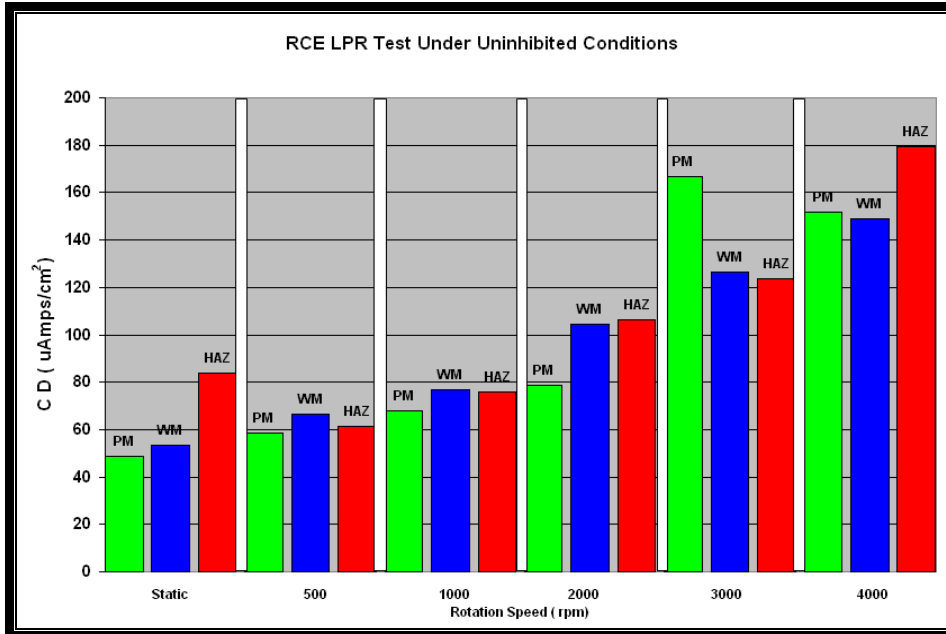


Figure 06-4: LPR current density under uninhibited conditions

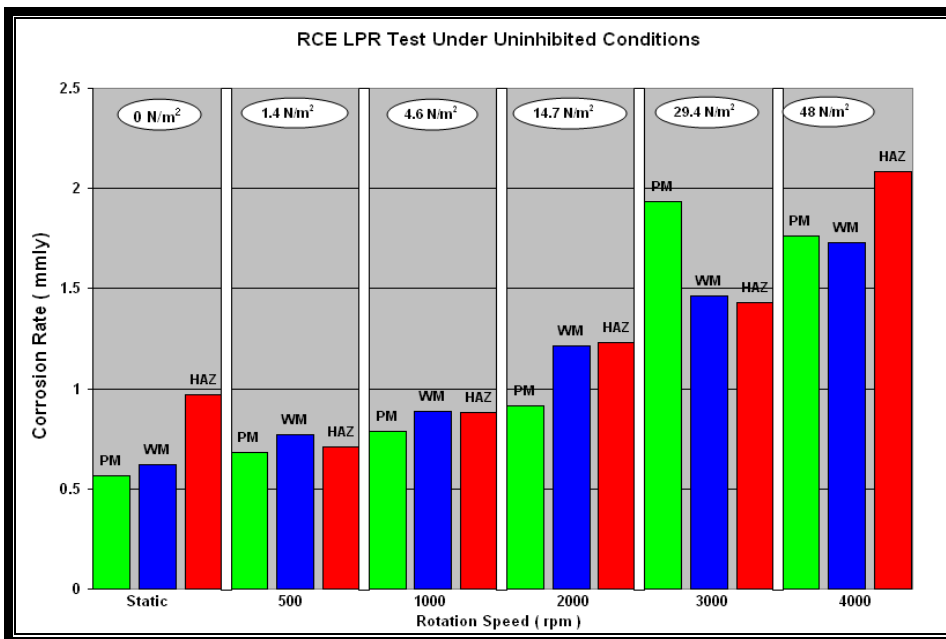
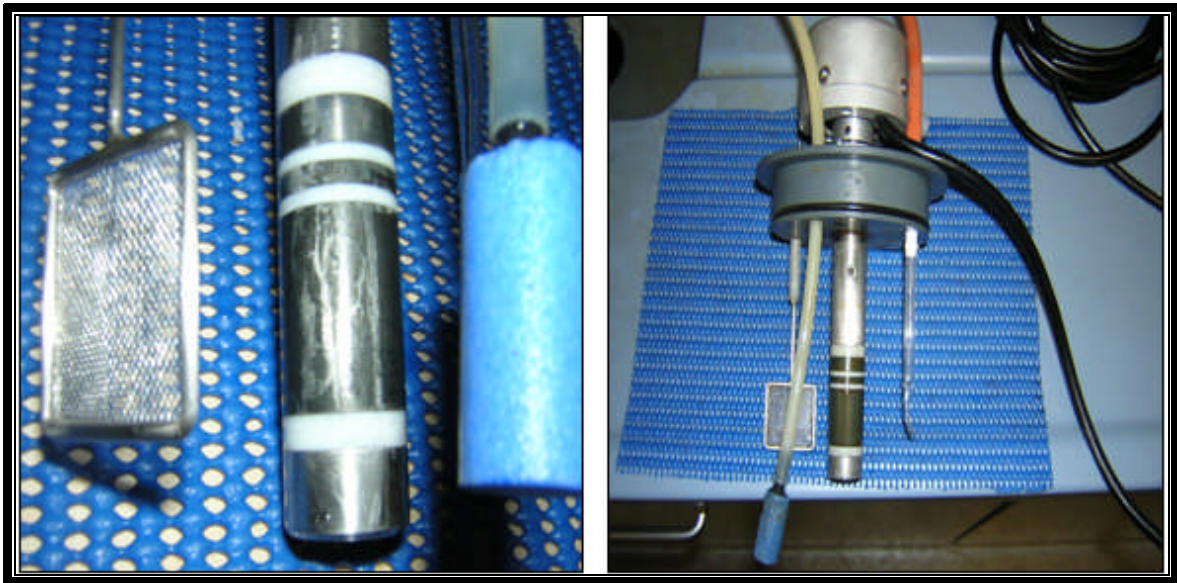


Figure 6-5: LPR corrosion rate under uninhibited conditions



(A)

(B)

**Figure 6-6: (A) corrosion product film was partially removed during rotation.
(B) Corrosion product film covered the three samples before rotation.**

6.3 Analysis of galvanic test under inhibited conditions for 3 days

The basic idea for this test was to investigate the corrosion currents between the individual elements that comprise the weldment. This experiment was run for 3 days under sweet corrosion (CO_2) conditions at different rotation rates. The variation of galvanic current over the time is shown in Figure 6-7. The corresponding current densities are given in Figure 6-8. The first couple of (PM-HAZ) exhibited a negative current, which indicated the preferential corrosion of the HAZ with respect to parent metal. However, the second couple WM-HAZ had a positive current, which meant that the WM corroded preferentially with respect to HAZ.

Figure 6-9 shows the average galvanic currents for each region of the weld and it can be seen that the sum of the anodic currents from the weld metal and the HAZ equal the cathodic current on the parent metal.

It was observed that a switching behaviour in the direction of the weld currents compared with uninhibited conditions. This might be due to the high flow rate conditions, where less compact/adherent films on the weld metal might be removed, while films on the parent metal remained intact, leading to a switch from cathodic to anodic behaviour on the weld metal.

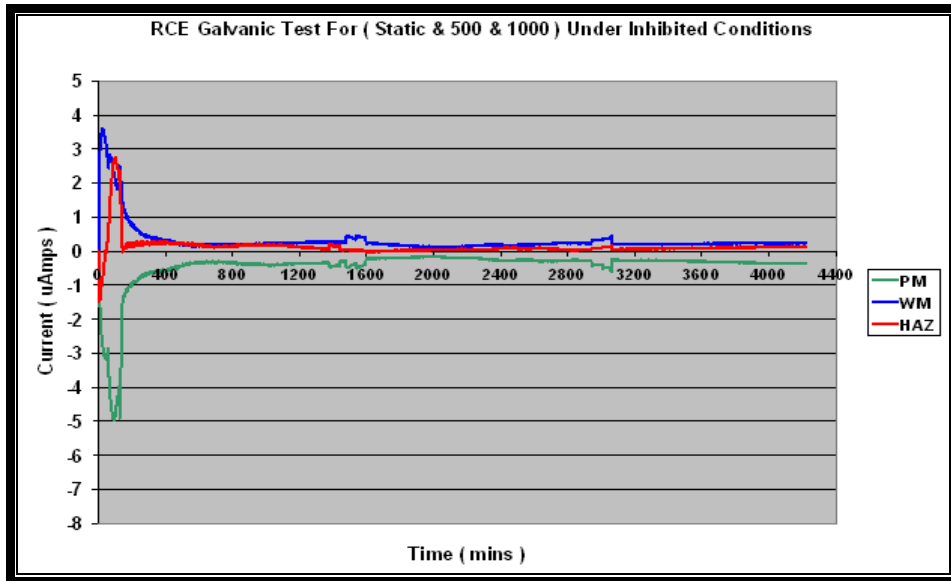


Figure 06-7: Galvanic current under inhibited conditions for 3 days

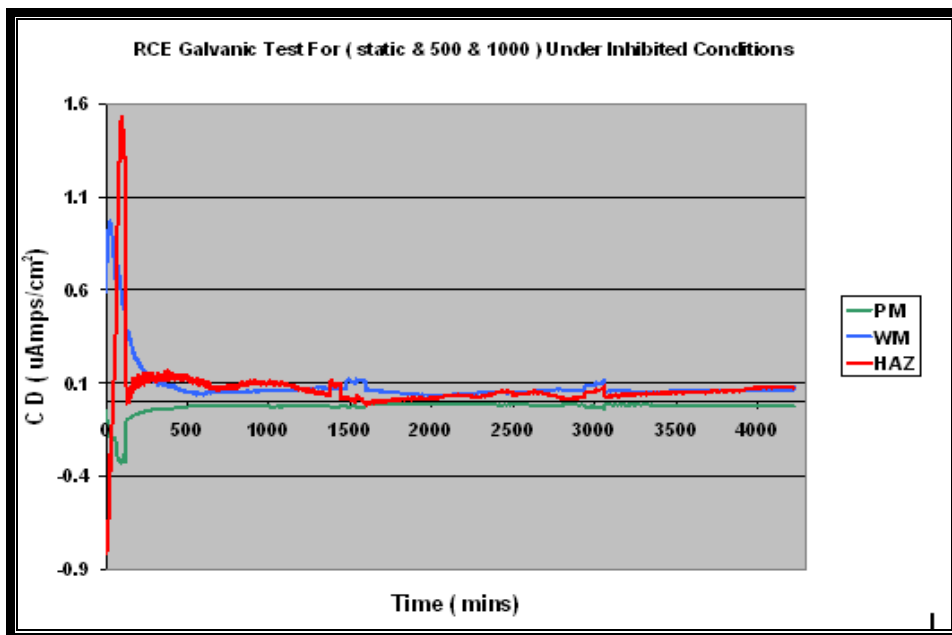


Figure 6-8: Galvanic current density under inhibited conditions

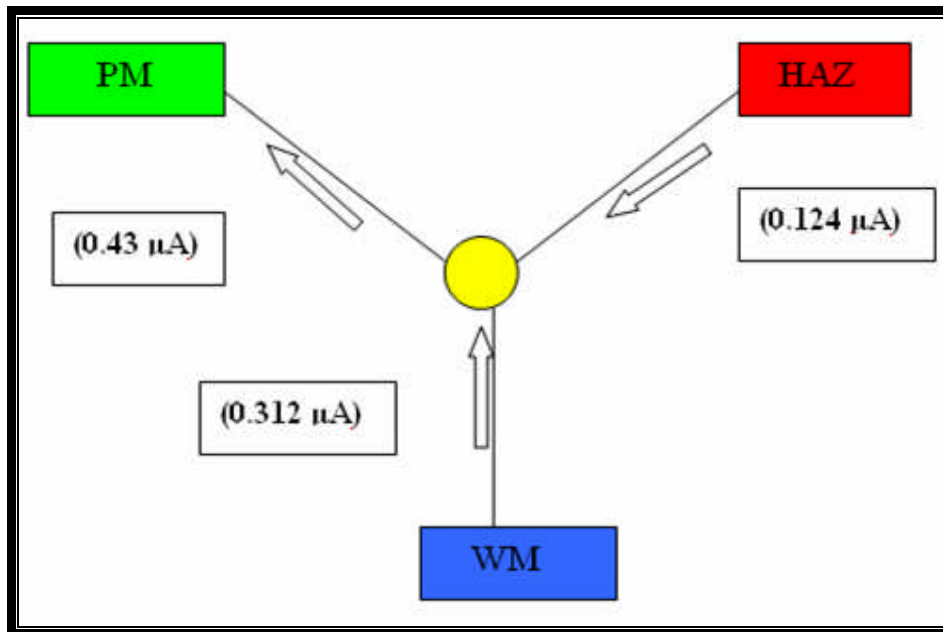


Figure 06-9: Average galvanic currents under inhibited conditions

6.4 Analysis of LPR tests under inhibited conditions

Figure 6-10 show results with galvanic corrosion currents used to express metal loss in inhibited solution. While the self corrosion rates of each weld section are shown in Figure 6-11. The test results plotted in Figure 6-11 show corrosion inhibitor performance over range of shear stresses (1.4-48 Pa), assessed using the RCE. It was clear that the corrosion inhibitor was less effective at high shear stress due to the increase in the corrosion rate of the parent metal, weld metal and HAZ. However, these results should be compared with corrosion rates with uninhibited conditions

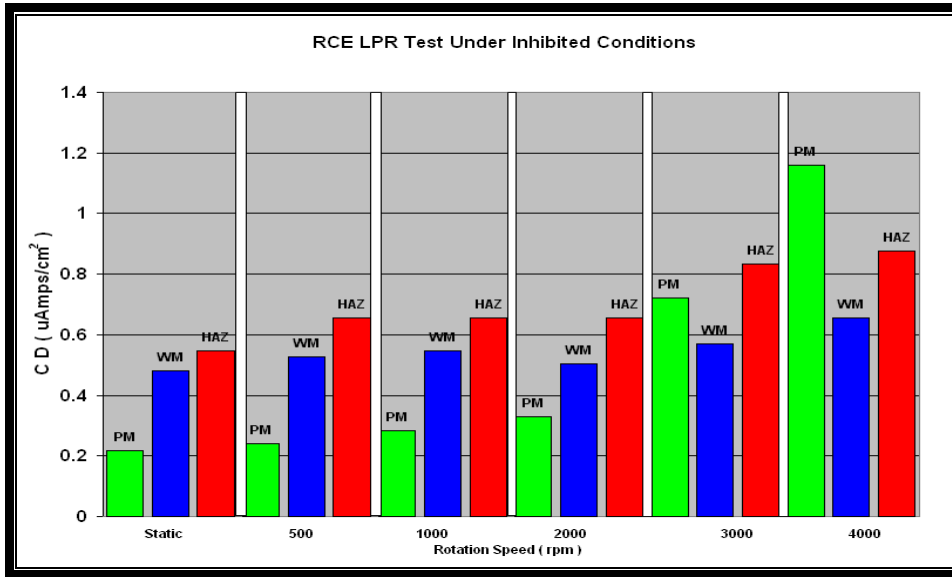


Figure 6-10: Current density under inhibited and sweet corrosion

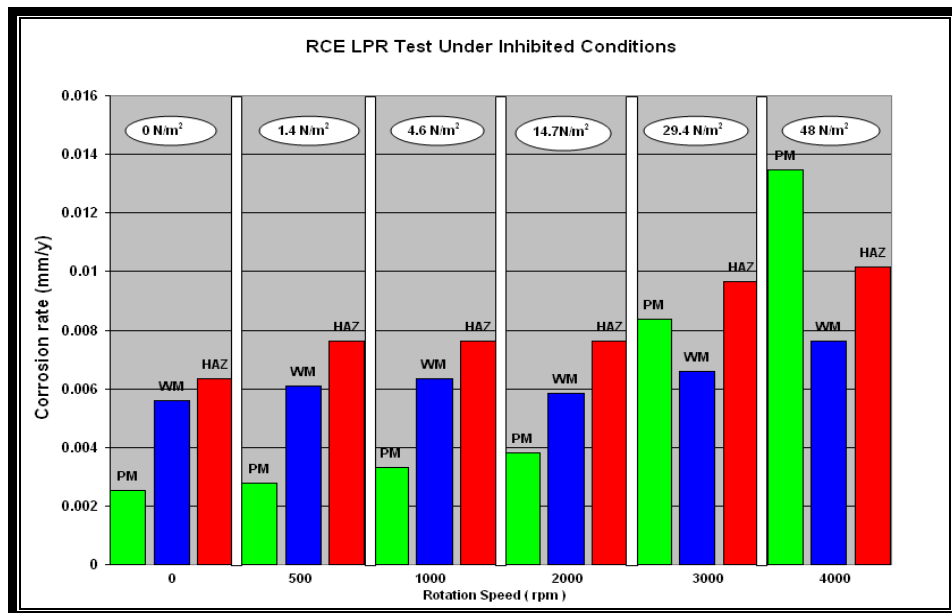


Figure 6-11: Corrosion rate under inhibited and sweet corrosion conditions

6.5 Inhibitor efficiency under (Static – 4000 rpm) and sweet conditions

Inhibitor efficiency comparisons for each weld section under static and different rotation speed conditions with inhibitor and with no inhibitor are shown in Figure 6-12

It was clear that the corrosion inhibitor had an effect on all weld regions due to high percentage efficiency, although it was proposed earlier that the inhibitor had a lower effect in reducing the corrosion rate for each weld region at high rotation speed. The efficiency was calculated with the formula provided in section (2.10.1).

The presence of the shear stress did not affect adversely the corrosion performance of inhibitor as it afforded more than 99% protection for the three weld regions under high rotation speed, especially for the parent metal. HAZ had the lowest average efficiency over the test period, possibly due to its non-homogenous microstructure. Flow velocity and shear stress might also play a part due to removing an existing film or retarding growth of such film. In general, when the corrosion inhibitor was present, the corrosion rate was in the region of 0.0025- 0.0076 mm/y, whereas the uninhibited corrosion rate was in the region 0.056-2.081mm/y.

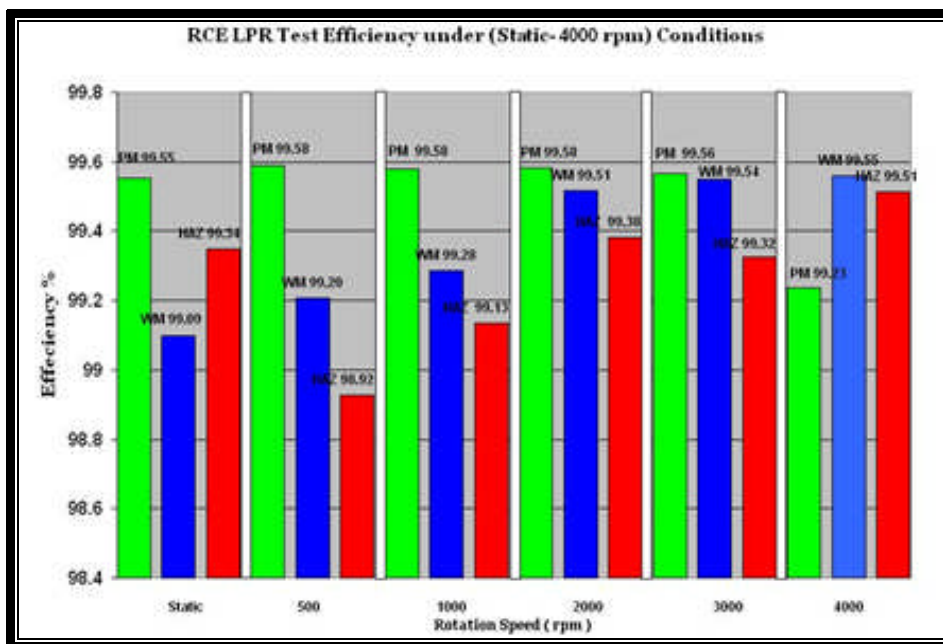


Figure 6-12: LPR inhibitor efficiency under CO₂ conditions for 3 days

7 Overview of the Most Significant Rotating Cylinder Electrode Results

A total of 4 series of experiments (2 without inhibitor & 2 with inhibitor) at room temperature were been conducted in this project. Tests were repeated in order to confirm the consistency of the results. The experiments were run for one day under sweet corrosion conditions through six different speeds of rotation (500-5000 rpm), as well as static conditions. The RCE was allowed to corrode under static conditions for almost 10 hours in order to establish a baseline corrosion rate, then the rotation speed was increased to 500 , 1000, 2000, 3000, 4000 and 5000 rpm. For the typical RCE shown in Figure 4-10, rotation rates between 500 and 5000 rpm correspond to a range of hydrodynamic parameters (Re , Sh , Sc) as shown in Table 5.

Table 5: Flow parameters

RPM	Flow velocity (m/s)	Reynolds number	Mass shear stress (Pa)	Sc	Sh
500	0.52	9950	1.40	522	464
1000	1.05	20000	4.55	522	753
2000	2.09	40100	14.8	522	1220
3000	3.14	60100	29.5	522	1620
4000	4.19	80200	48.0	522	1980
5000	5.24	100000	70.2	522	2330

An example of calculation is shown in Appendix 2

7.1 Analysis of galvanic couple tests under uninhibited & CO₂ conditions for one day

The experiments were run for one day under uninhibited and sweet corrosion conditions through six different speeds of rotation including static conditions. Tests were repeated twice in order to check the consistency of the results. The RCE was allowed to corrode

under static conditions for almost 10 hours in order to establish a baseline corrosion rate, then the rotation speed was increased to 500 , 1000, 2000, 3000, 4000 and 5000 rpm. In this series of tests, each segment of the weld was coupled through the ZRA for the galvanic current test followed, by the LPR test.

The variation of galvanic current over the time is shown in Figure 7-1 for both experiments 1 and 3. The corresponding current densities are given in Figure 7-2. The first couple of (PM-HAZ) exhibited a positive current and indicated the corroding preferentially of the parent metal with respect to HAZ. The second couple (WM-HAZ) exhibited a negative current which indicated that the HAZ was corroding preferentially with respect to weld metal.

In most cases, good agreement was obtained between the measured repeated test results also with those described previously under static and flowing conditions (sections 5 and 6). Figure 7-3 shows the average corrosion current to the HAZ, calculated from the average corrosion currents from PM and WM, where the total current was always zero.

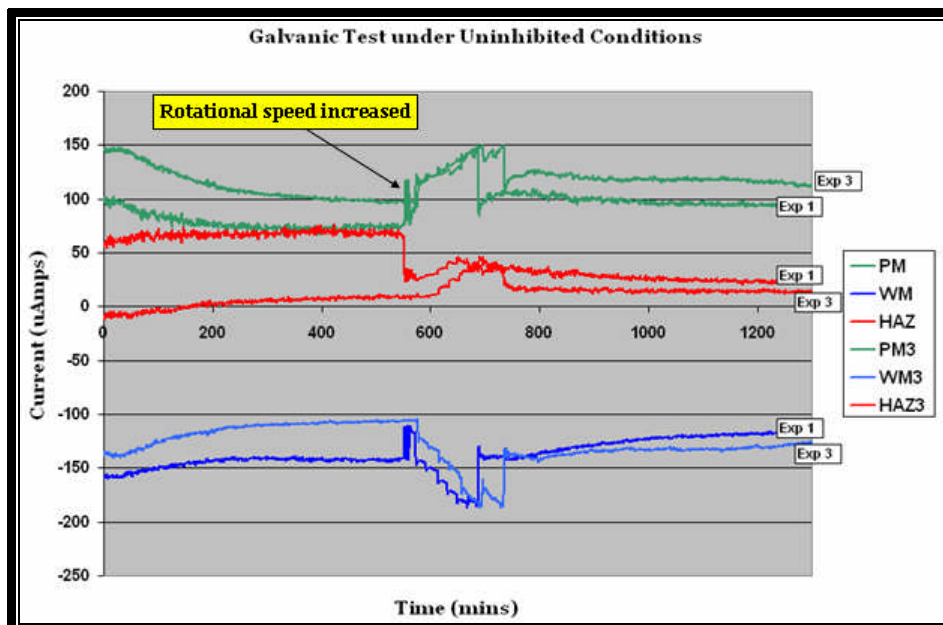


Figure 7-1: Galvanic current under uninhibited & CO₂ corrosion conditions

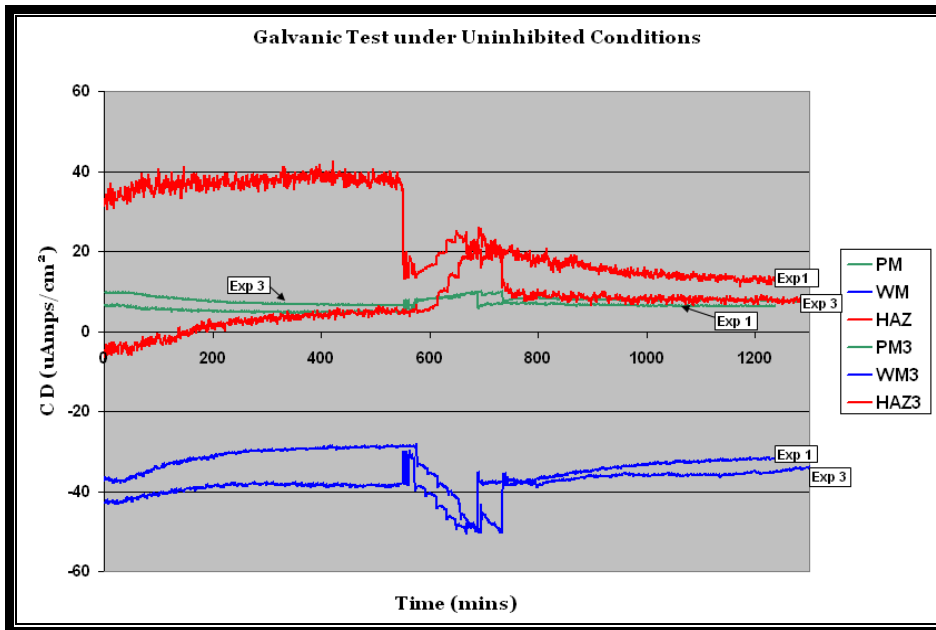


Figure 7-2: Galvanic current density under uninhibited & CO₂ corrosion conditions

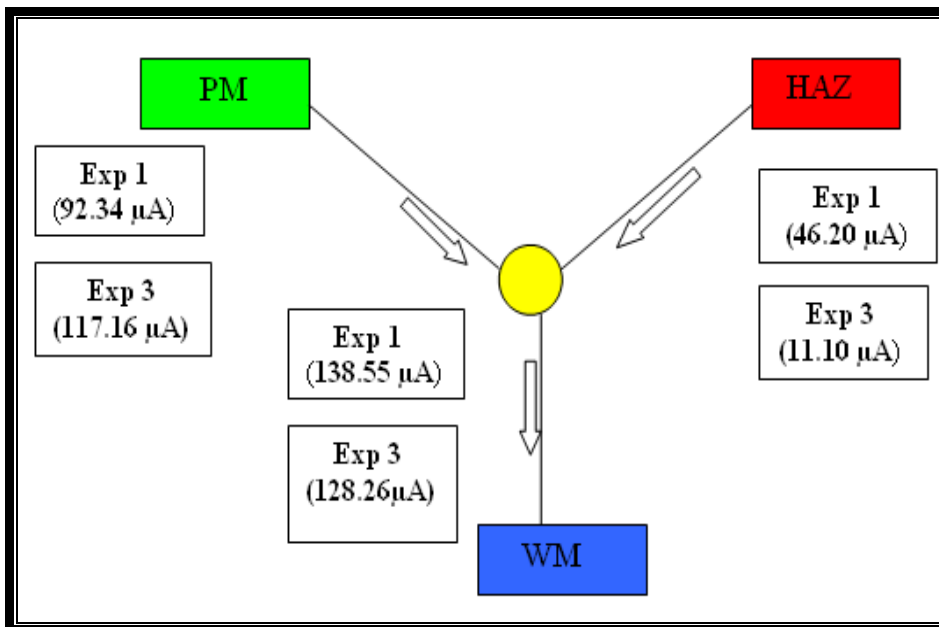


Figure 7-3: Average galvanic currents under uninhibited & CO₂ corrosion conditions

7.2 Analysis of LPR under uninhibited & sweet corrosion conditions after one day of exposure

A total of 2 series of experiments (without inhibitor) have been conducted in this project in order to present a reliable and consistent set of test results. In this series of tests, each segment of the weld was uncoupled in turn and its self corrosion rate was found by polarization resistance (LPR) measurements. After the LPR test was completed, electrode samples were reconnected and the galvanic current measurements were continued for a further 10 hours under stagnant conditions.

A significant increase of corrosion rate with rotation for all the three regions was observed. The variation of the current density over the rotation speeds for the two experiments are in shown in Figure 7-4 and Figure 7-5. The variations of corrosion rates as well as shear stress over the rotation speed for both experiments are shown in Figure 7-6.

During the static conditions, a black film was formed and covered all three sample surfaces. Predictably, there was an increase in the corrosion rate for each sample tested as the rotational speed and shear stress increased, with HAZ found to have the highest corrosion rate. The LPR corrosion rate was approximately; parent metal 0.56-1.76 mm/yr, WM 0.618-1.72 mm/y and HAZ 0.97-2.08 mm/y, over the whole range of the speeds.

Although two different flow geometries, flow channel and rotating cylinder, were studied, there appears to be a good correlation on the results measured under same static and flowing conditions, as shown in sections (5.1, 5.2, 5.6, and 5.7)

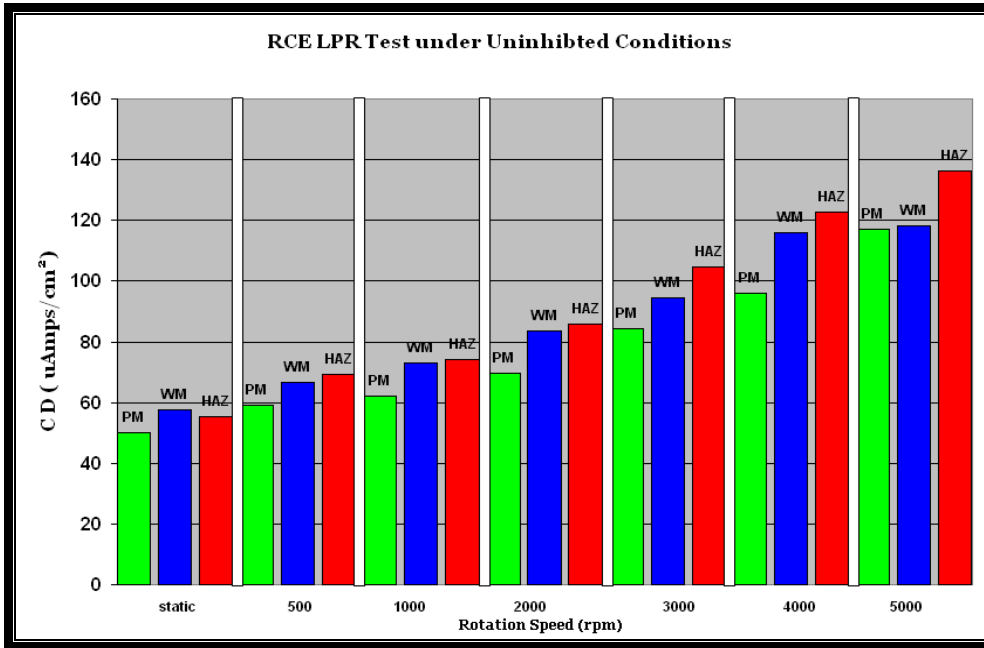


Figure 7-4: Corrosion current density under uninhibited & CO₂ conditions (Exp 1)

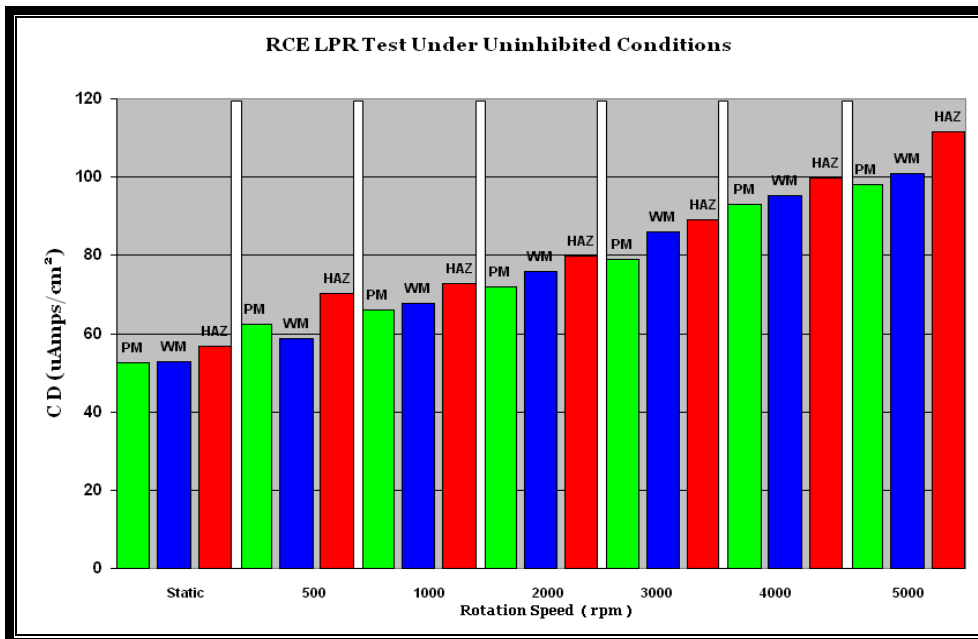


Figure 7-5: Current density under uninhibited & CO₂ conditions (Exp 3)

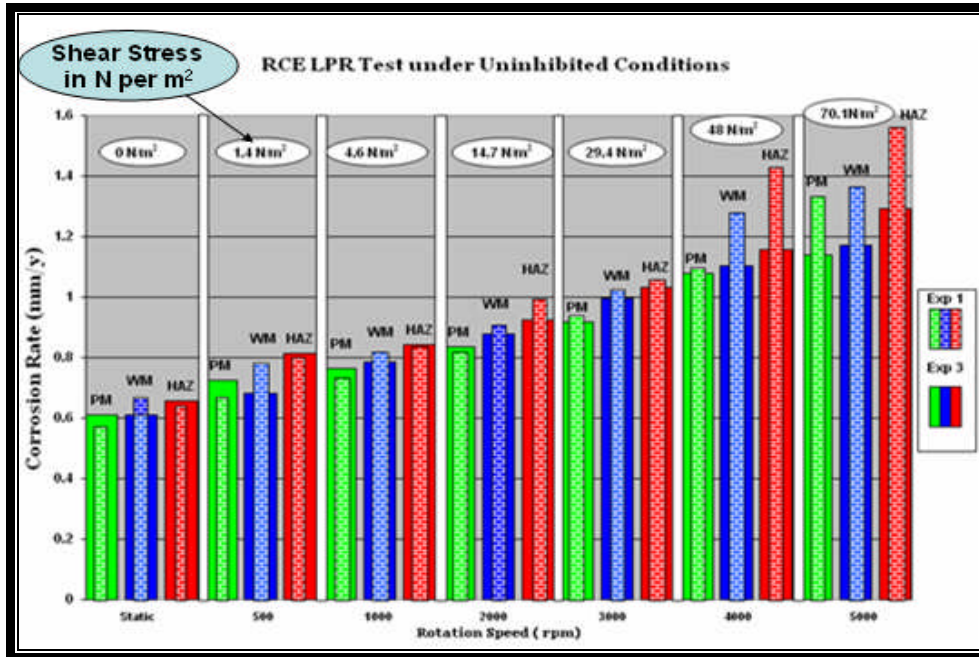


Figure 7-6: Corrosion rate under uninhibited & CO₂ conditions

7.3 Analysis of galvanic couple tests under inhibited & sweet corrosion conditions

The idea for this test was to investigate the corrosion galvanic currents between the individual elements that comprise the weldment under inhibited flowing conditions. A total of 2 series of experiments (with inhibitor) under room temperature have been conducted. The variations of galvanic currents over time for the two experiments are shown in Figure 7-7 and Figure 7-8. The corresponding current densities are given in Figure 7-9 and Figure 7-10.

The first couple (PM-HAZ) demonstrated a negative behaviour which indicated that parent metal was corroding preferentially with respect to HAZ. The second couple (WM-HAZ) exhibited cathodic behaviour. The implication of this was that HAZ corroded preferentially with respect to weld metal.

An increase in current density was observed, when the rotational speed was increased to (500, 1000, 2000, 3000, 4000 and 5000) rpm at 20 minutes intervals. The weld metal had a tendency towards more positive (anodic direction), although when the rotation

was stopped it tended to return back to its initial behaviour. The parent metal initially had more negative values (cathodic direction), although with time it tended to return back to its initial behaviour. It was observed that the inhibitor film took about one hour to be formed as it shown in Figure 7-8. Also it was noticed that current density for three the samples was progressively reduced towards the end of the test.

Figure 7-7 shows that high corrosion rates were observed when the rotation speed was increased. However in this experiment it appeared that had been leakage of oxygen into the cell resulting in yellow coloration of the solution from the formation of Fe (III) hydroxide complexes and brown rust formed across the three weld regions. This leak would explain the abnormally high corrosion rates measured. It has been reported that the combination of CO₂ and oxygen, in leaking pumps for example, is particularly corrosive [134].

Figure 7-11 shows the average galvanic currents for each region of the weld and it can be seen that the sum of the anodic currents from the weld metal and the HAZ equal the cathodic current on the parent metal.

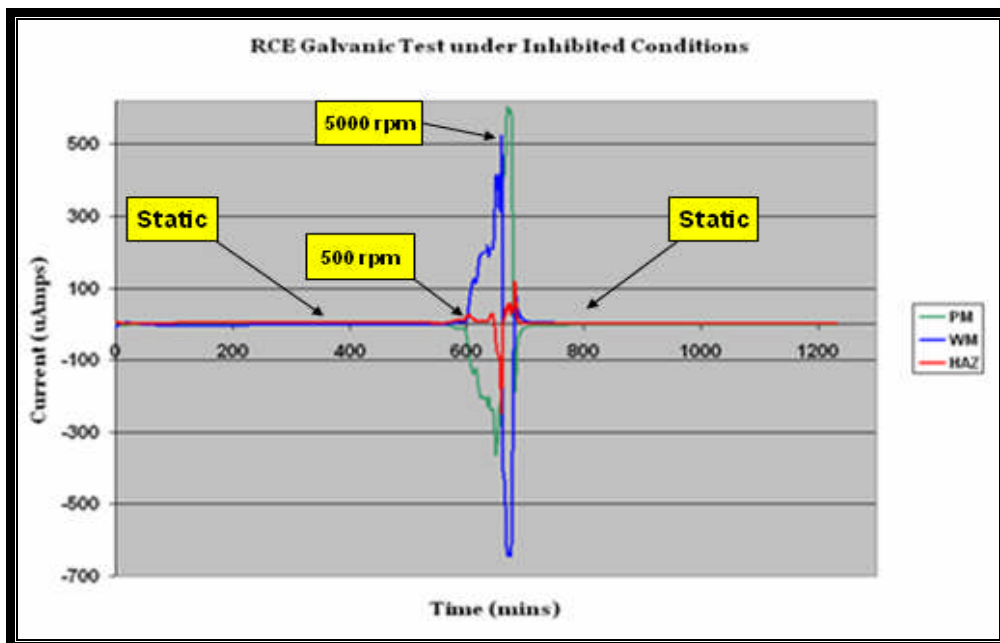


Figure 7-7: Galvanic current under inhibited & CO₂ conditions (Exp 2)

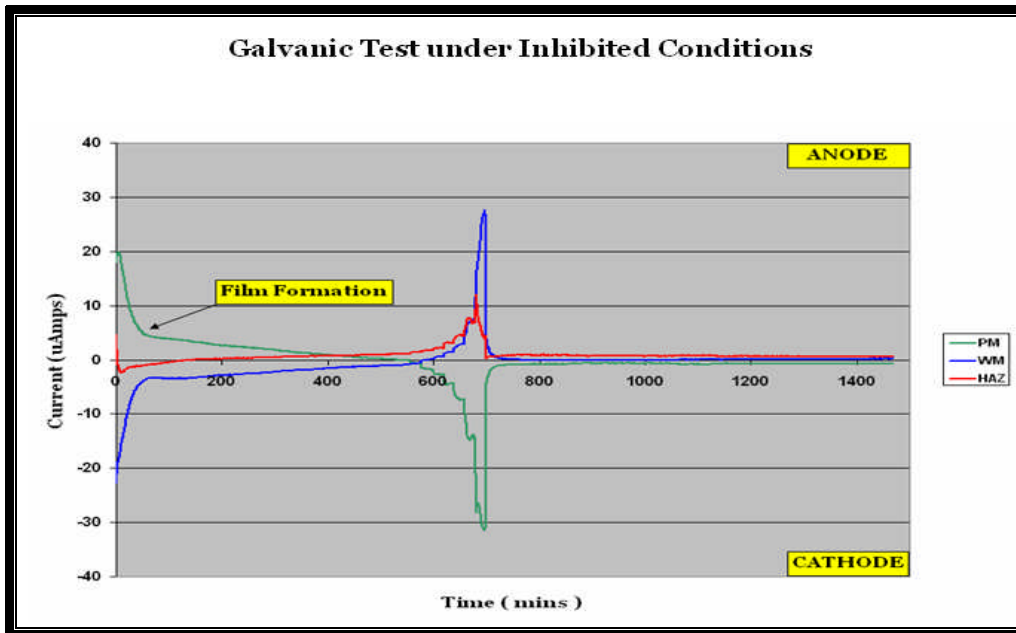


Figure 7-8: Galvanic current under inhibited & CO₂ conditions (Exp 4)

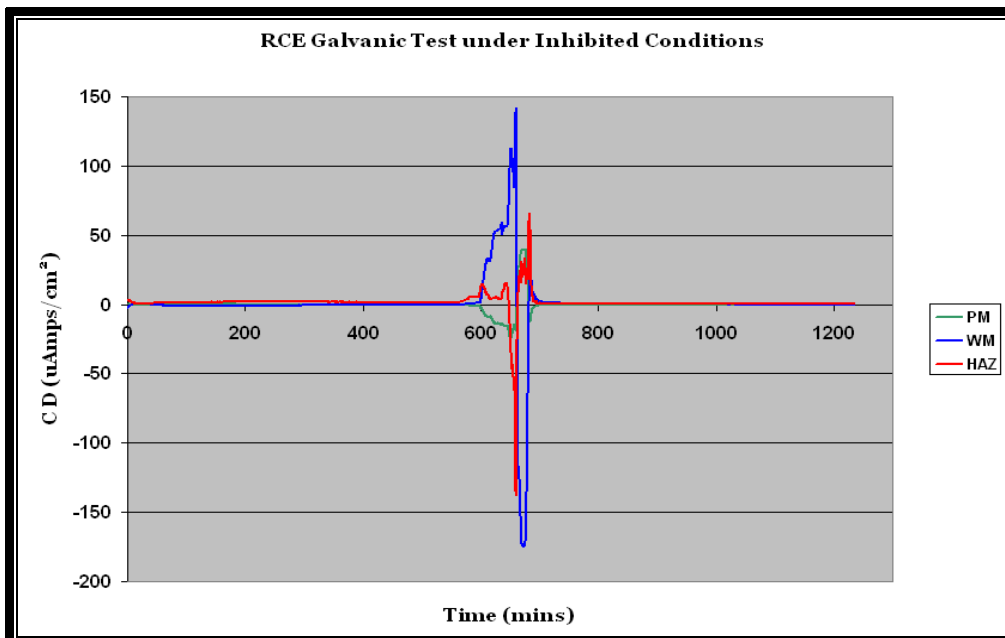


Figure 7-9: Galvanic current density under inhibited & CO₂ conditions (Exp2)

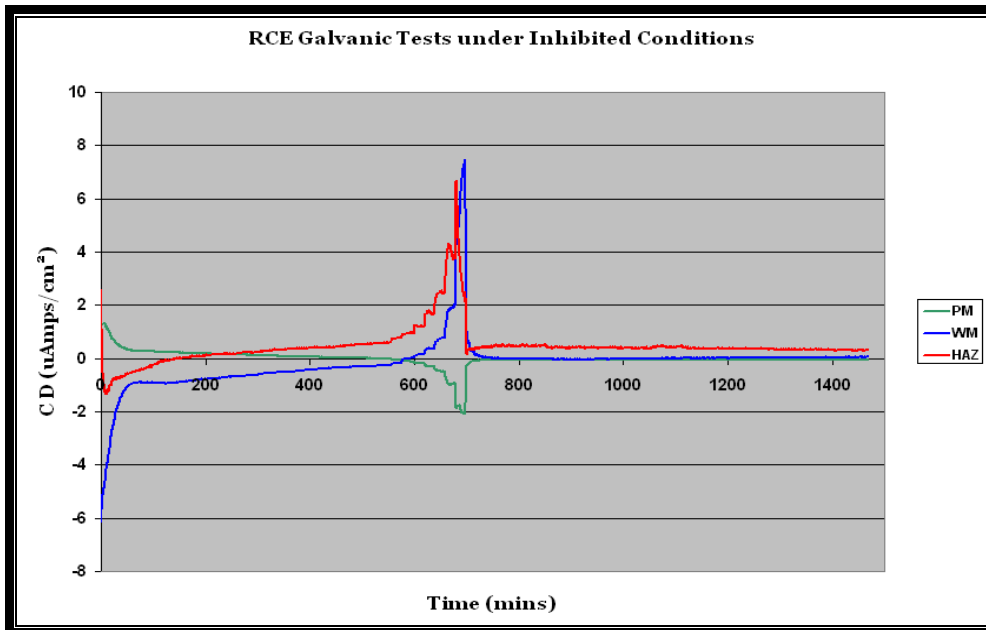


Figure 7-10: Galvanic current density under inhibited & CO₂ conditions (Exp 4)

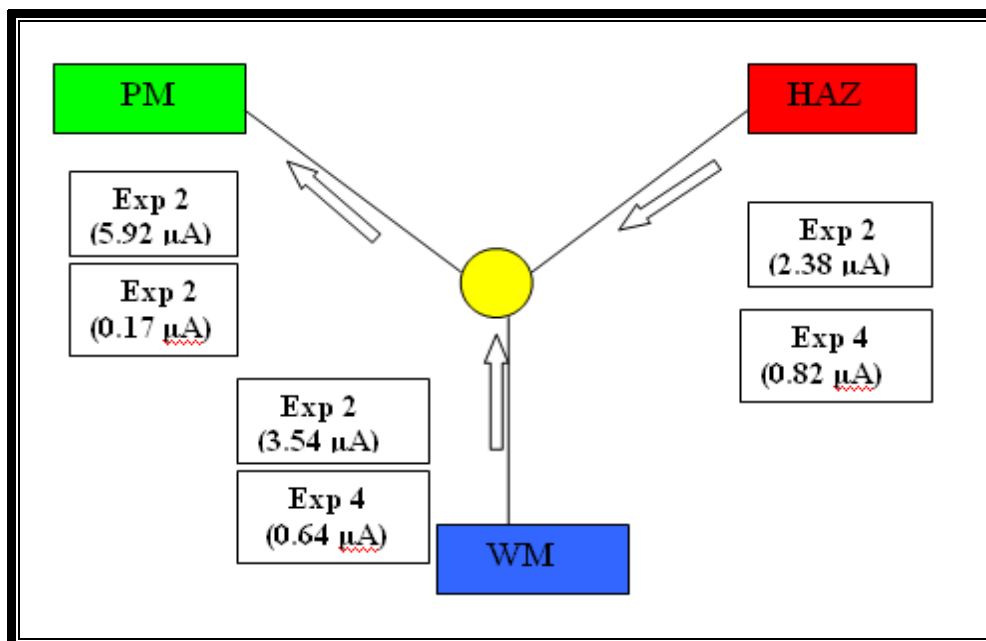


Figure 7-11: Average galvanic current density under inhibited & CO₂ conditions

7.4 Analysis of LPR test under inhibited & (CO₂) conditions

After the galvanic test was completed, the electrode samples were allowed to corrode in the corrosive electrolyte for a further 10 hours under stagnant conditions. It was observed that no black film was formed on the samples. Typically 10 hours after the beginning of the experiment under stagnant conditions, measurements of the LPR (corrosion rate) as a function of rotation speed was performed. The self corrosion rates of each weld section in inhibited solution for the two experiments are shown in Figure 7-14. Figure 7-12 and Figure 7-13 show the same results with corrosion currents densities over the time.

Overall, the addition of the inhibitor appears to provide a beneficial effect when compared to self corrosion rate values for the uninhibited system. Under inhibited conditions, HAZ exhibited the highest corrosion rate compared to other segments during the exposure time. As the rotation speed increased, turbulent flow and high shear stress produced conditions in which inhibitor molecules were easily stripped away from the metal surface, which was harmful to inhibition efficiency.

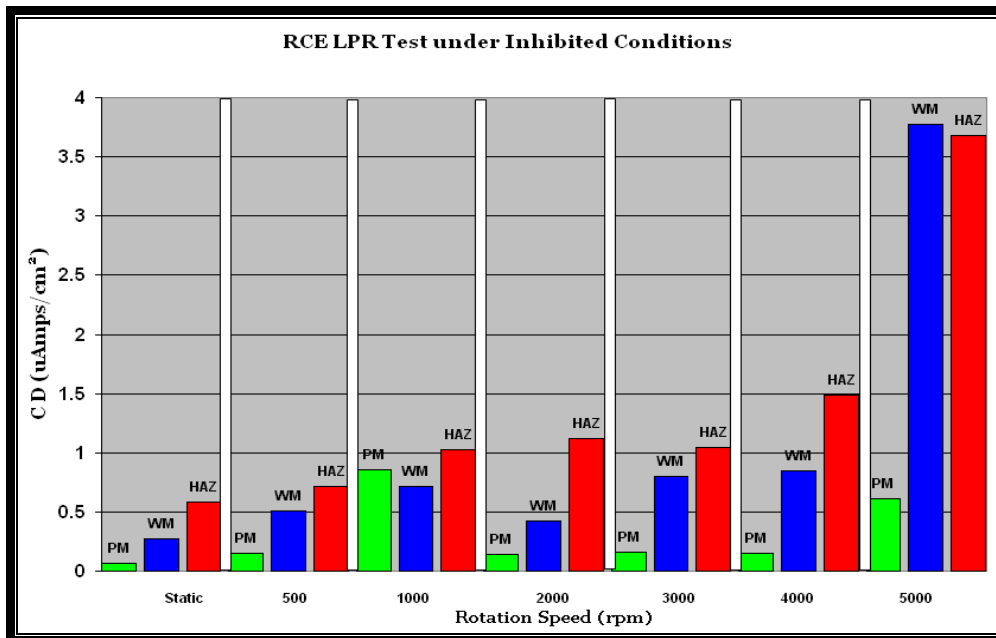


Figure 7-12: Current density under inhibited & CO₂ conditions (Exp2)

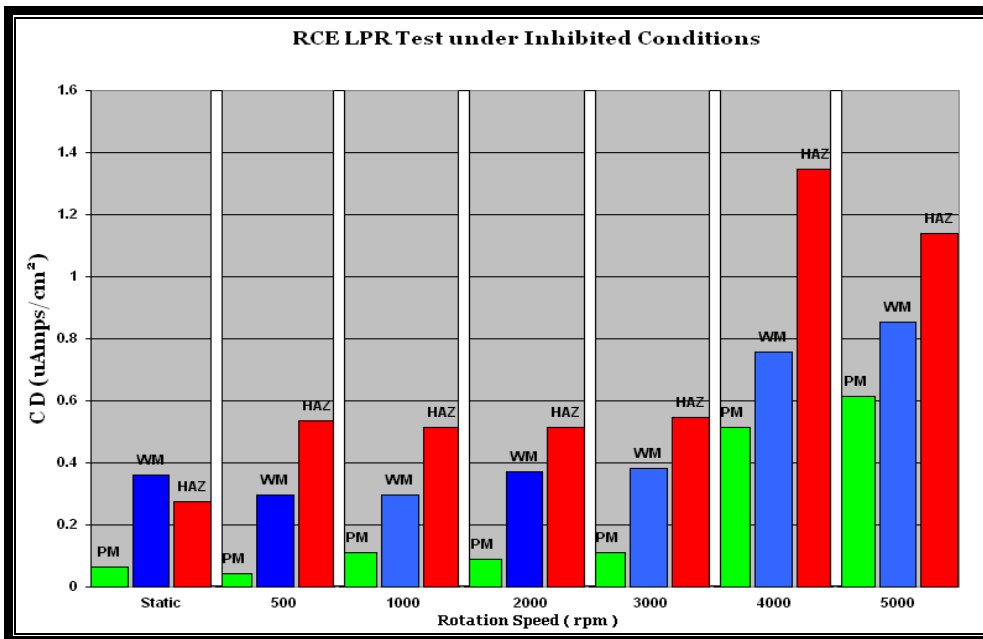


Figure 7-13: Current density under inhibited & CO₂ conditions (Exp 4)

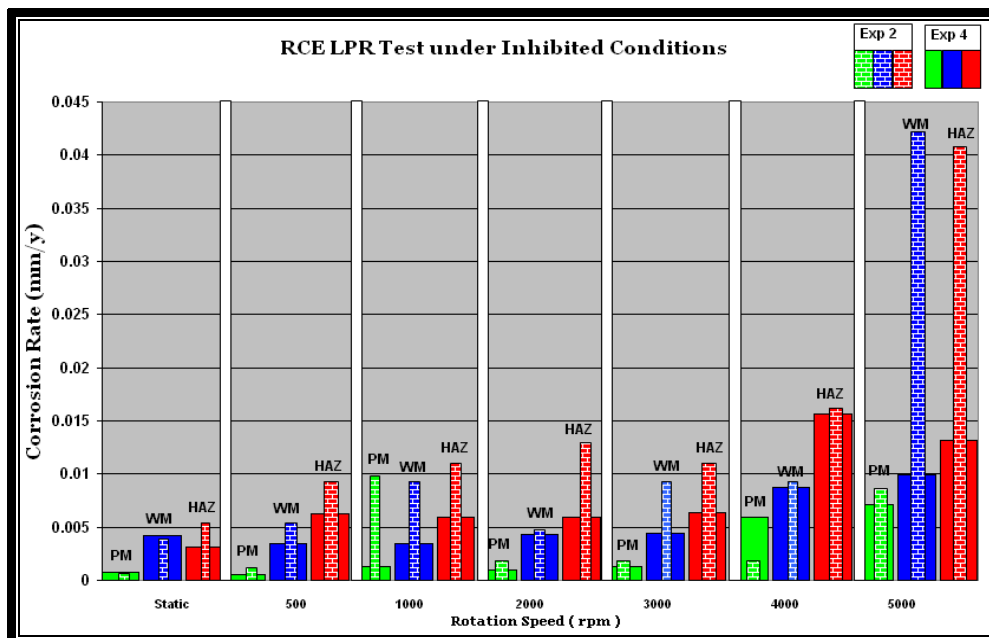


Figure 7-14: Corrosion rate under inhibited and sweet corrosion

7.5 Inhibitor efficiency for uninhibited & inhibited under (static-5000 rpm) conditions

Fluid flow and the resulting wall shear stress can have a significant effect on corrosion inhibitor efficiency. Inhibitor efficiency comparisons of each weld section under static and different rotation speed conditions for the total series of 4 experiments is shown in Figure 7.15 and Figure 7.16. It was clear that corrosion inhibitor had an effect on all weld regions due to the high percentage efficiencies.

From the graph it was observed that the parent metal, weld metal and HAZ have different inhibition percentages. Individual components of the weld material were seen to have fairly constant inhibitor efficiency over the range of static and flowing conditions (500-3000 rpm).

In general, the presence of the shear stress did not adversely affect the corrosion performance of inhibitor as this inhibitor tested afforded above 98% protection for the three samples up to 3000 rpm rotation speed, with the parent metal found to have the highest efficiency under static and flowing conditions.

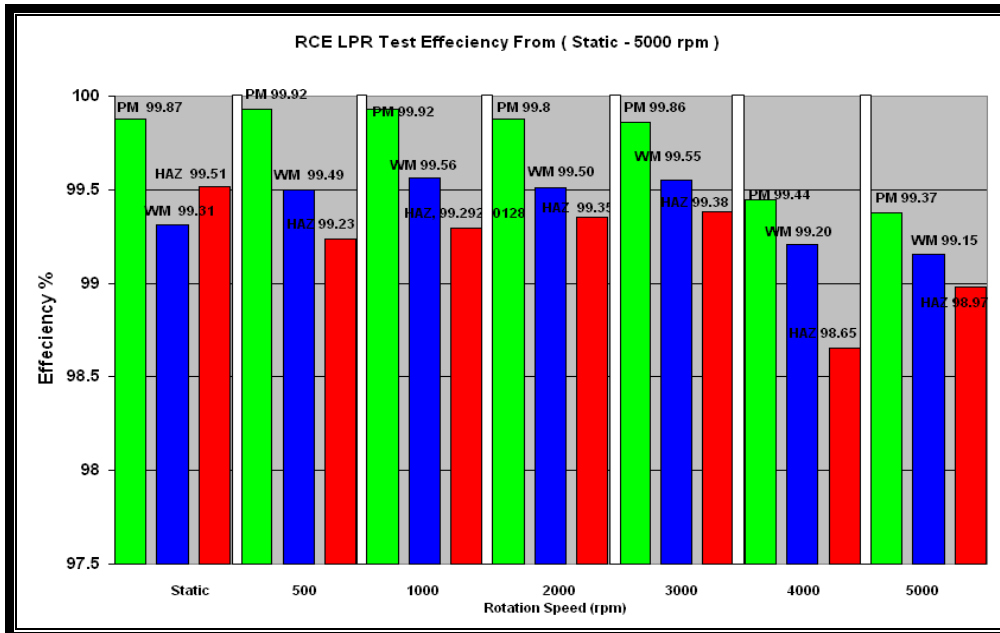


Figure 7-15: Inhibitor efficiency under CO₂ corrosion conditions (Exp1 – Exp 2)

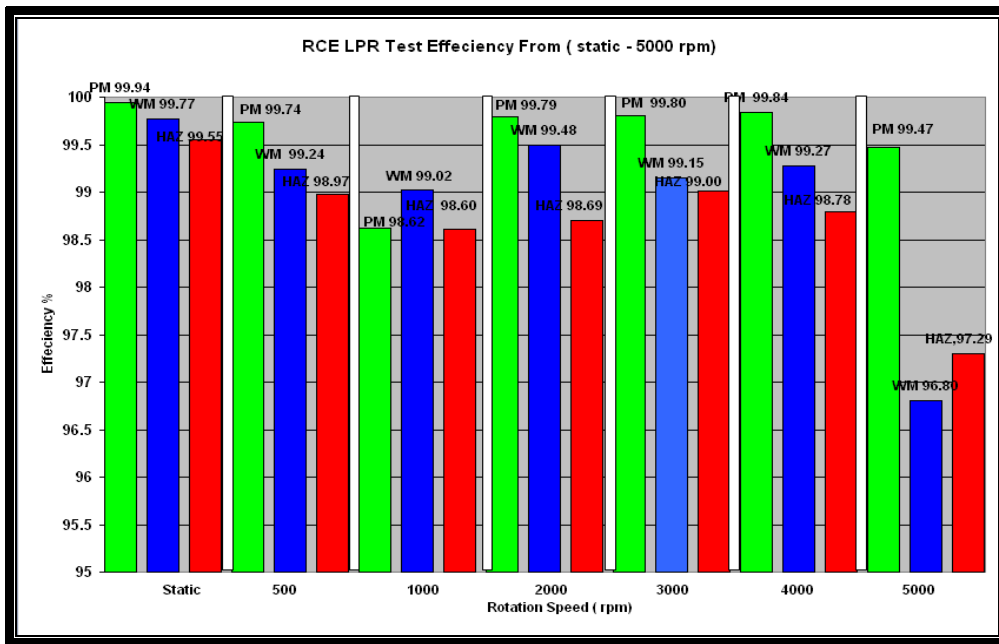


Figure 7-16: Inhibitor efficiency under CO₂ corrosion conditions (Exp 3 – Exp 4)

7.6 Comparison of LPR & galvanic current densities under uninhibited conditions

Figure 7-17 compares the LPR test (self corrosion) results and galvanic corrosion for the three zones. The total corrosion of the welded sections can be calculated from:

Total corrosion = Self corrosion + Galvanic. The corrosion rate is expressed as current density.

From the graph it was noticed that weld galvanic current density shows a cathodic response over the test period under static and flowing conditions. However, the galvanic current density of parent metal and HAZ were both anodic which indicates that parent metal and HAZ corroded preferentially with respect to WM. For the corrosion behaviour of the individual elements that comprise the weldment, a general observation indicated a rapid increase to the active value throughout the test. However, for the total corrosion with the galvanic contribution, there was a dramatic reduction only for the weld metal due to the weld metal galvanic behaviour (cathode).

The galvanic currents were high, as expected, at high rotation speed and the galvanic contributions to the corrosion of anodic weld segment was accordingly higher. Results obtained on different zones of the weldment show the effectiveness and protection achieved by changes in these galvanic current readings. Moreover, it was observed that the general corrosion rate is higher than the galvanic corrosion, which again indicates that galvanic current corrosion alone is sufficiently low enough not to necessitate to corrosion mitigation measures.

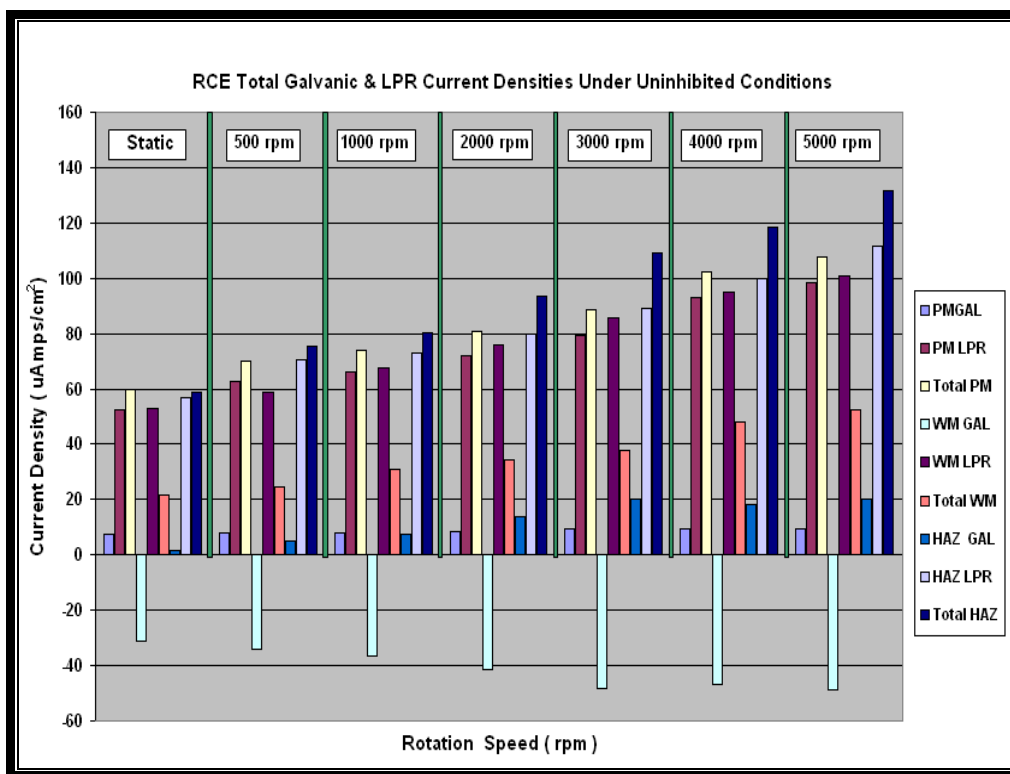


Figure 7-17: Comparison of LPR & galvanic current density under uninhibited conditions

7.7 Comparison of LPR & galvanic current densities under inhibited conditions

Figure 7-18 compares the LPR test (self corrosion) results and galvanic corrosion for the three zones with inhibitor under static and flowing conditions. Under static conditions, it was observed from the Figure that weld galvanic current density shows a

cathodic response. However, from the galvanic current density, the parent metal and HAZ behaves as an anode which indicates that parent metal and HAZ corroded preferentially with respect to WM. After the rotation speed was increased, both the galvanic currents and the self-corrosion rates for the weld metal and HAZ were found to increase with the shear stress and behave as an anode which indicates that weld metal and HAZ corroded preferentially with respect to PM.

In general, the inhibitor did not provide as much protection to the weld metal and HAZ as we expected and this is due to switching in the direction of the galvanic current flow when an inhibitor was added which resulted a preferential corrosion of the weld metal and HAZ with respect to parent metal. The reason for this galvanic current reversal was probably due to high flow rate conditions inducing a less compact/adherent inhibitor film on the weld metal and HAZ which might be removed, while films on the parent metal remained intact.

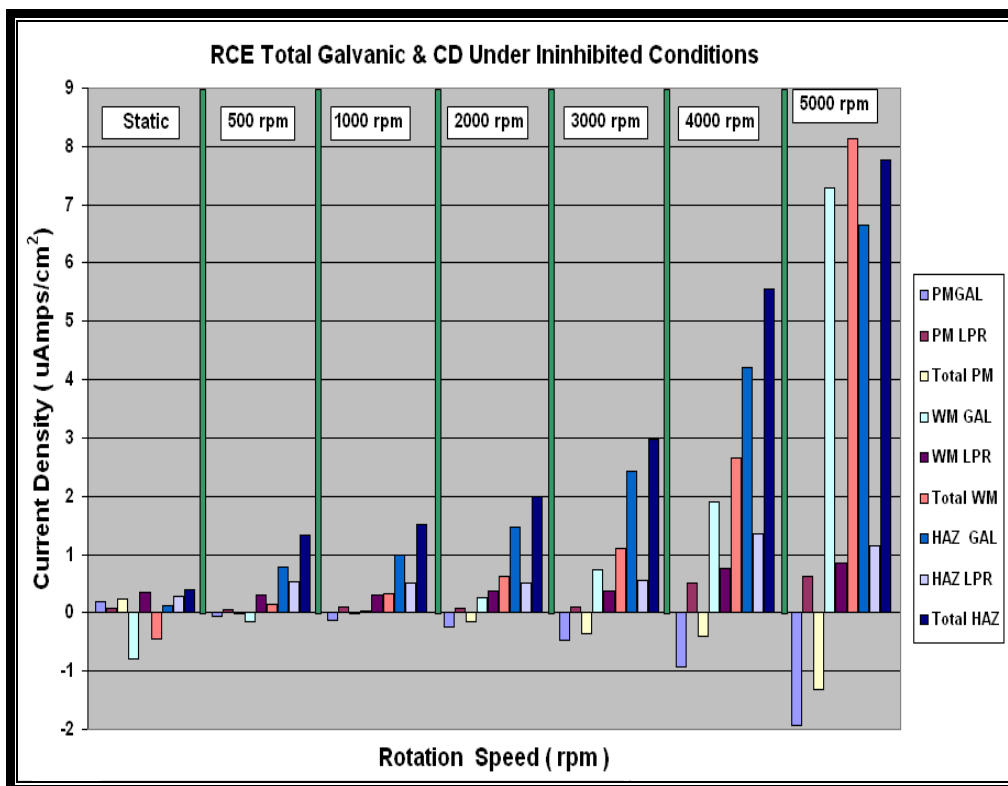


Figure 7-18: Comparison of LPR & galvanic current densities under inhibited conditions

8 Rotating Cylinder Electrode Results under High Temperatures (50⁰C & 70⁰C)

Since corrosion rates are thought to be affected by the formation of temperature dependent surface films, it was decided to compare the performance of inhibitor at various temperatures based on the degree of protection. The effects of hydrodynamics parameters on the corrosion rate of the weldment over a different range of temperatures (50⁰C and 70⁰C) were studied and covered the range from static to highly turbulent flow.

For inhibitor performance evaluation, corrosion rates were measured electrochemically at different rotating speeds, with the uninhibited baseline corrosion rate being measured first, followed by measurement of the inhibited corrosion rate.

8.1 Analysis of galvanic couple tests under uninhibited and CO₂ corrosion conditions at 50⁰C & 70⁰C

The idea for this test was to investigate corrosion currents between the individual elements that comprise the weldment at temperatures of 50⁰C and 70⁰C. Experiments at these two different temperatures were run for one day under uninhibited and sweet corrosion conditions through six different rotation speeds including static conditions. The galvanic test measurements were performed after 10 hours from the beginning of the test. The variation of galvanic current over the time is shown in Figures 8-1 and 8-2 for 50⁰ C and 70⁰ C respectively, while the corresponding current densities are given in Figures 8-3 and 8-4 for the two temperatures respectively.

It was clear from both experiments, that the same behaviour for the three weld regions was observed but with higher galvanic currents measured as the temperature increased. Both experiments showed that the first couple of (PM-HAZ) exhibited a positive current, which indicated the preferential corrosion of the parent metal with respect to HAZ. However, the second couple (WM-HAZ) had a negative current which meant that the HAZ corroded preferentially with respect to WM.

Figures 8-5 and 8-6 show the average galvanic currents for each region of the weld under two temperatures where the sum of the anodic currents from the parent metal and the HAZ is equal to the cathodic current on the weld metal. Despite the presence of a black surface deposit, assumed to be iron carbonate (FeCO_3), a significant increase in the galvanic corrosion current was observed at both temperatures.

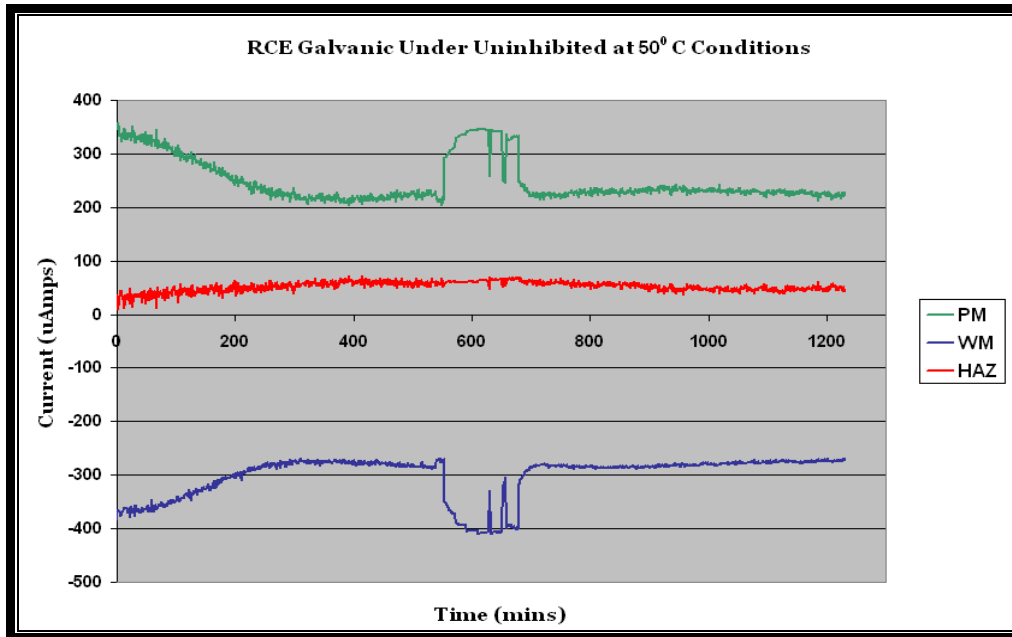


Figure 8-1: Galvanic current under uninhibited conditions

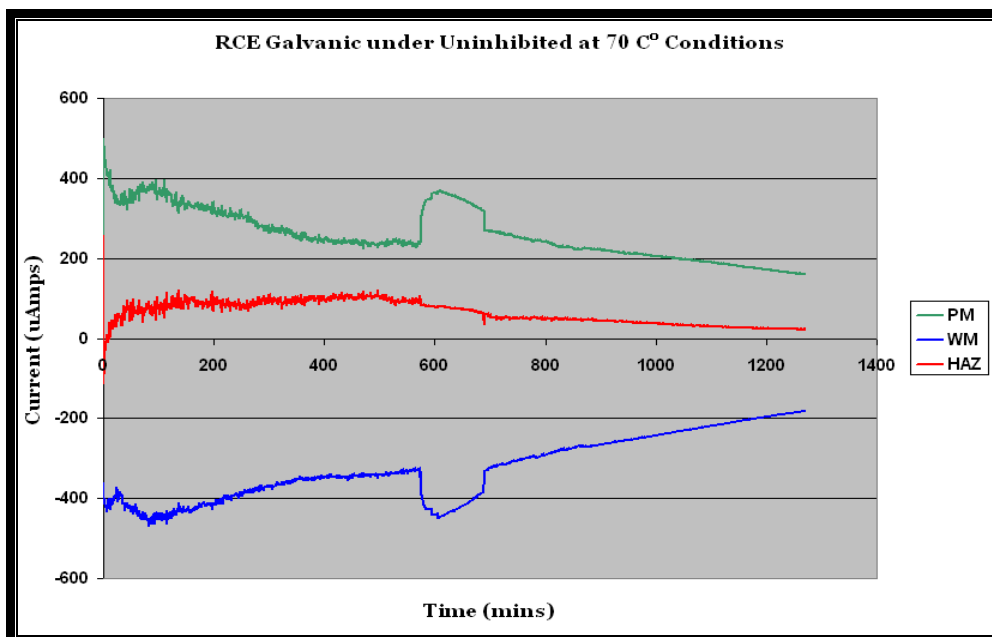


Figure 8-2: Galvanic current under uninhibited conditions at 70°C

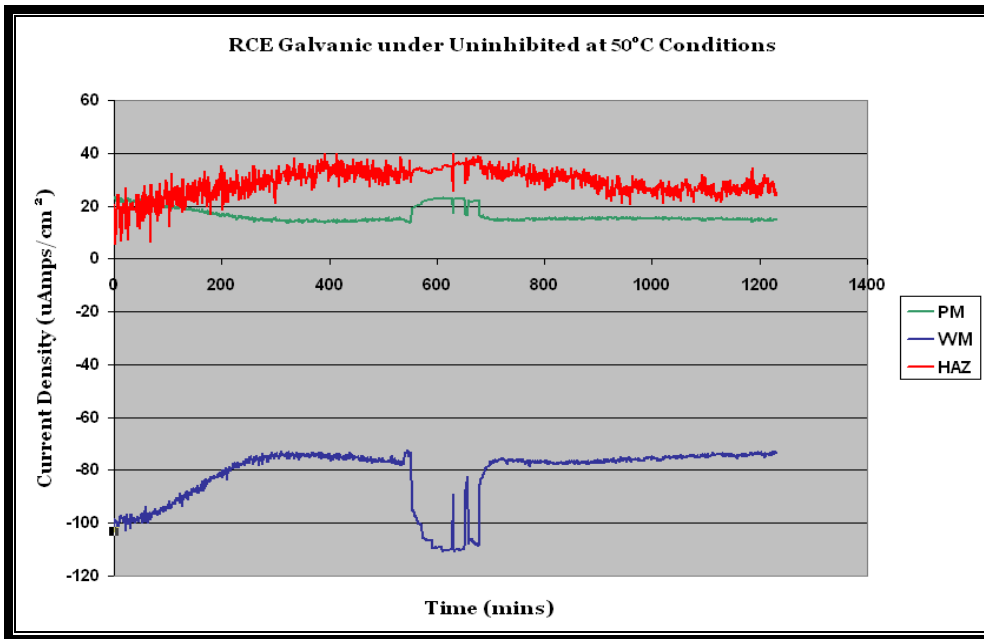


Figure 8-3: Galvanic current density under uninhibited conditions at 50°C

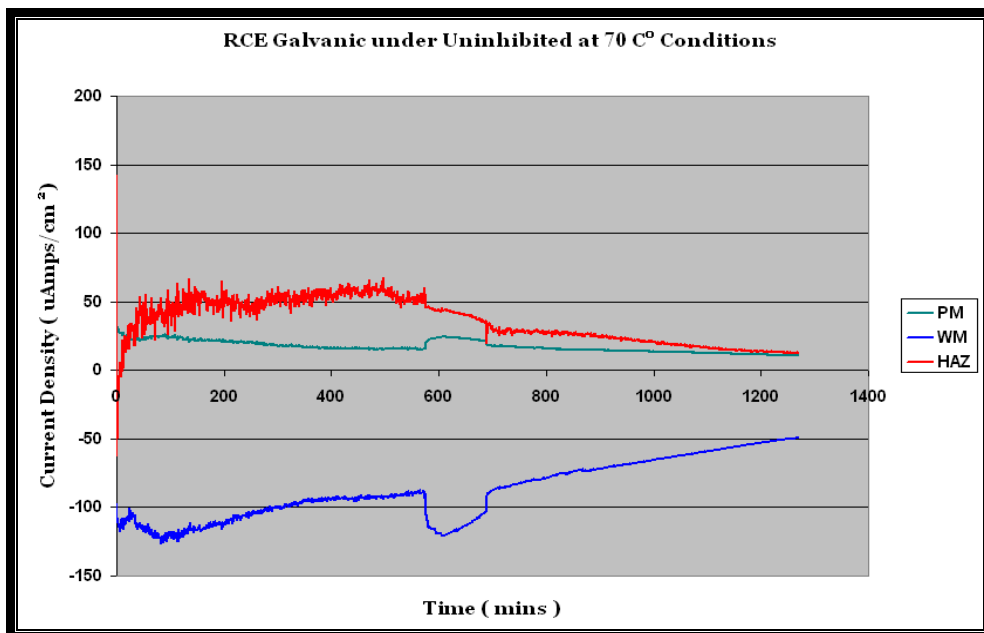


Figure 8-4: Galvanic current density under uninhibited conditions at 70°C

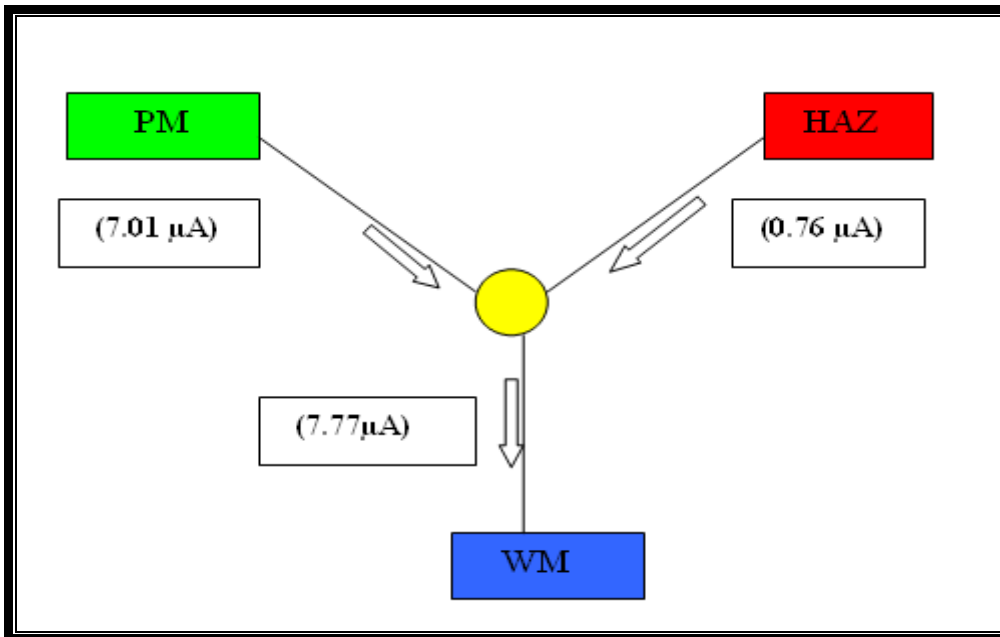


Figure 8-5: Average galvanic current under uninhibited at 50°C Conditions

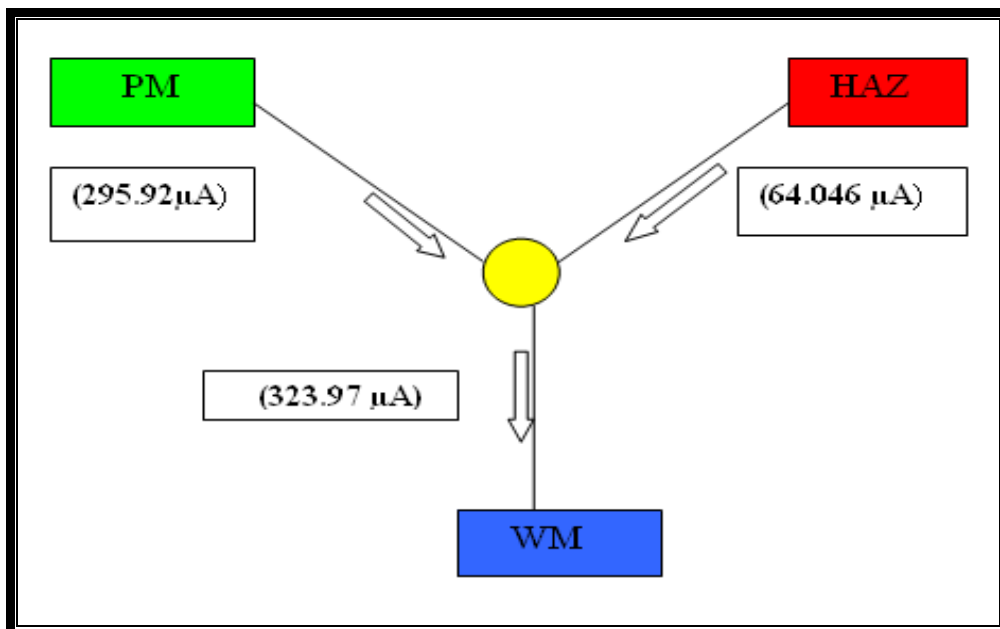


Figure 8-6: Average galvanic current under uninhibited at 70°C Conditions

8.2 Analysis of LPR tests under uninhibited and CO₂ corrosion conditions at 50°C & 70°C

The current density of each weld section at 50°C and 70°C are shown in Figures 8-7 and 8-8 respectively, while both Figures 8-9 and 8-10 show the self corrosion rates of each section. The results show the corrosion measurements over a range of shear stresses (1.4-48 Pa), assessed using the RCE. At higher temperatures, the measured values of corrosion rates showed a dependency on the rotation rate of the electrode, with the weld metal having the highest corrosion rate.

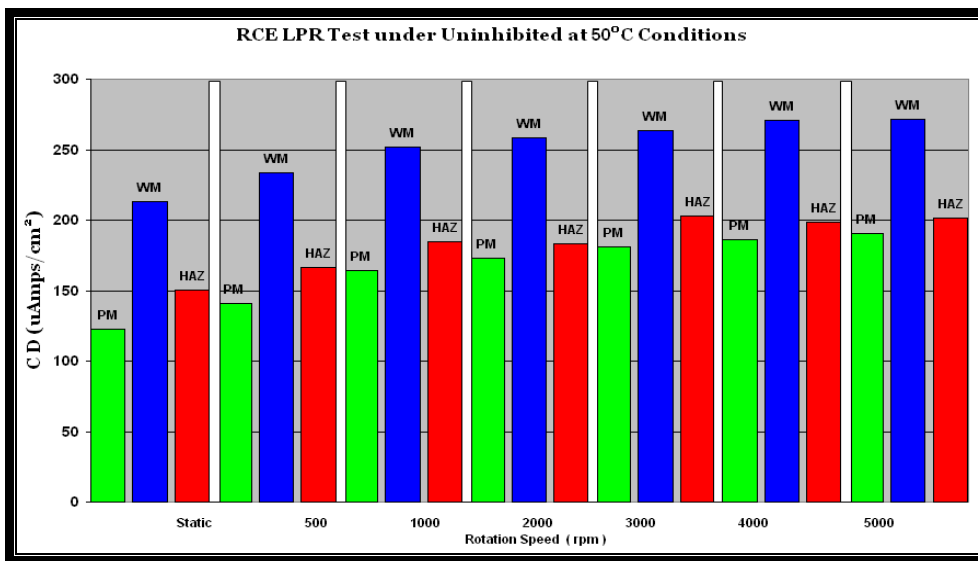


Figure 8-7: Current density under uninhibited and sweet corrosion at 50°C

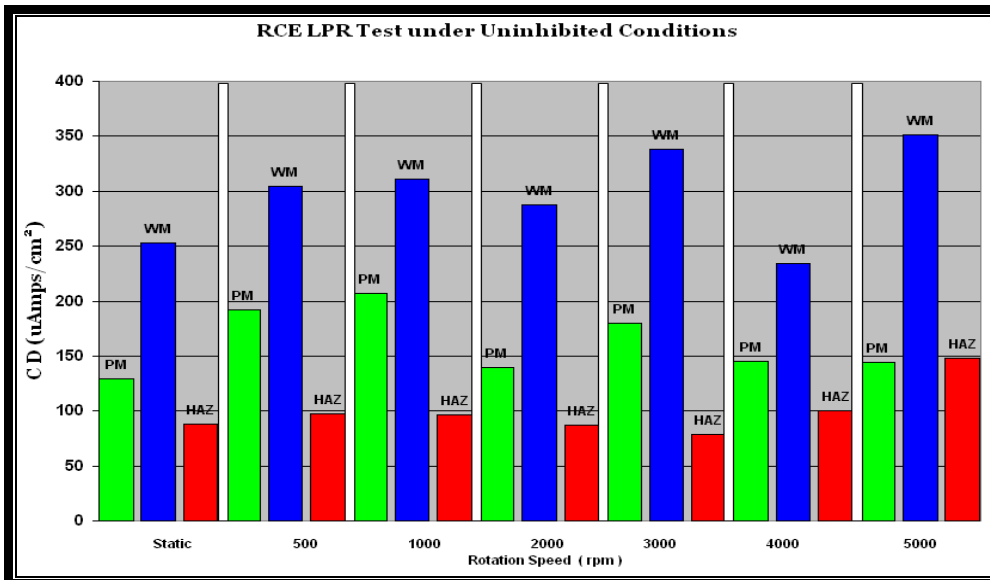


Figure 8-8: Current density under uninhibited and sweet corrosion at 70°C

The most important feature is that the measured values of corrosion rates for the weld regions are dependent on the temperature of the solution. As the temperature increases, the measured current density and corrosion rates also increase. Another feature that is also observed is the higher influence of the rotation rate of the electrode on the measured values of I_{corr} and self corrosion rates as the temperature increases. These features suggest that, as the temperature of the solution increases, the corrosion process occurring on the surface of the electrode exhibits a higher degree of diffusion or mass transfer.

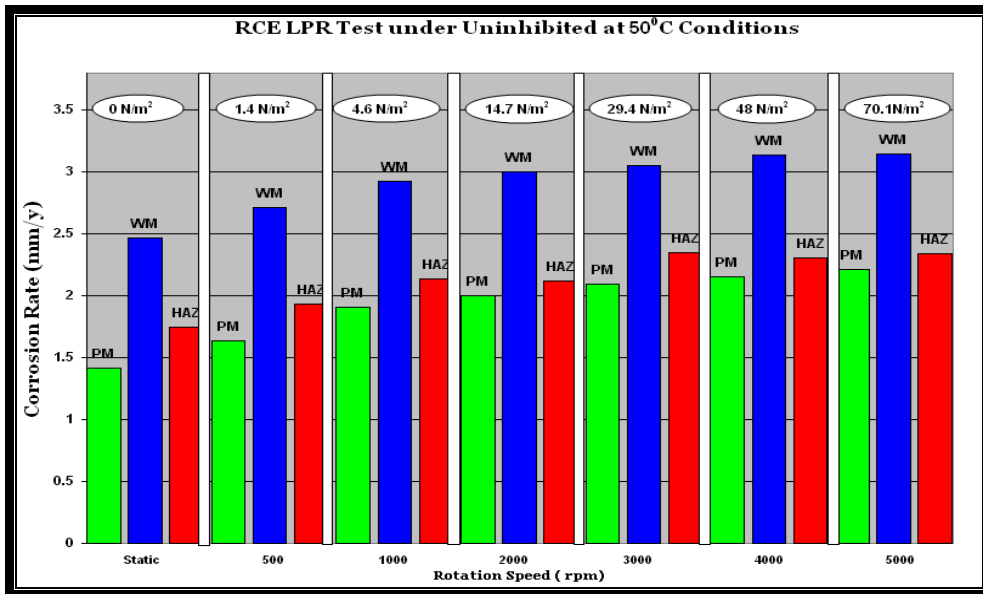


Figure 8-9: Corrosion rate under uninhibited and sweet corrosion at 50°C

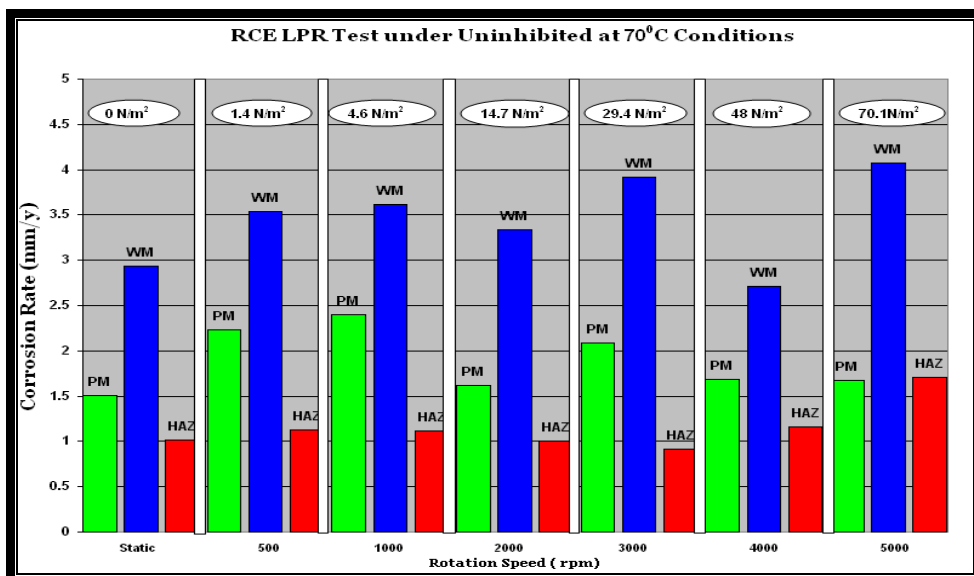


Figure 8-10: Corrosion rate under uninhibited and sweet corrosion at 70°C

8.3 Analysis of galvanic couple tests under inhibited and CO₂ corrosion conditions at 50°C & 70°C

This experiment was run for one day under inhibited and CO₂ conditions at different rotation rates. The variation of galvanic current over the time is shown in Figures 8-11 and 8-12. The corresponding current densities are given in Figures 8-13 and 8-14.

The first couple of PM-HAZ exhibited a negative current which indicated the preferential corrosion of the HAZ with respect to the parent metal. However, the second couple of WM-HAZ had a positive current, which meant that the WM corroded preferentially with respect to HAZ. Figures 8-15 and 8-16 show the average galvanic currents for each region of the weld and it can be seen that the sum of the anodic currents from the parent metal and the HAZ equal the cathodic current on the weld metal. It was observed that a switching behaviour in the direction of the weld segments currents occurred after the rotation of the electrode was stopped.

Both weld corrosion and inhibition were significantly affected by the hydrodynamics. Hence, the surface films on specific parts of the weld may have different morphologies and therefore may preferentially be removed under high shear stress conditions.

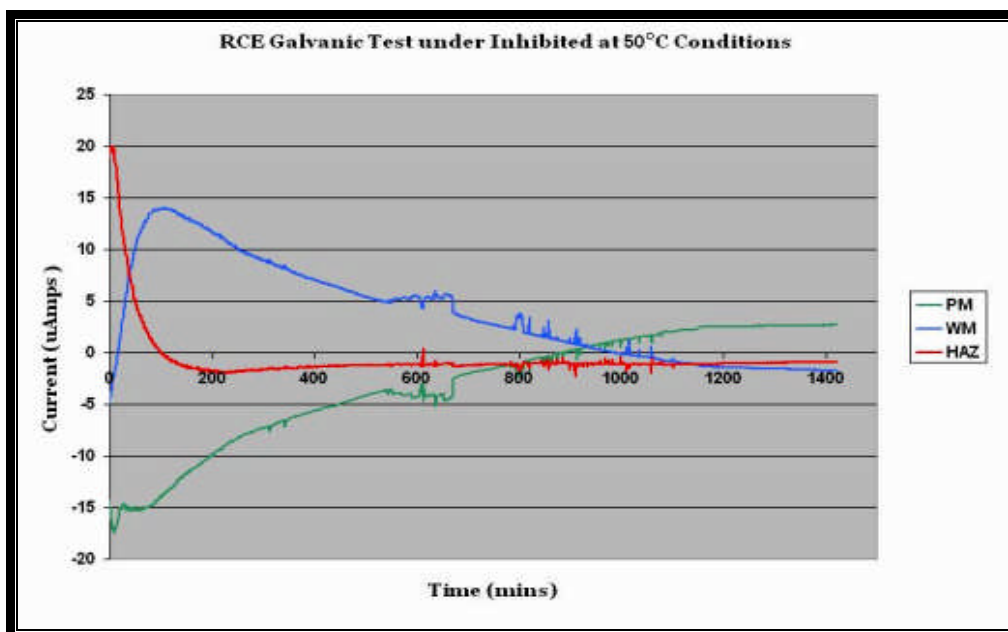


Figure 8-11: Galvanic current under inhibited conditions at 50°C

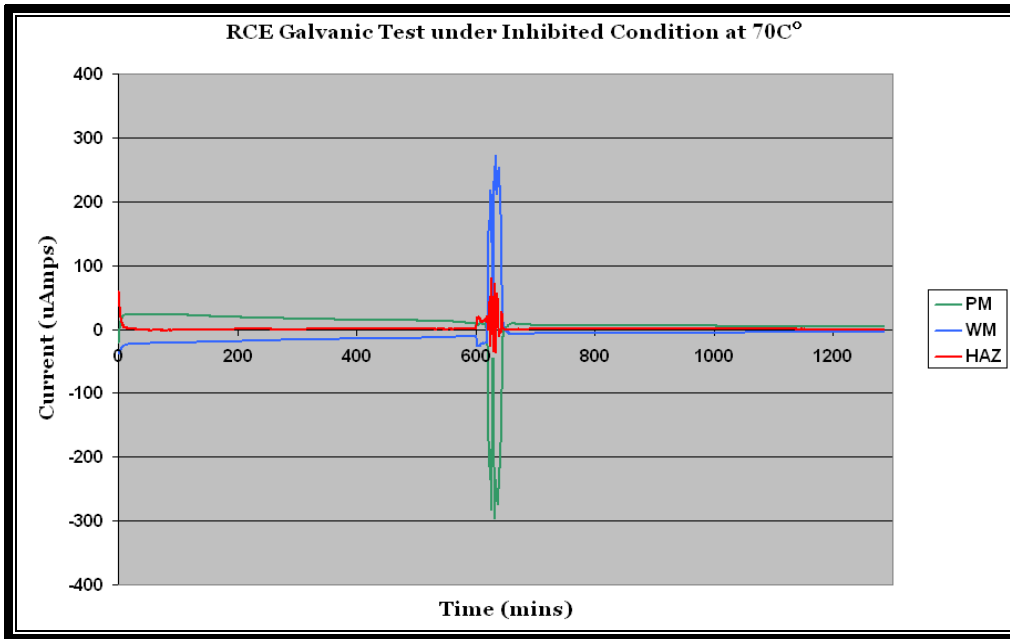


Figure 8-12: Galvanic current density under inhibited conditions at 70°C

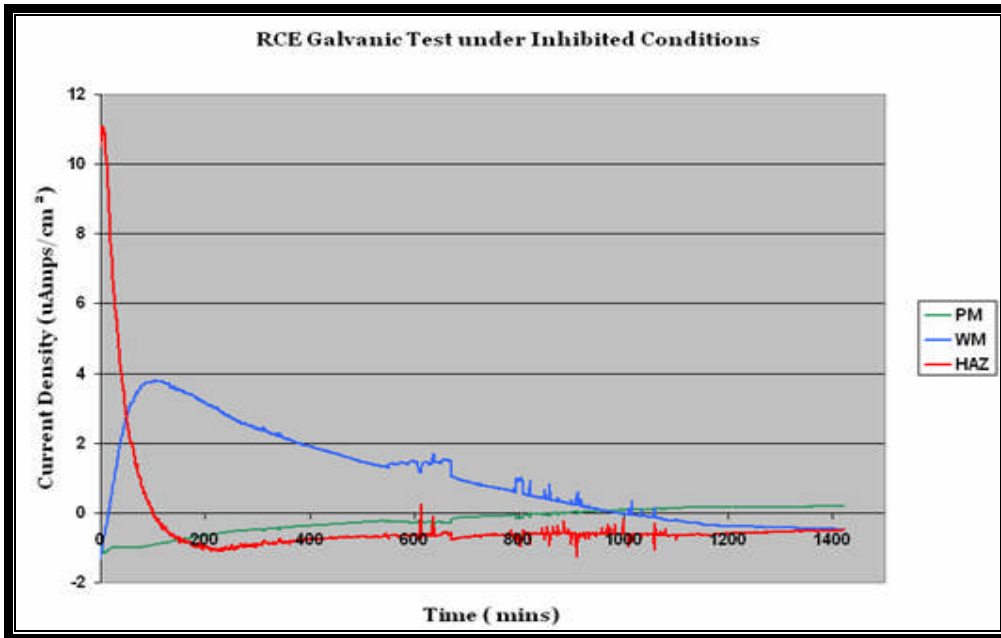


Figure 8-13: Galvanic current density under inhibited conditions at 50°C

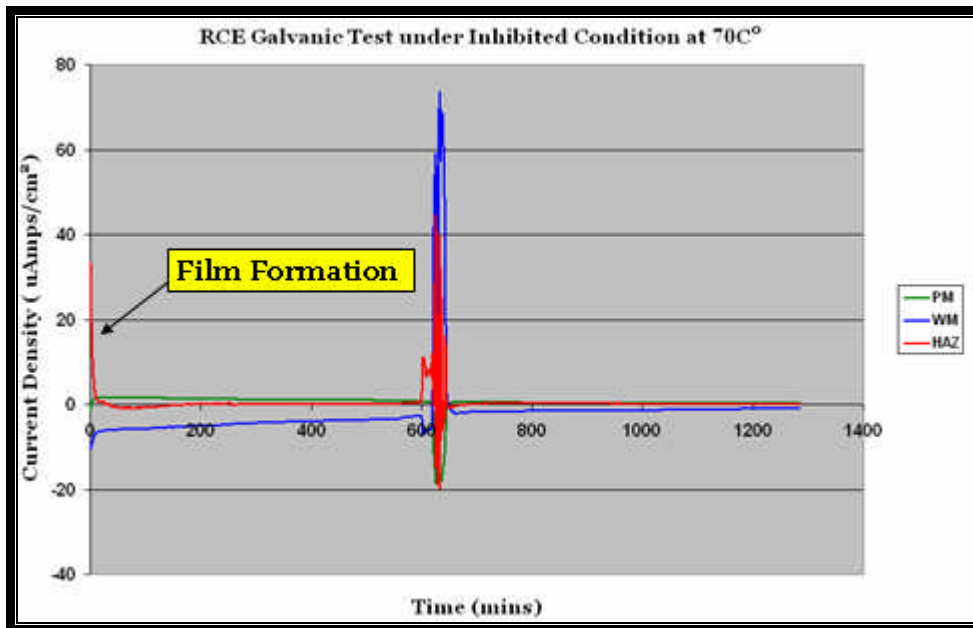


Figure 8-14: Galvanic current density under inhibited conditions at 70°C

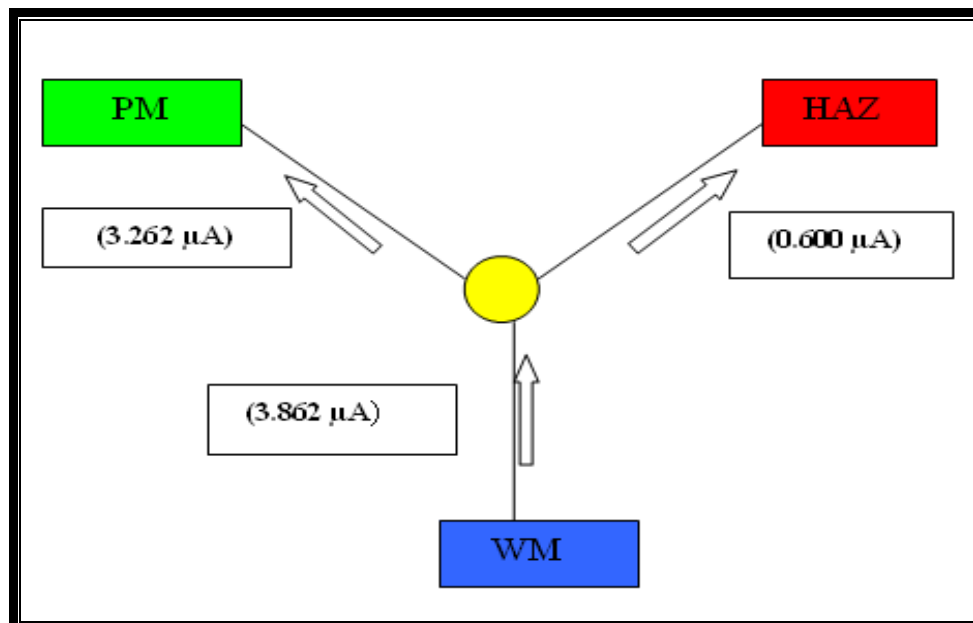


Figure 8-15: Average galvanic current under inhibited conditions at 50°C

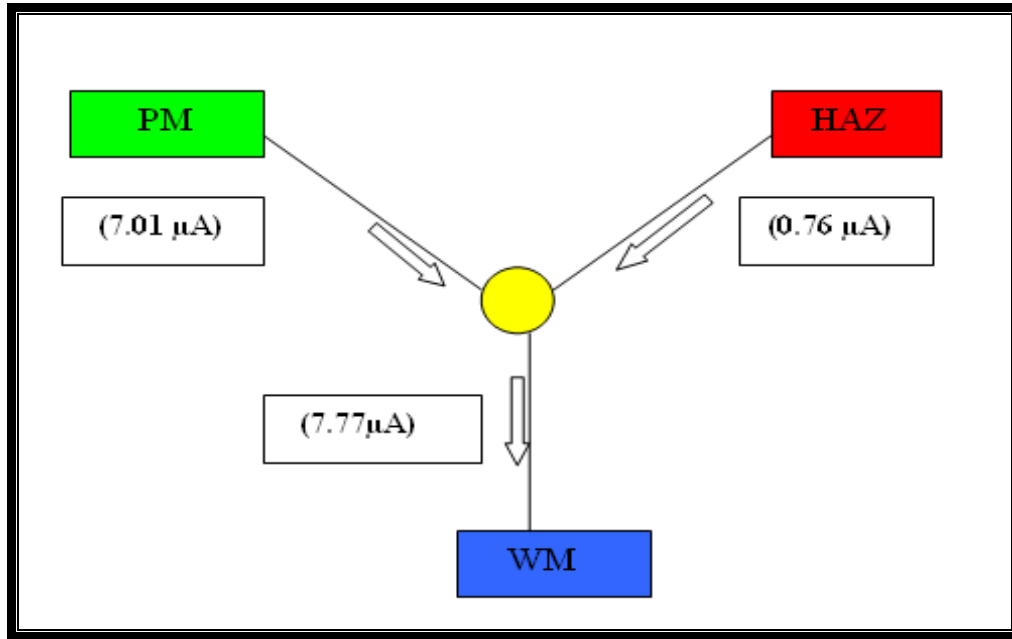


Figure 8-16: Average galvanic current under inhibited at 70°C Conditions

8.4 Analysis of LPR tests under inhibited conditions and CO₂ corrosion conditions at 50°C & 70°C

The current densities of each weld section in inhibited conditions at both temperatures are shown in Figures 8-17 and 8-18 respectively. Figures 8-19 and Figure 8-20 show the same results with self corrosion rates at both temperatures. The test results show corrosion inhibitor performance over a range of shear stresses (1.4-70 Pa).

It was clear that the corrosion inhibitor was less effective at high shear stress due to the increase in the corrosion rate, in the order HAZ > WM > PM as the rotational speed was increased. However, these results should be compared with corrosion rates with uninhibited conditions as shown in Figures 8-10 and 8-11. Despite the presence of an inhibitor, the measured corrosion rate showed a higher tendency to increase as the rotational speed of the electrode increases especially for the HAZ, while for the PM and WM the corrosion rate remains more or less constant for the rest of the tested rotation rates.

Similar results were obtained for 50°C but were even more pronounced at 70°C especially at 3000 rpm. This behaviour can suggest that an inhibitor film was protective and anchored to the surfaces. However, at 3000 rpm, the inhibitor began to be removed from the metal surface, an effect related to the observed increase in corrosion rate.

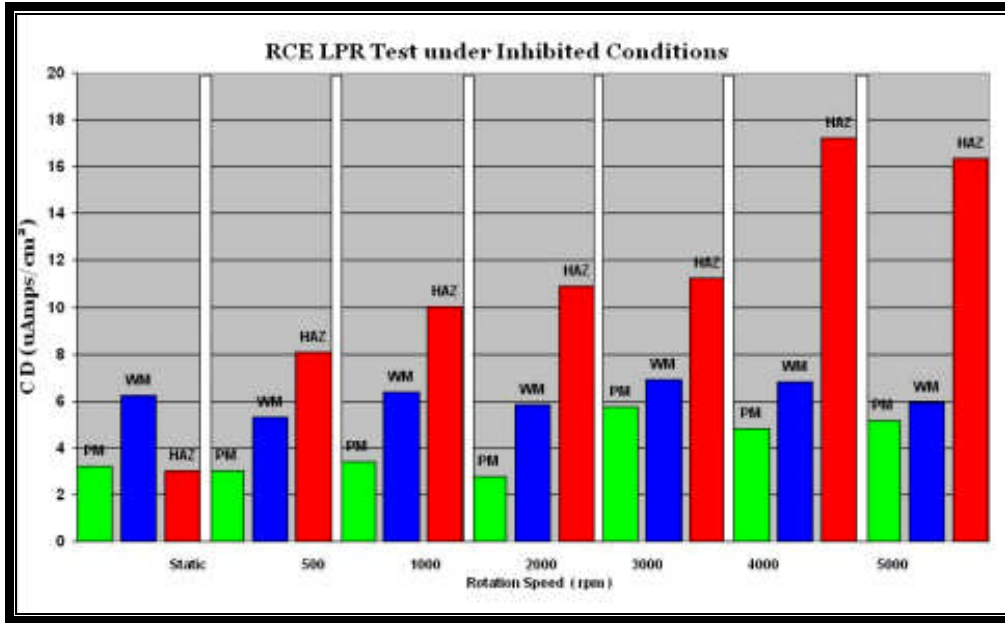


Figure 8-17: Current density under inhibited and sweet corrosion at 50°C

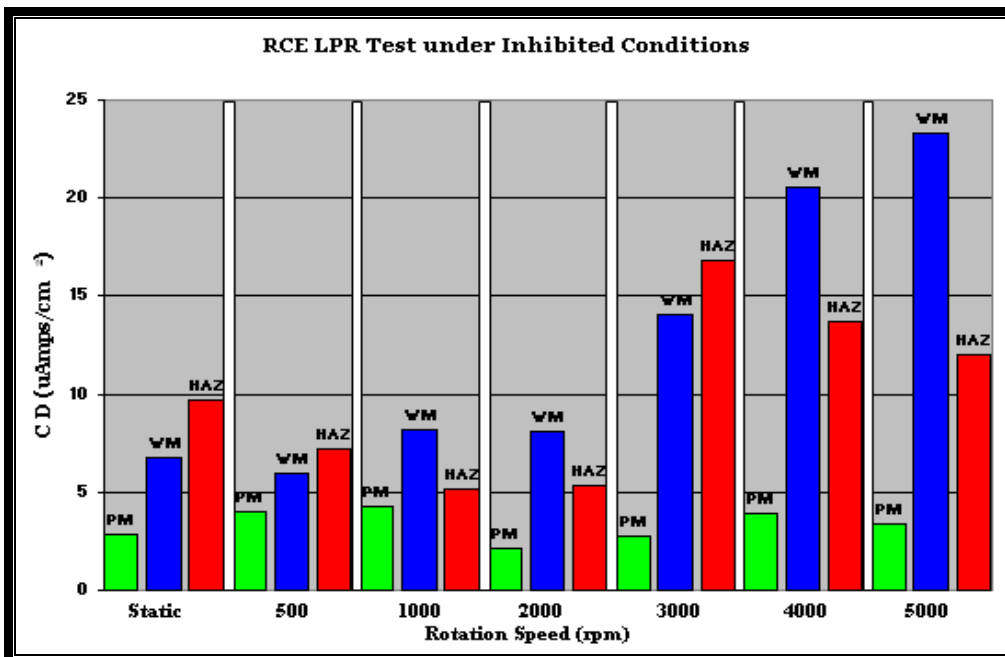


Figure 8-18: Current density under inhibited and sweet corrosion at 70°C

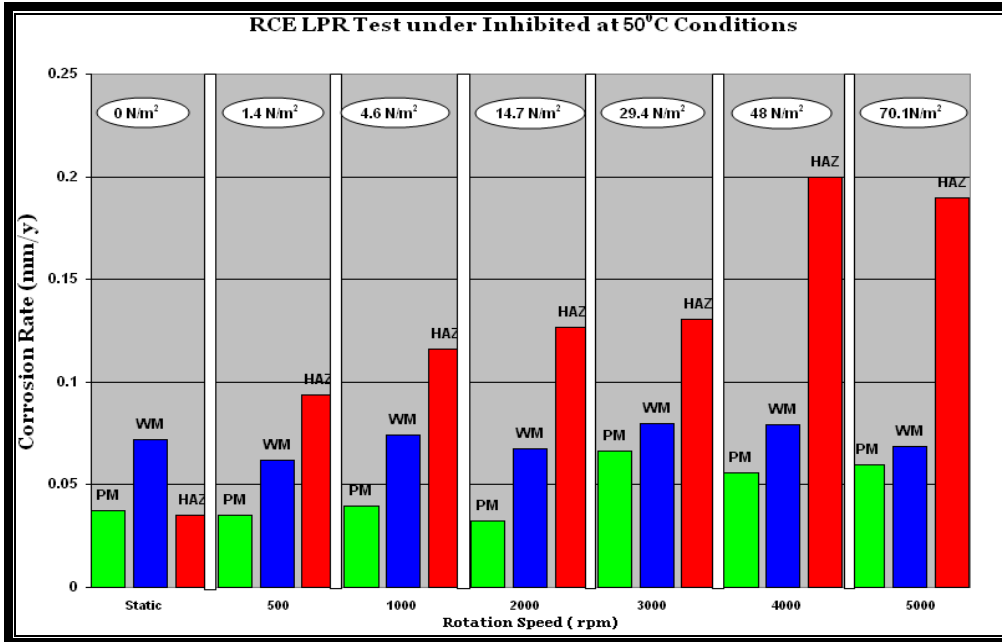


Figure 8-19: Corrosion rate under inhibited and sweet corrosion at 50°C

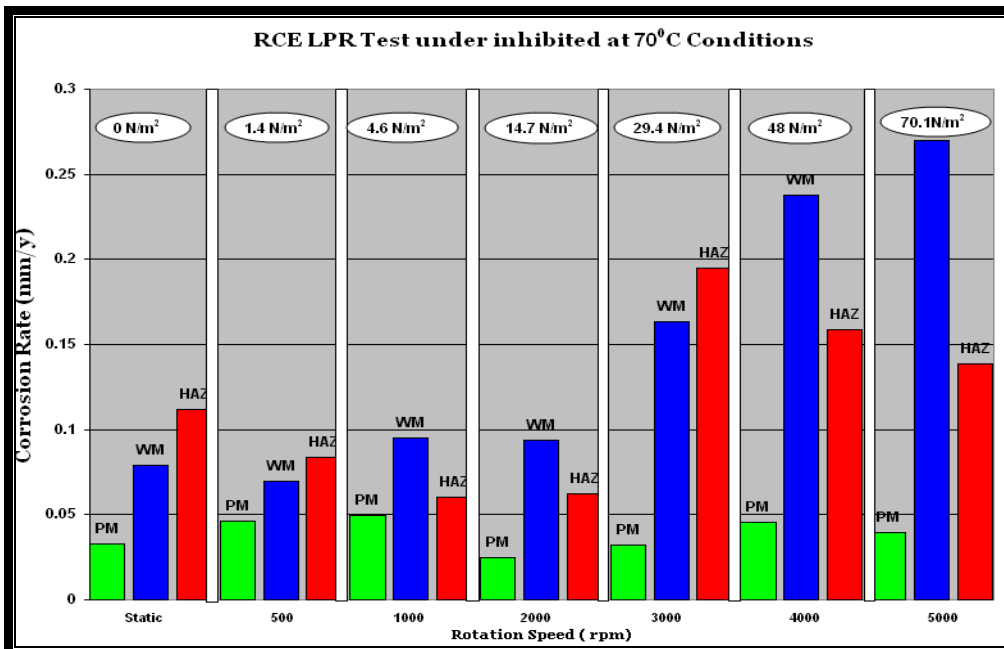


Figure 8-20: Corrosion rate under inhibited and sweet corrosion at 70°C

9 Electrochemical Impedance Spectroscopy

9.1 Preliminary Test

A preliminary test was carried out with a dummy cell in order to ensure that the instrument was functioning properly. The Nyquist impedance plot measured in Figure 9-1 in this test shows a semicircle. This means that this electrode reaction is controlled by only charge transfer. This behaviour can be interpreted according to a simple equivalent circuit model shown in Figure 3-3 (section 3.3.1).

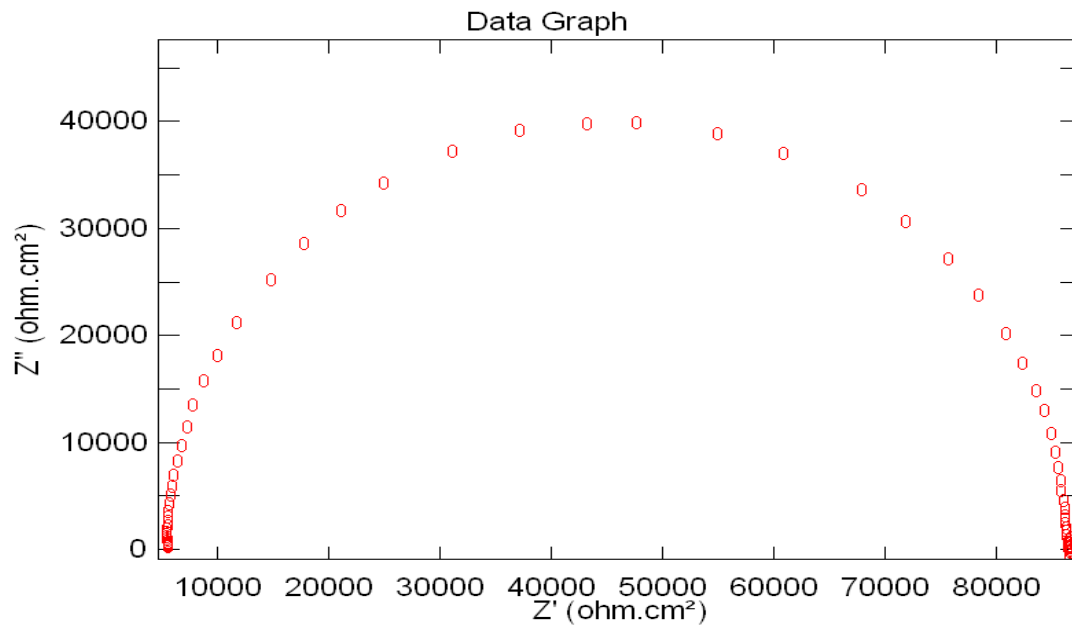


Figure 9-1: Nyquist plot for preliminary test carried out with a dummy cell

9.2 A.C. Impedance under Static & CO₂ Conditions

Figure 9-2 shows Nyquist impedance plot obtained immediately after the sample was immersed in the electrolyte saturated with CO₂ for 20 minutes. The graph shows a single depressed semicircle with its center under the real axis. This means that the electrode reaction is controlled by only charge transfer. There is no evidence of the formation of a protective FeCO₃ film because there is just one semicircle in the plot. It can be noticed that the solution resistance is very small (3-8Ω.cm²) due to high

conductivity of the solution (3.5% NaCl) while, the charge transfer resistance R_{ct} is approximately ($560 \Omega \cdot \text{cm}^2$) from the plot.

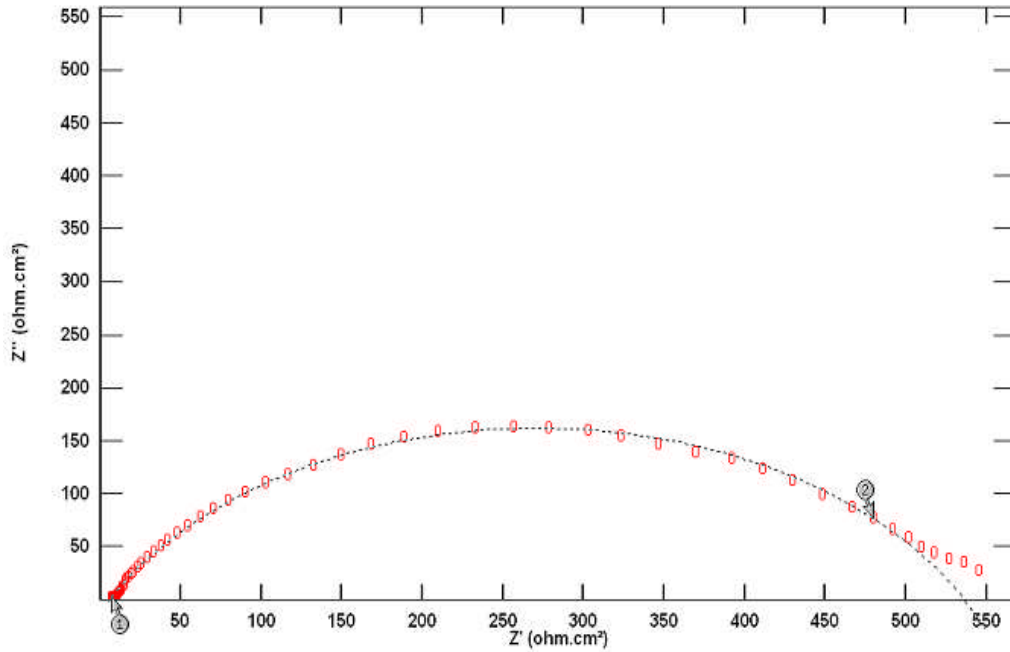


Figure 9-2: Nyquist plot of carbon steel under static and CO_2 conditions at initial stage of immersion

Typically, 10 hours after the beginning of the experiment, a second EIS measurement was conducted. A black film was observed by visual examination on the electrode surface at the end of this exposure time. Figure 9-3 shows one depressed semicircle with a long tail. The tail is inclined at an angle of 45° to the real axis at the very low frequencies. It can also be observed that the diameter of the semicircle increased with increasing time of exposure compared with Figure 9-2 with R_{ct} increased to ($700\Omega \cdot \text{cm}^2$). This means that the corrosion rate become lower at longer exposure time.

This behaviour suggests that diffusion through a film took place on the electrode surface. This film seems to provide protection to the metal by restricting the mass transfer of reactant and products between bulk solution and the metal, which was represented by an increase in the corresponding R_{ct} values.

This could be due to the formation of the thin layer of corrosion product, with a resistance that was much smaller than the charge transfer resistance. The semi circle representing the corrosion product film merged with the charge transfer loop and hence the EIS data are described by a simple capacitive semicircle

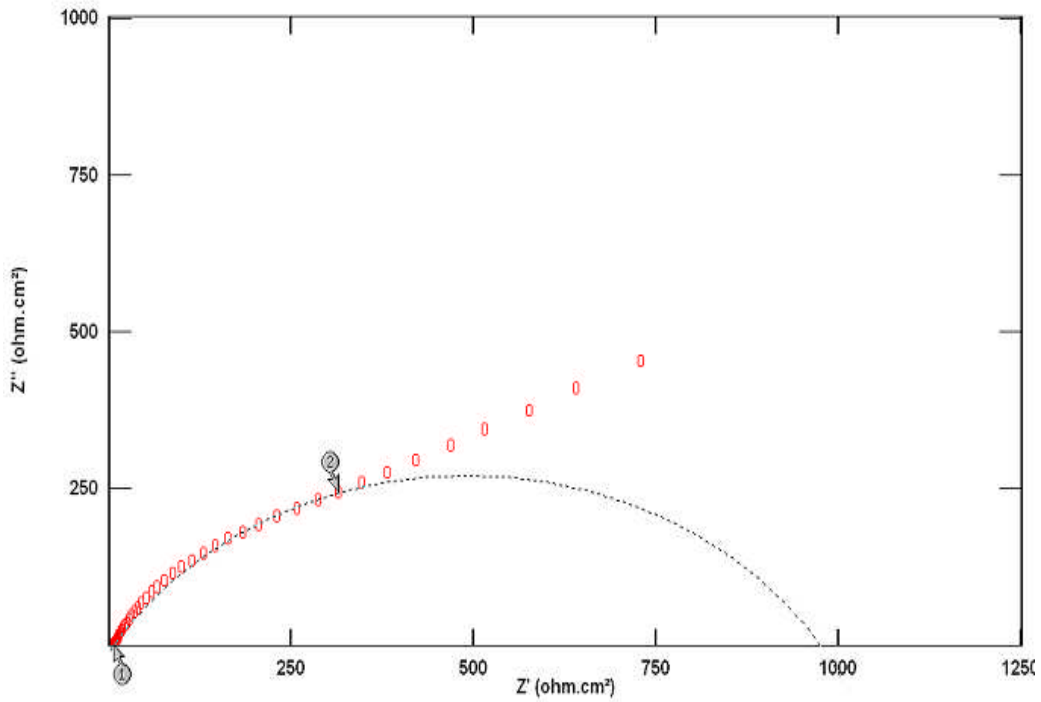


Figure 9-3: Nyquist plot of carbon steel under static and CO₂ conditions after 10 hour of immersion

9.3 A.C. Impedance under flowing & CO₂ conditions with the presence of inhibitor

Continuing the flow effect, study by AC impedance measurements were taken under flowing conditions in CO₂ saturated solution of 3.5% artificial sea water, at temperatures of 50⁰C and 70⁰C, at a rotation speed of 500 rpm with the presence of 30 ppm of green inhibitor. The aim was to make the use of this powerful technique to confirm the results obtained by the other techniques and extend our knowledge about CO₂ corrosion under inhibited and flowing conditions.

The impedance spectra measured for the three weld regions are presented as Nyquist plots. The inhibitor was injected into the cell before starting the test. The most successful application of EIS for evaluating inhomogeneous films on metal surfaces or rough and porous electrode coated metals was reported by Walter [129] who shows the proper equivalent circuit.

The film capacitance was interpreted as the combined capacitance of the electrical capacitor consisting of the metal and electrolyte, C_{dl} and the capacitance of the intact film, C_f . Therefore, two semicircles which present the relaxation processes of the film capacitor and the double layer appear in the Nyquist plot.

9.3.1 EIS for Parent metal at 50⁰ C and 70⁰ C

The impedance diagrams for the PM electrode sample after 10 hours of immersion time under rotational speed of 5000 rpm at 50⁰ C and 70⁰ C are presented in the Nyquist plots Figure 9-4 and Figure 9-5 respectively, where the real and imaginary impedance components are plotted over the range of frequencies used.

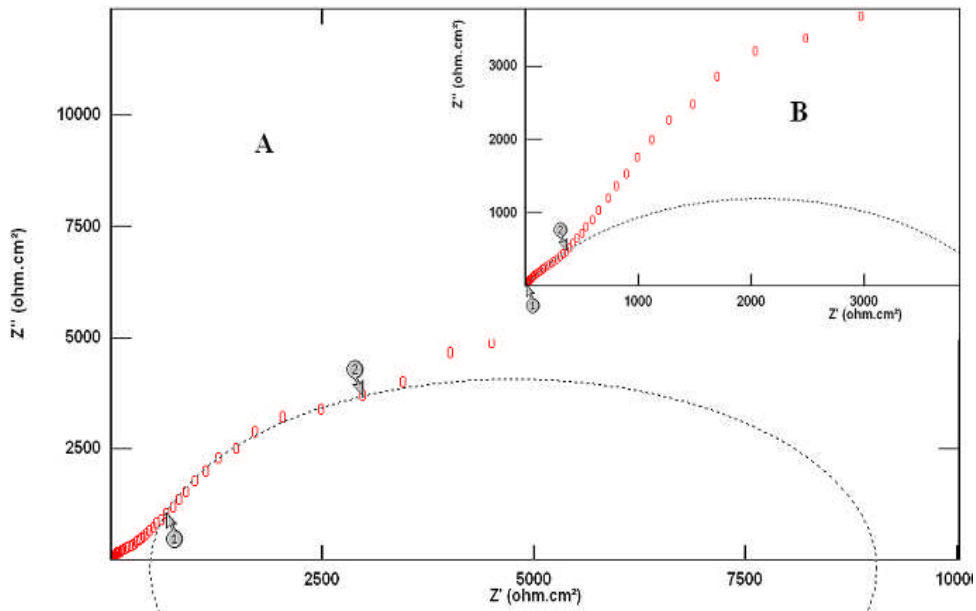


Figure 9-4: A) Nyquist plot for PM at 50⁰C under Flowing and CO₂ conditions after 10 hour of immersion, B) higher magnification of the high frequency region

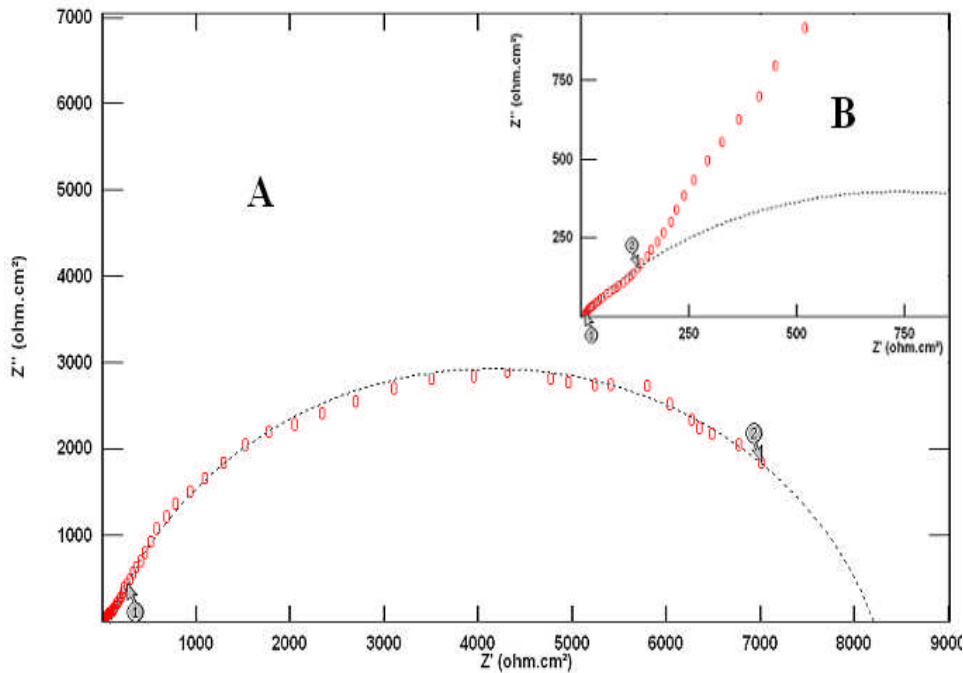


Figure 9-5: A) Nyquist plot for PM at 70⁰C under flowing and CO₂ conditions after 10 hour of immersion, B) higher magnification of the high frequency region

The shape of Nyquist plot for both graphs displays part of another semicircle at high frequency, which may represent the formation of an inhibitor film. This is in addition to a semicircle for the charge transfer process and diffusion tail at the low frequency region. It can be observed that at 50⁰C the film inhibitor (R_f) exhibited better inhibition performance than at 70⁰C. These could result from the porous inhibitor film formed on the metal surface. The diffusion impedance element suggests that the electrochemical processes might be controlled by the active species diffusing to the metal surface or corrosion products diffusing away from the metal surface through the inhibitor film.

Figures 9-6 and 9-7 summarise the findings from the impedance plots at low frequency region, including the solution resistance, charge transfer resistance (R_{ct}), cell capacitance (C_{dl}) and corrosion rates are listed. The charge transfer resistance R_{ct} , was evaluated by completing the lower frequency region to give a full semi circle. The fitting results clearly for the second loop at low frequency regions show that there was no significant difference of the R_{ct} between the two temperatures. Findings from the impedance plots at high frequency regions due to the formation of inhibitor film summarised in section 10.5 Figure 10-11.

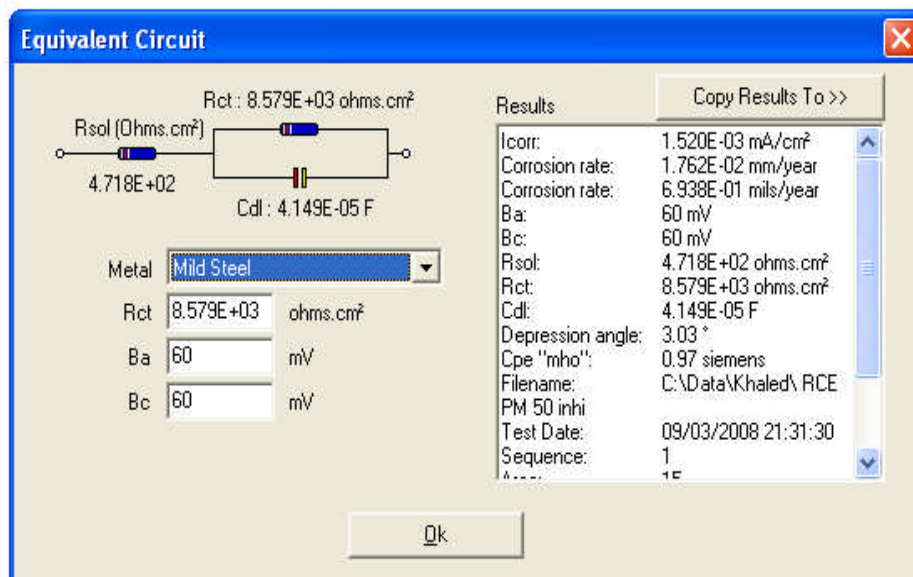


Figure 9-6: shows circuit parameters for PM at 50⁰C under inhibited and flowing conditions at lower frequency region

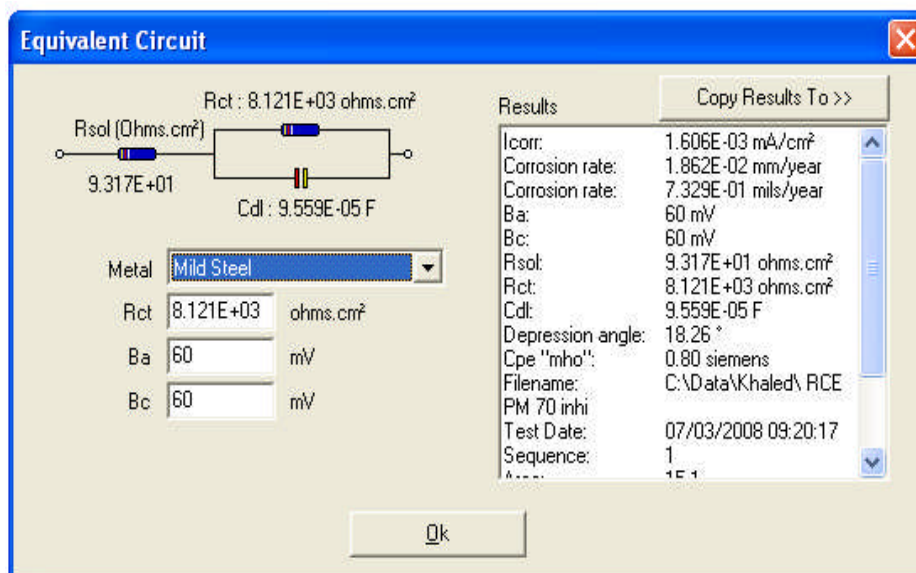


Figure 9-7: shows circuit parameters for PM at 70⁰C under inhibited and flowing conditions at lower frequency region

9.3.2 EIS for Weld Metal at 50⁰ C and 70⁰ C

The impedance diagrams obtained at various temperatures for the weld metal with inhibitor are presented as Nyquist plots in Figure 9-8 and Figure 9-9. It was observed that the Nyquist impedance plot measured at 50⁰C showed two semi circles. Similar findings were also observed at 70⁰C.

The increase in the size of the capacitive loop at 70⁰C can be connected to an improvement of the inhibitor film properties due to an increase in the speed of film formation. One can conclude that the growth of an inhibitor film on the metal surface seems to be affected by increasing the temperature.

The findings gathered from Figure 9-8 and Figure 9-9 were listed in Figures 9-10 and 9-11 respectively. It was observed at 50⁰C for the weld metal, a very low film resistance which caused a decrease of the R_{ct} and consequently an increase of the corrosion rate. Opposite findings were found at 70⁰C.

The noticeable differences in inhibitor film resistance (R_f) as well as R_{ct} , allows us to indicate that it has been better performance for the weld metal as the temperature was raised.

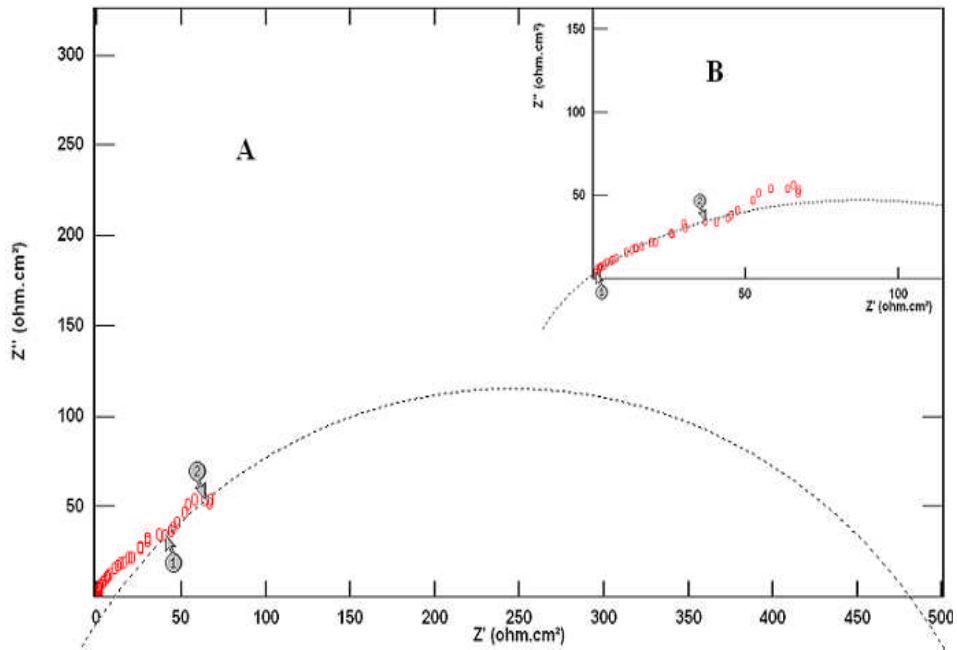


Figure 9-8: A) Nyquist plot for WM at 50^oC under flowing and CO₂ conditions after 10 hour of immersion, B) higher magnification of the high frequency region

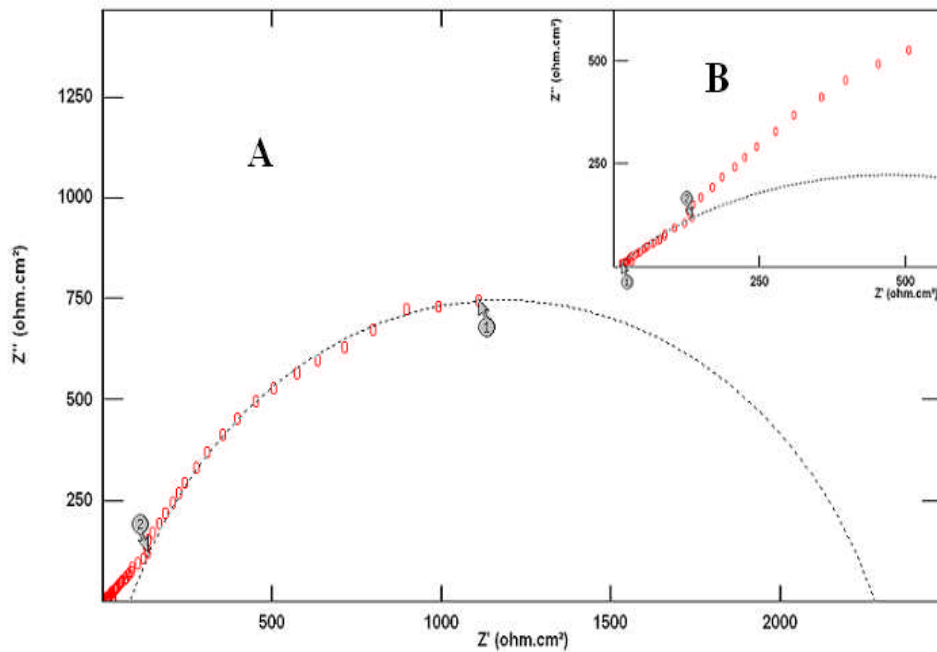


Figure 9-9: A) Nyquist plot for WM at 70^oC under flowing and CO₂ conditions after 10 hour of immersion, B) higher magnification of the high frequency region

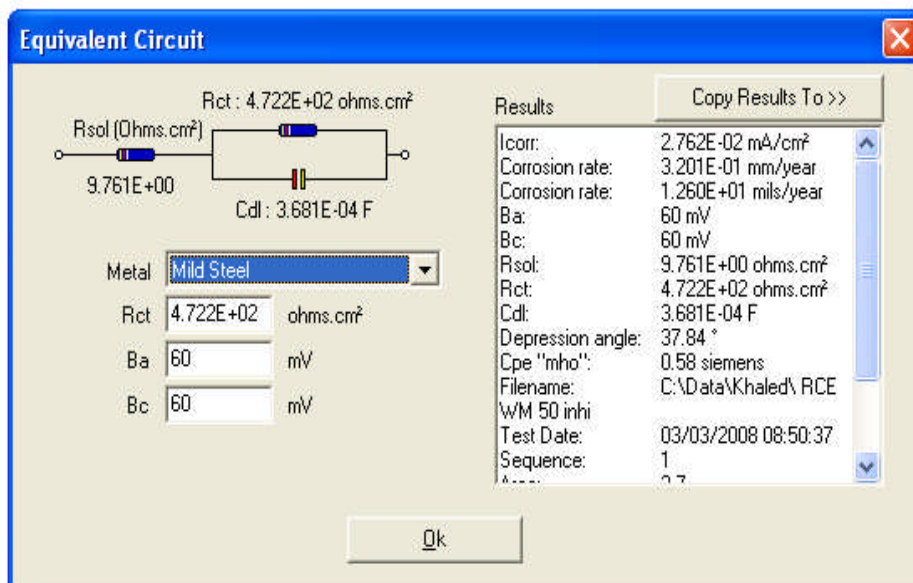


Figure 9-10: Shows circuit parameters for WM at 50°C under inhibited and flowing conditions

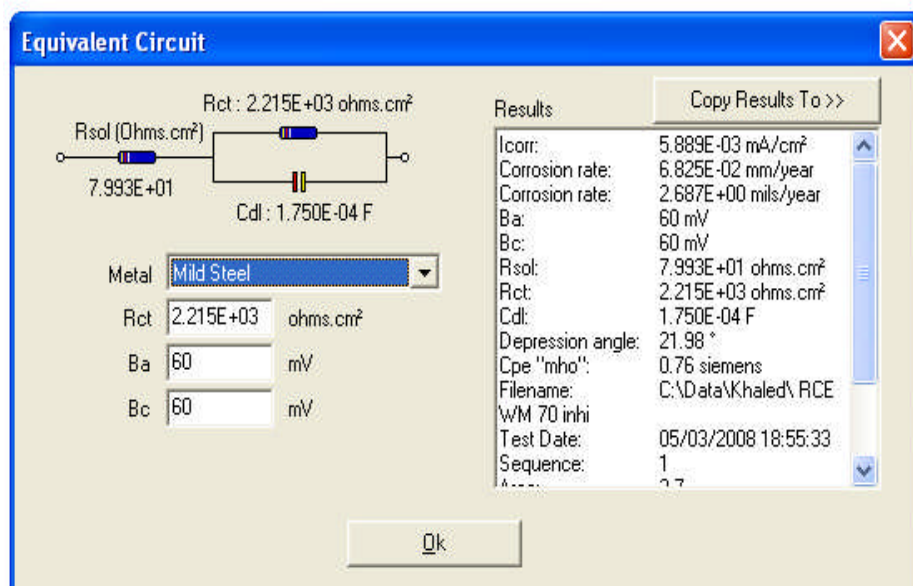


Figure 9-11: Shows circuit parameters for WM at 70°C under inhibited and flowing conditions

9.3.3 EIS for HAZ metal at 50⁰ C and 70⁰ C

Figure 9-12 and Figure 9-13 represents the AC impedance responses taken after 10 hours of immersion at 5000 rpm for HAZ at two different temperatures. Both graphs comprise two merged semicircles. This can be seen more clearly in the results at 70⁰C in Figure 9-13.

Figure 9-14 and Figure 9-15 sums up information obtained from the graphs. In those figures the charge transfer resistance R_{ct} , the cell capacitance C_{dl} and the corrosion rate are listed for different temperatures.

There was no significant difference of the R_{ct} between the two temperatures. However, at 70⁰C the inhibitor film resistance (R_f) clearly increase with temperature. This may indicate that the inhibitor film was promoted at higher temperature.

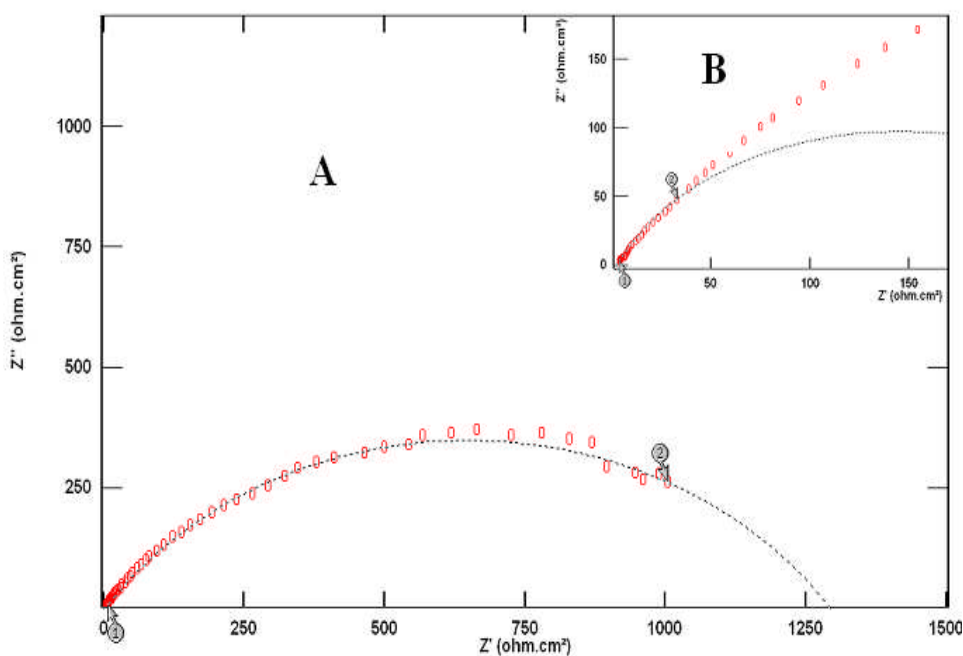


Figure 9-12: Nyquist plot for HAZ under flowing and CO₂ conditions after 10 hour of immersion at 50⁰C

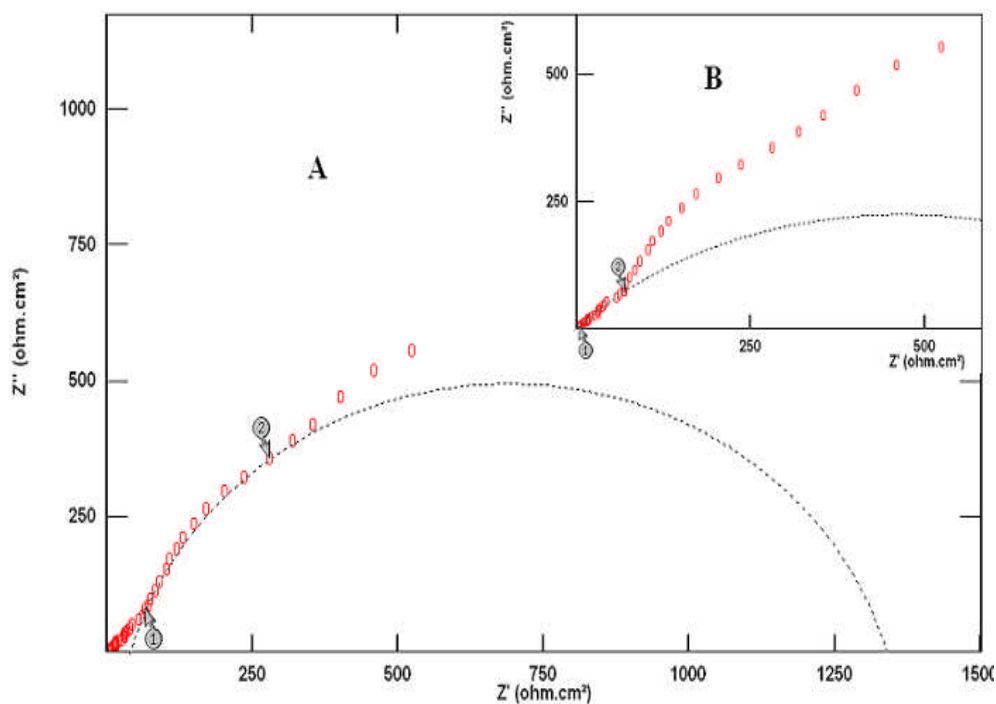


Figure 9-13: Nyquist plot for HAZ under flowing and CO₂ conditions after 10 hour of immersion at 70°C

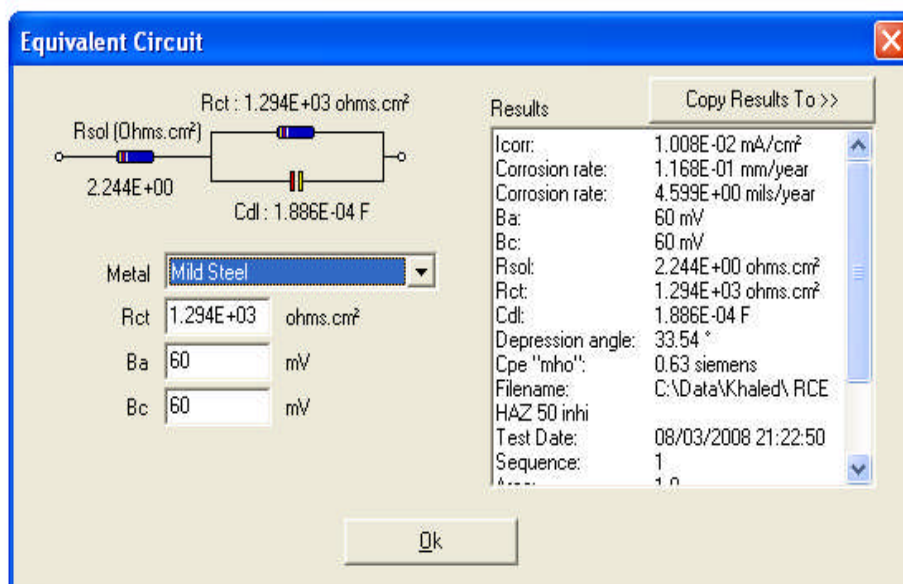


Figure 9-14: Shows circuit parameters for HAZ at 50°C under inhibited and flowing conditions

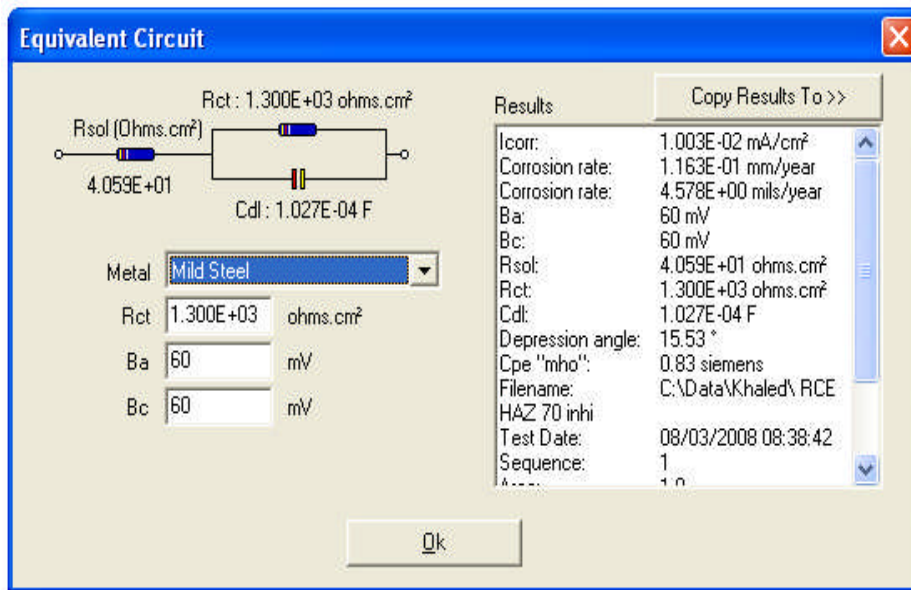


Figure 9-15: Shows circuit parameters for HAZ at 70°C under inhibited and flowing conditions

10 Discussion

The results and their interpretation were considered in some detail in the various sections of chapter 5. As already highlighted in the introduction of this thesis, carbon dioxide (CO₂) induced corrosion of weldments is of considerable practical significance. Hence the objective of this discussion is to bring together the major findings of the experimental work and place them in the context of the literature presented in the survey in chapter 1. The corrosion conditions were divided into two categories. The first was that of stagnant conditions, where the solution and the electrode were not subject to external agitation or movement. The second was that subjected to rotation where the corrosion rate values were much higher than those in stagnant conditions.

The effects of various hydrodynamics parameters on the corrosion rates of low carbon steel in CO₂ environments were studied. Two different flow geometries, a flow channel and a rotating cylinder electrode, were used to simulate laminar and turbulent flow, respectively. Comparisons were made over a wide range of parameters such as temperature and flow.

The hydrodynamic conditions studied covered the range from static to highly turbulent flow. The corrosion process was monitored by using three common electrochemical techniques: linear polarisation, galvanic current and electrochemical impedance spectroscopy (EIS). Comparison of the two flow geometries was carried out in terms of hydrodynamics, mass transfer and CO₂ corrosion.

This work was undertaken to study the use of electrochemical techniques or methods to determine the performance and effectiveness of the corrosion inhibitor and their effects on the weld sections of the steel by simulating conditions similar to actual conditions in down-hole tools / steel pipes. This project goes into more detail by analysing fully the three weld sections (parent metal, weld metal and heat affected zone).

10.1 Galvanic Current Measurements

10.1.1 Uninhibited Conditions

As shown in Figure 7-1, the parent metal and the HAZ were preferentially corroded in all the cases of galvanic corrosion investigated. This was considered to be a desirable situation where the localised corrosion of the weld was minimised. What is important in this experiment is the noticeable gradual decrease in galvanic current during the initial 10 hours pre-corrosion, which has to be associated with the formation of the stable protective film.

From Figure 10-1, it can be observed that as rotational speed was increased, the galvanic currents were found to increase with the shear stress so that the film of corrosion products which normally provide protection, are thinned or even partially removed causing high corrosion rates. Visual examination of samples after the test completion indicated that the three samples were partially covered with the protective film and so unable to provide complete protection.

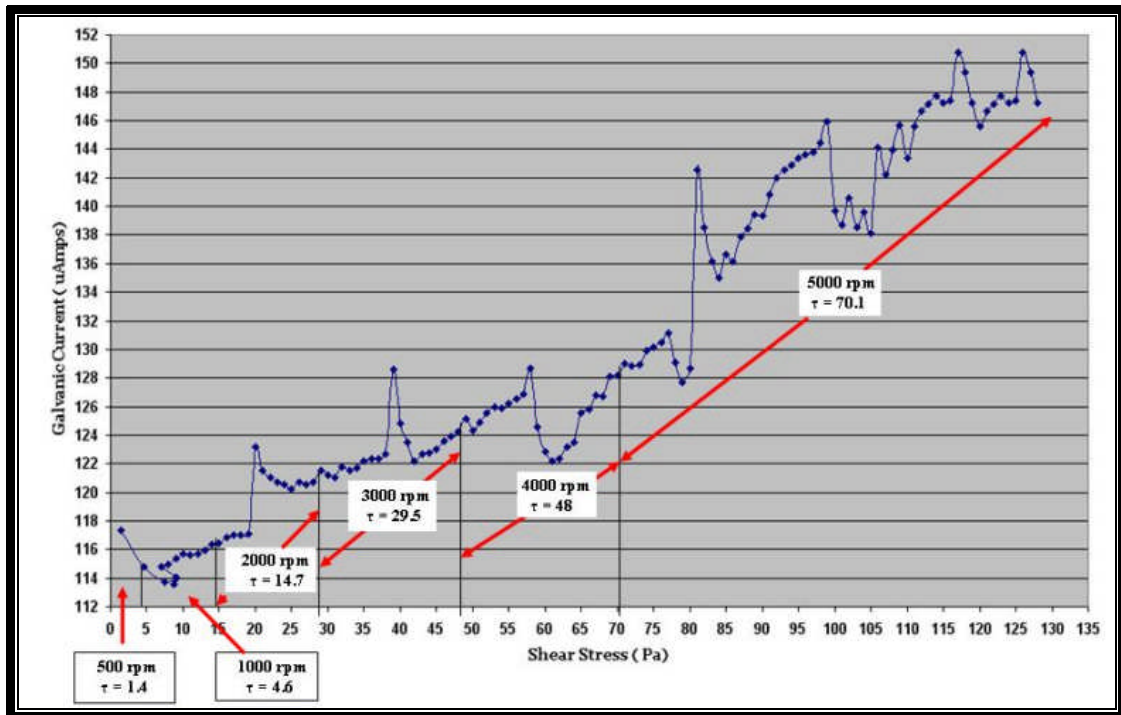


Figure 10-1: Galvanic current values as a function of the calculated shear stress and rpm

Although the anodic current measured on the parent material was larger than that on the HAZ, when the different electrode areas were taken into consideration their current densities were very similar.

10.1.2 Inhibited Conditions

Figure 7-7 shows the effect of 30ppm of CORR TREAT 05-193 on galvanic currents for the three weld regions. Upon initial exposure to the test conditions, the galvanic current of parent metal behaved as an anode which indicates that the parent metal corroded preferentially with respect to WM with an initial current of 20 μA compared to 150 μA for the uninhibited conditions.

The first observation, in Figure 7-8, is that the inhibitor film was formed after one hour of exposure time as a reduction in the galvanic currents.

With the presence of the inhibitor, a current reversal of the weld metal as well as HAZ towards an anodic direction, when the rotational speed was increased, resulted in accelerated corrosion of the weld. Hence localised corrosion took place that has sometimes been reported to occur in service [6, 30, and 32]. This phenomenon confirmed earlier results of an unsuitable inhibitor. It was previously considered [33] that under high flow rate conditions, less compact/adherent films/scales on the weld metal might be removed while films on the parent metal remained intact, leading to this switching phenomenon.

Significantly, when the RCE rotation was stopped, the galvanic currents decreased very rapidly to their previous level, suggesting that complete film removal had not occurred or that this inhibitor is capable of regaining its protection, once damaged.

It is suggested that both the presence of the inhibitor and the flowing conditions contribute to the reduction of the corrosion rate in CO_2 saturated solutions at lower pH. While the adsorbed inhibitor reduces the active areas, the flow at the active sites will act

as it behaves in the CO₂ solution without an inhibitor. It will initially raise the corrosion current, leading to increasing Fe²⁺ concentration at the surface; at the same time it will raise the corrosion potential to render the system in the possible domain of formation of FeCO₃. Hence, the surface will be covered by adsorbed inhibitors and thin isolated particles of FeCO₃ [78].

10.2 Self-corrosion rates

10.2.1 Uninhibited conditions

Figure 7-6, shows the self corrosion rates for the three weld regions at ambient temperature, measured by LPR as a function of rotational speed. Predictably, there was an increase in the corrosion rate for each sample tested as the rotational speed increased, with HAZ found to have the highest corrosion rate; in general, the weld metal corrosion rate falls to a level nearer to that of the parent metal corrosion rate.

As indicated before, when the rotational speed was increased, an increase in the shear stress values was also observed as shown in Figure 10-2, which corroborates observations made by Efird [75]. This shows that the corrosion rate cannot be controlled by chemical reaction. It seems more likely that a flow-dependent electrochemical reaction is rate determining.

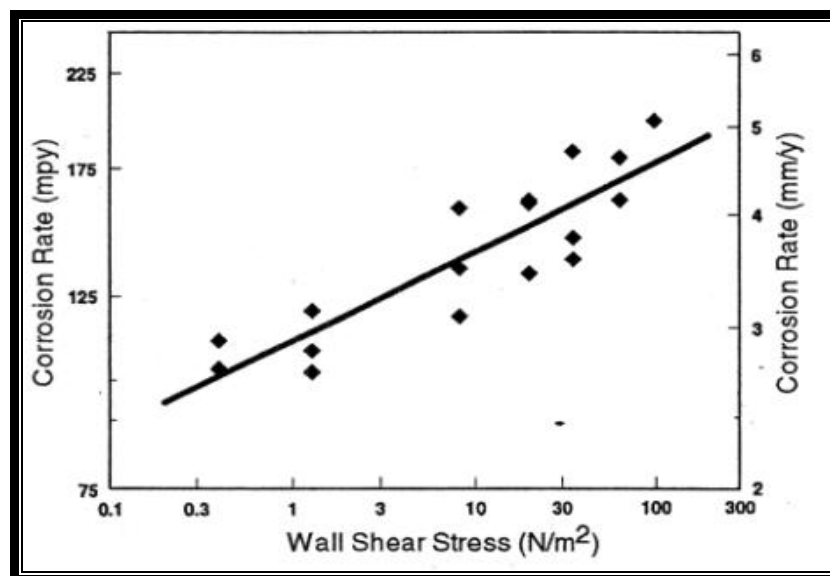


Figure 10-2: Corrosion rates of C steel as a function of shear stress for the RCE [75]

From the results obtained under stagnant conditions at room temperature, it was clear that the corrosion rates obtained correlated excellently with the predicted rates determined from Milliams and de Waard's nomogram [60] as shown in Figure 10-3.

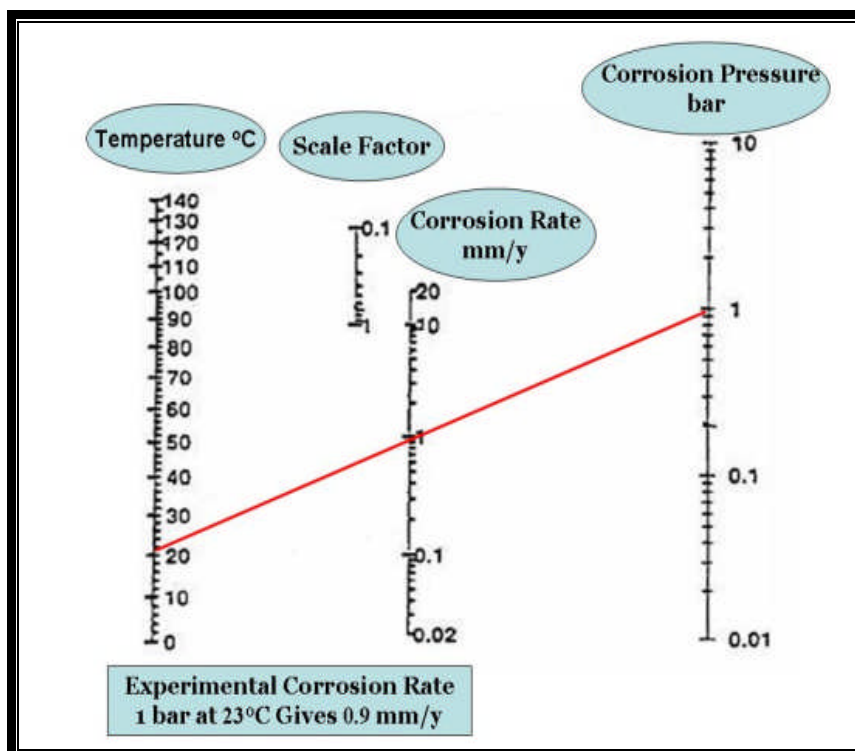


Figure 10-3: Nomograph for predicting CO₂ corrosion of welded X65 carbon steel based on stagnant and room temperature conditions [60]

There was evidence of a black surface film during the experiments, suggesting that a corrosion product was formed. It has been reported that as the solution becomes more alkaline (pH 5 and 6) under stagnant conditions, surface films composed of iron carbonate (FeCO₃) can be formed [45]. The literature suggests that the principal corrosion product is iron carbonate FeCO₃. This substance has a green colour in pure conditions but often turns brown when contaminated by small amounts of iron oxide either due to the presence of oxygen in the system or the introduction of oxygen to the system during specimen removal [136].

Despite the presence of the surface film, significant corrosion was evident from the build up of corrosion product on the three weld regions. During the stagnant conditions the surfaces were either partially covered with the protective film or the film formed was loosely adherent and therefore unable to provide complete protection. However, under flowing conditions it was observed to be a very loose black layer, which was left over the corroding steel. This film failed to decrease the corrosion rate as it was rapidly removed by the flow causing high corrosion rates. This was confirmed by visual examination of the samples after the test.

It was found that there was a reasonable correlation between microstructure and preferential weld corrosion. The weld metal had higher hardness and larger grain size, without any significant alloying addition, as the weld metal had a matching consumable composition.

It was reported in the literature that high HAZ hardness might encourage preferential HAZ corrosion. However, this was contrary to what was reported previously in section 4.1 as the HAZ hardness was lower than the weld metal and parent metal but still considered to have the highest corrosion rate. The HAZ region of the weld has an identical composition to the parent metal and thus differences in behaviour between the two regions are likely to be microstructurally related [98].

The most striking point of the data presented in Figure 7-6, is that the parent material had the lowest self-corrosion rates, while for the galvanic current measurements it had the most active potential, as it had the most anodic behaviour of the three weld regions.

Clearly, the three weld regions had differences in both microstructure and chemical composition and these are likely to have affected the self-corrosion rates.

10.2.2 Inhibited conditions

The inhibitor had a significant effect of reducing the self corrosion rates for the three weld regions to approximately 1% of their previous values. It was observed that the corrosion rate for the three weld regions hardly increased for the first two rotational up to 3000 rpm (shear stress of 29.4 Nm^{-2}), followed by a general tendency towards a higher corrosion rate when the rotational speed was increased in the following order 3000, 4000, 5000 rpm (shear stresses of 48 and 70 Nm^{-2}), this suggests inhibitor removal at high speeds, leading to high corrosion rates. In most cases, the inhibitor performed better in certain weld regions in the following order: Parent metal > weld metal > HAZ.

In addition to having the highest self-corrosion rates, the HAZ and weld metal had been the anodes in the galvanic corrosion test in inhibited conditions. As this behaviour was the reverse of that in uninhibited conditions, it is unlikely that microstructural differences are the explanation in this case. Rather, it appears that the adsorption characteristics can lead to poor inhibitor filming on specific parts, such as weld metal and HAZ, than parent metal which can cause a galvanic effect leading to PWC.

This agrees with work by Mendoza [47,] which reported a higher corrosion rate when the flow velocity is increased in the presence of some inhibitors. It has been suggested that this behaviour occurs because the increased fluid to wall shear stress partially removes, or makes thinner, the adsorbed inhibitor films. However, the shear stresses (Table 5) used during the inhibitor performance testing were lower than those indicated in the above works (142 Pa to 170 Pa), as having such effects on the corrosion inhibitors.

A number of studies [114,119] have demonstrated that at moderate ranges of flow (10-15 m/s), inhibitor performance has been found to be essentially independent of velocity. This is contrary to what has been reported previously in the results section of the present study where a velocity up to 5.24 m/s (5000 rpm) can be an important factor in

removing, either partially or totally the corrosion inhibitor film from the surface, causing high corrosion rates.

10.3 Total corrosion rates

10.3.1 Uninhibited conditions

The total corrosion rate of each weld region can be attributed to the sum of its self-corrosion and galvanic corrosion rates and these are shown for uninhibited static and 5000 rpm conditions in Figure 7-17. In each case, the galvanic contribution was much smaller than the self-corrosion rate. This is not surprising as carbon-manganese steel is inherently susceptible to high self-corrosion rates in carbonic acid, whereas the small compositional and microstructural differences between the weld regions would not have caused large galvanic differences. It was clear that the corrosion increased due to the high shear stress accompanied by an increase in mass transport at higher rotational speed.

The cathodic galvanic current contribution on the weld metal considerably reduced its total corrosion rate so that it displayed the lowest rate of the three weld regions. In consequence, the weld metal was partially cathodically protected by sacrificial corrosion of the parent material and the HAZ. This partial protection implies that the anodic and cathodic processes were occurring on all regions of the weldment.

10.3.2 Inhibited conditions

The corresponding total corrosion rates for the inhibited test solution are shown in Figure 7-18 and, again, there was a large increase in all rates at high shear stresses. The trend that was observed to prevail was that of increases in corrosion rates with increased rotation speed at high shear stress.

In static conditions the weld metal remained cathodic, whilst both parent metal and HAZ were anodic. In consequence, the magnitude of the weld metal total corrosion rate

was observed to decrease. However, at 5000 rpm, polarity reversal occurred, where the most cathodic region under uninhibited conditions become anodic in the presence of an inhibitor. It is apparent that the parent material remained fully protected due to the reduction of its self-corrosion contribution, as a result of an increase in the cathodic current.

This situation applies only to parent material located near to the weld, where the relative areas of the different weld regions are the same or similar to those considered in these experiments. At greater distances from the weld, the galvanic contribution would be smaller and some corrosion of the parent material would be expected.

When both the weld metal and HAZ became anodic due to current reversal, their galvanic corrosion rates greatly exceeded their self-corrosion rates (by a factor between 6 and 9), in contrast to the uninhibited conditions where the galvanic currents were relatively small. This behaviour, which is thought to result from poorer film formation on the weld metal and HAZ, would have contributed to severe localised corrosion of the weld.

10.4 Effects of higher temperatures and the role of surface films

10.4.1 Uninhibited conditions

Both temperature and flow are significant factors that influence corrosion rates. In work repeated in the literature for turbulent flow conditions, no maximum corrosion rate was observed between 40°C and 80°C. Instead, corrosion rates continued to increase with temperature [63].

Below, Figure 10-4 shows a comparison of the self corrosion rates in the present study for the weld regions under uninhibited conditions over a wide range of temperatures (room temperature, 50°C and 70°C) with hydrodynamics conditions covering the range from static to highly turbulent flow (5000 rpm).

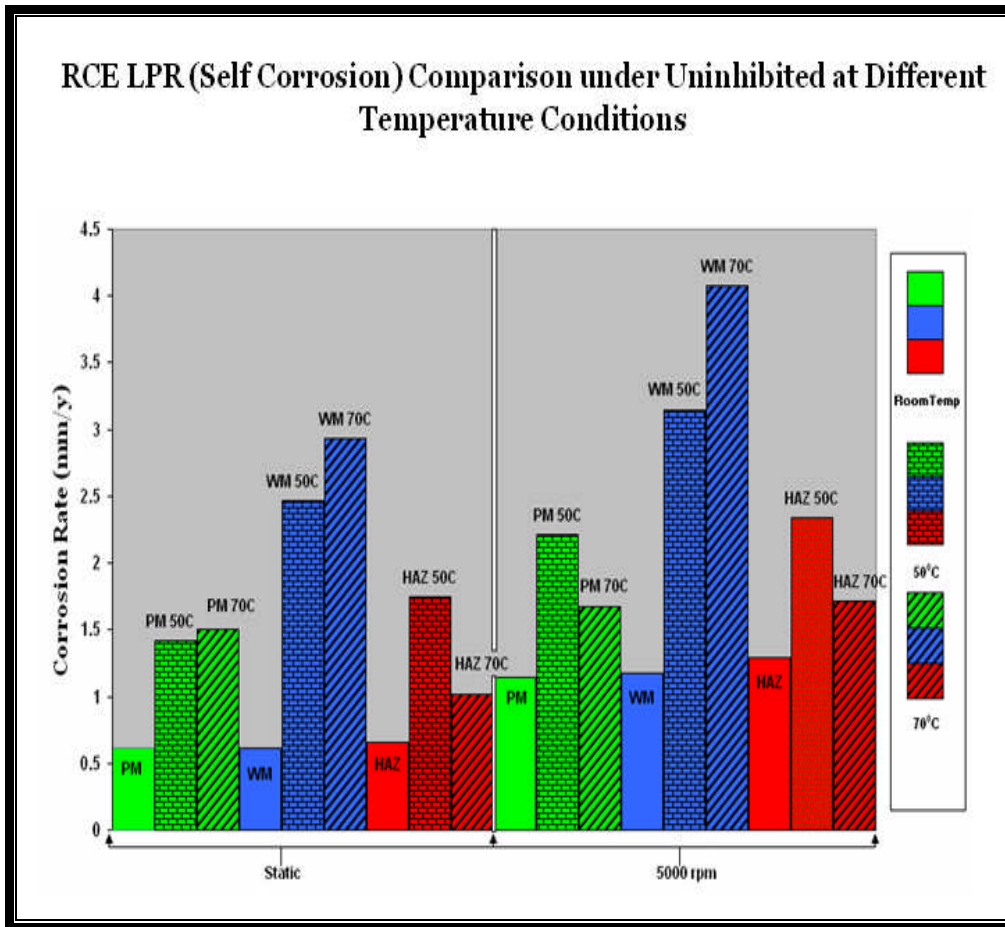


Figure 10-4: LPR test under different temperature and uninhibited conditions

There was a clear acceleration of self-corrosion rates of all three weld regions when the temperatures raised above ambient. It was observed that increasing the temperature from 50°C to 70°C, the self-corrosion on the weld metal showed a small further increase, while those on the parent metal and HAZ in flowing conditions both decreased.

These results agree with previous findings made by Mendoza [135]. He showed that as the solution temperature increases, the measured values of I_{corr} , hence the corrosion rate, also tend to increase, as well as having a dependency on the rotation rate of the electrode. This is shown in Figure 10-5.

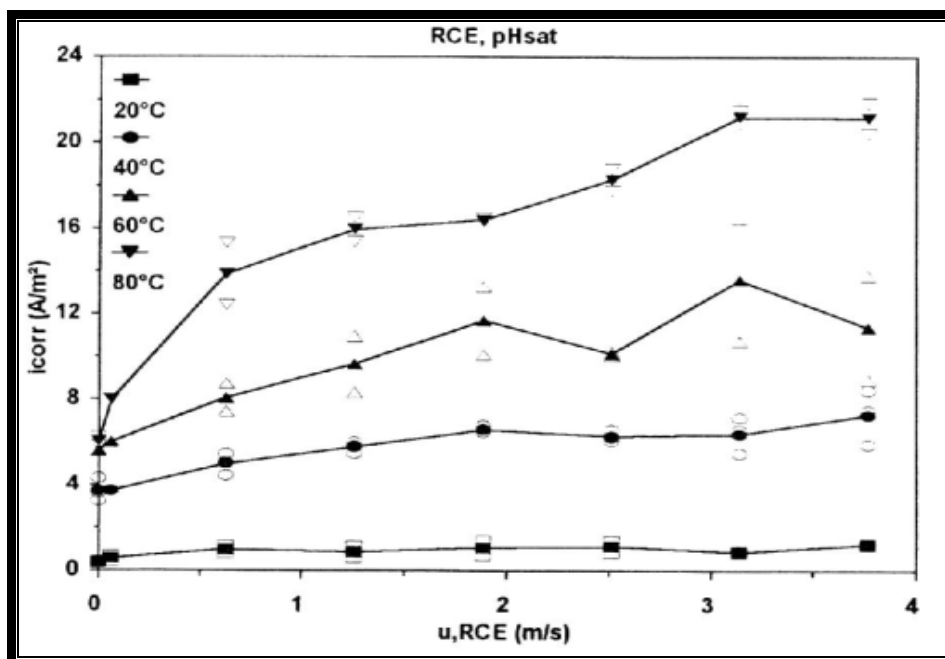


Figure 10-5: Corrosion rate densities as a function of the rotation speed of the electrode and solution temperature [135]

These findings agree with previous observations made by Eriksrud and Sontvedt, and reported by Wills [136]. They pointed out that the overall corrosion process taking place on the surface of the electrode changes from being mainly controlled by a charge transfer process at a low temperature to being influenced by mass transfer process at a higher temperature.

This was contrary to what Nescic [132] reported. He found that the flow dependence of the corrosion rate was less pronounced with increasing temperature because of the change in the corrosion process from partial mass transfer control at lower temperature (room temperature) to mixed charge transfer and chemical reaction control at higher temperatures (50°C and 80°C).

It was clear that under static conditions and low flow rates at room temperature, the corrosion rate obtained correlated excellently with the predicted rates determined from the Milliams and de Waard nomogram. However, under flowing conditions with higher temperature of 50°C and 70°C, the results are not predicted so well because at a higher temperature the nomogram does not include flow parameters, which must be considered also.

During 10 hours of stagnation conditions, a black and thick corrosive product accumulated on the weldment elements, which was in agreement with what had been reported in the literature review, and continued to have same color even when the rotational speed was increased. However, other workers report changes in colour at high fluid velocities as oxidation conditions change. Furthermore, oil field in flow systems, corrosion films obviously can grow for months without giving protection unless the steel is exposed to stagnant conditions [57]

When CO₂ is added in aqueous solution, it is hydrated and forms a weak carbonic acid (H₂CO₃). This weak acid provides a source of H⁺ especially in acidic solution (pH<4) where its reduction is the dominant cathodic reduction. However, in pH range 4-6, the additional direct reduction of H₂CO₃ becomes more important and is considered to be the cause for CO₂ solution being more corrosive than pH alone. The concentration distribution of the carbonate species in solution was proposed by Mendoza [135] and is presented in Figure 10-6 as a function of solution pH. It can be seen that between 0 and 3, the predominant carbonate species is the H₂CO₃ while between regions 5 and 7 the predominant carbonic species is the bicarbonate HCO₃⁻ ion. However, further than 12 pH, the predominant species is the carbonate (CO₃⁻²) ion.

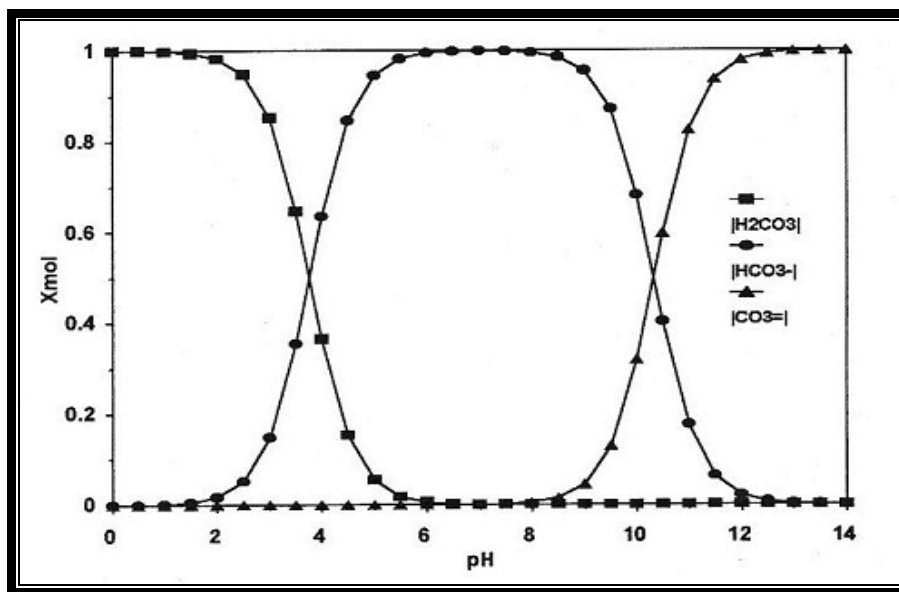


Figure 10-6: Relative concentration of carbonate species as a function of pH, 25C, 1 bar [135]

Several works have reported [63, 64], that in the presence of CO₂ and protective corrosion product films, high flow rate, can influence the transport of cathodic species towards the steel surface, yielding an increase of metal dissolution. At the same time, flow may stimulate the removal of Fe²⁺ ions from the steel surface which may cause lower surface supersaturation and slower precipitation rates. This in turn yields less protective films and, hence, higher corrosion rates.

10.4.2 Inhibited conditions

Addition of the inhibitor reduced the self-corrosion rates on all weld regions at these temperatures (50°C and 70°C) under static and flowing conditions, as shown in Figure 10-7 compared to uninhibited ones.

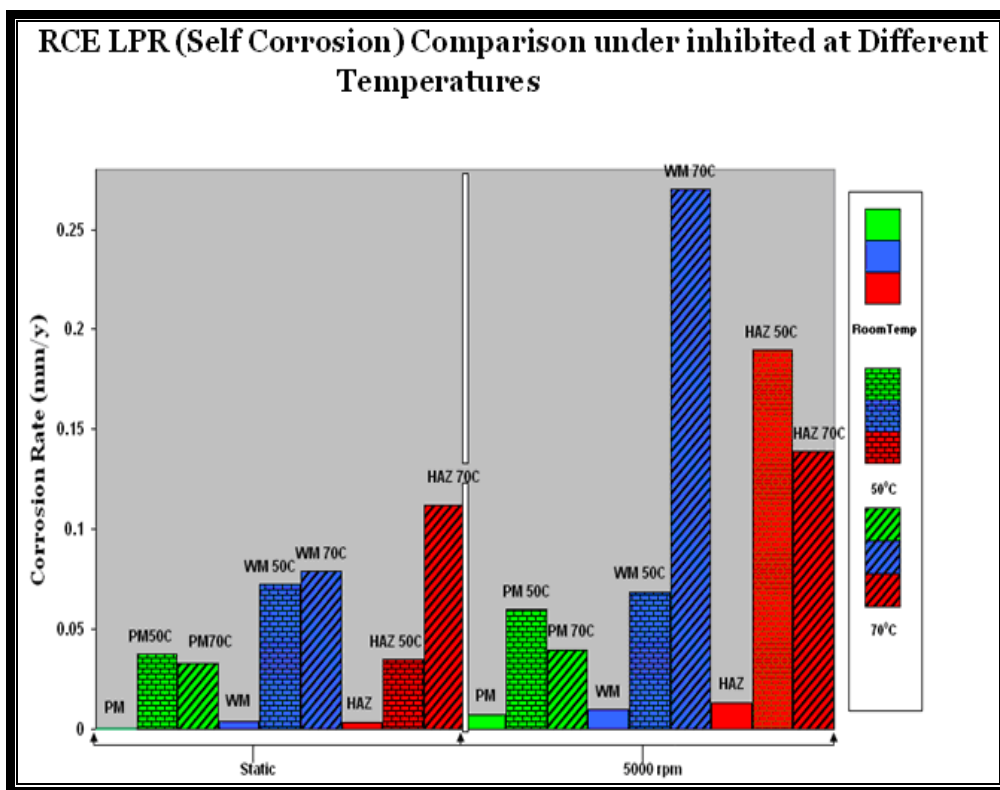


Figure 10-7: LPR test under different temperature and inhibited conditions

Under static conditions, the inhibited corrosion rate generally increased with increasing temperature. However, under flowing conditions, upon addition of the inhibitor, an increase of the test solution temperature to 70°C caused a decrease in the corrosion rate

of the parent metal and HAZ compared to the corrosion rate measured at 50°C. This suggests adsorption of the inhibitor is promoted by temperature, while for the weld metal, there was an increase in the weld metal corrosion rate, as compared with the temperature of 50°C, by a factor of four.

It is thought by authors Dawson and Omonua [18, 30] that this effect is dependent on the steel microstructure and the pre-corrosion time, which both have the detrimental influence on inhibition efficiency; however, in this case the proposed mechanism is related to the inhibitor film rather than a corrosion product film that was responsible for this behaviour as no corrosion product films were visible.

Despite inhibitor additions not being particularly effective in the experiments studied under flowing conditions, it can be seen that the presence of an inhibitor reduced the corrosion rate for the parent metal and HAZ, whereas for the weld metal, it was less efficient in these conditions and this was the cause of the localised weld corrosion.

10.5 Electrochemical Impedance Spectroscopy (EIS)

Electrochemical techniques have all been employed by various researchers to assess the carbon dioxide corrosion mechanism [118]. In the present work, the electrochemical impedance technique was used to support the analysis of the LPR data. The R_s value can be measured and in addition possible effects of diffusion identified. For diffusion controlled systems, measuring at very low frequencies is necessary to obtain the low frequency value for polarisation resistance, which is the sum of charge transfer resistance and diffusion resistance [131]. The disadvantage of the EIS measurements are that adequately low frequency experiments could take days and the system then changes, invalidating the measurements.

Another practical difficulty for the EIS technique is in providing curves with a completed semicircle as a deflection was noticeable for the semicircles of the Nyquist plots before they were completed.

The poor fitting of very low frequency data points suggests that there are some other interfacial structures on the electrode surface. It is believed to be incorrect to interpret either of the actual low frequency Z' axis intercept as the sum of R_s and R_p . Instead, curve-fitting technique was used to obtain these values, as shown in Figure 10-8.

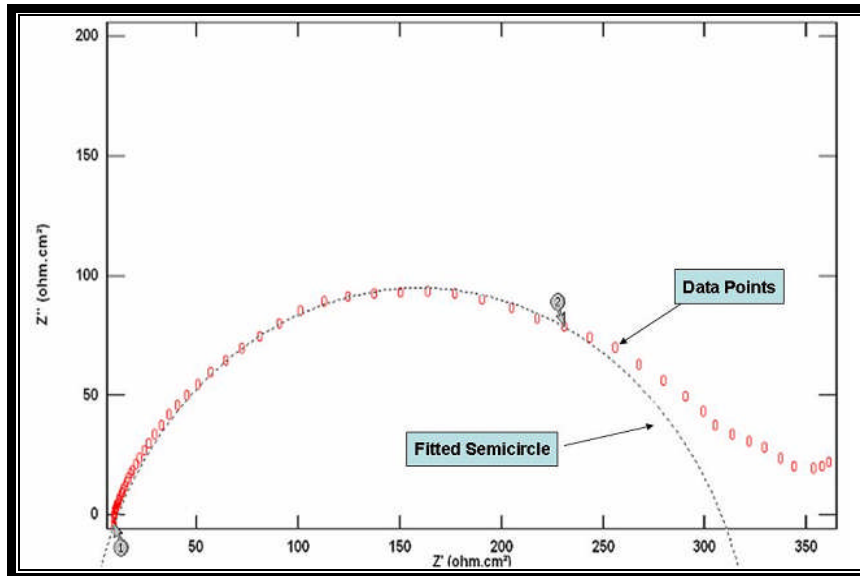


Figure 10-8: Semicircle fitting of a typical Nyquist plot

The EIS test is effectively comprised of different LPR tests where a sinusoidal signal is applied each time with a decreasing frequency. The LPR method is actually a particular frequency point of the EIS test. The LPR test is done by the application of a potential ΔE with a given sweep rate. The time during which the potential is applied can then be calculated and presented as a frequency.

In the case of the LPR tests that were run here, this frequency point was 4 mHz on the Nyquist plot, as this is the effective test frequency that had been used in the LPR measurements (one cycle in 240s) as shown in Figure 10-9.

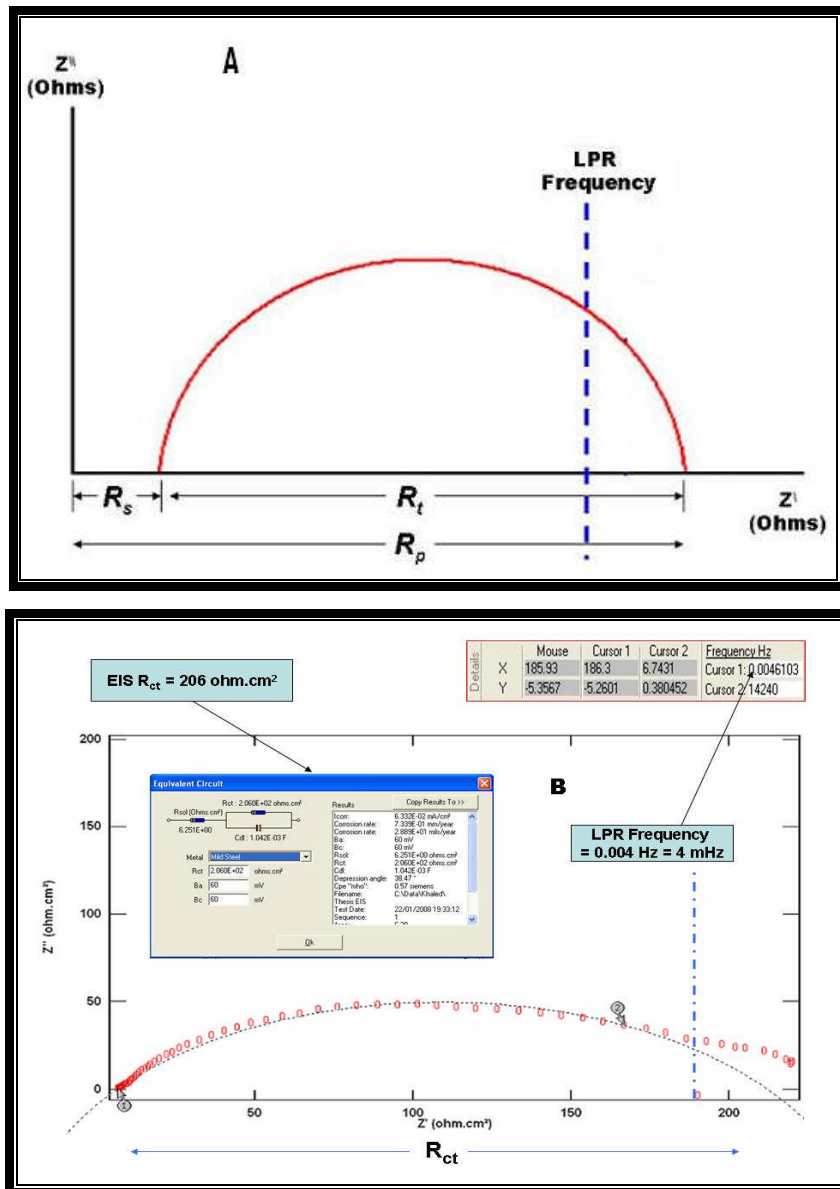


Figure 10-9: Location of the LPR frequency on the Nyquist plot (from the EIS test) A) when solution resistance is high, (B) when solution resistance is low

The reason for using EIS was to evaluate whether the LPR results were valid. The EIS results for the three weld regions at higher temperatures under inhibited and 5000 rpm will be briefly discussed first. Experiments for each were conducted at least twice to make sure the result was reproducible and reliable.

The curved shapes for the Nyquist plots, determined for tested weldment specimens, represent a slightly different behaviour, as shown in chapter 9, i.e. all these Nyquist plots have two semicircles. The first one (is the high frequency semicircle) appears to

predominate for all regions, presumably due to the formation of an inhibitor film. This is in addition to a semicircle for charge transfer process and a diffusion tail at the low frequency region. The diffusion impedance element suggests that the electrochemical process might be controlled by the active species diffusing to the metal surface or corrosion product diffusing away from the metal surface through the inhibitor film.

It has been suggested that the depressed semicircle is not uncommon for iron dissolution in an acidic media and that the heterogeneous surface roughness and the non-uniform distribution of current density on the surface may be related to this [129].

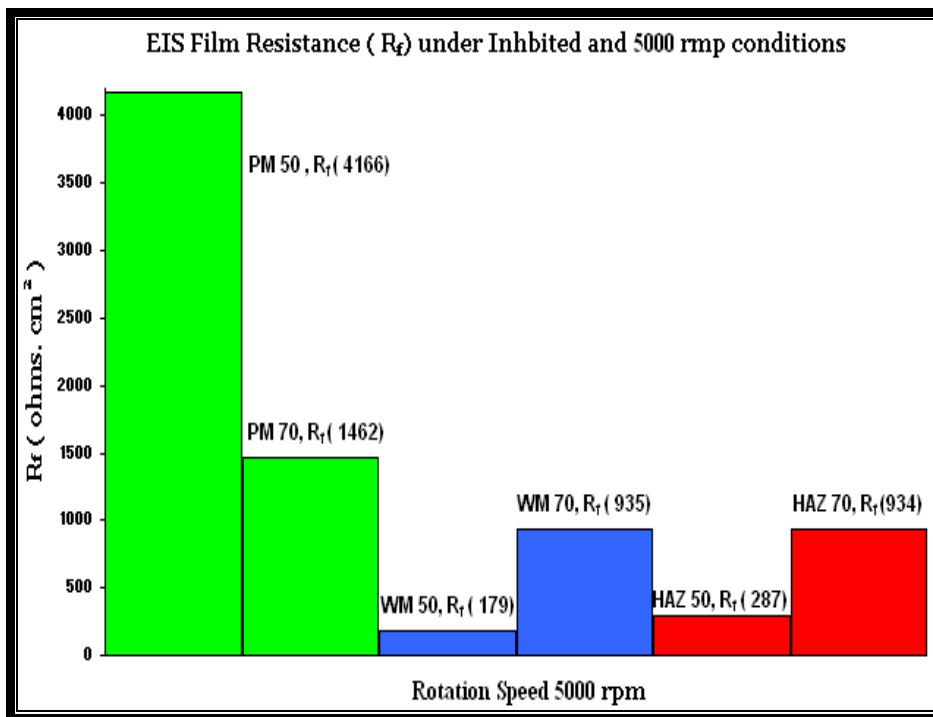


Figure 10-10: EIS film Resistance (R_f) for the three weld regions

As shown in Figure 10-10, the inhibitor film detected at high frequency at 50°C for the parent metal was higher than for the weld metal and HAZ. This film resistance on the parent metal was reduced at 70°C but is still considered more protective than on the weld and HAZ (R_f). These observations demonstrated that the quality of the inhibitor film was significantly improved with the increase in temperature.

From the above curve fitting results of R_f , one can conclude that the small semicircle at high frequency for the weld metal and HAZ at 50⁰C, indicated low inhibitor film resistance. However, it was observed during the EIS testing procedure, that the parent metal demonstrates a more protective inhibitor film with a higher film resistance, which could be seen from the larger diameter of the high frequency semicircle.

These data indicate that the adsorption process of the inhibitor is temperature dependent and the enhancement of this protective inhibitor film was supported by an increase of the inhibitor film resistance as the temperature increased from 50⁰C to 70⁰C, especially for the weld metal and HAZ.

The larger incomplete semicircle formed at lower frequencies for the three weld regions indicated the charge transfer resistance. This second semicircle was followed then by the diffusion tail, representing the diffusion controlled corrosion process taking place at the metal substrate.

It is possible to assume that the lower frequency semicircle is also affected by film formation as this semicircle tends to diminish in size, suggesting progressive removal of the inhibitor film from the electrode surface due to high shear stress which indicates that the adsorption process of the inhibitor is flow dependent.

Similarly, it was suggested in the literature review that the mass transport, caused by rotational movement of the electrode, supplies the cathodic reactants namely H⁺ ions and H₂CO₃, to the surface. This flow increases the rate of the corrosion reaction, and is thought to be the reason behind the reduction of the R_{ct} and thereby an increase of the corrosion rate [112]. It is clear that the inhibitor effectiveness was greater on the parent metal compared with the weld metal and HAZ impedance.

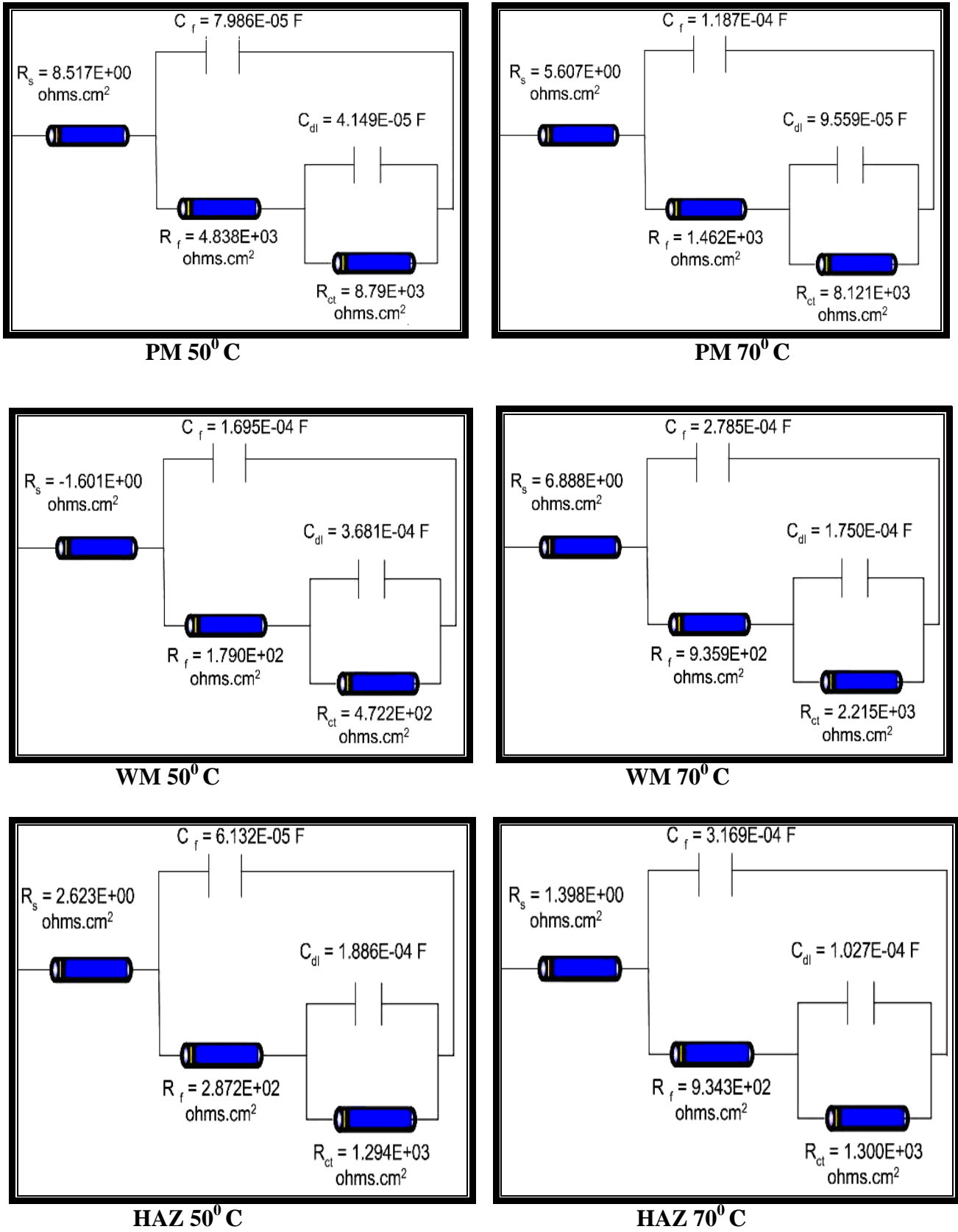


Figure 10-11: EIS circuit parameters (PM, WM, HAZ, 5000 rpm, 30 ppm inhibitor, 50°C and 70°C)

The electrical equivalent circuit is commonly used to describe electrochemical behaviour and to calculate its parameters of interest. Due to the similarity of the impedance spectra at 50⁰C and 70⁰C under inhibited conditions, the same equivalent circuit was used to represent the data.

In general, the fitting results Figure 10-11 show that as C_f reduces R_f increases, then, as C_f increases, R_f decreases. The initial behaviour could be associated with the formation of surface films and inhibitor adsorption covering large areas of the weldment regions, while the later behaviour is associated with the exposed and increased area of unoxidised Fe_3C and its negative influence on the corrosion process. It has been suggested that Fe_3C plays a key role in the inhibitor performance. As more Fe_3C is accumulated on the surface of the samples, it is more difficult for the inhibitor to reach the anodic sites [47].

The above interpretation is in agreement with surface and cross-sectional examination as shown in SEM images in section 11.2, where it can be observed that the accumulation of Fe_3C over wide area of the parent metal surface under highly turbulent flow. In contrast, on the weld metal was less accumulation, hence less corrosion, which can be confirmed from the cathodic behaviour in the galvanic test.

The polarisation resistance (R_p) values obtained with the direct current method (LPR) were close to the charge transfer resistance (R_{ct}) obtained by the EIS technique. Since results obtained by either technique were close, either experimental technique can be used to calculate corrosion rates with the same degree of confidence.

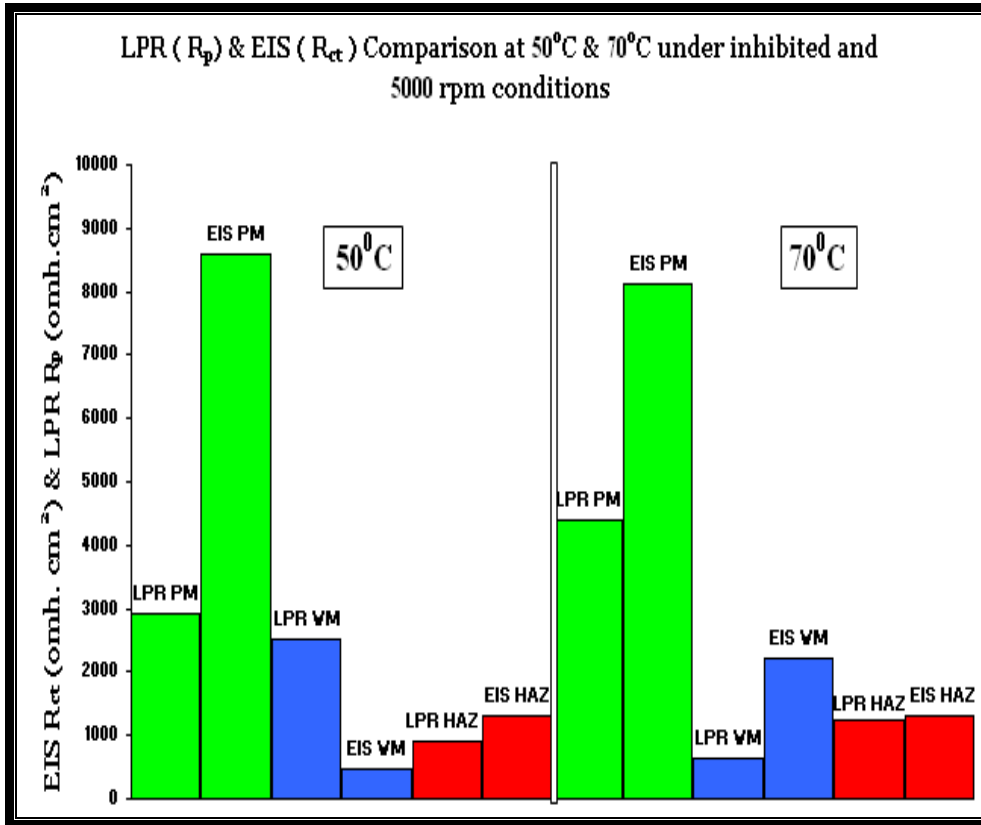


Figure 10-12: Comparison of the LPR (R_p) and EIS (R_{ct}) for the three weld regions

As shown in Figure 10-12, EIS consistently gave a higher R_{ct} compared to the corresponding LPR (R_p). The only exception was one value with the LPR polarisation resistance of the weld metal being higher than the impedance value.

A calculated corrosion rate can be obtained, which is based on the assumption of a charge transfer controlled corrosion process. The EIS corrosion rate is then compared with the experimental LPR corrosion rate.

Assuming that R_{ct} is inversely proportional to corrosion rate, Figure 10-13, shows the comparisons among the corrosion rates obtained from the EIS and LPR at 50°C-70°C. The corrosion rates from these two different methods were not substantially different.

As the temperature is increased, the two techniques diverge in their predicted values which leads to minor inconsistencies between the corrosion rates obtained from the LPR technique and the EIS for the weld metal.

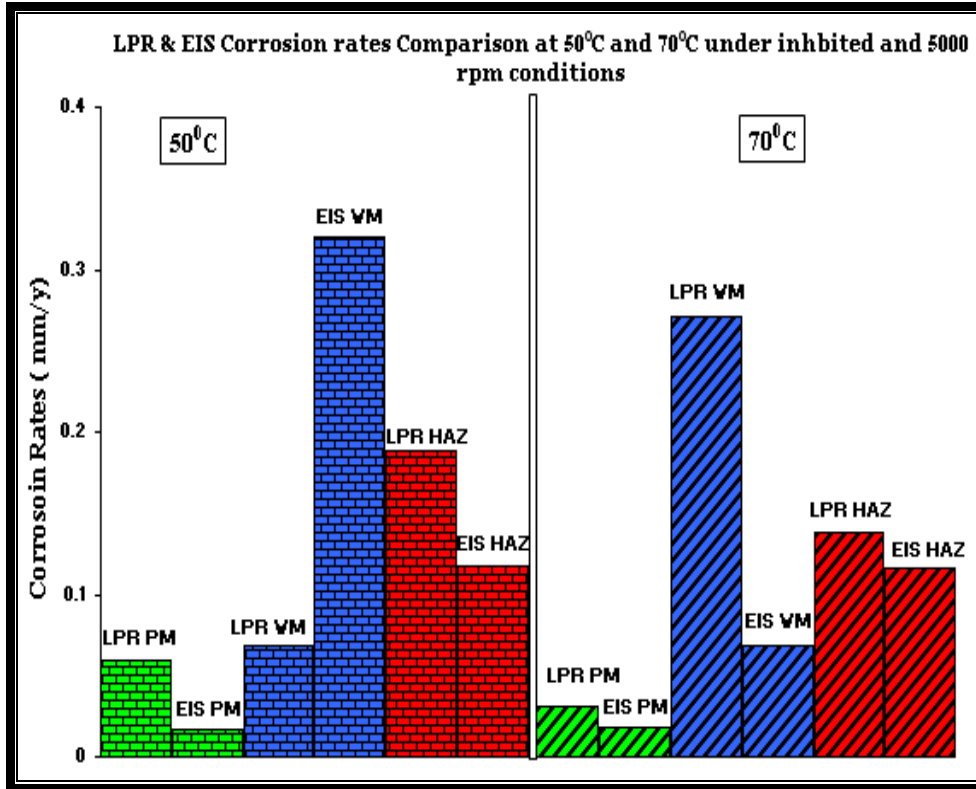


Figure 10- 13: Corrosion rates comparison for the three weld regions at 50⁰C & 70⁰C

Therefore, it is concluded that both the EIS and LPR techniques follow the same pattern, but for absolute values, the EIS technique is the more reliable corrosion measurement method for this particular project.

From the above discussions, one can deduce that the weld metal has the highest susceptibility of electrochemical attack, as the impedance (Nyquist) plot appears to uphold this claim. It does appear that the consistency in the anodic behaviour and susceptibility to the attack of the weld metal is due to the inhibitor addition, acting simultaneously with an increase of the rotational speed. Hence high corrosion rates are presumably due to the loss of the inhibitor film from the weld metal under high shear stress which was formed during stagnant conditions.

11 Surface characterisation (XRD, SEM and XPS)

11.1 XRD Test

Different surface analysis techniques were employed to study the corrosion product surface film in both static and flowing CO₂ corrosion systems (in a solution of initial pH of 5). The visual examination of the surface morphology and the determination of the elements and chemical composition of the corrosion products are of great significance in examining the corrosion behaviour in CO₂ saturated solutions, when related to the other electrochemical results.

The corrosion product which formed over the three regions of the weldment has been characterised using the techniques of X-ray diffraction (XRD) and scanning electron microscopy (SEM/EDX). In the case where EDX provided insufficient information to identify the corrosion products, X-ray photoelectron spectroscopy (XPS) was performed to supplement the EDX data.

Two common features were discovered among the regions: (1) surfaces with no inhibitor show dark film present containing iron carbide (Fe₃C) and (2) thin crystalline features were found to be iron carbonate (FeCO₃) films. The most evident changes in corrosion morphology emerged with variation in flow and inhibitor additions.

Figures 11-1 and 11-2 are the X-ray diffraction spectra attempts for the weldment surface as a function of relative intensity and goniometry setting (2θ) after 5 days exposure in 3.5% artificial seawater under static and CO₂ conditions at 70⁰C. The identity of the crystalline nature of the surface film was investigated with the X-ray diffraction analysis in order to identify the chemical compositions and phases present.

The corrosion product was analysed after several attempts. As shown in Figure 11-1B, the first attempt was carried out with an analysis by a short scan to determine the characteristics of the surface film. The scan was carried out from 10-160⁰ at 0.08⁰ steps, 2 seconds per steps and the spectra have been smoothed and then the background

subtracted. Scan result shows higher angle ferrite peaks, which are in agreement with standard values of JCPDS 97, plus the Kbeta stimulated peaks.

It was hoped that this test would clearly establish the presence of iron carbonate. However, the X-ray did not detect the presence of iron carbonate in the corrosion product. This is consistent with what was reported by Wills [140] for work done by Ikeda et al. who could not conclusively identify iron carbonate below temperatures of 80°C.

The XRD analysis showed no obvious crystalline compounds, with the exception of Fe. Distinctive, d-spacing responses have by far the strongest relative intensity, which may indicate that the other compounds are not crystalline.

Unfortunately, the presence of the corrosion product layer (FeCO_3) was not detected possibly because the scanning time was not really sufficient. However, additional tests were required to resolve this ambiguity by using a longer scan period.

For the second attempt Figure 11-1C, XRD did not revealed anything more useful than what was obtained in the first attempt. There were very small peaks in the positions relating to FeCO_3 and Fe_3C , but the scanning time available was not long enough to give a very satisfactory signal-to-noise ratio. However, the evidence was good enough to be worth an overnight scan which was carried out during the third attempt.

In order to achieve well defined peaks from any FeCO_3 crystals, a test was carried out on a relatively lengthy period, i.e. overnight, of continuous scanning on the sample powder which had been scratched from the corrosion layer on the surface. The XRD analysis shows low peaks corresponding to iron carbonate and iron carbide as indicated by the relative FeCO_3 and Fe_3C peak intensity as shown in Figure 11-2.

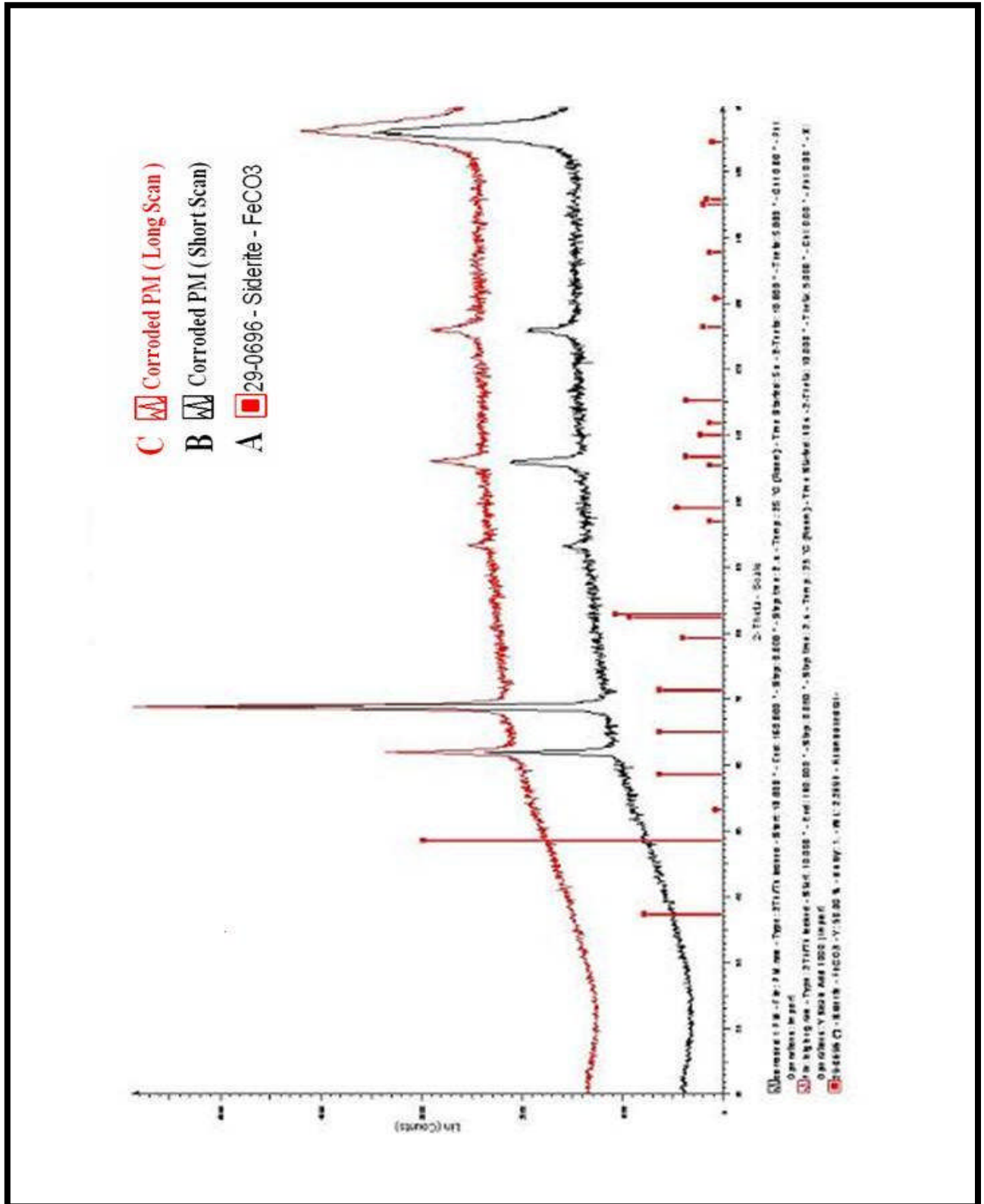


Figure 11-1: XRD patterns of corrosion products of weldment metal after 5 days of exposure in 3.5% artificial seawater under different scan periods:
 A) standard FeCO₃ peaks, B) short scan exposure, C) long scan exposure

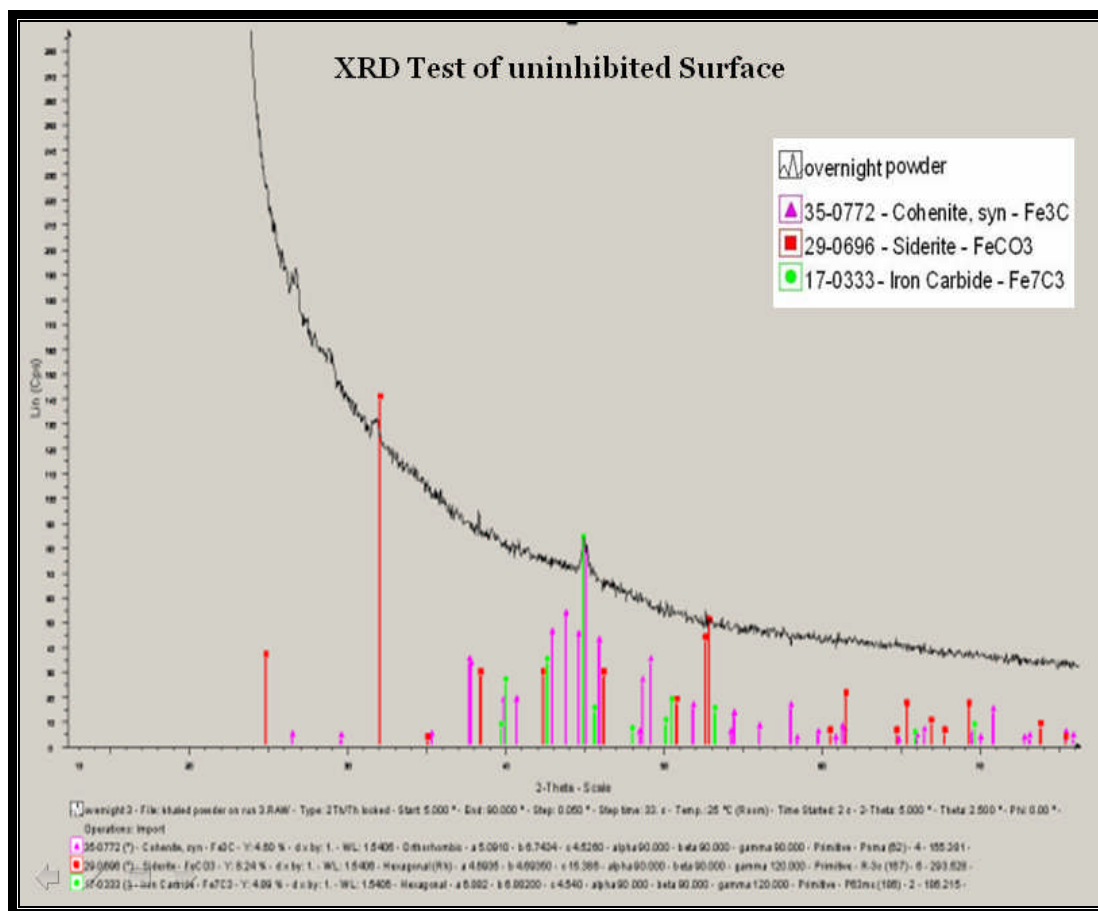


Figure 11-2: XRD patterns of corrosion products of weldment metal after 5 days of exposure in 3.5% artificial seawater for an overnight scan

Figure 11-2, shows a typical XRD pattern of the powder sample. All the diffraction peaks can be readily indexed to the hexagonal phase of FeCO_3 , which is in agreement with standard values of JCPDS (1997) and shown overlaid with the standard spectrum for FeCO_3 , confirming the presence of FeCO_3 . In addition to the iron carbonate (Siderite) phase, which was detected, larger quantities of iron carbide (Fe_3C) accompanied the iron carbide Fe_7C_3 phases.

It was clear that the main peak of the experimental work was lower than that of the main peak of iron carbonate reference pattern, which as reported earlier, was due to the small quantity of FeCO_3 crystallite. With the build up of thin corrosion product on the surface, it was expected that iron carbonate would be detected.

In addition, iron carbide with both phases (Fe_3C & Fe_3C_7) was also detected. The formation of both carbide phases and their presence in the corrosion products is likely to be due to the preferential dissolution of ferrite into Fe^{2+} , as mentioned in the literature review. Fe_3C_7 is considered to be one of the iron carbide phases that is difficult to be produced as a single phase. This phase converts easily into cementite at a temperature of 600°C [137].

Comparison of the D values of these patterns with the standard values suggested that while the thin iron carbonate (FeCO_3) was the phase formed over the surface, there were also peaks corresponding to the iron carbide phases which plays a major part on the layer formed on the surface. From this it can be inferred that the iron carbonate thickness was not enough to protect the surface. The large cathodic area of Fe_3C seems to have a more important impact on the electrochemical behaviour than the poorly formed FeCO_3 products.

From the results produced in this work, it can be demonstrated that the presence of only a thin corrosion product layer (in this case FeCO_3) can be attributed to the insufficient concentration of the Fe^{2+} , which has a large influence on the formation of the corrosion product (FeCO_3). It has previously been reported that an increase in iron ion concentration results in higher supersaturation, leads to the precipitation of protective corrosion films [65]. Furthermore, Videm [138] in his study found that at 70°C , 50 ppm Fe^{2+} could reduce the corrosion rate of carbon steels from 5 mm/y to 2 mm/y at pH 4 by the formation of more protective corrosion product films.

It can be seen that the direct precipitation, from a solution of FeCO_3 , is unlikely to occur in a short time, because the Fe^{2+} concentrations present in solution is far below that required for FeCO_3 precipitation.

Though Fe^{+2} was not directly measured during the corrosion experiments, the dissolved and accumulated Fe^{2+} , as a consequence of the corrosion process, was estimated from the metal loss, as shown in Appendix 4.

11.2 SEM/EDX analyses

11.2.1 Under Static Conditions

Figures 11-3 and 11-4 are the SEM micrographs for the weld metal immersed in 3.5% artificial seawater, saturated with CO₂, at an initial pH 5, corroded under static conditions for 5 days at a temperature of 70⁰C, followed by an uninhibited one with a rotational speed of 5000 rpm for 3 hours.

In the absence of an inhibitor, SEM and EDX spectra analysis for the corrosion layer on the weld metal showed an indication of the formation of an extremely thin black product on the surface. An EDX scan was taken to confirm this, but the presence of carbon on the surface could not be determined adequately.

In a high magnification photograph, see Figure 11-5, it can be observed that a uniform corrosion process took place leaving a lamellar layer present on top of the entire weld metal surface, which can be associated with unoxidised Fe₃C residues that accumulate on the surface after the preferential dissolution of ferrite (α -Fe) into Fe⁺².

Figure 11-6 shows an EDX scan of the element distribution through a single point of the layer, being enriched in carbon but with no indication of an oxygen peak, which seems to exclude the possibility of FeCO₃ being formed on the surface. In addition small Pd (palladium) and Au (gold), Ca peaks were visible. It is likely that the Pd and Au were formed during the FIB procedure. The source of the Ca was suspected to be due to the precipitation from the artificial seawater.

No salt deposit was expected to be dispersed over the layer as the sample was rinsed using tap water immediately after completion; the sample was then dried by isopropanol using a hair dryer leaving a fine brown corrosion product, which was probably due to contamination by small amounts of iron oxide.

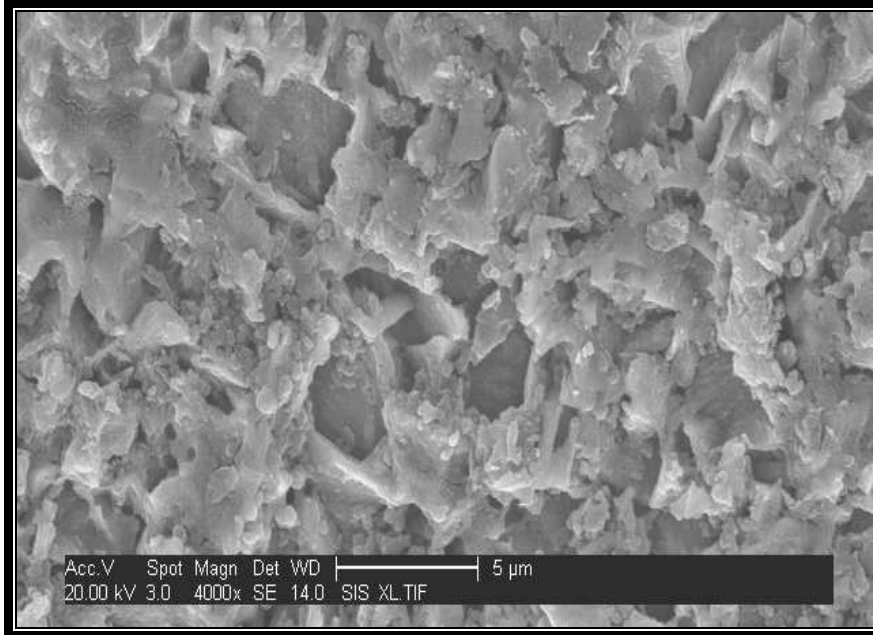


Figure 11-3: SEM image of weld metal X65 C-steel exposed to static and 70°C conditions

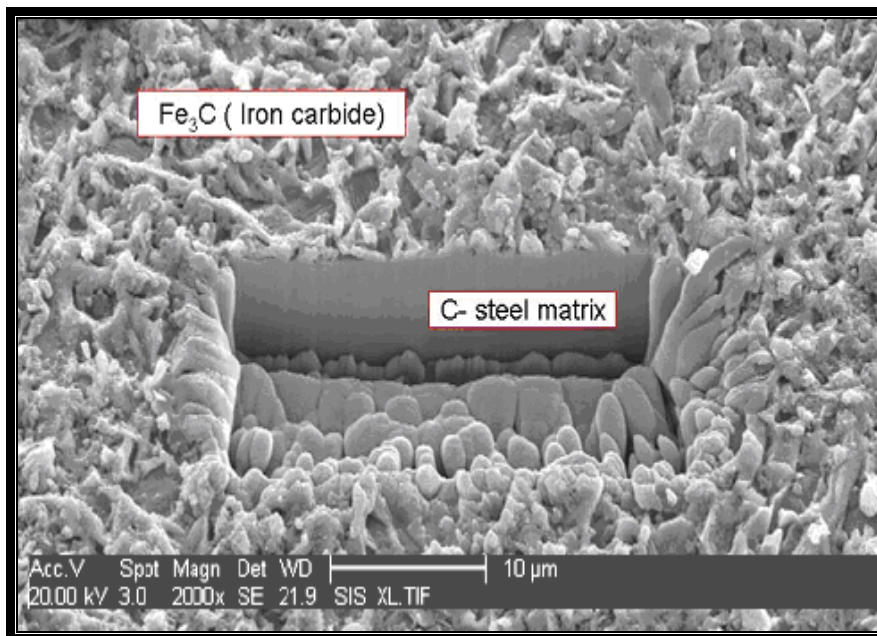


Figure 11-4: FIB etched cross-section of the weld metal under static and 70°C conditions

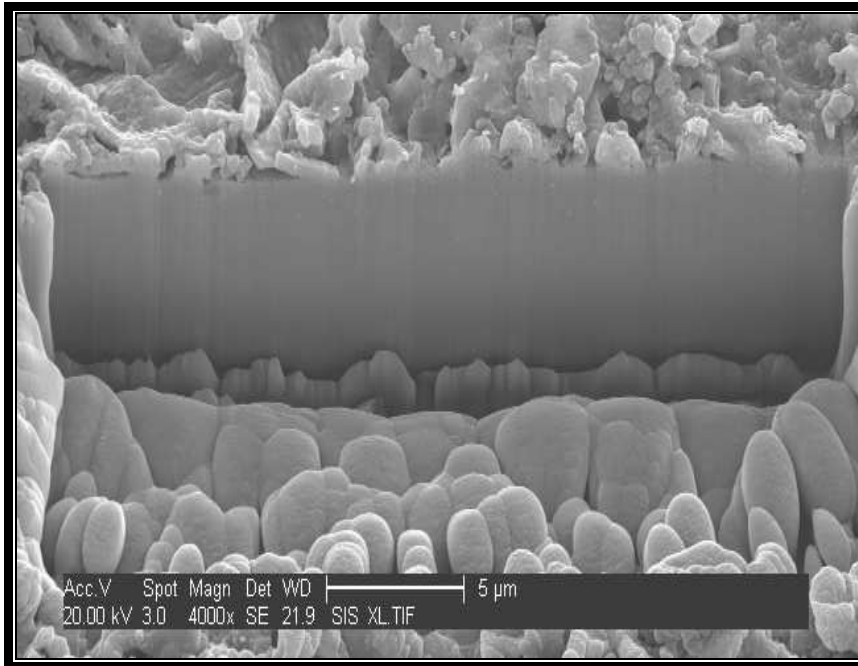


Figure 11-5 : Higher magnification of FIB etched cross-section for the weld metal

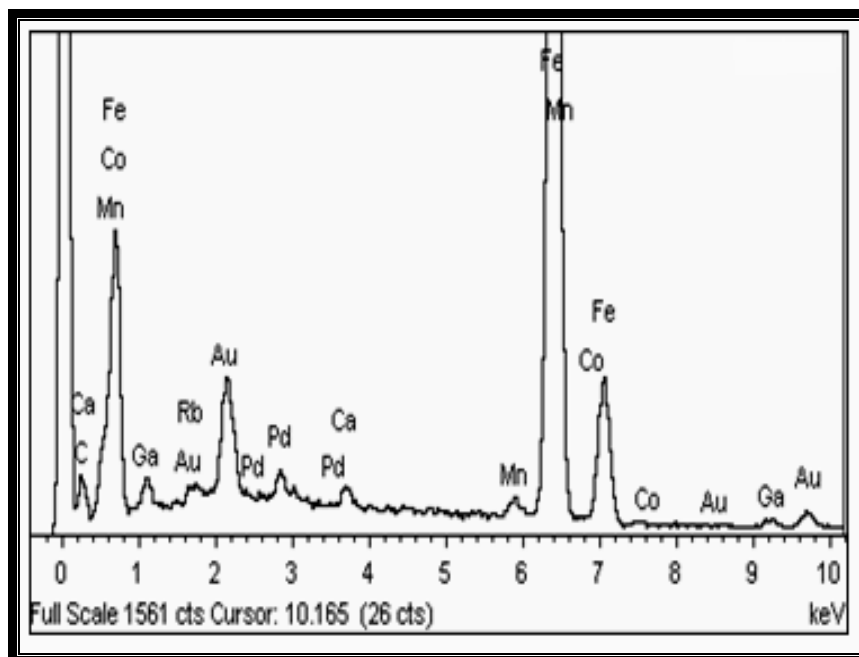


Figure 11-6 : Corresponding EDX spectrum of the corrosion products film

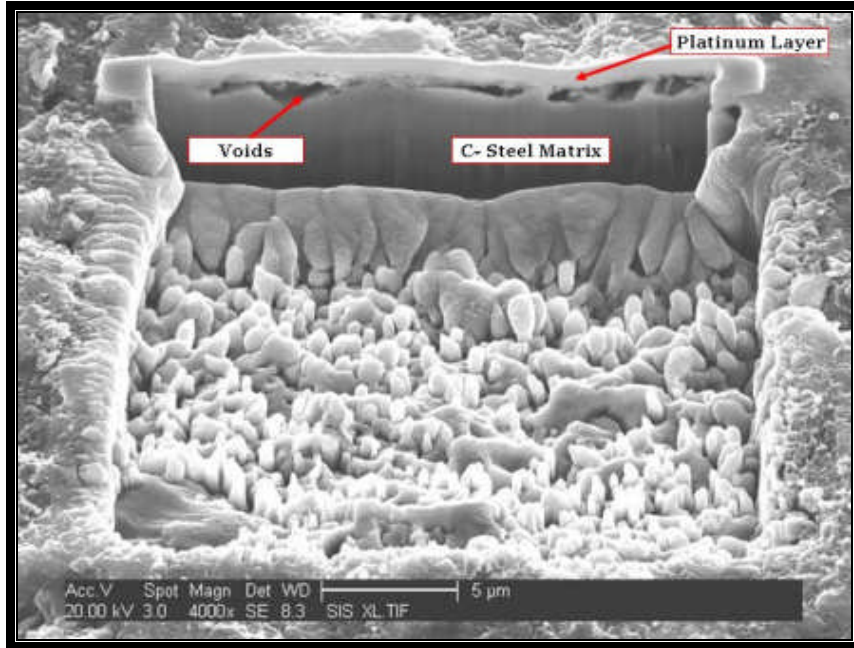
Table 1 EDX analysis of the corrosion product film on weld metal under static conditions

Element	Weight%	Atomic%
C	0.77	0.38
Ca	0.64	0.97
Mn	1.06	1.18
Fe	84.1	91.3
Co	0.32	0.33
Ga	1.88	1.63
Rb	0.76	0.54
Pd	2.15	1.23
Au	8.34	2.65
Totals	100.00	

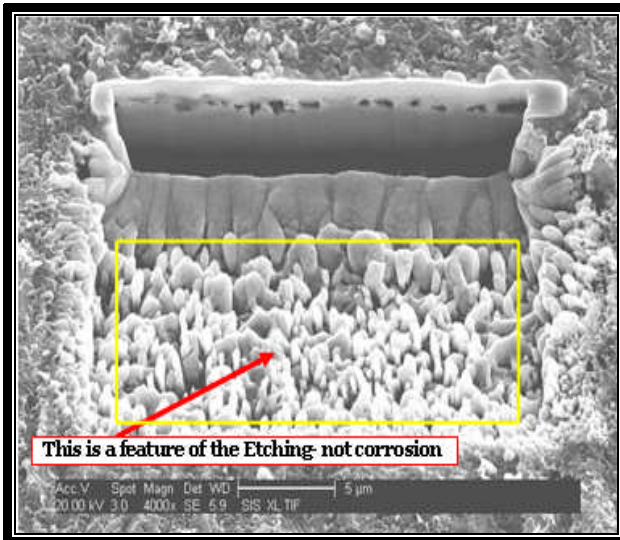
From the results exposed in this work, it can be demonstrated that the formation of FeCO_3 films was not enough to either reduce the diffusion of cathodic reactants towards the surface sample or to trap all the dissolved Fe^{2+} released from the corrosion process that seems to diffuse towards the bulk solution. This evidence may clarify why these films do not have an important impact in the electrochemical process as a physical barrier to reduce the corrosion rate.

11.2.2 Under Flowing Conditions

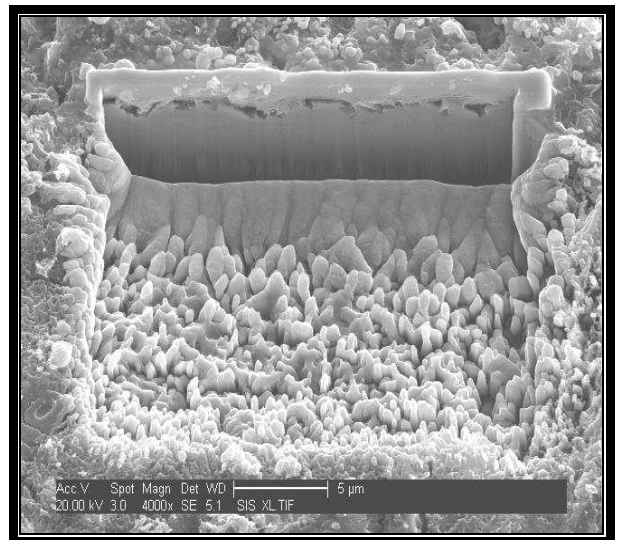
The appearance of the corroded surface can be observed in Figures 11-7 A, B, C for the three weld regions (PM, WM and HAZ) respectively. They show the surface morphology after 3 hours at a rotational speed of 5000 rpm at 70°C .



(A)



(B)



(C)

**Figure 11-7: FIB cross section of welded X65 c-steel exposed to RCE: 5000 rpm and 70°C.
 (A) Parent metal. (B) Weld metal. (C) HAZ**

All figures show a distinct platinum layer is clearly visible from the FIB micrograph. The importance of using FIB for analysis is evident here, as the image is able to give an in-depth view of the nature of the corrosion product layer, if it exists.

Large voids are seen at the surface for the three weld regions, as a consequence of preferential dissolution of the ferrite, leaving cementite the original Fe_3C structure present. These voids were interconnected with each other as a network with an increased surface area for the reactive species to move to the metal surface and cause further corrosion.

Consistent with the analysis of the film thickness, the corrosion rates for the weld metal and HAZ, measured by EIS and LPR, showed a very high corrosion rate. This is reflected by a sharp decrease of R_{ct} values for the EIS and low R_p for the LPR.

The SEM photograph with the highest magnification Figure 11-7, shows the ‘skeleton’ of the iron carbide left from the pearlite after the surrounding Fe was dissolved from the corroded matrix of the steel. This shows that the Fe_3C was not detached from the three weld region surfaces under high turbulent condition. The possible reason for the low corrosion rate for the parent metal under this condition, compared to weld metal and HAZ, is due to the relationship between the thin iron carbonate film and the carbide phase that could reinforce the protective layer and anchor it to the parent metal [104].

Others show in their studies that the accumulation of the carbides in the corrosion product has been seen as the cause of increasing corrosion rate for the ferritic-pearlitic steels [47].

EDX analysis in Figure 11-8 and Table 2, revealed the presence of significant iron level for the three weld regions with high level of C presence on the parent metal compared to the weld and HAZ. It was speculated that the high C level on the parent metal corresponded to the presence of more cementite (Fe_3C). Results obtained in section 10.41 (Figure 10.4.1-1) contradict this assumption as the parent metal has the lowest corrosion rate under same conditions (70°C , 5000 rpm and uninhibited). As a result the

high C level on the parent metal was suspected to be contaminat from the analysis system.

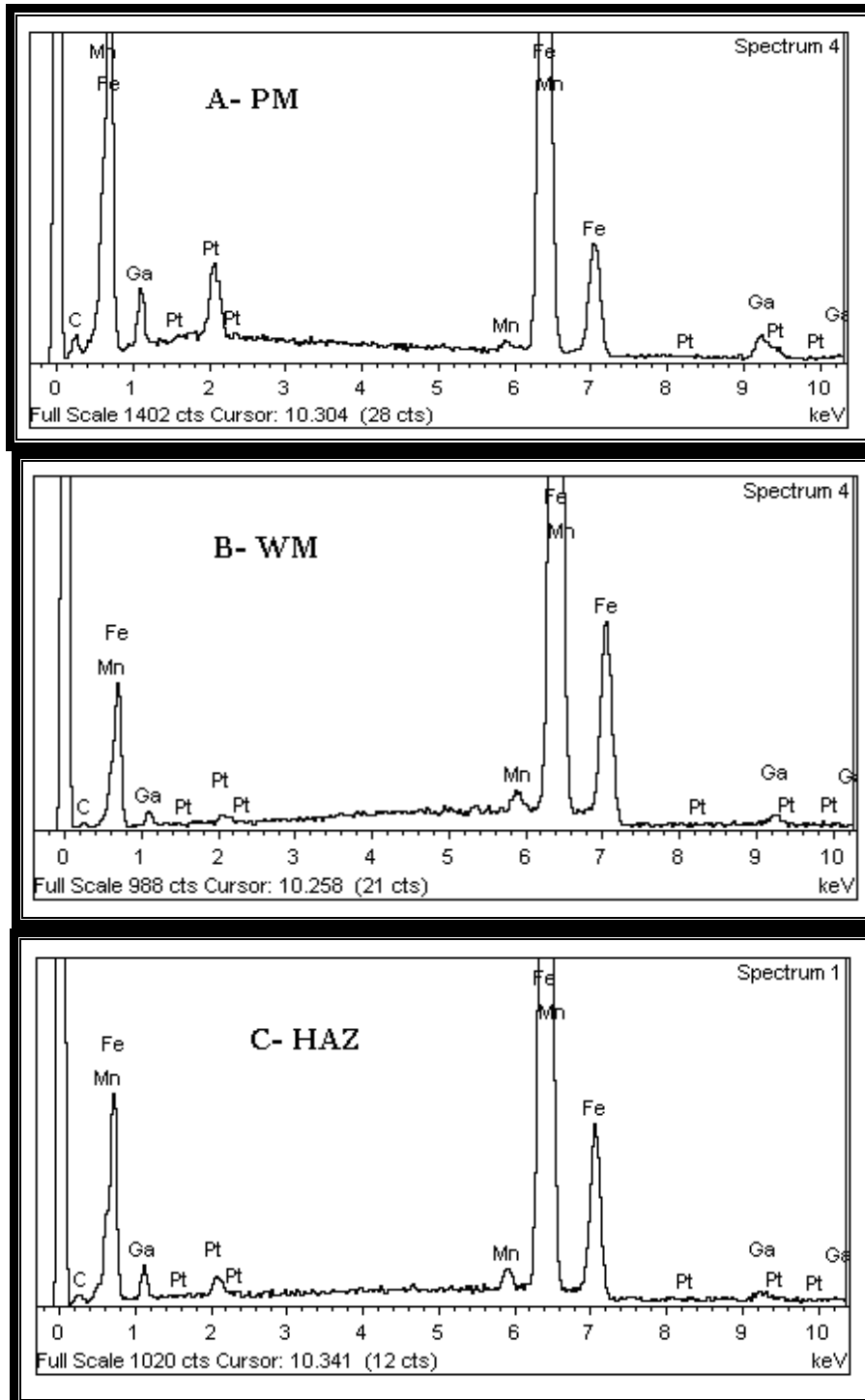


Figure 11-8: EDX spectra showing the elements for the A) Parent metal, B) Weld metal and C) HAZ

Element	Weight%	Atomic%
C	0.83	3.76
Mn	1.03	1.03
Fe	96.1	93.9
Ga	1.38	1.08
Pt	0.58	0.16
Totals	100.00	

Element	Weight%	Atomic%
C	3.75	16.2
Mn	0.56	0.53
Fe	82	76.4
Ga	6.48	4.84
Pt	7.19	1.92
Totals	100.00	

(A)

(B)

Element	Weight%	Atomic%
C	1.31	5.89
Mn	1.50	1.48
Fe	93.1	90.3
Ga	2.35	1.83
Pt	1.65	0.46
Totals	100.00	

(C)

Table 2 EDX analysis of the corrosion product film on the A) Parent metal, B) Weld metal, C) HAZ under flowing conditions at 70°C

11.3 XPS analyses

The advantage of using XPS lies not only in its chemical specificity but also in its surface sensitivity, since XPS is inherently sensitive only to the outermost surface layers, (few nanometers), of the corroding coupon, such that only the surface active species are detected. It is thought that it is these components that control corrosion.

The XPS scan of the sample (retrieved after 3 hours of immersion in inhibited, saturated CO₂ solution with inhibitor concentration of 30ppm and 3.5 % artificial sea water under 5000 rpm at 70⁰C) indicated the presence pf O, C, Cl, Fe and S at the sample surface.

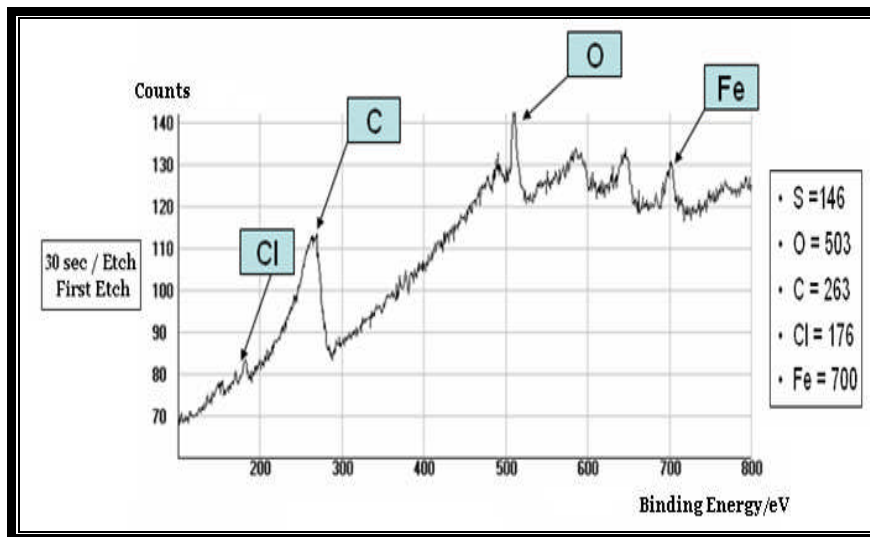


Figure 11-9: Initial high resolution XPS scan of the films found on the corrosion specimen at 70⁰C under inhibited and turbulent flow of 5000 rpm.

Figure 11-9, shows the high resolution XPS scans after etching the sample for the first time (30 second per etch). The high resolution spectra for the elements detected iron, oxygen, chlorine and carbon. An examination of the Fe peaks reveals a peak at a binding energy of 700eV. The scan of O binding energies reveals a single peak at 503eV associated with atmospheric contamination. The presence of O cannot be used to identify the presence of FeCO₃ because its characteristic peak should be at 531.9eV [139], superimposed with the dominant one at 503eV. The scan of the C binding energies reveals one peak at 263eV which corresponds to the steel surface with some corrosion product, while the Cl peak around 176eV can be associated to the solution residue.

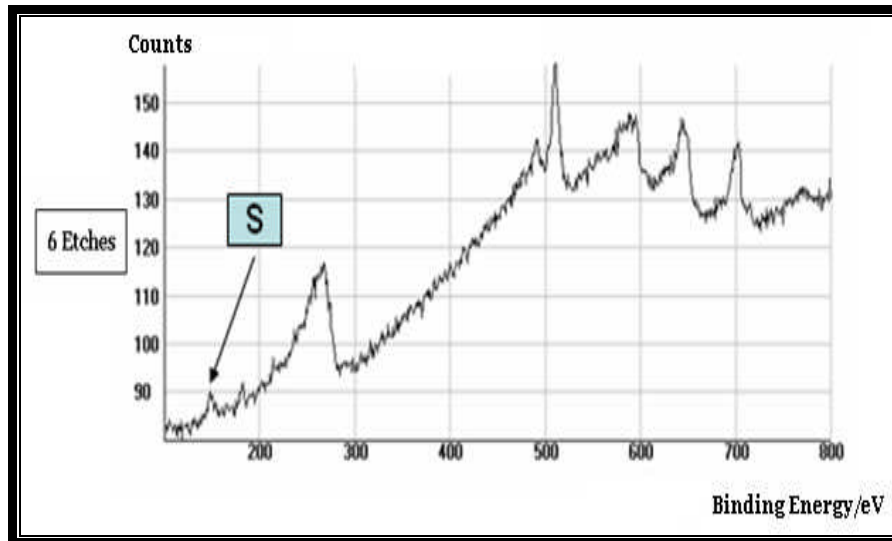


Figure 11-10: High resolution XPS scans after 6 etches showing the sulfur element detected at 70°C under inhibited and turbulent flow of 5000 rpm.

Figure 11-10, shows distinct peaks observed for similar elements to those of the first graph. The only difference is that the intensity of the peaks appears lower after further etching and sulfur ion peak was detected. The ions containing sulphur and oxygen can be for example thiosulphate, which was a component of the inhibitor.

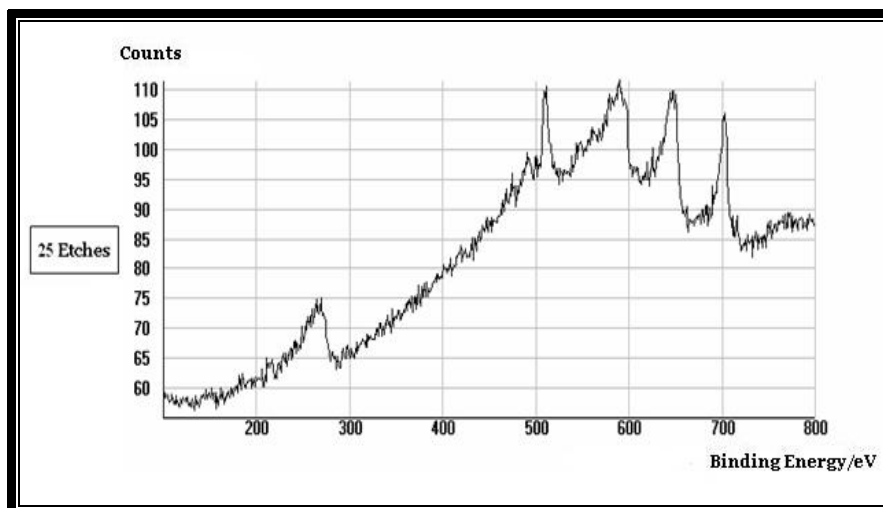
Corrosion inhibitors containing thiosulphate have been shown to be particularly effective in controlling PWC if applied at the correct dosage rate before the onset corrosion. If insufficient dosage of corrosion inhibitor is applied, including those containing thiosulphate PWC rates may be exacerbated [23].

It was proposed that the detection of the sulfur ion is usually attributed to a sulphide-type species. Consequently, if the sulfur detected originated from the thiosulphate, then it would appear to fragment when adsorbing to the steel surface. Moreover, with XPS analysis on mild steel strips immersed in 1.0 ppm thiosulphate, 3.5% NaCl saturated with CO₂ solutions at pH 5.5, without pre-corrosion provided an indication as to how thiosulphate inhibits a clean surface rather than on a pre-corroded one. Thiosulphate ions were not detected on the surface by instead S²⁻ ions, in small amount, and not everywhere [140].

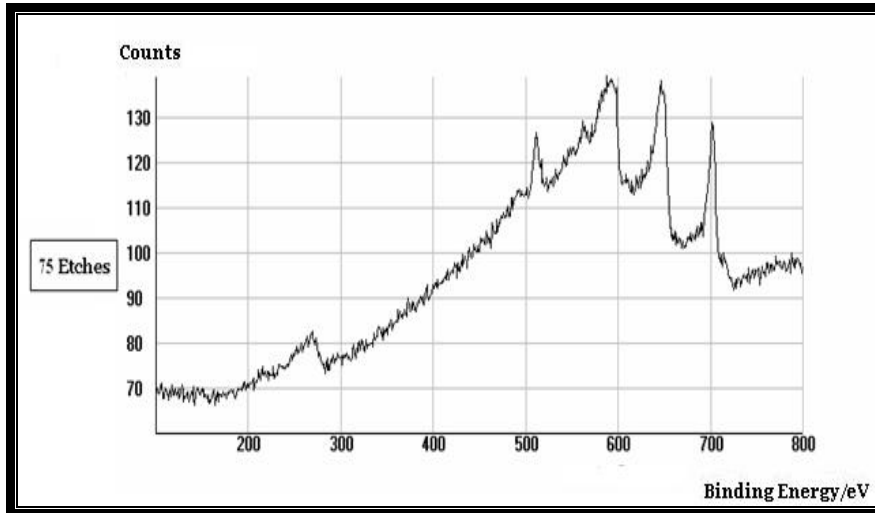
It is believed that the addition of inhibitor which is considered as mixed inhibitor in solution containing thiosulphate assist in the inhibition of the surfaces by adsorbing to the surface and producing stable iron sulfide film which can effectively form a corrosion inhibiting barrier to restrict the diffusion of ions or molecules to or from the metal surface. It was proposed that the corrosion inhibiting effect of the thiosulphate ions is more pronounced in the range of 5.0- 7.5 pH [141].

The O, Cl, S, and C peaks on the remaining Figures (11-11A-B), changed more significantly as they diminished in intensity towards lower as the etching increased. Furthermore the dominant Fe peak was consistent over the etching with an increase in the intensity of the peak as the substrate was progressively exposed.

Figure 11-12, shows etching time as a function of the etching counts for each element where an increase of the Fe element was noticed while for the rest elements where decreased.



(A)



(B)

Figure 11-11 (A-B) : High resolution XPS scans of the films found on the corrosion specimen at 70°C under inhibited and turbulent flow of 5000 rpm after 25 and 75 etches

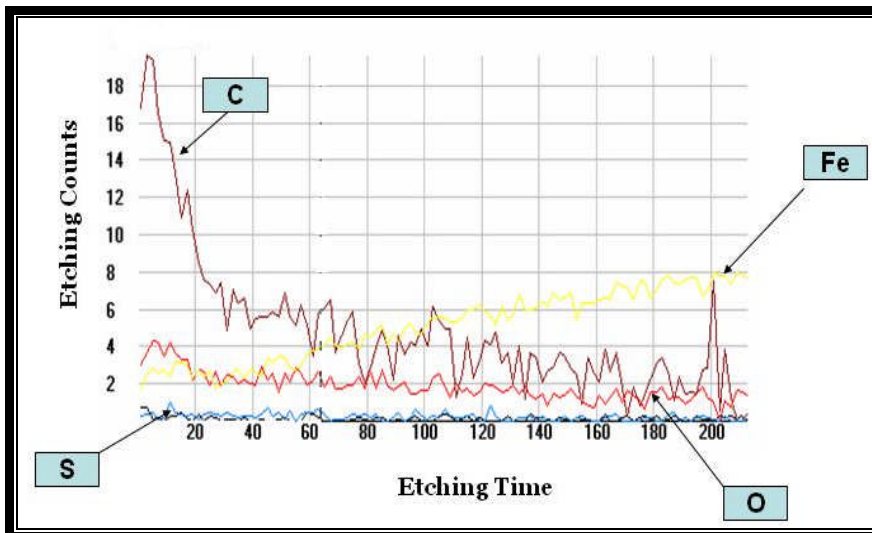


Figure 11-12: XPS depth profile for inhibited weldment under flowing (5000 rpm) and 70°C conditions

12 Conclusions

1. Measurements of the galvanic currents between the weld metal, heat affected zone and parent metal showed that for the uninhibited sample under static conditions, preferential corrosion occurred on the parent metal rather than the weld metal or HAZ. This is the ideal solution as corrosion is distributed over the large area of parent material.
2. The rates of galvanic and self-corrosion in each region of welded X65 pipeline steel exposed to artificial seawater saturated with carbon dioxide at 1 bar pressure were shown to increase with flow rate due to corrosion product film removal under high wall shear stress conditions.
3. In the presence of inhibitor at high flow rates, a current reversal took place and the weld metal became anodic, resulting in localised weld corrosion.
4. In general, increasing temperature lead to an increase in the self corrosion rates of all three weld regions, in both static and flowing conditions. An exception to this behaviour occurred at 70°C where in some cases the corrosion rate decreased due to formation of more protective film.
5. Localised corrosion was shown to be most severe with high flow rates at 70°C and this is typical of conditions found in oil and gas pipelines. This behaviour was attributed to corrosion product and inhibitor films being less protective on the weld metal than on other regions of the weld. This behaviour explains the localised weld corrosion that is sometimes observed in oil and gas pipelines.
6. Electrochemical impedance spectroscopy was shown to be a useful tool for studying corrosion processes in the presence of CO₂ and for evaluating the mechanism of the corrosion inhibitors.

7. EIS and LPR measurements showed a very good correlation when converted to corrosion rates. Although the EIS gave more reliable quantitative measurement, the LPR was preferred for qualitative investigation of the inhibitor performance.
8. EIS showed the presence of a corrosion inhibitor film on the metal surface, which was detected by a second semicircle on the impedance plot at high frequency.
9. By comparing the inhibitor film resistances for the three weld regions, it was shown that weld metal was the least protected and hence preferential corrosion occurred on the weld metal.
10. Based on XRD results, no significant FeCO_3 film was detected. This was shown to be due to the low level of dissolved iron concentration, Fe^{2+} , below that required for FeCO_3 precipitation. However, the corrosion product films found covering the surfaces of the three weld regions contained significant amounts of iron carbide (Fe_3C), which most likely formed as a consequence of preferential dissolution of the ferrite from the microstructure.
11. Surface observation by SEM showed that under uninhibited conditions, the residue of Fe_3C formed on the steel surface had a more important influence on the electrochemical behaviour than the poorly formed FeCO_3 products.
12. The unstable nature and uneven accumulation of the Fe_3C along the three weld regions may have a major impact on the protective nature of the thin corrosion product film and the role of the corrosion inhibitor, which was designed to interact with the corrosion product to form protective layers
13. A very striking point in this case was that the parent metal was anodic in the galvanic tests and this was attributed to the observed Fe_3C accumulation on the parent metal compared to the other welds regions.

14. By means of XPS it was demonstrated that sulphur was present on the surface of an inhibited sample and this is thought to have arisen from thiosulphate ions in the inhibitor.
15. From these results it was demonstrated that the performance of the inhibitors in CO₂ corrosion not only depends on their molecular structure, but also on the microstructure of the each weld region and its interaction with inhibitor film formation.
16. Overall, it appears that the surface films play an important role in effective inhibition and this inhibition is more effective on a clean surface rather than on a pre-corroded one.

13 Recommendations for future work

Suggestion for further work can be summarized as follows:

- A study of the effect of corrosion inhibitors should be undertaken at higher velocity and higher shear stress in order to assess the very severe conditions present in the field..
- Further work will be necessary at different temperatures as well as different concentrations and sizes of suspended sand to simulate certain down hole conditions that are very demanding for effective corrosion inhibition.
- The effect of pre-corrosion time, before addition of the inhibitor, and the effect of Fe^{2+} concentration should be taken in consideration.
- In field environments substances such as H_2S are sometimes present, along with dissolved CO_2 . Therefore a qualitative investigation on the effect of these substances on the corrosion process of the weldment in turbulent flow and high temperature can be recommended.
- More work has to be done in order to provide more evidence on the effect of microstructure and corrosion product films on inhibitor efficiency. Particularly, in order to clarify the influence of cementite accumulation on the surface it will be very useful to monitor the system for longer periods.

14 References

1. Fontana, M.G. (1987), *Corrosion Engineering*, 3rd edition, McGraw-Hill, New York
2. Newton, L.E., Jr. and Hausler, R.H. (2005), Methodology to Study Cost Of Corrosion, *Corrosion Engineering, Science and Technology*, Vol 40, No 4, University of Cantabria, Spain
3. Crolet, J.L. Bonis, J.L. (1991), Prediction of the Risks of CO₂ Corrosion in Oil and Gas Wells, *SPE Production Engineering*, Vol. 6, pp. 449-453.
4. Newton, L.E., Jr. and Hausler, R.H. (1984), *CO₂ Corrosion In Oil and Gas Production*, National Association Of Corrosion Engineering, Houston , Texas, USA
5. Lopez. D.A, Perez, T. and Simison, S.N, (2003), The Influence of Microstructure and Chemical Composition of Carbon and Low Alloy Steel in CO₂ Corrosion, A State-of-the-art Appraisal, *Material and Design* 24,16 July 2003 pp 561-575
6. I.G Winning, N.Bretherton ,A.McMahon ,Derek McNaughtan. (2004). Evaluation Of Weld Corrosion Behaviour and Application of Corrosion Inhibitors and Combined Scale/Corrosion Inhibitors. Aberdeen, UK.
7. Alawadhi,K, M.Robinson, G Winning; A. Chalmers (2008).Inhibition of Weld Corrosion in Flowing Brines Containing carbon dioxide. Corrosion, conference and Expo (March 16-20), paper 08622.
8. Schmitt, G. and Horst Meier, M. (2006), Fundamental Aspects of CO₂ Metal loss corrosion – part11: Influence of deferent parameters on CO₂ Corrosion Mechanism *61st Annual Conference & Exposition*, Corrosion, Germany
9. Turnbull, A., Coleman, D., Griffiths, A.J., Francis, P.E. and Orkney, L. (2003). Effectiveness of Corrosion Inhibitors in Retarding the Rate of Propagation of Localized Corrosion, *Corrosion*, Vol. 59, No. 3, pp. 250-257.
10. Ruzic, V. (2005) *Mechanisms of protective FeCO₃ scale removal in single-phase flow-accelerated CO₂ corrosion of mild steel*, PhD thesis, The University of Queensland, (unpublished).
11. Sun, Y and Nestic, S. (2004). A parametric study and modeling on localized CO₂ corrosion in horizontal wet gas flow. *Corrosion, paper no. 380 (Houston, TX: NACE International)*.
12. Clover.Y, Kinsella.B, Demarco.R.(2005). The influence of microstructure on the corrosion rate of various carbon steels. Australia, Journal of Applied Electrochemistry 35:139–149.

13. Schmitt, G. and Feinen, S. Effect of Anions and Cations on The Pit Initiation in CO₂ Corrosion of Iron and Steel, *Corrosion/2000, paper no.1, (Houston, TX: NACE International, 2000).*
14. Han, J., Yang, Y. Brown, B. and Nescic , S. "Electrochemical Investigation of Localized CO₂ Corrosion on Mild Steel", *Corrosion/2007, paper No. 07323 (Houston, TX: NACE,2007.)*
15. Corrosion Doctors, Retrieved June 9, 2006, from <http://www.corrosion-doctors.org/>
16. Shiffler D.A. (2006). Understanding and Modeling Galvanic Corrosion in Marine Environments. Arlington, *Corrosion, paper 06283, VA USA.*
17. Hara, T., Asahi, H., Kaneta, H. Effect of flow velocity on carbon dioxide corrosion behaviour in oil and gas environments. *CORROSION/98, paper 118, NACE International,Houston, TX.*
18. J.L. Dawson, J.W. Palmer, P.J. Moreland.(1997). Preferential Corrosion of Carbon Steel Weldments in Oil and Gas Production Systems". Paper No. 466, NACE International, Houston, Tx, USA.
19. "EFC 39. The Use of Corrosion Inhibitors in Oil & Gas Production",. Palmer et al Pub. May 2004.
20. Palmer, J.W. Hedges, W. Dawson, J.L.(2004). The Use of Corrosion Inhibitors in Oil & Gas Production. *NACE International. TX, USA.*
21. Nose, K. Asahi, H. Nice P.I. and Martin, J. Corrosion Properties of 3% Cr Steels in Oil and Gas Environments, *CORROSION'01, NACE International, Houston, TX, 2001, paper no. 82.*
22. Nice, P.I., Takabe H. and Ueda, M., The Development of Low Cr Steel OCTG for CO₂ Environments, *Eurocorr'2001, Lake Garda, Italy, 2001*
23. Queen, D. Lee, C-M. Palmer, J. and Gulbrandsen, E.(2004). Guidelines for the Prediction, Control and Monitoring of Preferential Weld Corrosion of Ferritic Steels in Wet Hydrocarbon Production Systems Containing CO₂. *1st Int. Symposium on Oilfield Corrosion, Paper no. SPE 87552, Society of Petroleum Engineers, Richardson, TX.*
24. Turgoose, S., Palmer, J. & Dicken, G. (2005). Preferential Weld Corrosion of 1% Ni Welds: Effect of Solution Conductivity and Corrosion Inhibitors", Paper No. 05275, *Corrosion, NACE, Houston.*
25. Denpo, K. and Ogawa, H., *UMIST Corrosion & Protection Centre 20th Anniversary Conference*, pp 285-288, 1992.

26. Lee, C-M. and Woollin, P. Preferential weld corrosion: Effects of weldment microstructure and composition, *CORROSION/2005*, paper no. 05277, (Houston, TX: NACE International,(2005).
27. Obeyesekere, N.U., Naraghi, A.R., Abhayarathna, A. and Prasad, R. Environmentally Friendly Corrosion Inhibitors for CO₂ Corrosion in North Sea Oil Fields, *CORROSION/2000*, paper no.00020 (Houston, TX: NACE, 2000).
28. Chalmers, Alison., McNaughtan, D., Winning, I.G. McNeil, S.(2006). Laboratory Development of a Corrosion Inhibitor for a North Sea Main Oil Line offering Enhanced Environmental Properties and Weld Corrosion Protection, *Corrosion*, No 06487, *NACE International (Houston, TX 2006)*.
29. D'Arcy, C.J. and Still, J.R.(2003), Trial and Tribulations of Inhibitors, *Corrosion Management*, Vol.56,pp16-20.
30. Omonua, J.O, (2004), *Evaluation of Oilfield Corrosion Inhibitors for Down-Hole Protection of Steels*, Msc thesis, Cranfield University, School of Industrial and Manufacturing Science, Offshore and Ocean Technology (unpublished).
31. Strutt, J.E, Turner, W.H.D, and Billingham (1982), Techniques for assessment and of prevention of weld corrosion, IBM 82, *NACE International*, Edinburgh, UK.
32. Otu,S, (2005). *Evaluation and Performance of Oilfield Corrosion Inhibitors for Down-hole Protection of Welded Steels*, Msc thesis, Cranfield University, School of Industrial and Manufacturing Science, Offshore and Ocean Technology.
33. Palmer, J.W. and Dawson, J.L. (1993), Inhibition of Weld Corrosion under Flowing Conditions – Its Development of Test Procedures, *Corrosion*, Houston, Texas, USA.
34. Olsen, S. Sundfær, B. and Enerhaug, J. Weld corrosion in C-steel pipelines in CO₂ environments – Comparison between field and laboratory data”, *Corrosion/97*, Paper no. 43, *NACE International (Houston, TX 1997)*.
35. Gulbrandsen, E. and Dugstad, A.(2005), Corrosion Loop Studies Of Preferential Weld Corrosion and Its Inhibition In CO₂ Environments’, *Corrosion*, No 05276, Kjeller, Norway.
36. Kinsella B; Tany. J.; Bailey S.(1998).Electrochemical impedance spectroscopy and surface characterization techniques to study carbon dioxide corrosion product scales. *Corrosion*, Houston, Tex., vol. 54, No10, pp. 835-842.

37. D.Vedapuri,C.Kang,D.Dhanbalan and M.Gopal,(2000).Inhibition of Multiphase Wet Gas Corrosion. Corrosion,paper No.43,(Huston,TX:NACE International.
38. Pots, B.F.M. Mechanistic Models for the Prediction of CO₂ Corrosion Rates under Multiphase Flow Conditions”, *Corrosion '95, NACE International, Houston, TX, 1995, paper no. 137*
39. De Waard, C., Lotz U. and Milliams, D.E. Predictive Model for CO₂ Corrosion Engineering in Wet Natural Gas Pipelines, *Corrosion*, Vol. 47, 1991, p. 976.
40. Nestic, S., Wang, J., Cai, Y. and Xiao, Integrated CO₂ corrosion – multiphase flow model, *Corrosion/04*, paper no. 626 (Houston, TX: NACE International, 2004).
41. Palacios, C.A. and Shadley, J.R.(1991) Characteristics of corrosion scales on steels in a CO₂ saturated NaCl brine, *Corrosion* ;47(2):122 –127.
42. Dugstad, A. (1998).Mechanism of protective film formation during CO₂ corrosion of carbon steel, *Corrosion ,Paper 31 Houston, TX: NACE International, 1998.*
43. Nestic, S., Postlethwaite, J., and Olsen, S. (1996), An electrochemical model for prediction of corrosion of mild steel in aqueous carbon dioxide solutions. *Corrosion*; 52(4):280 –294.
44. Dugstad, A. Formation of Protective Corrosion Films during CO₂ Corrosion of Carbon Steel, *Eurocorr'97, Norway, Trondheim, 1997.*
45. Nestic, S. Nordsveen, M, Nyborg, R. and Stangeland, A. Mechanistic Model for CO₂ Corrosion with Protective Iron Carbonate Films. *Corrosion/2001 Paper no. 40*, (Houston, TX: NACE International, 2001).
46. Nestic, S. and Lee, K.J., The mechanistic model of iron carbonate film growth and the effect on CO₂ Corrosion of Mild Steel. Paper no. 237 *Corrosion/02.*
47. Mora-Mendoza JL, Turgoose S. (2002). Fe₃C Influence on the Corrosion Rate of Mild Steel in Aqueous CO₂ Systems under Turbulent Flow Conditions. *Corrosion Science.* (44)1223 –1246.
48. Wang, H.B., Shi, H., Kang, C. and Jepson, W.P. (2001), Characterization of inhibitor and corrosion product film using electrochemical impedance spectroscopy (EIS). *Corrosion, Paper No. 01023.*
49. De Waard, C. and Milliams, D.E. (1975) *Corrosion* 31, 177.
50. Wang, F. (1999) *Modeling of Aqueous Carbon Dioxide Corrosion in Turbulent Pipe Flow*, Department of Chemical Engineering, University of Saskatchewan.

51. S.Nesic, L.Lunde. (1994) Carbon Dioxide Corrosion of Carbon Steel in Two-Phase Flow. *Corrosion*, Vol.50, p.717.
52. Wang, S., George, K. and Nesic, S. High Pressure CO₂ Corrosion Electrochemistry and the Effect of Acetic Acid, *Corrosion'04, NACE International, Houston, TX, paper no. 375*.
53. Sun, Y and Nesic, S. A Parametric Study and Modelling on Localized CO₂ Corrosion in Horizontal Wet Gas Flow", *Corrosion'04, NACE International, Houston, TX, 2004, paper no. 380*.
54. Dugstad A (1998).Mechanism of protective film formation during CO₂ corrosion of carbon steel, *Corrosion, Paper 31 Houston, TX: NACE International, 1998*.
55. E. W. J. van Hunnik, B. F. M. Pots and E. L. J. A. Hendriksen. (1996). The formation of protective FeCO₃ corrosion product layers in CO₂ corrosion. *CORROSION*, NACE International, Houston, TX, *paper no.6*.
56. Munoz, A., Genesca, J., Duran, R. and Mendoza, J. Mechanism of FeCO₃ Formation on API X70 Pipeline Steel in Brine Solutions Containing CO₂, *Corrosion'05, NACE International, Houston, TX, 2005, paper no. 297*.
57. Dugstad, A. The Importance of FeCO₃ supersaturation on the CO₂ corrosion of carbon steels, *Corrosion'92, NACE International, Houston, TX, 1992, paper no.14*
58. Kinsella, B.J., Tan, Y-J, and Bailey, S. (1998). Studies of CO₂ Corrosion Product Scales using Electrochemical Impedance Spectroscopy and Surface Characterisation Techniques, *Corrosion - NACE*, 54, 835-842
59. Olsen, S. and Dugstad, A. (1991) Corrosion under dewing conditions, *Corrosion, Paper No. 472*.
60. Nomogram for predicting CO₂ corrosion of carbon steel is based on the deWaard-Milliams equation, Retrieved June, 20, from <http://www.xs4all.nl/~cdewaard/#CO2>.
61. Schmitt, G., Bosch, C., Mueller, M. and Siegmund, G. A Probabilistic Model for Flow Induced Localized Corrosion, *Corrosion'00, NACE International, Houston, TX, 2000, paper no. 49*.
62. Schmitt, G. and Mueller, M. Critical Wall Shear Stresses in CO₂ Corrosion of Carbon Steel, *Corrosion'99, NACE International, Houston, TX, 1999, paper no.44*.
63. Dugstad, A., Lunde, L. and Videm, K. Parametric Study of CO₂ Corrosion of Carbon Steel, *Corrosion'94, NACE International, Houston, TX, 1994, paper no.14*
64. .Nesic, S., Nordsveen, M., Nyborg, R. and Strangeland, A. A Mechanistic Model for CO₂ Corrosion with Protective Iron Carbonate Films, *Corrosion'01, NACE International, Houston, TX, 2001, paper no. 40*.

65. Netic, S. and Lee, K.L.J. A Mechanistic Model for Carbon Dioxide Corrosion of Mild Steel in the Presence of Protective Carbonate Layers – Part 3: Film Growth Model, *Corrosion*, Vol. 59, 2003, pp. 616- 628.
66. Fontana, M.G. (1986) *Corrosion Engineering*: McGraw-Hill, p.556.
67. Efir, K. D, (2000), *Jet Impingement Testing for Flow Accelerated Corrosion*, Corrosion, Corrosion International, Inc, The Woodlands, Texas, USA.
68. Garverick, S.L.(1994), *Corrosion in the Petrochemical Industry – Essential Research*, ASM International; The Material Information Society; USA, pp.259-295.
69. Bard, A.J. and Faulkner, L.R. (1980) *Electrochemical Methods, Fundamentals and Applications*; Wiley& Sons, USA.
70. Chen, T.Y., Moccari, A.A. and MacDonald, D.D. (1992) Development of Controlled Hydrodynamic Techniques for Corrosion Testing; *Corrosion*, V.48; no 3 March, pp.239-255.
71. Schmitt, G. and Bakalli, M. A Critical Review of Measuring Techniques for Corrosion Rates under Flow Conditions, Laboratory of Corrosion Protection Germany, *Corrosion NACE 2006 paper No 06539*.
72. Gabe, D.R., Wilcox, G.D., Gonzalez-Garcia, J. and Walsh, F.C. The Rotating Cylinder Electrode: Its Continued Development and Application, *Journal of Applied Electrochemistry* 28(1998) 759.
73. Pine Research Instrumentation. Study of Mass-Transport Limited Corrosion Using Rotated Cylinder Electrodes. Technical Note, March 2006.
74. Papavinasam, S., Revie, R.W., Attard, M., Demoz, A. and Michaelian, K. (2003), Comparison of Laboratory Methodologies to Evaluate Corrosion Inhibitors for Oil and Gas Pipelines, *Corrosion*, Vol.59, No10, pp 897-912.
75. Efir, K.D., Wright, E.J., Boros, J.A. and Hailey, T.G. (1993), Correlation of Steel Corrosion in Pipe Flow with Jet Impingement and Rotating Cylinder Tests, *Corrosion*, 49, 992.
76. Gabe, D.R. and Wilcox, G.D. (1988), Influence of Turbulent Flow on the Localized Corrosion Process of Mild Steel With Inhibited Aqueous Carbon Dioxide System' ,*Journal of Applied Electrochemistry*, 28, 759-780.
77. Silverman, D.C. (1988), Rotating Cylinder Electrode – Geometry Relationships for Prediction of Velocity- Sensitive Corrosion, *Corrosion* 44 (1988) 42.
78. Al-Sayed, M.S.A.(1989) Effect of Flow and pH on CO₂ Corrosion and Inhibitions, PhD Thesis, UMIST, (unpublished).

79. Finnemore E.J. and Franzini J.B. (2002)., Fluid Mechanics with Engineering Applications', Tenth edition, McGraw Hill Book Company, New York.
80. Turbulent Wake Flow behind a Circular Cylinder, Retrieved July, 28, from <http://www.eng.fsu.edu/~shih/succeed/cylinder/cylinder.htm>.
81. Chen TY.,Moccari A.A , Mac Donald D.(1992). Development of Controlled Hydrodynamic Techniques for Corrosion Testing. *Corrosion*, V.48, No 3, 239-255.
82. Chesnut, G. and Choi, H.J. (1994), Laboratory Testing and Selection of Corrosion Inhibitors for the Continuous Application in multiphase pipelines', *Corrosion, paper r# 35, NACE, Houston, TEXAS, USA*
83. .Nesic , S., Solvi, G.T. and Skjerve, S. (1997). Comparison of Rotating Cylinder and Loop Methods for Testing CO₂ Corrosion Inhibitors, *British Corrosion Journal*, 2(4), p.269-277.
84. Dougherty, J.A. and Stegmann, D.A.W. (1996), The Effect of the Flow on Corrosion Inhibitor Performance, *Chemical Treatment*, p47-53, St. Louis, USA.
85. Denpo, K. and Ogama, H. (1993) Fluid Flow effects on CO₂ Corrosion Resistance of Oil Well Materials, *Corrosion*, 49(6), p.442.
86. Dawson, J.L.,shih, C. and Miller, R.G. (1990) Inhibitor Evaluation Under controlled Hydrodynamic Shear, Paper #14,Vol (1), NACE, Houston, Texas, *Material Performance*, p43.
87. Papavinasam, S., Revie, R.W. and Attard, M. (1999), *Inhibitor Selection for Internal Corrosion Control of Pipelines:1. Laboratory Methodologies*, Ottawa, Ontario, Canada.
88. De Marco, R., Durnie, W., Jefferson, A., Kinsella, B. and Crawford, A. (2002), Persistence of Carbon Dioxide Corrosion Inhibitors', *Corrosion*, Vol 85, No.4, pp.354-363.
89. Shi-Liang Fu John G, Antoine M. (1996). Corrosion Resistance of Some Downhole Tubing Materials and Inhibitor Effectiveness in Sweet Environments. *Corrosion, NACE International, Houston, TX, paper no.21.*
90. Bartos, M. and Watson, J.D. (2000) Oilfield Corrosion Inhibition under Extremely High Shear Conditions, *Corrosion*, Sugar Land, TX, USA.
91. Paolinelli, L.D, Perez, T and Simison, S.N.(2008). The Effect of Pre-Corrosion and Steel Microstructure on Inhibitors Performance in CO₂ Corrosion. *Corrosion Science*, Pages 2456-2464, Vol 50.No 9.

92. S. Sawada, J. Kubo, C.L. Page.(2007). Electrochemical injection of organic corrosion inhibitors into carbonated cementitious materials: Part 1. Effects on Pore Solution Chemistry. *Corrosion Science*. (49) 1186–1204
93. Nathan, C.C. (1973) *Corrosion Inhibitors*, National Association of Corrosion Engineering, Houston, Texas, USA.
94. Gulburandsen, E., Nesic, S., Stagland, A., Burchart, T. and Sundfaer, B. (1998) Effect of Pre Corrosion on the Performance of Inhibitors for CO₂ Corrosion of Carbon steel, *Corrosion* , No13, Houston, TX, USA.
95. Lopez. D.A, Perez, T. and Simison, S.N, (2003), The Influence of Microstructure and Chemical Composition of Carbon and Low Alloy Steel in CO₂ Corrosion, A State-of-the-art Appraisal', *Material and Design* 24,16 July 2003, pp. 561-575.
96. Kumator, G.Hagher, 2004, 'Novel Methods to Control Corrosion under Thermal Insulation', Cranfield University, School of Industrial and Manufacturing Science, Offshore and Ocean Technology.
97. Robinson,M.J.(2005) Corrosion in the offshore environment. Cranfield University.
98. Rothwell, A.N (1986). The preferential corrosion of weldments', UMIST University, Thesis No 773 (unpublished).
99. Shreir,L.L,jarman,R.A.,andBurstien,GT(1994),corrosion,Vol.1,(3rd edition),Butterwo rth-Heinemann,Woburn,MA,USA.
100. D.A.Lopez , S.N. Simison,S.R.(2005). Inhibitors Performance in CO₂ Corrosion EIS Studies on the Interaction between their Molecular Structure and Steel Microstructure. *Corrosion science*, Volume 47, Issue 3, Pages 735-755.
101. Srdjan Nesic. (2007). Key issues Related to Modelling of Internal Corrosion of Oil and Gas Pipelines - A review *Corrosion Science*, (49) 4308–4338.
102. L.J. Oblonsky,G.R. Chesnut, T.M. Devine.(1995).*Corrosion*, (51) 891.
103. E.C. French,R.L. Martin,J.A. Dougherty, P.(1989).*Corrosion*, 28 (8) 46.
104. H. Malik, (1995).*Corrosion* 51 (4) 321.
105. D.A. Lopez, S.N. Simison, S.R. de Sanchez, (2003) The influence of Steel Microstructure on CO₂ Corrosion. EIS Studies on the Inhibition Efficiency of benzimidazole, *Electrochim. Acta*, (48) 845–854.
106. Lopez DA, Schreiner WH. (2004). The Influence of Carbon Steel Microstructure on Corrosion Layers: An XPS and SEM Characterization. *Appl Surf. Sci*, 77-97.
107. Paolinelli, L.D., T. Perez, and S.N. Simison,(2004). *CONAMET/SAM*, Paper 81.

108. Paolinelli, L., T. Perez, and S.N. Simison, (2006). The Influence of Cr content on the efficiency of inhibitor of C-Mn Steel CO₂ Corrosion. *NACE &Expo Corrosion*,TX,USA, Paper 06369.
109. Paolinelli, L., T. Perez, and S.N. Simison, (2007). The influence of Steel Microstructure, Chemical Composition and Pre-corrosion CO₂ Corrosion Inhibitor Efficiency. *NACE &Expo Corrosion* , Paper 07311, 2007.
110. Kapusta, S. and S. Canter. (1994). *CORROSION*, NACE. Paper 10.
111. Gulbrandsen E, Nyborg R, Loland T, Nisancioglu K,(2000). Effect of steel microstructure and composition on inhibition of CO₂ corrosion. *Corrosion*, Paper No 23, Houston, TX: NACE International.
112. Mora-Mendoza,S. Turgoose. (2002).Influence of Turbulent Flow on the Localized Corrosion Process of Mild Steel with Inhibited Aqueous Carbon Dioxide Systems. *Corrosion Science*,vol.58,No.7,pp.608-618.
113. C. C. Nathan.(1973), 'Corrosion inhibitors' National Association of Corrosion engineering ,NACE, Houston,Texas,USA.
114. J. Kvarekval and E. Gulbrandsen "high Temperature ad High Flow Velocity Tests for CO₂ Corrosion "Institute for Energy Technology (IFE),Paper 01025 corrosion 2001.
115. S. Nestic and K.J.Lee. (2002). "The Mechanistic Model of Iron Carbonate Film Growth and the Effect on CO₂ Corrosion of Mild Steel". Paper No.237, *CORROSION*.
116. X. Jiang, Y.G. Zheng, W. Ke,(2004), 'Effect of Flow Velocity and Entrained Sand on Inhibition Performances of Two Inhibitors for CO₂ Corrosion of N80 steel in 3% NaCl solution', *Corrosion Science*,47,shenyang,China.
117. Chen Chevron, Huey J.(1999). Evaluation the Effects of Test methods and Fluids Compositions on The performance of Corrosion Inhibitors. *Petroleum Technology Company*, paper No 10, CA.
118. J.L. Mora-Mendoza, J.G. Chacon-Nava, G. Zavala-Olivares, M.A. Gonzalez-Nunez, and S. Turgoose, (2002). Influence of Turbulent Flow on the Localized Corrosion Process of Mild Steel with Inhibited Aqueous Carbon Dioxide Systems. *Corrosion*, Vol.58, No7, pp 608-617.
119. J.W. Palmer. (2006). Corrosion Control By Film Forming Inhibitors. *NACE &Expo Corrosion*. Paper number 06119,UK

120. P.Altoe, G.PA.(1996). Evaluation of Oil field Corrosion Inhibitors on CO₂ Contain Media: A kinetic study, Elsevier science – *Electrochemical Acta*, vol 41 pp 1165-11172, UK
121. Bartos, M and Watson, J. D. (2000). Oilfield Corrosion Inhibition under Extremely High Shear Conditions. *Corrosion*, Orlando, USA, Paper 68.
122. Retrieved June 9, 2006, from <http://www.corrosion-doctors.org/>.
123. Pascale, Bommersbach. (2006). Hydrodynamic Effect on the Behavior of a Corrosion Inhibitor film: Characterization by Electrochemical Impedance Spectroscopy, France, *Electrochemical Acta*, (51) 4011–4018.
124. J. Tan, S. Bailey, B. Kinsella. (1996). *Corrosion science*, (38) 1681-1690.
125. Y. Chen, W.P. Jepson.(1999). EIS Measurement for Corrosion Monitoring under Multiphase Flow Conditions, *Electrochemical Acta*, Vol 44, Pages 4453-4464, Athens, USA.
126. Hussain, E. A. M. (1994). Evaluation of Corrosion Protective Coatings on Steel Using Electrochemical Impedance Spectroscopy.Msc thesis, Cranfield University.
127. N. Ochoa, F. Moran, N. Pebere, B. Tribollet. (2005). *Corrosion Science*. (47) 593.
128. S.P.Parakala. (2005). EIS Investigation of carbon Dioxide and Hydrogen Sulfide Corrosion under film forming. PhD Thesis, Ohio University.
129. Walter, G.W. (1986). A review of impedance plot methods used for Corrosion Performance Analysis of Painted Metals. *Corrosion Science*, 26 (9), p. 681-703.
130. Hemmingsen, H. Hovdan, P. Sanni, N.O. Aagotnes.(2002). The Influence of Electrolyte Reduction Potential on Weld Corrosion. *Electrochimica Acta*.(47), 3949-3955.
131. Y.J.Tan,S.B.Bailey and B.Kinsella.(1996). An Investigation of the Formation and Destruction of Corrosion Inhibitor Films Using Electrochemical Impedance Spectroscopy (EIS). *Corrosion Science*, Vol.38, No.9, pp. 1545-1561.
132. Nestic , S., Solvi, G.T. and J.Enerhaug, S. (1995). Comparison of Rotating Cylinder and Pipe Flow Tests for flow-Sensitive carbon Dioxide Corrosion.Vol.51, No.10. *NACE International*. TX.
133. E. Blasco-Tamarit, A. Igual-Munoz, J. Garca Anto.(2007) Effect of temperature on the galvanic corrosion of a high alloyed austenitic stainless steel in its welded and non-welded condition in LiBr solutions.. *Corrosion Science*, Vol.49, No.9, pp. 4472-4490.

134. J. Kvarekval and E. Gulbrandsen. (2005). "Effect of Oxygen Contamination on Inhibition studies in carbon dioxide Corrosion". Corrosion, NACE International, paper No 01054, TX, USA.
135. M. Mendoza. (1997). Kinetic Studies of CO₂ Corrosion Processes under Turbulent Flow. PhD Thesis, UMIST.
136. Wills, P,(1998), *Sweet Corrosion in pipelines under two Phase flow*.Msc thesis, Cranfield University.
137. E.McCafferty,J (1997) *Corrosion Science*, Vol.39, pp. 243.
138. K. Videm, "The Influence of pH and Concentration of Bicarbonate and Ferrous Ions on the CO₂ Corrosion of Carbon Steels," CORROSION'93, NACE International, Houston, TX, 1993, paper no.83.
139. J.K. Heuer, J.F. Stubbins (1999). An XPS characterization of FeCO₂ films from CO₂ corrosion. *Corrosion Science*. (30) 1231–1243.
140. International Application Published under patent cooperation treaty (PCT), No WO 98/11277-19 march1998, Aberdeenshire , UK.
141. F. Zucchi, G. Trabanelli, C. Monticelli, V. Grassi (2000). SCC inhibition of a C-steel in acidic 5% NaCl solutions in the presence of thiosulphate. *Corrosion Science*. (42), 505-515

15 Appendixes

Appendix (1)

Calculation of corrosion rate from LPR measurements

Given area $A=32 \text{ cm}^2$ for steel under static conditions

From the figure below: $R_p=1500 (\Omega \text{ cm}^2)$

From Eq. 25
$$i_{corr} = \frac{B}{R_p} = \frac{15}{1500} = 0.01 \frac{\text{mV}}{\Omega \text{ cm}^2} \quad \text{Where } \frac{\text{V}}{\Omega} = \text{Amp}$$
$$= 0.01 \frac{\text{mA}}{\text{cm}^2} = 10 \frac{\mu\text{A}}{\text{cm}^2}$$

We know that $1 \frac{\mu\text{A}}{\text{cm}^2} = 0.0116 \frac{\text{mm}}{\text{y}}$ then the corrosion rate = $0.116 \frac{\text{mm}}{\text{y}}$ or $0.12 \frac{\text{mm}}{\text{y}}$

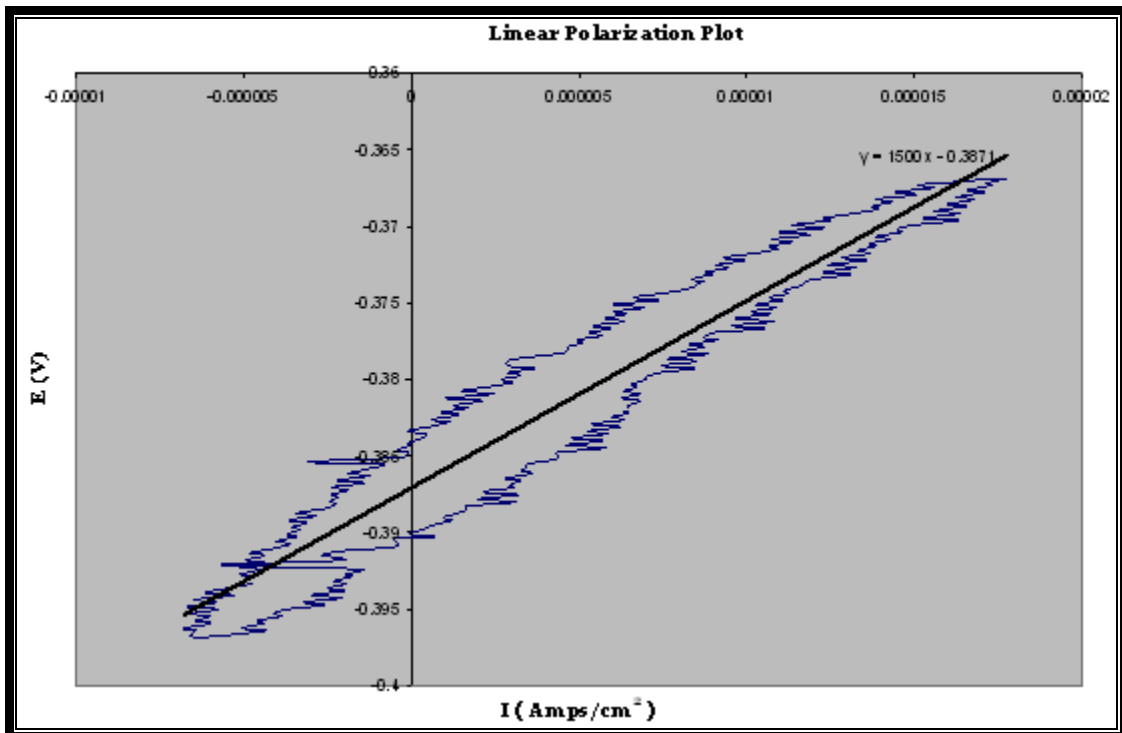


Figure 15-1: LPR result for carbon steel under static conditions

Appendix (2)

Calculation of shear stress

For an incompressible fluid ($\gamma = \rho * g = \text{constant}$) we can integrate an equation for shear stress from point 1 to another point on the same stream line. In this case we are considering a parallel channel with a gap between the two parallel plates , where the distance between them is L from the following derivation of Bernoulli's theorem : -

$$\frac{p_1}{\gamma} + \frac{V_1^2}{2g} + Z_1 = \frac{p_2}{\gamma} + \frac{V_2^2}{2g} + Z_2 + hf \quad (4)$$

Where $V_1 = V_2$ & $Z_1 = Z_2$

$$\text{Where } hf \text{ is wall friction loss} = \frac{p_1 - p_2}{f} \quad (5)$$

$$\text{From Darcy Equation } hf = \frac{fL}{D_h} \times \frac{V^2}{2g} f \quad (6)$$

Substitute (5) in (6)

$$\frac{fL}{D_h} \times \frac{V^2}{2g} = \frac{P_1 - P_2}{\gamma} \quad (7)$$

Where D_h for flow channel = $4 R_h$ & $R_h = A / p = A / 2(b + h)$

Where p is parameter & b is channel length & h is the gap between two plates

Substitute (5) in (4)

$$\frac{fL}{4 \times \frac{bh}{2(h+b)}} \times \frac{V^2}{2g} = \frac{\Delta p}{\gamma} \quad \text{Assume } h + b \approx b$$

After rearranging

$$f \frac{\gamma V^2}{8g} = \frac{h\Delta p}{2L} \quad \text{Where } \left(\frac{h\Delta p}{L} = \tau \right)$$

Hence the final equation for channel flow shear stress is:-

$$\tau = f \frac{\gamma V^2}{8g} \quad (8)$$

To establish equation for friction factor substitute flow channel hydraulic radius in (3)

$$f = \frac{32 \times \nu}{V \times h}$$

Numerical calculation for flow velocity and shear stress for the flow channel

Given information

(ρ) is the sea water density (1025 kg/m³)

(μ) water viscosity (10.72 x 10⁻⁴ Pa .s)

($\nu = \mu / \rho$) Kinematics viscosity of sea water = (1.046 x 10⁻⁶ m²/s)

Flow channel dimensions = L x h = 39 mm X 1 mm = 39mm² → 39 x 10⁻⁶ m²

Where

L is channel flow Length in (m)

h is the gap between the two parallel plates in (m)

$$\text{Average velocity (V)} = \frac{Q}{A} = \frac{2.41 \times 10^{-5}}{39 \times 10^{-6}} = 0.61 \text{ m/s}$$

$$\text{Reynolds number (Re)} = \frac{\rho V D_h}{\mu} = \frac{1024 \times 0.61 \times 0.002}{10.72 \times 10^{-4}} = 1165.3 \text{ (laminar Flow)}$$

$$\text{Friction factor (f)} = \frac{32 \times \nu}{V \times h} = \frac{32 \times 1.046 \times 10^{-6}}{0.6 \times 0.001} = 0.0556 \text{ m/s}^2$$

$$\text{Hence the shear stress } \tau = f \frac{\gamma V^2}{8g} = \frac{0.0556 \times 1024 \times 0.6^2}{8} = 2.56 \text{ Pa}$$

Appendix (3)

Calculation of RCE hydrodynamic parameters

For 500 rpm

Given parameters:

$$d_{RCE} = 20 \text{ mm} = 0.02 \text{ m} \qquad D_{H_2CO_3} = 2 \times 10^{-9} \frac{m^2}{s}$$

$$\mu = 1.07 \times 10^{-3} (Pa.s) \qquad \rho = 1024 \frac{kg}{m^3}$$

$$u = \frac{\pi d_{RCE} (rpm)}{60} = \frac{\pi (0.02)(500)}{60} = 0.52 \frac{m}{s}$$

$$Re = \frac{\rho u d_{RCE}}{\mu} = Re = \frac{(1024)(0.52)(0.02)}{1.07 \times 10^{-3}} = 9,950 \quad (\text{Turbulent Flow})$$

$$\text{From Eq 20 } \tau_{RCE} = 0.079 Re_{RCE}^{-0.3} \rho u_{RCE}^2$$

$$\tau_{RCE} = 0.0791(9952.89)^{-0.3} (1024)(0.52)^2 = 1.38 Pa$$

$$Sc = \frac{1.07 \times 10^{-3}}{(1024)(2 \times 10^{-9})} = 522$$

$$Sh = 0.0791(9952.89)^{0.7} (522.46)^{0.356} = 461$$

Appendix (4)

Mass calculation of Fe^{2+} corroded from known area and test duration of the three weld regions (PM, WM, HAZ).

For the Parent Metal:

$$A = 4.3\text{cm}^2, \rho = 7.9 \frac{\text{g}}{\text{cm}^3} \text{ and Total corrosion rates} = \text{LPR} + \text{Galvanic} = 1.24 \frac{\text{mm}}{\text{y}} = 0.124 \frac{\text{cm}}{\text{y}}$$

Mass of Fe corroded:

$$= \frac{(0.124) \cdot (4.3) \cdot (7.9)}{(24) \cdot (365)} = 0.0004808 \frac{\text{g}}{\text{y}}$$

Mass in 3 h test:

$$= (0.0004808) \cdot (3) = 0.00144 \frac{\text{g}}{3\text{h}} = 1.44 \frac{\text{mg}}{3\text{h}}$$

We know that the solution volume is 0.8 L. Hence concentrate of Fe^{2+}

$$\frac{1.442}{0.8} = 1.803 \text{ppm}$$

$$\text{Given } 1\text{ppm} = \frac{1\text{mg}}{\text{L}} = \frac{0.001\text{g}}{\text{L}} \text{ then the estimate } \text{Fe}^{2+} \text{ dissolve in the solution} = 1.803\text{ppm}$$

Similar equations were used for the WM and HAZ with given

$$\text{Area WM} = 1.08\text{cm}^2 \text{ \& Total Corrosion rate } Cr_T = 0.163 \frac{\text{cm}}{\text{y}}$$

$$\text{HAZ} = 0.54\text{cm}^2 \text{ \& Total corrosion rate } Cr_T = 0.22 \frac{\text{cm}}{\text{y}}$$

So the total estimation of Fe^{2+} in the solution from the weld regions

$$\text{Total} = 1.803 + 0.597 + 0.401 = 2.80 \text{ppm}$$

Appendix (5)

List of Symbols

Symbol	Meaning	Units
R_{FeCO_3}	Precipitation rate of iron carbonate	mm/y
K_{sp}	Solubility limit	-
$\frac{A}{V}$	Surface area –to–volume ratio	1/m
C_r	Corrosion rate,	mm/y
$C_{Fe^{2+}}$	Iron ions concentration	kmol/m ³
$C_{CO_3^{2-}}$	carbonate ions concentration	kmol/m ³
CO_3^{-2}	Carbonate ions	-
HCO_3^{-}	Bicarbonate ions	-
T	Absolute temperature,	K ⁰
ν	Kinematics viscosity	
U	velocity	m/s
b_a, b_c	Anodic and cathodic Tafel slope	V/decade
D	Diffusion coefficient	m ² /s
F	Faraday constant	(96,490 C/equiv.)
i_a	Anodic current density	A/m ²
i_c	Cathodic current density	A/m ²
k_m	Mass transfer coefficient	m/s
P_{CO_2}	Partial pressure of carbon dioxide gas	Bar
μ	Viscosity	Pa .s
d_{RCE}	Diameter of the rotating cylinder electrode	mm

τ_{RCE}	Shear stress of the Rotating Cylinder Electrode	N/m^2
f	Friction coefficient	-
h	Gap between two plates (Flow channel)	mm
ρ	Density	Kg/m^3
Re	Reynolds number	-
Sc	Schmidt number	-
Sh	Sherwood number	-

Appendix (6)

GLOSSARY

Activation control

Ac corrosion rate is activation controlled when the rate is determined by how fast a metal electrode is able to transfer its electrons to electrolyte electrochemically active species.

Anode

The electrode at which oxidation or corrosion of some component occurs (opposite of cathode). Electrons flow away from the anode in the external circuit.

Anodic current

Refers to the electrical current withdrawn from test electrode during (oxidation) polarization.

Anodic inhibitor

A chemical substance or combination of substances that prevent or reduce the rate of the anodic or oxidation reaction by a physical, physico-chemical or chemical action.

Anodic polarization

The change in the initial anode potential resulting from current flow effects at or near the anode surface. Potential becomes more noble (more positive) because of anodic polarization

Brine

Seawater containing a higher concentration of dissolved salt than that of the ordinary ocean

Cathode.

The electrode of an electrolytic cell at which reduction is the principal reaction. Typical cathodic processes are cation' taking up electrons and being discharged, oxygen being reduced and the reduction of an element or group of elements. Contrast with anode.

Cathodic inhibitor.

A chemical substance or mixture that prevents or reduces the rate of the cathodic or reduction reaction by physical, physico-chemical or chemical action.

cathodic polarization.

Polarization of the cathode; change of the electrode potential in the active (negative) direction due to current flow; a reduction from the initial potential resulting from current flow effects at or near the cathode surface. Potential becomes more active (negative) because of cathodic polarization.

Current density.

The current flowing to or from a unit area of an electrode surface, generally expressed as amps per sq m or milliamperes per sq cm.

Heat-affected zone.

That portion of the base metal that was not melted during welding, but whose microstructure and mechanical properties were altered by the heat; Refers to area adjacent to a weld where the thermal cycle has caused microstructural changes which generally affect corrosion behavior

Diffusion coefficient.

A factor of proportionality representing the amount of substance diffusing across a unit area through a unit concentration gradient in unit time.

Electrochemical cell.

An electrochemical system consisting of an anode and a cathode in metallic contact and immersed in an electrolyte. (The anode and cathode may be different metals or dissimilar areas on the same metal surface).

Inhibitor.

A chemical substance or combination of substances that, when present in the environment, prevents or reduces corrosion without significant reaction with the components of the environment.

Open-circuit potential.

The potential of an electrode measured with respect to a reference electrode or another electrode when no current flows to or from it.

Parts per million.

A measure of proportion by weight, equivalent to one unit weight of a material per million (10^6) unit weights of compound. One part per million is equivalent to 1 mg/g

Polarization resistance.

The slope (dE/di) at the *corrosion potential* of a potential (E)/current density (i) curve. Also used to describe the method of measuring corrosion rates using this slope.

Sweet corrosion

Corrosion occurring in oil or gas wells because of the high CO₂ content of the crude from these areasfluid.